Winter 2001

Nonlinear Response and Fatigue Estimation of Surface Panels to White and Non-White Gaussian Random Excitations

Jean-Michel Dhainaut
Old Dominion University

NONLINEAR RESPONSE AND FATIGUE ESTIMATION OF SURFACE PANELS TO WHITE AND NON-WHITE GAUSSIAN RANDOM EXCITATIONS

by

Jean-Michel Dhainaut
B.S. May 1997, Parks College of Saint Louis University
M.S. May 1998, Parks College of Saint Louis University

A Dissertation Submitted to the Faculty of
Old Dominion University in Partial Fulfillment of the
Requirement for the Degree of

DOCTOR OF PHILOSOPHY

AEROSPACE ENGINEERING

OLD DOMINION UNIVERSITY
December 2001

Approved by:

Chuh Mei (Director)

Howard F. Wolfe (Member)

Robert L. Ash (Member)

Donald Kunz (Member)

ABSTRACT

NONLINEAR RESPONSE AND FATIGUE ESTIMATION OF SURFACE PANELS TO WHITE AND NON-WHITE GAUSSIAN RANDOM EXCITATIONS

Jean-Michel Dhainaut
Old Dominion University, 2001
Director: Dr. Chuh Mei

In stochastic structural dynamics, the majority of analyses have dealt with linear structures under stationary, Gaussian, and band-limited white noise excitations. Although these simplifying assumptions may be justified, in many processes experimental data have shown quite frequently the non-stationary and non-Gaussian characteristics of the loads. An efficient finite element modal formulation has recently been developed to extend the analysis to nonlinear structural responses. Laminated plate theory and von Karman large displacement relations are used to derive the nonlinear equations of motion for an arbitrarily laminated composite panel subjected to combined acoustic and thermal loads. The nonlinear equations of motion in structural node degrees of freedom are then transformed to a set of coupled nonlinear equations in truncated modal coordinates with rather small degrees of freedom. Recorded B-1B flight acoustic pressure fluctuations have shown the non-white power spectral density (PSD) characteristics. This work presents for the first time the nonlinear large amplitude response and fatigue life estimation of arbitrary laminated composite panels subjected to non-white pressure fluctuations with or without a high thermal environment. The Palmgrem-Miner theory is combined with the rainflow counting cycles method in time domain, and with transformed Gaussian models in the frequency domain, to estimate the panel fatigue life.

Equivalent band-limited White Noise Sound Pressure Level excitations (EWSPL), which have the same acoustic power within the bandwidth as the B-1B flight data, are generated. Nonlinear response and fatigue life are predicted for the identical panels subjected to EWSPL. Monte Carlo numerical simulation is used for the analysis of the EWSPL. Results show that the flight data with non-white PSD give higher stress characteristics and shorter fatigue life than the corresponding EWSPL.

ACKNOWLEDGEMENTS

I would like to express gratitude and appreciation to my advisor Dr. Chuh Mei for his invaluable guidance, encouragement, and advice throughout the entire course of this study. I wish to sincerely thank my guidance and dissertation committee members, Dr. Howard Wolfe, Dr. Robert Ash, and Dr. Donald Kunz for their valuable time and suggestions.

Special thanks are due to Dr. Howard Wolfe for many helpful discussions and for allowing me to benefit from his in-depth knowledge in sonic fatigue.

I am grateful to all my family members, especially to my parents whose support and encouragement has always been a source of inspiration for me.

Finally, I would like to thank all of my colleagues, especially Juan Pelaez, Kaveh Ghayour, Guanfeng Cheng, Zhi Yang, and Mohamed Azzouz for their friendship and support.

Jean-Michel Dhainaut

December 2001

TABLE OF CONTENTS

LIST OF TABLES

LIST OF FIGURES

NOMENCLATURE

English symbols

a	element length
b	element width
$\{a\}$, $\{b\}$	generalized coordinates
A	element area
$[A]$	membrane stiffness of matrix
$[B]$	coupling stiffness matrix
$[B_b]$	bending strain interpolation function
$[B_m]$	in-plane strain interpolation function
$[B_\theta]$	large deflection interpolation function
$[C]$	interpolation function matrix
D, $D(t)$	damage
$[D]$	bending stiffness matrix
E	Young's modulus
$E[]$	expected value of []
F	functional
f_c	cut-off frequency
f_0	mean frequency
G	deterministic function
G_{12}	modulus of rigidity
G_p	cross-spectral density function
h	plate thickness

$[H]$	displacement function matrix
kur	kurtosis
K	experimental material property
$[k]$, $[K]$	element and system stiffness matrices
$[K_1]$	combined system linear stiffness matrix
$[K_2]$	combined system nonlinear stiffness matrix
$[K_L]$	combined system linear stiffness matrix
$\lfloor K_L \rfloor$	modal linear stiffness matrix
$[\overline{K}_q]$, $[\overline{K}_{qq}]$	modal nonlinear stiffness matrices
L	panel length
m	mean
m_i	statistical moments
m_k	local minima
M_k	local maxima
$[m]$, $[M]$	element and system mass matrices
$[\overline{M}]$	modal mass matrix
N, N	number of cycles to failure
$\{N\}$, $\{M\}$	force and moment resultant vectors
$\{N_{\Delta T}\}$	in-plane thermal force resultant vector
$\{M_{\Delta T}\}$	thermal moment resultant vector
$[n_1]$, $[N_1]$	element and system first-order nonlinear stiffness matrices
$[n_2]$, $[N_2]$	element and system second-order nonlinear stiffness matrices
$\{p\}$, $\{P\}$	element and system force vectors

p_0	reference pressure
$\{\overline{P}\}$	modal force vector
q	modal displacement
$Q(t)$	load function
$[Q]$	lamina reduced stiffness matrix
$[\overline{Q}]$	transformed lamina reduced stiffness matrix
std	standard deviation
s	stress amplitudes
$\hat{s}$	power spectrum
skew	skewness
S, S	stress range/stress
t	time
T	length of the time interval
$[T_b]$, $[T_m]$	transformation matrices
$[T_\varepsilon]$, $[T_\sigma]$	strain and stress transformation matrices
TP	sequence of turning points
u, v	in-plane displacements
$\{w_b\}$, $\{w_m\}$	element bending and membrane nodal displacements
w	element nodal displacements
W	work
$\{W\}$	system nodal displacements
(x, y, z)	cartesian coordinates
(x_1, x_2, x_3)	cartesian coordinates

Z	non-dimensional stress range

Greek symbols

α	thermal expansion coefficient
β	experimental material property
Δ	incremental value
Δt	time step
Δt_s	Nyquist-Shannon time step
ΔT	temperature variation
ΔT_c	critical buckling temperature
$\varepsilon(t)$	strain tensor
$\{\varepsilon\}$	total strain vector
$\{\varepsilon^o\}$	in-plane strain vector
$\{\varepsilon_m^o\}$	membrane strain vector
$\{\varepsilon_\theta^o\}$	von-Karman strain vector
ϕ	fiber orientation angle
ϕ_i	sequence of phases
$\{\phi\}$, $\{\Phi\}$	element and system eigenvector
$[\Phi]$	system eigenvector matrix
$\{\kappa\}$	bending curvature vector
λ	eigen-value for buckling problem
μ	crossing intensity
ν_{12}, ν_{21}	Poisson's ratios

$[\theta]$	slope matrix
ρ	mass density
σ	standard deviation
σ_{12}	stress in 1-2 direction
σ^2	variance
$\{\sigma\}$	stress vector
γ	shear stress
ω	frequency
ξ	structural damping ratio
(ξ, η)	spatial coordinates

Subscripts

b	bending
c	center
cr	critical
ext	external
F	rainflow matrix
$\hat{F}$	max-min matrix
int	internal
m	membrane
mb, bm	membrane-bending, bending-membrane
n_i	number of cycles at a specified load condition
NB	stiffness matrices due to $\{N_b\}$
Nm	stiffness matrices due to $\{N_m\}$

$N\Delta T$	stiffness matrices due to $\{N_{\Delta T}\}$
u, v, w	in-plane and transverse displacements
RFC	rainflow counting cycles
T^f	fatigue life
ΔT	thermal
x	x direction
y	y direction
xy	xy direction

CHAPTER 1

INTRODUCTION

Sonic fatigue has become a major problem for aircraft, missiles, and spacecraft where highly reliable structures are required. In fact, it was not until the late 1950's when the first incident on aircraft structures in close proximity to high intensity jet exhaust noise was reported that a research effort was then undertaken [1]. Experimental work was carried out on some full-scale models, and tests were made on large prototype assemblies (Figures 1.1 and 1.2). Load processes, whose time histories frequently reveal considerable non-Gaussian and non-white properties, were recorded. Due to analytical limitations, theoretical studies were performed using simple panel models under the influence of a fluctuating random pressure with Gaussian and white-noise spectral characteristics. In these early works, the predictions generally overestimated the response levels, and it was not possible to get better agreement than within a factor of two. As the power of the engines increased and aircraft pushed their performance envelope further, new problems arose. Apart from the large pressure fluctuation within the engine vicinity, a large thermal stress region, due mainly to aerodynamic heating, had to be included in the analytical models. It soon became apparent that with the theoretical and computational tools available at that time, a complete model from structure to fatigue life estimation was far too complicated. Therefore, the process designs for industry were based on experimental data and empirical relations derived from testing to modify the simple analytical predictions.

The journal model used for this work is the *AIAA Journal*

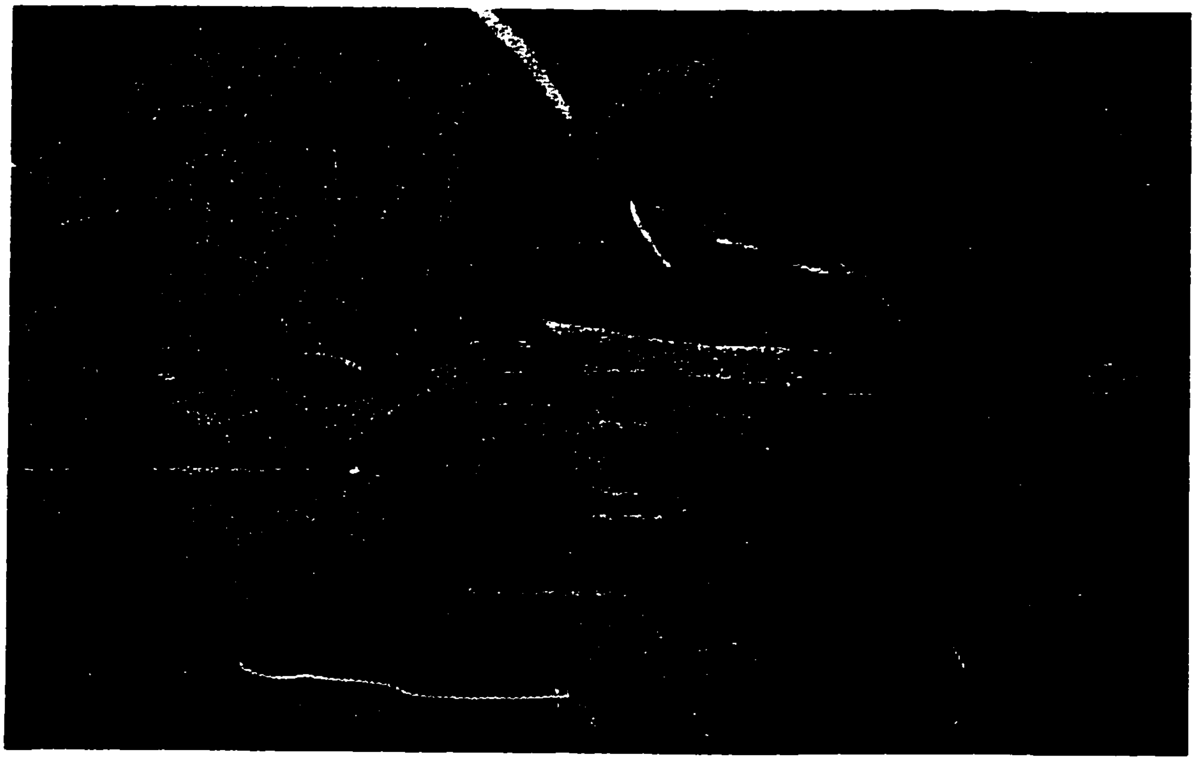

Figure 1.1 Sonic Fatigue Failure from B-47 Test Performed in 1952 [1]

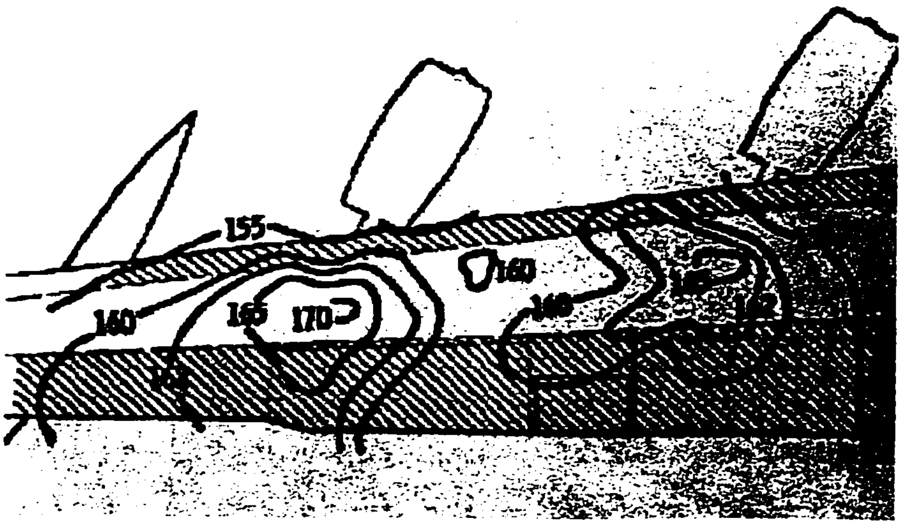

Figure 1.2 Contours of Overall Sound Pressure Levels on a B-52 Wing during Take-Off, 1958 [1]

Although, the power of the engines was still increasing dramatically, the use of higher air bypass ratios to reduce environmental noise moderated the increases in radiated sound pressure levels. This engine noise alleviation, combined with improved design guidelines, retarded further analytical developments. This was the state of the art by the early 1970's. It was not until the 1980's that new interest arose in association with the use of advanced composite materials. One of the major advantages that composite materials provide over metals is an increased strength to weight ratio. The added strength of the composite allows thinner and less stiff panels, resulting in relatively large displacements under normal acoustic loading and finite thermal deformation or buckling at temperatures that are lower than those that are typical of homogeneous metals. Both of these effects were nonlinear, and they could not only severely limit structural fatigue life but also made predicting fatigue life extremely difficult. A better understanding of these nonlinear random vibrations, coupled with high temperature distortion effects, was therefore necessary so that more accurate analytical models could be developed.

The first approach to overcome the lack of a complete theoretical treatment led to the development of new design guidelines. It was quickly realized that with the multitude of composite stacking, it was impractical as well as inefficient to test experimentally every conceivable design configuration. This brought an urgent need for fatigue analysis and design guidelines that were in close agreement with actual behavior. The improvements in the understanding of the fatigue mechanism, in conjunction with the explosive growth in computational performance, offers new possibilities to researchers in refining models involving both acoustic and thermal loading.

The prediction of the fatigue life of a structure can be approached either through a crack growth analysis or a Miner's law calculation [2]. The former approach is related to the low-cycle failure, while Miner's law is related to high-cycle fatigue failure, which is more widely used within the aerospace industry and will be reviewed in the present work. It is important to keep in mind that the fluctuating stress responsible for fatigue failure is in the form of a continuous random process. Therefore, techniques for predicting statistical averages and distributions of random loading characteristics relevant to fatigue have to be available. From Figure 1.3 it is seen that a clear-cut definition of response "cycle" and "peak" presents difficulties once the response is no longer narrow-band. On this subject, opinions differ as to how the response should be processed to yield relevant peak and cycle information. Should double maxima, such as those marked 'A' in Figure 1.3, be counted as two significant peaks? Should the minor maxima just be disregarded? These questions are still open. This work does not intend to arbitrate among the different "counting" approaches, but rather it is concerned with the statistical distributions obtained for the "peaks" once they have been defined in a certain fashion in terms of the maxima and crests. Once the fatigue theorists decide just how the peak information needs to be handled in their calculations, the considerations illuminated in this work should be relevant.

Before moving into a detailed literature survey on sonic fatigue analytical approaches, a brief discussion of the different sources of acoustic and thermal loadings is addressed.

1.1 Acoustic Loads

Early work on acoustic loading was concerned with sound radiation caused by high

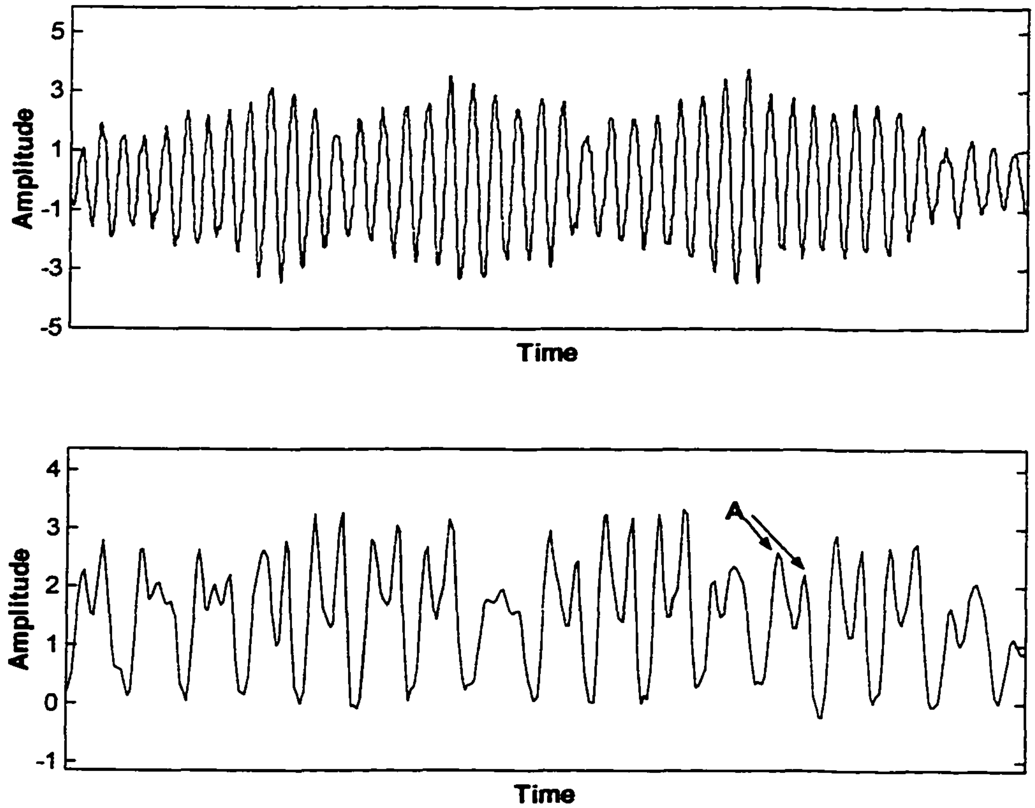

Figure 1.3 Sample for Narrowband and Broadband Signal

velocity jets. In 1952, Lord Lighthill [3, 4] showed theoretically the dependence of the intensity of sound radiation on jet exhaust velocity. For near-field pressure fluctuation around a jet engine, a semi-empirical method was produced by the Engineering Sciences Data Unit (ESDU) [5]. Reviews of jet exhaust impingement models were given by Lansing et al. [6] in 1972 and modeling the effects of ground reflection on radiated pressure fluctuations was discussed by Scholton [7] in 1973. Another source giving rise to pressure fluctuations is the turbulent boundary layer. Early measurements were made by Bull [8] for subsonic boundary layers, and, in a more recent work, Mixson and

Roussos [9] discussed the existing data for Mach numbers up to 2.5. In addition to the structures that are subjected to widely distributed acoustic loads, local high intensity pressure fluctuations arise from instabilities such as cavities, separated flow, and shock waves. In this respect, there has not been extensive study of these phenomena although in 1972 Coe and Chyu [10, 11] conducted a useful investigation study on a scaled model.

1.2 Thermal Loads

The thermal problem in aerospace applications has its origins in the late 1940s. During World War II, airplane speeds had become high enough for compressibility phenomena to play a significant role in performance. Mainly, there are three sources of loads exerted on the external surfaces. These are pressure, skin friction (shearing stresses), and aerodynamic heating. Pressure and skin friction play important roles in aerodynamic lifting and drag, but aerodynamic heating is more predominant and can affect the structural behavior in many ways. In 1956, Bisplinghoff [12] identified the basic structural and aeroelastic considerations for high-speed vehicles: (i) the material's properties are degraded at elevated temperatures, (ii) allowable stresses are reduced and (iii) time dependent material behavior such as creep come into play. The effects of aerodynamic heating become significant at Mach numbers above 2.5. Early approaches were described in a 1956 paper by Van Driest [13] and in a 1960 text by Truitt [14]. The difficulties presented by high temperatures accompanying flights at supersonic speeds became evident and became known as the *thermal barrier*. For a long time, the thermal barrier caused concern that large structural weight increases would be required to keep material temperatures within allowable limits. Subsequently, Hoff [15] and Heldenfels

[16] found that these concerns did not materialize because the problems were overcome through research and the development of effective thermal structures.

1.3 Analytical Approaches for Response Analysis

Stochastically excited linear systems have been studied in great detail, and numerous analytical techniques exist for both stationary and nonstationary problems. Unfortunately, the majority of structural responses are nonlinear and not many techniques exist for the analysis. Crandall and Zhu [17], To [18], Roberts [19], and Spanos and Lutes [20] have presented excellent and comprehensive reviews on techniques for nonlinear random vibrations. The various approaches are given briefly in the following paragraphs.

1.3.1 Fokker-Planck-Kolmogorov (FPK) Equations Approaches

The FPK equations approaches give an exact solution for a restricted class of simple problems. If the excitation is sufficiently broadband, it is possible to model the response as a multi-dimensional Markov process. On the basis of this Markov model, which is essentially a diffusion process, one can formulate governing equations in time. The most general extension of FPK equations approaches to nonlinear second order equations was due to Caughey [21]. Exact steady-state solutions of a rather wide class of Multi-Degrees-of-Freedom (MDOF) nonlinear systems to white noise are available [22, 23]. In general, the transitional Probability Density Function (PDF) cannot be found with the FPK equations approach. Without this transitional probability, it is generally impossible to obtain the correlation function and Power Spectral Density (PSD) of the response. The difficulty in dealing exactly with solutions of stochastically excited nonlinear systems has led to an intensified effort to develop approximate methods that will tackle a broader class of problems than presently with the FPK analysis.

1.3.2 Perturbation Approaches

In this approximate method, the stochastically exited nonlinear system is treated in the same way as a deterministically excited system. The solution is represented as an expansion of the powers of a small parameter which specifies the size of the nonlinearity. The perturbation approach was applied to a continuous nonlinear system by Lyon [24] and to discrete nonlinear systems by Crandall [25]. The perturbation approximation, however, will not give accurate results for systems possessing large nonlinearities [26] as shown in Figure 1.4.

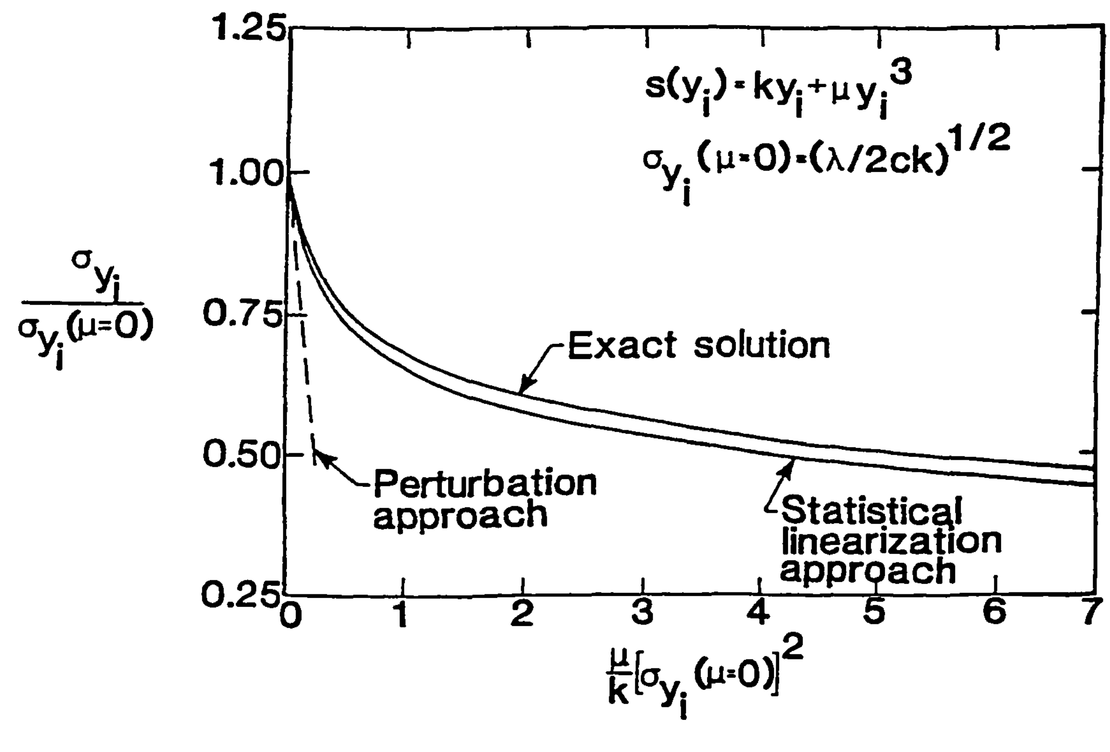

Figure 1.4 RMS Responses of a Hardening System by Perturbation, EL and FPK Approaches [26]

1.3.3 Equivalent Linearization (EL) Approaches

The EL approaches technique is based on the concept of replacing the nonlinear system with an equivalent linear system such that the difference between the two systems is minimized. Basically, the method is the statistical extension of the well-known Krylov-Bogoliubov equivalent linearization method for deterministic vibration problems. The extension of this approximate method to problems of random excitations was made independently by Booton [27] and Caughey [28]. Atalik and Utku [29] have presented a direct and generalized procedure for the equivalent linearization approach for the MDOF nonlinear systems that may be nonlinear in inertial, velocity, and restoring forces. The coefficients of the equivalent linear system can be obtained by direct application of partial differentiation and expectation operators to the functionals involving nonlinear terms. For mathematical derivations of the equivalent linearization technique and its applications to a variety of nonlinear dynamic systems, readers are referred to the book by Roberts and Spanos [30]. Sakata and Kimura [31] developed a method to calculate the nonstationary response of a nonlinear system subjected to non-white excitation. The method consists in modification of the EL and the use of the moment equations of the equivalent linear system to evaluate the mean square response. The limitation here is the assumption of a Gaussian response in order to obtain the higher moments (order greater than two) from the second order moments.

1.3.4 Numerical Simulation Approaches

The Monte Carlo simulation method estimates the response statistics of randomly excited nonlinear structural systems [32-34]. In the past, both analog and digital computational systems have been used for Monte Carlo simulations. Only digital systems are used presently. The approach mainly consists of generating a large number of sample excitations, calculating the corresponding response samples, and processing the desired response statistics. Obviously, this approach can be used for estimating the response statistics of both stationary and nonstationary excitations. The major drawback of this approach is the computation time and cost.

The various analysis techniques discussed for nonlinear random vibration systems in Section 1.3 did not consider the thermal environment. A brief review of sonic fatigue analysis and design methods for aircraft and spacecraft structural panels in a combined thermal acoustic environment is presented.

1.4 Nonlinear Random Response of Panels in an Elevated Thermal Environment

Sonic fatigue design guides have been developed for metallic structures by Rudder and Plumblee [35] and for graphite-epoxy composite structures by Holehouse [36]. The design guides were based on the semi-empirical test data or Miles' simplified single-mode approach.

Vaicaitis and his coworkers have used the Galerkin's method (to Partial Differential Equations (PDE) and the modal approach) in conjunction with the time domain Monte Carlo numerical simulation [32-34] for the prediction of nonlinear response of isotropic [37, 38] and composite [39, 40] panels subjected to acoustic and thermal loads. Lee [41-43] has used the PDE/Galerkin method in conjunction with the equivalent linearization [30] technique and investigated the thermal effects on the dynamics of vibrating isotropic plates and the improvement of variance and cumulants using an abridged Edgeworth series [44]. The use of the PDE/Galerkin method, however, limits its applicability to a simple panel platform of rectangular shape and simple boundary conditions.

Extension of the Finite Element (FE) method to nonlinear response of isotropic beam and plate structures under combined acoustic and thermal loads was first reported by Locke and Mei [45, 46] using the EL technique with an iterative scheme. The application of the FE/EL procedure was further extended to composite panels by Mei and Chen [47]. In the FE/EL solution procedure, the thermal postbuckling or thermal finite deflection structural problem is solved first. The thermal deflection and thermal stresses are treated as known preconditions for the subsequent random response analysis. The random response thus considers only one of the two coexisting thermal postbuckling positions [48]. The FE/EL method, therefore, does not give accurate predictions for snap-through and large-amplitude nonlinear random motions. Experiments by Ng and Clevenson [49], Istenes et al. [50], and Murphy et al. [51, 52] have shown that the dynamic response of acoustically excited thermally buckled plates may exhibit the following two types of motion: (i) small amplitude vibrations about one of the coexisting static equilibrium configurations, and (ii) large amplitude nonlinear snap-through oscillations between and over the two postbuckling positions. Reviews of large deflection analyses in sonic fatigue design have been given by Mei and Wolfe [53], Benaroya and Rebak [54], Vaicaitis [37], Clarkson [55], and Wolfe et al. [56].

1.5 Models for Structural Reliability Analysis

Fatigue life analysis is divided into two main categories as indicated by experimental observations. At low stress levels (high-cycle fatigue), the pre-crack initiation period may constitute a significant percentage of the usable fatigue life, whereas at high stress amplitude (low-cycle), fatigue cracks start to develop during early cycles. The transition between low and high-cycle fatigue usually occurs between 10^1 and 10^5 cycles. Because of the nature of the random loading in this work, only high-cycle fatigue conditions are addressed.

1.5.1 Stress-Life (S-N) Diagrams

The first systematic and quantitative investigation of fatigue damage was provided by August Wöhler in 1858 and resulted in the widely known S-N curves (i.e., stress (S) versus number (N) of cycles to failure). This curve conveniently displays basic fatigue data in the elastic stress range. Because of the scatter in fatigue life data at any stress level, it has been agreed that there is not just one S-N curve for a given material, but a family of S-N curves, using probability of failure as a parameter. These curves are called S-N-P curves. The above curves can generally be found in fatigue structural design manuals. For instance, a design guide was developed by the Air Force in 1975 for military aircraft [35]. Analytical representation of the S-N curves is commonly given in the form $N=K\,S^{-\beta}$ where β and K are material parameters estimated from test data. Due to the high uncertainty in the relationship between S and N, the parameters K and β are regarded as random variables [57, 58]; in such cases, statistical analysis leads to an expression for N in terms of the statistics of the dispersed data. It should be realized that the S-N approach, though still widely used in design applications, does not deal with any physical phenomena within the material. Only the total life to fatigue fracture is considered.

1.5.2 Cumulative Damage Theories

The stress amplitude experienced by a structural member may often vary during its service life. In such case, i.e., under a variable amplitude loading, the direct use of standard S-N curves is not possible. To estimate fatigue life in more general circumstances, Palmgren [59] and Miner [2] proposed that fatigue fracture is a result of linear accumulation of partial fatigue damage. The weakness of that approach is it does not account for sequential effects. That is, it assumes that damage caused by a stress cycle is independent of where it occurs in the load history. To overcome the shortcomings of the Palmgren-Miner approach, a number of nonlinear damage hypotheses have been proposed. One of the first was proposed by Marco and Strakey [60], in which the classical Palmgren-Miner hypothesis, linear accumulation of partial fatigue damage, has an exponent that is a function of the stress level. Many other examples of nonlinear damage accumulation can be found in the literature [61-63]. In general, they all require material and shaping constants that have to be determined from a series of step tests, which requires a large amount of testing.

1.5.3 Continuum Damage Mechanics

In the previous section, the damage accumulation rules were presented in relation to fatigue due to loading at various amplitudes. The concept of cumulative damage, however, has a much wider meaning and is used to characterize globally all deterioration phenomena taking place in the material. Despite the diversity of these phenomena, it is useful to try to describe them jointly within a single model. Models of this type utilize a damage measure $D(t)$ and an external load function $Q(t)$. One can postulate the following general differential equation of the model,

$$\frac{dD(t)}{dt} = f\left[D(t), Q(t)\right] \tag{1.1}$$

When the right hand side of Equation 1.1 is independent of the damage $D(t)$, then the solution of the equation with the initial condition $D(0)=0$ is given by the previous Palmgren-Miner equation. For more details on the derivation see Bolotin [64] and Madsen et al. [58]. When the right hand side of Equation 1.1 is not zero or independent of $D(t)$, the continuum damage mechanics attempt to introduce a variable, treated as an internal variable of the material, which will describe the fine details of the fatigue-fracture pattern. The first characterization of damage along this line of work was done in 1958 by Kachanov [65], who introduced a scalar measure of damage $D(t)$ to characterize macroscopically the internal degradation of the material. An important extension to Kachanov's idea was to incorporate damage into the general constitutive equations of the deformed body. Much work was done in this area [66, 67, 68], and in general the equations can be represented as

$$\varepsilon(t) = F(S, D) \tag{1.2}$$

where ε is the strain tensor, S is the stress and D a damage measure (scalar or tensor), and F is an appropriate functional. This approach to fatigue life estimation is only applicable to some very special cases in low-cycle fatigue and will not be considered in this work.

1.6 Statistical Characterization of Non-Gaussian and Non-Stationary Random Loads

Throughout their service life, aerospace structures are subjected to loads that vary with time in a very complicated manner. Most traditional fatigue analyses are based upon a representation of loads in the form of periodic deterministic functions of time, and the basic characteristics of fatigue accumulation are expressed in terms of the number of loading cycles. At present, it is widely accepted that fatigue analyses performed under constant cyclic amplitude representations does not represent adequately the complexity of the fatigue process under actual complicated loadings. Irregular time histories, such as random loads that fluctuate in time continuously, must be considered and suitably modeled.

There are situations where the load acting on a structure cannot be assumed to be Gaussian and/or stationary. An important problem that arises is the effective characterization of such random processes. For the purpose of fatigue analysis, we are interested primarily in the description of high statistical moments (mean, variance, skewness, and kurtosis) of non-Gaussian load (stress) processes. The fluctuating pressure fields experienced by high-speed flight vehicles frequently exhibit considerable nonstationary and non-Gaussian characteristics. These properties are, of course, reflected in the response of aircraft and spacecraft surface panels. An additional source of deviation from a normal distribution arises from the nonlinear panel behavior. It is well known that there are numerous possibilities for mathematical representation of non-normal random processes depending on the application convenience. Generally, a non-Gaussian process is created by functional transformation from a Gaussian process. The Weibull distribution has been widely used in the characterization of random loading-based fatigue lifetime and has fit experimental data quite well at high stress levels [69]. On the other hand, relatively little work on nonstationary stochastic fields has been published to date. In this regard, Hammond and Moss [70] were concerned with characterizing the time varying nature of the nonstationary signal, and Merritt [71] with nonstationary gunfire environments. Piersol [72] has presented an optimum analysis procedure for the nonstationary vibro-acoustic data measured during space vehicle launches. Dargahi-Noubary [73] has presented a uniformly modulated nonstationary model for the seismic records of earthquakes and underground nuclear explosions.

No literature was found on nonlinear panel response at elevated temperatures subjected to nonstationary excitation.

1.7 Cycles Counting

Recalling that stress response for fatigue failure is in the form of a continuous random process, techniques for predicting statistical averages and distributions of random loading characteristics relevant to fatigue are needed. If the stress produced by the random load is "narrow band" then the stress history has more or less the appearance of a sine wave of slowly varying frequency and amplitude. For each upward crossing of zero, the stress time history displays a single peak (Figure 1.3-a). As the load bandwidth increases, the time history displays multiple peaks for each upward crossing of zero (Figure 1.3-b), and there is no obvious definition of stress cycles. The stress time history is usually reduced to a sequence of events that can be regarded as compatible with constant amplitude data. Those methods are known as cycle *counting techniques*. Dowling [74] provided an excellent summary of the different counting methods.

The three methods of cycle counting most commonly used are: (i) the *peak counting* method, (ii) the *range counting* method, and (iii) the *rainflow* counting method. In the *peak counting* method, a stress cycle is attributed to each peak that lies above zero with the amplitude of the cycle being placed equal to the value of the peak. The *range counting* method considers two half-cycles associated with each positive or negative peak. Methods (i) and (ii) yield similar results for narrow band processes, but quite different results may be obtained for wide band processes. The *rainflow* method uses a specific cycle counting scheme to account for effective stress ranges and identified stress cycles related to closed hysteresis loops in the cyclic stress-strain curves. This counting method was developed by Professor T. Endo and his colleagues [75] in Japan around 1968. It is generally thought that rainflow counting yields the most realistic estimate of fatigue damage. Typically, the *peak counting* method will yield a higher estimate of the damage while the *range counting* method will predict less damage. Because of the heuristic nature of the standard rainflow counting techniques, as well as their complicated sequential structure, it is difficult to determine the probability distribution of the rainflow amplitudes for a random process. In recent years, a new definition of the rainflow cycle amplitude has been given by Rychlik [76, 77, 78] that expresses the rainflow cycle amplitude in an explicit analytical manner and provides the basis for deriving the long-time distribution for ergodic stationary processes. The new definition is based on the assumption that the sequence of extrema has some type of Markov structure. Bishop and Sherrat [79, 80] developed a theoretical solution for the estimation of the rainflow range density functions using statistics computed directly from power spectral density data. Dirlik [81] produced an empirical closed form expression for the probability density function of rainflow ranges using extensive computer simulations to model the signals using the Monte Carlo technique.

At this time, the state of the art for sonic fatigue design, in addition to the old existing design guides, is the incorporation of fatigue analysis within the commercial Finite Element codes (NASTRAN, ALGOR, ANSYS, etc.). The Structural Acoustic Branch at NASA Langley Research Center currently has implemented some of their nonlinear acoustic panel response problems using an *equivalent linearization* RMS approach [82, 83]. This approach aims to appropriately linearise the system based upon RMS statistics. However, the new vibration tools being used for this work rely on accurate evaluation of all statistical moments up to the fourth moment, rather than just the zero-th moment used for the RMS calculation.

1.8 Motivation and Dissertation Organization

Sonic fatigue has been considered as one of the major design considerations for the Joint Strike Fighter (JSF). In addition, the surface panels of many high-speed flight vehicles (e.g., the X-33, RLV, X-38, and Hyper-X etc.) presently under development will be exposed to high levels of acoustic pressure fluctuations and elevated temperatures. At present almost all the sonic fatigue design guides are based on experimental data and/or very simplified models. It was quickly realized that with the multitude of different composite stackings and new materials being introduced constantly, it was impractical as well as inefficient to test every conceivable design configuration experimentally. This brought an urgent need for improved sonic fatigue analysis and design methods for aircraft and spacecraft structural panels. Recorded B-1B flight acoustic pressure fluctuations have shown the non-white power spectral density (PSD) characteristics. The objective of the present work is to present a versatile finite element modal formulation that could predict the stress response of an arbitrary laminated composite panel subjected to random loadings in an elevated thermal environment. The finite element formulation presented is capable of predicting responses under non-white pressure fluctuations. The linear/nonlinear large amplitude responses and fatigue life estimation of panels subjected to non-white pressure fluctuations and a generated equal power white noise are compared.

The organization of this work is as follows. In Chapter 1, a synopsis and literature survey is given of the existing knowledge on random dynamics and fatigue technology. Attention is focused on features of the responses and fatigue phenomena that are of prime interest in stochastic modeling. Chapter 2 contains the mathematical development of the nonlinear finite element model of an arbitrarily laminated panel subjected to a set of simultaneously applied thermal and acoustic loads. The governing equations of motion are derived in structural degree of freedom. Chapter 3 is entirely directed toward theories of high-cycles random fatigue life estimations. Special emphasis is given to the rainflow counting cycle method (RFC) and to Dirlik's approach in the frequency domain. In addition, two classes of models are distinguished and analyzed for the fatigue life estimation of slightly nonlinear responses (transformed Gaussian Models) and Gaussian processes with non-zero mean (SMCTP). Chapter 4 uses the theory of the previous two Chapters and goes through the preliminary tasks and procedures to solve the fatigue problem. These include solving the linear eigen-value problem for the modal transformation as well as the critical buckling temperature. Apart from these, numerical considerations like the integration scheme, time step, sampling frequency and others are also addressed. Finally, the basic Matlab commands for fatigue life estimation are highlighted with numerical examples. Chapter 5 presents the validation of the modal finite element and the RFC counting cycle methods. Discussions of fatigue life for rectangular panels subjected to: (i) recorded pressure fluctuations and simulated white noise, (ii) recorded pressure fluctuations and simulated white noise in a high temperature environment are given. Numerical results include time histories, probability/amplitude peak distributions and PSD of panel maximum deflection and stress/strain. Finally, concluding remarks and possibilities for future research work are presented in Chapter 6.

CHAPTER 2

FINITE ELEMENT FORMULATION

The governing nonlinear equations of motion are derived for an arbitrarily laminated composite rectangular plate subjected to a set of simultaneously applied thermal and acoustic loads. The thermal load is taken to be an arbitrary steady-state temperature distribution, i.e., $\Delta T=\Delta T(x,y,z)$. The acoustic excitation is assumed either to be a band-limited white or non-white Gaussian random pressure, uniformly distributed over the structural surface. The finite element formulation is based on the von Karman large deflection theory and the classic laminated plate theory (CLPT). The following assumptions are made throughout the derivation:

(1) The panel is thin ($L/h>20$).

(2) In-plane inertia, rotatory inertia, and transverse shear deformation effects are negligible.

(3) von Karman nonlinear strain-displacement relations are valid.

(4) The quasi-steady state thermal stress theory with arbitrary temperature distribution is applied.

(5) Proportional damping, $\xi_r\omega_r=\xi_s\omega_s$, is used.

(6) Straight lines perpendicular to the midsurface before deformation remain straight and perpendicular after deformation.

(7) The transverse normals do not experience elongation, i.e., they are inextensible.

Bogner-Fox-Schmit (BFS) [84] C^1 conforming rectangular elements are adopted in the derivation. A C^1 conforming element is one that provides inter-element continuity of the displacement field, w(x,y) in the z-direction, and its first derivatives $w_{,x}$ and $w_{,y}$, but not inter-element continuity of all second derivatives of w(x,y).

2.1 Displacement Functions

The BFS element has a total of 24 degrees of freedom (DOF): 16 bending DOF $\{w_b\}$ and 8 in-plane DOF $\{w_m\}$ in each element (Figure 2.1).

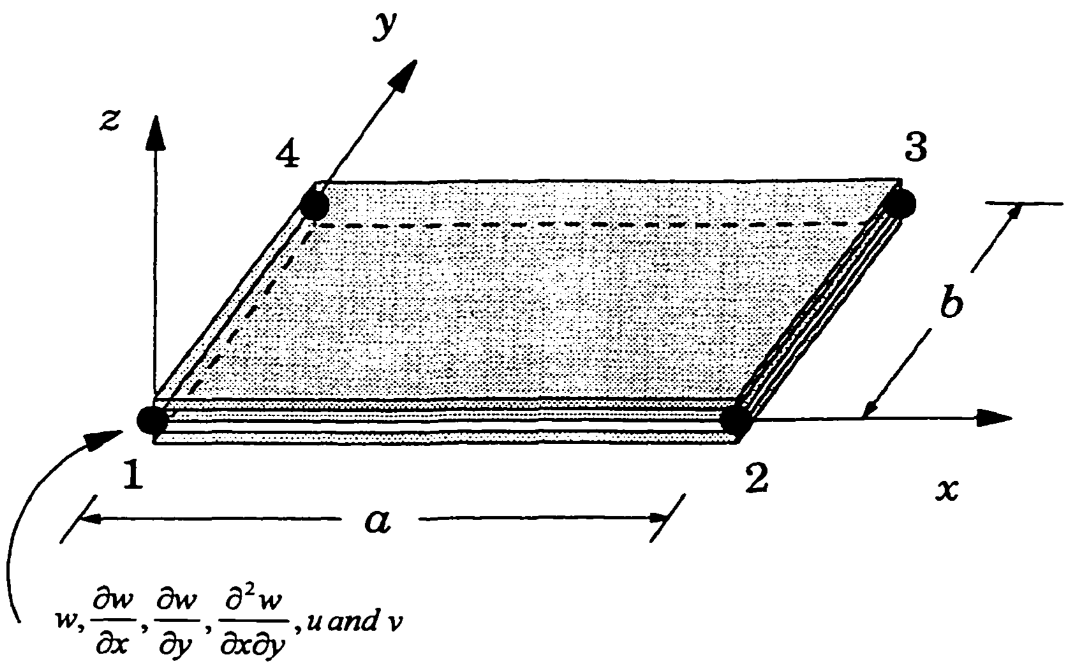

Figure 2.1 Nodal Degrees of Freedom of a BFS C^1 Conforming Rectangular Element

The 16 bending DOF $\{w_b\}$ and 8 in-plane DOF $\{w_m\}$ are expressed as

$$\begin{aligned}\{w_b\} = \{&w_1 \; w_2 \; w_3 \; w_4 \; w_{,x_1} \; w_{,x_2} \; w_{,x_3} \; w_{,x_4} \; w_{,y_1} \; w_{,y_2} \; w_{,y_3} \; w_{,y_4} \\ &w_{,xy_1} \; w_{,xy_2} \; w_{,xy_3} \; w_{,xy_4}\}^T\end{aligned} \tag{2.1}$$

$$\{w_m\} = \{u_1 \; u_2 \; u_3 \; u_4 \; v_1 \; v_2 \; v_3 \; v_4\}^T \tag{2.2}$$

The bending displacement w and the in-plane displacements u, v are approximated as a bi-cubic and a bi-linear polynomial function in x and y, which can be written as,

$$\begin{aligned} w &= a_1 + a_2 x + a_3 y + a_4 x^2 + a_5 xy + a_6 y^2 + a_7 x^3 + a_8 x^2 y + a_9 xy^2 + a_{10} y^3 \\ &\quad + a_{11} x^3 y + a_{12} x^2 y^2 + a_{13} xy^3 + a_{14} x^3 y^2 + a_{15} x^2 y^3 + a_{16} x^3 y^3 \\ &= [H_w(x,y)]\{a\} \\ u &= b_1 + b_2 x + b_3 y + b_4 xy \\ &= [H_u(x,y)]\{b\} \\ v &= b_5 + b_6 x + b_7 y + b_8 xy \\ &= [H_v(x,y)]\{b\} \end{aligned} \tag{2.3}$$

where the interpolation functions are

$$\begin{aligned} [H_w(x,y)] &= \{1 \;\; x \;\; y \;\; x^2 \;\; xy \;\; y^2 \;\; x^3 \;\; x^2y \;\; xy^2 \;\; y^3 \;\; x^3y \;\; x^2y^2 \;\; xy^3 \\ &\qquad x^3y^2 \;\; x^2y^3 \;\; x^3y^3\} \\ [H_u(x,y)] &= \{1 \;\; x \;\; y \;\; xy \;\; 0 \;\; 0 \;\; 0 \;\; 0\} \\ [H_v(x,y)] &= \{0 \;\; 0 \;\; 0 \;\; 0 \;\; 1 \;\; x \;\; y \;\; xy\} \end{aligned} \tag{2.4}$$

and the generalized coordinates are

$$\begin{aligned} \{a\} &= \{a_1 \;\; a_2 \;\; a_3 \;\; a_4 \;\; a_5 \;\; a_6 \;\; a_7 \;\; a_8 \;\; a_9 \;\; a_{10} \;\; a_{11} \;\; a_{12} \;\; a_{13} \;\; a_{14} \;\; a_{15} \;\; a_{16}\}^T \\ \{b\} &= \{b_1 \;\; b_2 \;\; b_3 \;\; b_4 \;\; b_5 \;\; b_6 \;\; b_7 \;\; b_8\}^T \end{aligned} \tag{2.5}$$

The generalized coordinates $\{a\}$ and $\{b\}$ are related to the nodal DOF vectors by the two transformation matrices $[T_b]$ and $[T_m]$, respectively, as

$$\begin{aligned} \{a\} &= [T_b]\{w_b\} \\ \{b\} &= [T_m]\{w_m\} \end{aligned} \tag{2.6}$$

The detailed derivation of bending and in-plane transformation matrices $[T_b]$ and $[T_m]$ is given in Appendix A. The element displacement functions then can be rewritten in terms of nodal displacement vectors as

$$
\begin{aligned}
w &= [H_w(x,y)]\{a\} = [H_w(x,y)][T_b]\{w_b\} \\
u &= [H_u(x,y)]\{b\} = [H_u(x,y)][T_m]\{w_m\} \\
v &= [H_v(x,y)]\{b\} = [H_v(x,y)][T_m]\{w_m\}
\end{aligned}
\tag{2.7}
$$

2.2 Nonlinear Strain-Displacement Relations

The von-Karman large deformation strain-displacement relations are given by

$$
\{\varepsilon\} = \begin{Bmatrix} \varepsilon_x \\ \varepsilon_y \\ \gamma_{xy} \end{Bmatrix} = \{\varepsilon^o\} + z\{\kappa\}
\tag{2.8}
$$

where $\{\varepsilon\}$ is the total strain vector measured at the stress-free (flat at T_{ref}) state. The in-plane strain vector $\{\varepsilon^o\}$ consists of two components, the membrane strain $\{\varepsilon_m^o\}$ and the non-linear von-Karman strain $\{\varepsilon_\theta^o\}$, as

$$
\begin{aligned}
\{\varepsilon^o\} &= \{\varepsilon_m^o\} + \{\varepsilon_\theta^o\} \\
&= \begin{Bmatrix} \dfrac{\partial u}{\partial x} \\ \dfrac{\partial v}{\partial y} \\ \dfrac{\partial u}{\partial y} + \dfrac{\partial v}{\partial y} \end{Bmatrix} + \frac{1}{2} \begin{Bmatrix} \left(\dfrac{\partial w}{\partial x}\right)^2 \\ \left(\dfrac{\partial w}{\partial y}\right)^2 \\ 2\dfrac{\partial w}{\partial x}\dfrac{\partial w}{\partial y} \end{Bmatrix}
\end{aligned}
\tag{2.9}
$$

The bending curvature vector $\{\kappa\}$ is defined as

$$\{\kappa\}=\begin{Bmatrix} -\dfrac{\partial^2 w}{\partial x^2} \\ -\dfrac{\partial^2 w}{\partial y^2} \\ -2\dfrac{\partial^2 w}{\partial x\partial y} \end{Bmatrix} \tag{2.10}$$

By using the finite element displacement functions in section 2.2, the in-plane strain vector components and the curvature vector components can be rewritten in terms of the element nodal displacement vector as follows

$$\begin{aligned}\{\varepsilon_m^o\} &= [C_m][T_m]\{w_m\} \\ &= [B_m]\{w_m\}\end{aligned} \tag{2.11}$$

$$\begin{aligned}\{\varepsilon_\theta^o\} &= \frac{1}{2}[\theta]\begin{Bmatrix} \dfrac{\partial w}{\partial x} \\ \dfrac{\partial w}{\partial y} \end{Bmatrix} \\ &= \frac{1}{2}[\theta][C_\theta][T_b]\{w_b\} \\ &= \frac{1}{2}[\theta][B_\theta]\{w_b\}\end{aligned} \tag{2.12}$$

$$\begin{aligned}\{\kappa\} &= [C_b][T_b]\{w_b\} \\ &= [B_b]\{w_b\}\end{aligned} \tag{2.13}$$

where

$$[C_m]=\begin{bmatrix} \dfrac{\partial}{\partial x}[H_u(x,y)] \\ \dfrac{\partial}{\partial y}[H_v(x,y)] \\ \dfrac{\partial}{\partial y}[H_u(x,y)]+\dfrac{\partial}{\partial x}[H_v(x,y)] \end{bmatrix}$$

$$=\begin{bmatrix} 0 & 1 & 0 & y & 0 & 0 & 0 & 0 \\ 0 & 0 & 0 & 0 & 0 & 0 & 1 & x \\ 0 & 0 & 1 & x & 0 & 1 & 0 & y \end{bmatrix} \tag{2.14}$$

$[\theta]$ is the slope matrix

$$[\theta]=\begin{bmatrix} \dfrac{\partial w}{\partial x} & 0 \\ 0 & \dfrac{\partial w}{\partial y} \\ \dfrac{\partial w}{\partial y} & \dfrac{\partial w}{\partial x} \end{bmatrix} \tag{2.15}$$

and

$$[C_\theta]=\begin{Bmatrix} \dfrac{\partial}{\partial x}[H_w(x,y)] \\ \dfrac{\partial}{\partial y}[H_w(x,y)] \end{Bmatrix}$$

$$=\begin{bmatrix} 0 & 1 & 0 & 2x & y & 0 & 3x^2 & 2xy & y^2 & 0 & 3x^2y & 2xy^2 & y^3 & 3x^2y^2 & 2xy^3 & 3x^2y^3 \\ 0 & 0 & 1 & 0 & x & 2y & 0 & x^2 & 2xy & 3y^2 & x^3 & 2x^2y & 3xy^2 & 2x^3y & 3x^2y^2 & 3x^3y^2 \end{bmatrix} \tag{2.16}$$

$$[C_b]=\begin{bmatrix} -\dfrac{\partial^2}{\partial x^2}[H_w(x,y)] \\ -\dfrac{\partial^2}{\partial y^2}[H_w(x,y)] \\ -2\dfrac{\partial^2}{\partial x \partial y}[H_w(x,y)] \end{bmatrix}$$

$$=-\begin{bmatrix} 0 & 0 & 0 & 2 & 0 & 0 & 6x & 2y & 0 & 0 & 6xy & 2y^2 & 0 & 6xy^2 & 2y^3 & 6xy^3 \\ 0 & 0 & 0 & 0 & 0 & 2 & 0 & 0 & 2x & 6y & 0 & 2x^2 & 6xy & 2x^3 & 6x^2y & 6x^3y \\ 0 & 0 & 0 & 0 & 2 & 0 & 0 & 4x & 4y & 0 & 6x^2 & 8xy & 6y^2 & 12x^2y & 12xy^2 & 18x^2y^2 \end{bmatrix} \tag{2.17}$$

The matrices $[B_m]$, $[B_\theta]$, and $[B_b]$ are the strain interpolation matrices corresponding to in-plane, large deflection, and bending strain components, respectively. Similarly, the subscripts m, θ, and b denote that the strain components are due to membrane, large deflection, and bending, respectively.

2.3 Constitutive Relations

The linear constitutive relations for the k^{th} orthotropic lamina (Figure 2.2) in the principal material coordinates (x_1, x_2) are

$$\begin{Bmatrix} \sigma_1 \\ \sigma_2 \\ \tau_{12} \end{Bmatrix}_k = \begin{bmatrix} Q_{11} & Q_{12} & 0 \\ Q_{12} & Q_{22} & 0 \\ 0 & 0 & Q_{66} \end{bmatrix}_k \left(\begin{Bmatrix} \varepsilon_1 \\ \varepsilon_2 \\ \gamma_{12} \end{Bmatrix} - \begin{Bmatrix} \alpha_1 \\ \alpha_2 \\ 0 \end{Bmatrix}_k \Delta T \right) \tag{2.18}$$

where $[Q]_k$ is the reduced stiffness matrix of the composite lamina, and $\{\alpha\}_k$ is the coefficient of thermal expansion. The terms in $[Q]$ can be evaluated as follows

$$\begin{aligned} Q_{11} &= \frac{E_1}{1-\nu_{12}\nu_{21}} \\ Q_{12} &= \frac{\nu_{12}E_2}{1-\nu_{12}\nu_{21}} = \frac{\nu_{21}E_1}{1-\nu_{12}\nu_{21}} \\ Q_{22} &= \frac{E_2}{1-\nu_{12}\nu_{21}} \\ Q_{66} &= G_{12} \end{aligned} \tag{2.19}$$

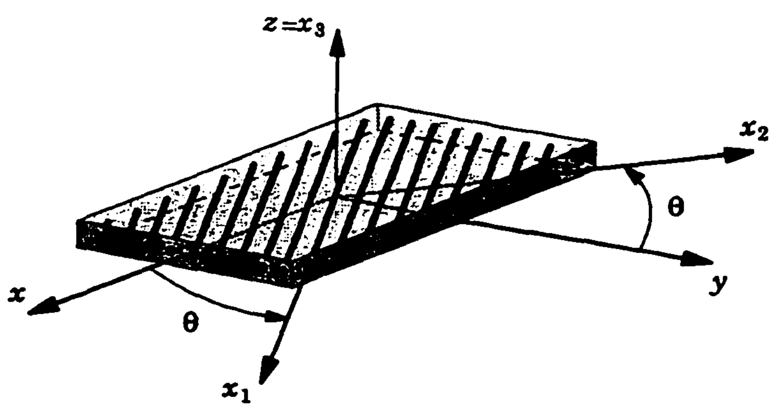

Figure 2.2 A Fiber-Reinforced Lamina with Global and Material Coordinate Systems

Consider the composite lamina in Figure 2.2 having an arbitrary orientation angle θ. The stress and strain transformation relations from the principal directions x_1, x_2 to x, y body directions are

$$\begin{Bmatrix} \sigma_1 \\ \sigma_2 \\ \tau_{12} \end{Bmatrix} = [T_\sigma(\theta)] \begin{Bmatrix} \sigma_x \\ \sigma_y \\ \tau_{xy} \end{Bmatrix}, \quad \begin{Bmatrix} \varepsilon_1 \\ \varepsilon_2 \\ \gamma_{12} \end{Bmatrix} = [T_\varepsilon(\theta)] \begin{Bmatrix} \varepsilon_x \\ \varepsilon_y \\ \gamma_{xy} \end{Bmatrix} \tag{2.20}$$

where

$$[T_\sigma(\theta)] = \begin{bmatrix} c^2 & s^2 & 2sc \\ s^2 & c^2 & -2sc \\ -sc & sc & c^2 - s^2 \end{bmatrix}, \quad [T_\varepsilon(\theta)] = \begin{bmatrix} c^2 & s^2 & sc \\ s^2 & c^2 & -sc \\ -2sc & 2sc & c^2 - s^2 \end{bmatrix} \tag{2.21}$$

with c=cos(θ), s=sin(θ). Thus, the stress-strain relations for a generalized k^{th} lamina, with an orientation angle θ (Figure. 2.3), taking into consideration temperature change, becomes

$$\{\sigma\}_k = \begin{Bmatrix} \sigma_x \\ \sigma_y \\ \tau_{xy} \end{Bmatrix}_k = \begin{bmatrix} \overline{Q}_{11} & \overline{Q}_{12} & \overline{Q}_{16} \\ \overline{Q}_{21} & \overline{Q}_{22} & \overline{Q}_{26} \\ \overline{Q}_{61} & \overline{Q}_{62} & \overline{Q}_{66} \end{bmatrix}_k \left(\begin{Bmatrix} \varepsilon_x \\ \varepsilon_y \\ \gamma_{xy} \end{Bmatrix} - \Delta T \begin{Bmatrix} \alpha_x \\ \alpha_y \\ \alpha_{xy} \end{Bmatrix}_k \right) \tag{2.22}$$

or

$$\{\sigma\}_k = [\overline{Q}]_k \left(\{\varepsilon\} - \Delta T \{\alpha\}_k\right) \tag{2.23}$$

where $[\overline{Q}]_k$,the transformed reduced stiffness matrix, is given by

$$[\overline{Q}]_k = [T_\sigma(\theta)]^{-1} [Q] [T_\varepsilon(\theta)] \tag{2.24}$$

The resultant forces and moments per unit length are

$$\left(\{N\}\ ,\ \{M\}\right) = \int_{-h/2}^{h/2} \{\sigma\}_k (1, z) dz \tag{2.25}$$

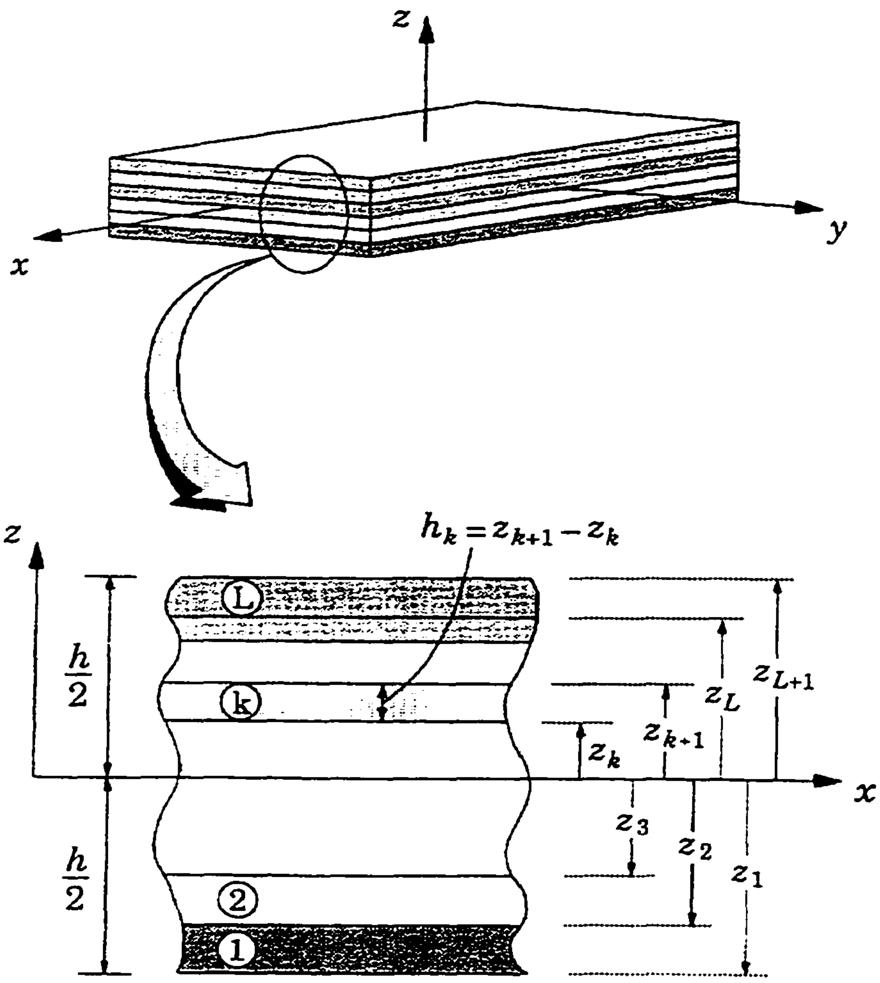

Figure 2.3 Coordinate System and Layer Numbering for a Typical Laminated Plate

and the constitutive equations for a laminate can be written as

$$\begin{Bmatrix} N \\ M \end{Bmatrix} = \begin{bmatrix} A & B \\ B & D \end{bmatrix} \begin{Bmatrix} \varepsilon^o \\ \kappa \end{Bmatrix} - \begin{Bmatrix} N_{\Delta T} \\ M_{\Delta T} \end{Bmatrix} \tag{2.26}$$

where $[A]$, $[B]$, and $[D]$ are the laminate extensional, extension-bending, and bending stiffness matrices, respectively, and are given by

$$\begin{aligned} A_{ij} &= \int_{-h/2}^{h/2} \left(\overline{Q}_{ij}\right)_k dz \\ &= \sum_{k=1}^{L} \left(\overline{Q}_{ij}\right)_k (z_{k+1} - z_k) \end{aligned} \qquad i,j = 1,2,6$$

$$\begin{aligned} B_{ij} &= \int_{-h/2}^{h/2} \left(\overline{Q}_{ij}\right)_k z dz \\ &= \frac{1}{2}\sum_{k=1}^{L} \left(\overline{Q}_{ij}\right)_k \left(z_{k+1}^2 - z_k^2\right) \end{aligned} \qquad i,j = 1,2,6 \qquad (2.27)$$

$$\begin{aligned} D_{ij} &= \int_{-h/2}^{h/2} \left(\overline{Q}_{ij}\right)_k z^2 dz \\ &= \frac{1}{3}\sum_{k=1}^{L} \left(\overline{Q}_{ij}\right)_k \left(z_{k+1}^3 - z_k^3\right) \end{aligned} \qquad i,j = 1,2,6$$

The vectors $\{N_{\Delta T}\}$ and $\{M_{\Delta T}\}$ are the in-plane force and moment due to thermal expansion

$$\begin{aligned} \left(\{N_{\Delta T}\}\ ,\ \{M_{\Delta T}\}\right) &= \int_{-h/2}^{h/2} \left[\overline{Q}\right]_k \Delta T \{\alpha\}_k (1, z) dz \\ &= \sum_{k=1}^{L} \int_{z_k}^{z_{k+1}} \left[\overline{Q}\right]_k \Delta T \{\alpha\}_k (1, z) dz \end{aligned} \qquad (2.28)$$

Substituting Equations 2.11 thru 2.13 into Equation 2.26, the resultant force and moment vectors $\{N\}$ and $\{M\}$ per unit length can be written as

$$\begin{aligned} \{N\} &= [A]\{\varepsilon^o\} + [B]\{\kappa\} - \{N_{\Delta T}\} \\ &= [A]\{\varepsilon_m^o\} + [A]\{\varepsilon_\theta^o\} + [B]\{\kappa\} - \{N_{\Delta T}\} \\ &= \{N_m\} + \{N_\theta\} + \{N_B\} - \{N_{\Delta T}\} \end{aligned} \qquad (2.29)$$

$$\begin{aligned} \{M\} &= [B]\{\varepsilon^o\} + [D]\{\kappa\} - \{M_{\Delta T}\} \\ &= [B]\{\varepsilon_m^o\} + [B]\{\varepsilon_\theta^o\} + [D]\{\kappa\} - \{M_{\Delta T}\} \\ &= \{M_m\} + \{M_\theta\} + \{M_D\} - \{M_{\Delta T}\} \end{aligned} \qquad (2.30)$$

or, in terms of the element nodal displacement vectors, as follows

$$\{N\} = [A][B_m]\{w_m\} + \frac{1}{2}[A][\theta][B_\theta]\{w_b\} + [B][B_b]\{w_b\} - \{N_{\Delta T}\} \qquad (2.31)$$

$$\{M\} = [B][B_m]\{w_m\} + \frac{1}{2}[B][\theta][B_\theta]\{w_b\} + [D][B_b]\{w_b\} - \{M_{\Delta T}\} \qquad (2.32)$$

2.4 Equations of Motion in Structural Node Degree of Freedom

The element nonlinear equations of motion are derived applying the principle of virtual work,

$$\delta W = \delta W_{\text{int}} - \delta W_{ext} = 0 \tag{2.33}$$

which states that for an element in equilibrium, the total work done by internal and external forces (including inertia forces by means of D'Alembert's principle) on an infinitesimal virtual displacement is null. The internal and external work on a plate element produced by internal and external forces, respectively, are given by

$$\delta W_{\text{int}} = \int_A \left(\{\delta \varepsilon^o\}^T \{N\} + \{\delta \kappa\}^T \{M\} \right) dA \tag{2.34}$$

$$\delta W_{ext} = \int_A \left\{ \delta w \left(p(x,y,t) - \rho h w_{,tt} \right) - \delta u \left(\rho h u_{,tt} \right) - \delta v \left(\rho h v_{,tt} \right) \right\} dA \tag{2.35}$$

where A is the element area.

Recalling Equations 2.11 to 2.13, the virtual in-plane strain, $\{\delta\varepsilon^o\}$, and curvature, $\{\delta\kappa\}$, vectors can be expressed as

$$\begin{aligned} \{\delta \varepsilon^o\} &= \delta \{\varepsilon_m^o + \varepsilon_\theta^o\} \\ &= \delta \left([B_m]\{w_m\} + \frac{1}{2}[\theta][B_\theta]\{w_b\} \right) \end{aligned} \tag{2.36}$$

$$\{\delta \kappa\} = \delta([B_b]\{w_b\}) = [B_b]\{\delta w_b\} \tag{2.37}$$

where

$$\delta([B_m]\{w_m\}) = [B_m]\{\delta w_m\} \tag{2.38}$$

$$\delta\left(\frac{1}{2}[\theta][B_\theta]\{w_b\}\right)=\frac{1}{2}[\delta\theta][B_\theta]\{w_b\}+\frac{1}{2}[\theta][B_\theta]\{\delta w_b\}$$

$$=\frac{1}{2}[\theta][B_\theta]\{\delta w_b\}+\frac{1}{2}[\theta][B_\theta]\{\delta w_b\} \tag{2.39}$$

$$=[\theta][B_\theta]\{\delta w_b\}$$

Substituting Equations 2.38 and 2.39 into 2.36, the virtual in-plane strain can be rewritten as

$$\{\delta\varepsilon^o\}=[B_m]\{\delta w_m\}+[\theta][B_\theta]\{\delta w_b\} \tag{2.40}$$

Finally, the internal work is expanded into many terms by replacing the resultant force and moment vectors $\{N\}$ and $\{M\}$ (Equations 2.31 and 2.32), together with the virtual in-plane strain, $\{\delta\varepsilon^o\}$, and curvature, $\{\delta\kappa\}$, vectors (Equations 2.37 and 2.40) into Equation 2.34, to get

$$\delta W_{\text{int}} = \int_A([B_m]\{\delta w_m\}+[\theta][B_\theta]\{\delta w_b\})^T$$

$$\cdot\left([A][B_m]\{w_m\}+\frac{1}{2}[A][\theta][B_\theta]\{w_b\}+[B][B_b]\{w_b\}-\{N_{\Delta T}\}\right)dA$$

$$+\int_A([B_b]\{\delta w_b\})^T$$

$$\cdot\left([B][B_m]\{w_m\}+\frac{1}{2}[B][\theta][B_\theta]\{w_b\}+[D][B_b]\{w_b\}-\{M_{\Delta T}\}\right)dA$$

where the terms of product are listed as follows

$$\int_A\{\delta w_m\}^T[B_m]^T[A][B_m]\{w_m\}dA \tag{2.41-1}$$

$$\int_A\frac{1}{2}\{\delta w_m\}^T[B_m]^T[A][\theta][B_\theta]\{w_b\}dA \tag{2.41-2}$$

$$\int_A\{\delta w_m\}^T[B_m]^T[B][B_b]\{w_b\}dA \tag{2.41-3}$$

$$-\int_A\{\delta w_m\}^T[B_m]^T\{N_{\Delta T}\}dA \tag{2.41-4}$$

$$\int_A \{\delta w_b\}^T [B_\theta]^T [\theta]^T [A][B_m]\{w_m\} dA \tag{2.41-5}$$

$$\int_A \frac{1}{2} \{\delta w_b\}^T [B_\theta]^T [\theta]^T [A][\theta][B_\theta]\{w_b\} dA \tag{2.41-6}$$

$$\int_A \{\delta w_b\}^T [B_\theta]^T [\theta]^T [B]\,[B_b]\{w_b\} dA \tag{2.41-7}$$

$$-\int_A \{\delta w_b\}^T [B_\theta]^T [\theta]^T \{N_{\Delta T}\} dA \tag{2.41-8}$$

$$\int_A \{\delta w_b\}^T [B_b]^T [B][B_m]\{w_m\} dA \tag{2.41-9}$$

$$\int_A \frac{1}{2} \{\delta w_b\}^T [B_b]^T [B][\theta][B_\theta]\{w_b\} dA \tag{2.41-10}$$

$$\int_A \{\delta w_b\}^T [B_b]^T [D][B_b]\{w_b\} dA \tag{2.41-11}$$

$$-\int_A \{\delta w_b\}^T [B_b]^T \{M_{\Delta T}\} dA \tag{2.41-12}$$

The digit after the equation number 2.41-x indicates the term number. For instance, term 6 is the same as Equation 2.41-6. Expressions for the linear stiffness matrices will be given first. Next, expressions for the first-order nonlinear stiffness matrices, depending linearly on $\{w_b\}$ or $\{w_m\}$, will be expressed. Finally, expressions for the second-order nonlinear stiffness matrix depending quadratically on $\{w_b\}$, and thermal load vectors will be addressed.

2.4.1 Linear Stiffness Matrices

Terms 1, 3, 9, and 11 can be combined in matrix form as

$$\begin{Bmatrix} \delta w_b \\ \delta w_m \end{Bmatrix}^T \begin{bmatrix} k_b & k_{bm} \\ k_{mb} & k_m \end{bmatrix} \begin{Bmatrix} w_b \\ w_m \end{Bmatrix} \tag{2.42}$$

where the linear bending, bending-membrane, and membrane stiffness matrices, respectively, are

$$[k_b] = \int_A [B_b]^T [D][B_b] dA \tag{2.43}$$

$$[k_{mb}] = [k_{bm}]^T = \int_A [B_m]^T [B][B_b] dA \tag{2.44}$$

$$[k_m] = \int_A [B_m]^T [A][B_m] dA \tag{2.45}$$

It can be easily determined by inspection that

$$\begin{aligned} [\theta]^T \{N_{\Delta T}\} &= \begin{bmatrix} \frac{\partial w}{\partial x} & 0 \\ 0 & \frac{\partial w}{\partial y} \\ \frac{\partial w}{\partial y} & \frac{\partial w}{\partial x} \end{bmatrix}^T \begin{Bmatrix} N_{\Delta Tx} \\ N_{\Delta Ty} \\ N_{\Delta Txy} \end{Bmatrix} \\ &= [N_{\Delta T}][B_\theta]\{w_b\} \end{aligned} \tag{2.46}$$

where $[N_{\Delta T}]$ is the resultant thermal force matrix

$$[N_{\Delta T}] = \begin{bmatrix} N_{\Delta Tx} & N_{\Delta Txy} \\ N_{\Delta Txy} & N_{\Delta Ty} \end{bmatrix} \tag{2.47}$$

Substituting Equation 2.46 into term 8 yields

$$-\begin{Bmatrix} \delta w_b \\ \delta w_m \end{Bmatrix}^T \begin{bmatrix} k_{N\Delta T} & 0 \\ 0 & 0 \end{bmatrix} \begin{Bmatrix} w_b \\ w_m \end{Bmatrix} \tag{2.48}$$

where the thermal stiffness matrix is

$$[k_{N\Delta T}] = \int_A [B_\theta]^T [N_{\Delta T}][B_\theta] dA \tag{2.49}$$

2.4.2 First-Order Nonlinear Incremental Stiffness Matrices

Adding terms 2 and 5 and rewriting the resulting terms using Equation 2.51 and breaking $[n_{1Nm}]$ into two equal terms yields

$$\frac{1}{2}\begin{Bmatrix}\delta w_b \\ \delta w_m\end{Bmatrix}^T \begin{bmatrix} n_{1Nm} & n_{1bm} \\ n_{1mb} & 0 \end{bmatrix}\begin{Bmatrix} w_b \\ w_m \end{Bmatrix}$$

$$= \frac{1}{2}\{\delta w_b\}^T [n_{1Nm}]\{w_b\} + \frac{1}{2}\{\delta w_m\}^T [n_{1mb}]\{w_b\} + \frac{1}{2}\{\delta w_b\}^T [n_{1bm}]\{w_m\}$$

$$= \frac{1}{2}\{\delta w_m\}^T \int_A [B_m]^T [A][\theta][B_\theta] dA\{w_b\} + \{\delta w_b\}^T \int_A [B_\theta]^T [\theta]^T [A][B_m] dA\{w_m\}$$

$$= \frac{1}{2}\{\delta w_m\}^T \int_A [B_m]^T [A][\theta][B_\theta] dA\{w_b\} + \frac{1}{2}\{\delta w_b\}^T \int_A [B_\theta]^T [\theta]^T [A][B_m] dA\{w_m\}$$

$$+ \frac{1}{2}\{\delta w_b\}^T \int_A [B_\theta]^T [\theta]^T [A][B_m] dA\{w_m\}$$

$$= \frac{1}{2}\{\delta w_m\}^T \int_A [B_m]^T [A][\theta][B_\theta] dA\{w_b\} + \frac{1}{2}\{\delta w_b\}^T \int_A [B_\theta]^T [\theta]^T [A][B_m] dA\{w_m\}$$

$$+ \frac{1}{2}\{\delta w_b\}^T \int_A [B_\theta]^T [N_m][B_\theta] dA\{w_b\} \tag{2.50}$$

By inspection it is seen that

$$[\theta]^T [A][B_m]\{w_m\} = [\theta]^T \{N_m\} = [N_m][B_\theta]\{w_b\} \tag{2.51}$$

where the matrix $[N_m]$, which depends directly on membrane displacement $\{w_m\}$, is

$$[N_m] = \begin{bmatrix} N_{mx} & N_{mxy} \\ N_{mxy} & N_{my} \end{bmatrix} \tag{2.52}$$

Consequently, the first-order nonlinear incremental stiffness matrices are linearly dependent on $\{w_b\}$ and $\{w_m\}$, and are, respectively

$$[n_{1mb}] = [n_{1bm}]^T = \int_A [B_m]^T [A][\theta][B_\theta] dA \tag{2.53}$$

$$[n_{1Nm}] = \int_A [B_\theta]^T [N_m][B_\theta] dA \tag{2.54}$$

Adding terms 7 and 10 and following a similar procedure as for terms 2 and 5, we have

$$\frac{1}{2}\begin{Bmatrix}\delta w_b\\ \delta w_m\end{Bmatrix}^T\begin{bmatrix}n_{1nb} & 0\\ 0 & 0\end{bmatrix}\begin{Bmatrix}w_b\\ w_m\end{Bmatrix}$$

$$=\frac{1}{2}\{\delta w_b\}[n_{1nb}]\{w_b\}$$

$$=\{\delta w_b\}^T\int_A[B_\theta]^T[\theta]^T[B][B_b]dA\{w_b\}+\frac{1}{2}\{\delta w_b\}^T\int_A[B_b]^T[B][\theta][B_\theta]dA\{w_b\}$$

$$=\frac{1}{2}\{\delta w_b\}^T\int_A[B_\theta]^T[\theta]^T[B][B_b]dA\{w_b\}+\frac{1}{2}\{\delta w_b\}^T\int_A[B_\theta]^T[\theta]^T[B][B_b]dA\{w_b\}$$

$$+\frac{1}{2}\{\delta w_b\}^T\int_A[B_b]^T[B][\theta][B_\theta]dA\{w_b\}$$

$$=\frac{1}{2}\{\delta w_b\}^T\int_A[B_\theta]^T[N_b][B_\theta]dA\{w_b\}+\frac{1}{2}\{\delta w_b\}^T\int_A[B_\theta]^T[\theta]^T[B][B_b]\{w_b\}\tag{2.55}$$

$$+\frac{1}{2}\{\delta w_b\}^T\int_A[B_b]^T[B][\theta][B_\theta]dA\{w_b\}$$

By inspection it is determined that

$$[\theta]^T[B][B_b]\{w_b\}=[\theta]^T\{N_B\}=[N_B][B_\theta]\{w_b\}\tag{2.56}$$

where the matrix $[N_B]$ depends directly on the bending displacement $\{w_b\}$, and is given by

$$[N_B]=\begin{bmatrix}N_{Bx} & N_{Bxy}\\ N_{Bxy} & N_{By}\end{bmatrix}\tag{2.57}$$

The first-order nonlinear incremental stiffness matrix is linearly dependent on $\{w_b\}$, and becomes

$$[n_{1NB}]=\int_A\left([B_\theta]^T[\theta]^T[B][B_b]+[B_\theta]^T[N_B][B_\theta]+[B_b]^T[B][\theta][B_\theta]\right)dA\tag{2.58}$$

2.4.3 Second-Order Nonlinear Incremental Stiffness Matrix

The second-order nonlinear stiffness matrix is derived from term 6

$$\frac{1}{3}\begin{Bmatrix}\delta w_b\\ \delta w_m\end{Bmatrix}^T\begin{bmatrix}n_{2b} & 0\\ 0 & 0\end{bmatrix}\begin{Bmatrix}w_b\\ w_m\end{Bmatrix} \tag{2.59}$$

where the second-order incremental nonlinear stiffness matrix is quadratically dependent on $\{w_b\}$ through the relation

$$[n_{2b}] = \frac{3}{2}\int_A [B_\theta]^T[\theta]^T[A][\theta][B_\theta]dA \tag{2.60}$$

2.4.4 Thermal Load Vectors

Terms 4 and 12 are thermal load vectors and can be described as

$$-\begin{Bmatrix}\delta w_b\\ \delta w_m\end{Bmatrix}^T\begin{Bmatrix}p_{b\Delta T}\\ p_{m\Delta T}\end{Bmatrix} \tag{2.61}$$

where the element bending and membrane force vectors, due to thermal effects, are

$$\{p_{b\Delta T}\} = \int_A [B_b]^T\{M_{\Delta T}\}dA \tag{2.62}$$

and

$$\{p_{m\Delta T}\} = \int_A [B_m]^T\{N_{\Delta T}\}dA \tag{2.63}$$

Combining Equations 2.42, 2.48, 2.53-4, 2.58-9 and 2.61, the virtual work of the internal forces on a plate element becomes

$$\begin{aligned}\delta W_{int} = &\begin{Bmatrix}\delta w_b\\ \delta w_m\end{Bmatrix}^T\left(\begin{bmatrix}k_b & k_{bm}\\ k_{mb} & k_m\end{bmatrix} - \begin{bmatrix}k_{N\Delta T} & 0\\ 0 & 0\end{bmatrix} + \frac{1}{2}\begin{bmatrix}n_{1Nm}+n_{1NB} & n_{1bm}\\ n_{1mb} & 0\end{bmatrix}\right.\\ &\left.+\frac{1}{3}\begin{bmatrix}n_{2b} & 0\\ 0 & 0\end{bmatrix}\right)\begin{Bmatrix}w_b\\ w_m\end{Bmatrix} - \begin{Bmatrix}\delta w_b\\ \delta w_m\end{Bmatrix}^T\begin{Bmatrix}p_{b\Delta T}\\ p_{m\Delta T}\end{Bmatrix}\end{aligned} \tag{2.64}$$

From Equation 2.35, the virtual work of the external forces on a plate element is

$$\delta W_{ext} = \int_A [\delta w(-\rho h\ddot{w} + p(t)) + \delta u(-\rho h\ddot{u}) + \delta v(-\rho h\ddot{v})]dA \tag{2.35}$$

where $p(t)$ is the random fluctuation pressure generated by the acoustic excitation.

Using the element displacement functions, Equation 2.7, the inertia and partial displacement variables in Equation 2.34 can be rewritten as

$$\begin{aligned}
\delta w &= [H_w][T_b]\{\delta w_b\} \\
\dot{w} &= [H_w][T_b]\{\dot{w}_b\} \\
\ddot{w} &= [H_w][T_b]\{\ddot{w}_b\} \\
\delta u &= [H_u][T_m]\{\delta w_m\} \\
\ddot{u} &= [H_u][T_m]\{\ddot{w}_m\} \\
\delta v &= [H_v][T_m]\{\delta w_m\} \\
\ddot{v} &= [H_v][T_m]\{\ddot{w}_m\}
\end{aligned} \tag{2.65}$$

Substituting the above expressions into Equation 2.35, the finite element form of the virtual work due to the external forces on an element becomes

$$\begin{aligned}
\delta W_{ext} = \int_A \Big[& \{\delta w_b\}^T [T_b]^T [H_w]^T \left(-\rho h [H_w][T_b]\{\ddot{w}_b\}\{w_b\} + p(x,y,t)\right) \\
& + \{\delta w_m\}^T [T_m]^T [H_u]^T \left(-\rho h [H_u][T_m]\{\ddot{w}_m\}\right) \\
& + \{\delta w_m\}^T [T_m]^T [H_v]^T \left(-\rho h [H_v][T_m]\{\ddot{w}_m\}\right)\Big] dA \\
= -& \begin{Bmatrix} \delta w_b \\ \delta w_m \end{Bmatrix}^T \begin{bmatrix} m_b & 0 \\ 0 & m_m \end{bmatrix} \begin{Bmatrix} \ddot{w}_b \\ \ddot{w}_m \end{Bmatrix} + \begin{Bmatrix} \delta w_b \\ \delta w_m \end{Bmatrix}^T \begin{Bmatrix} p_b(t) \\ 0 \end{Bmatrix}
\end{aligned} \tag{2.66}$$

where $[m_b]$ and $[m_m]$ are the bending and in-plane mass matrices defined, respectively as

$$[m_b] = \int_A \rho h [T_b]^T [H_w]^T [H_w][T_b] dA \tag{2.67}$$

$$[m_m] = \int_A \rho h \left([T_m]^T [H_u]^T [H_u][T_m] + [T_m]^T [H_v]^T [H_v][T_m]\right) dA \tag{2.68}$$

and the random force vector $\{p_b(t)\}$ is defined as

$$\{p_b(t)\} = \int_A [T_b]^T [H_w]^T p(x,y,t)\, dA \tag{2.69}$$

Combining Equations 2.64 and 2.66 into Equation 2.33, the element equations of motion for a plate under combined acoustic and thermal load can be expressed as

$$\begin{bmatrix} m_b & 0 \\ 0 & m_m \end{bmatrix}\begin{Bmatrix} \ddot{w}_b \\ \ddot{w}_m \end{Bmatrix} + \left(\begin{bmatrix} k_b & k_{bm} \\ k_{mb} & k_m \end{bmatrix} - \begin{bmatrix} k_{N\Delta T} & 0 \\ 0 & 0 \end{bmatrix}\right)\begin{Bmatrix} w_b \\ w_m \end{Bmatrix}$$
$$+\left(\frac{1}{2}\begin{bmatrix} n_{1Nm}+n_{1NB} & n_{1bm} \\ n_{1mb} & 0 \end{bmatrix} + \frac{1}{3}\begin{bmatrix} n_{2b} & 0 \\ 0 & 0 \end{bmatrix}\right)\begin{Bmatrix} w_b \\ w_m \end{Bmatrix} = \begin{Bmatrix} p_{b\Delta T} \\ p_{m\Delta T} \end{Bmatrix} + \begin{Bmatrix} p_b(t) \\ 0 \end{Bmatrix} \tag{2.70}$$

For simplicity and ease in the physical understanding, Equation 2.70 is rewritten as

$$\begin{bmatrix} m_b & 0 \\ 0 & m_m \end{bmatrix}\begin{Bmatrix} \ddot{w}_b \\ \ddot{w}_m \end{Bmatrix} + \left(\begin{bmatrix} k_b & k_B \\ k_B^T & k_m \end{bmatrix} - \begin{bmatrix} k_{N\Delta T} & 0 \\ 0 & 0 \end{bmatrix}\right)\begin{Bmatrix} w_b \\ w_m \end{Bmatrix}$$
$$+\left(\begin{bmatrix} k_{1Nm}+k_{1NB} & k_{1bm} \\ k_{1mb} & 0 \end{bmatrix} + \begin{bmatrix} k_{2b} & 0 \\ 0 & 0 \end{bmatrix}\right)\begin{Bmatrix} w_b \\ w_m \end{Bmatrix} = \begin{Bmatrix} p_{b\Delta T} \\ p_{m\Delta T} \end{Bmatrix} + \begin{Bmatrix} p_b(t) \\ 0 \end{Bmatrix} \tag{2.71}$$

where the first-order nonlinear stiffness matrices, depending linearly on $\{w_b\}$ and $\{w_m\}$, are

$$([k_{1Nm}],[k_{NB}],[k_{1bm}]) = \frac{1}{2}([n_{1Nm}],[n_{NB}],[n_{1bm}]) \tag{2.72}$$

and the second-order matrix quadratically dependent on $\{w_b\}$ is

$$[k_{2b}] = \frac{1}{3}[n_{2b}] \tag{2.73}$$

The subscripts B, $N\Delta T$, Nm, and NB denote the stiffness matrix corresponding to the laminate extension-bending $[B]$, in-plane force components $\{N_{\Delta T}\}$, $\{N_m\} = [A]\{\varepsilon_m^0\}$, and $\{N_B\} = [B]\{k\}$, respectively.

Assembling all the elements and taking into account the kinematic boundary conditions, the system equations of motion in structural node DOF can be represented as follows

$$\begin{bmatrix} M_b & 0 \\ 0 & M_m \end{bmatrix}\begin{Bmatrix} \ddot{W}_b \\ \ddot{W}_m \end{Bmatrix}+\left(\begin{bmatrix} K_b & K_B \\ K_B^T & K_m \end{bmatrix}-\begin{bmatrix} K_{N\Delta T} & 0 \\ 0 & 0 \end{bmatrix}\right)\begin{Bmatrix} W_b \\ W_m \end{Bmatrix}$$

$$+\left(\begin{bmatrix} K_{1Nm}+K_{1NB} & K_{1bm} \\ K_{1mb} & 0 \end{bmatrix}+\begin{bmatrix} K_{2b} & 0 \\ 0 & 0 \end{bmatrix}\right)\begin{Bmatrix} W_b \\ W_m \end{Bmatrix}=\begin{Bmatrix} P_{b\Delta T} \\ P_{m\Delta T} \end{Bmatrix}+\begin{Bmatrix} P_b(t) \\ 0 \end{Bmatrix} \quad (2.74a)$$

or

$$[M]\{\ddot{W}\}+([K]-[K_{N\Delta T}]+[K_1]+[K_2])\{W\}=\{P_{\Delta T}\}+\{P(t)\} \quad (2.74b)$$

where $[M]$, $[K]$, and $\{P\}$ denote the system mass, linear stiffness matrices, and load vector, respectively; and $[K_1]$ and $[K_2]$ denote the first-order and second-order nonlinear stiffness matrices which depend linearly and quadratically on displacement $\{W\}$.

For given temperature rise ΔT and random loads, Equation 2.74 can be solved by numerical integration in the structural node DOF. This approach has been carried out for random response analysis with simulated random loads by Green and Killey [85] and Robinson [86]. It turned out to be costly computationally because of the following:

(i) the large number of DOF of the system,

(ii) the nonlinear stiffness matrices $[K_1]$ and $[K_2]$ have to be assembled and updated from the element nonlinear stiffness matrices at each time step, and

(iii) the allowable integration time step was extremely small.

Consequently, in the solution procedure in Chapter 4, Equation 2.74 is transformed into a set of truncated modal coordinates with rather small DOF.

CHAPTER 3

FATIGUE ANALYSIS AND RAINFLOW CYCLES

Experience has shown that structures that are subjected to periodic loads fail after a finite number of load cycles at a stress that is significantly lower than their predicted static failure loads. This phenomenon is known as fatigue. It is common practice for designers to work with S-N curves, which are empirical data relating the failure stress levels to the number of load cycles. The S-N curves are obtained by performing tests in which the specimens are loaded by periodic (mostly harmonic) loads with amplitudes that are changed between specimens and observing the number of cycles to failure. Many specimens must be tested in order to generate a reliable S-N curve, and such curves have been produced in many design manuals. When plotted using logarithmic scales, these data usually yield a trend toward a straight line with negative slope.

Experienced designers use the S-N curves only as guidelines. The reason is that actual structures do not have geometrical configurations and loading conditions that are consistent with the published test specimen data. Usually practical loadings are not harmonic and certainly do not have constant amplitude cycles. The oscillating load does not always have zero mean, and the ratio between maximum and minimum amplitudes does not always coincide with fatigue tested specimens, and therefore with the data contained in the manuals. During the past 40 years, theories for damage accumulation were developed and applied. Most of these applications were based on experimental observations, and during the early periods of the design to fatigue, most procedures were not explained theoretically. One way to deal with varying amplitude loads is to form equivalent load cycles and then to use one of the many damage accumulation methods. The equivalent load cycles are formed by pairing the local maxima with the local minima, and there are many definitions of cycle counting in the literature. The *Rainflow Cycle* (RFC) method was first introduced by Endo in 1967. (More details are given in a paper by Matsuishi and Endo [75].) Subsequently, it has become the most commonly used cycle counting method in engineering. The validity of the RFC method has been studied, e.g., Dowling [74], where the accuracy of fatigue life predictors, which were based on eight commonly used cycle counting methods, were investigated. The conclusion of Dowling's confirmation experiment was that "... the counting of all closed hysteresis loops as cycles by means of the rainflow counting method allows accurate life predictions. The use of any method of cycle counting other than range pair or rainflow methods can result in inconsistencies and gross differences between predicted and actual fatigue lives."

The original definition by Endo is a complicated recursive algorithm. Since then, several equivalent algorithms for counting rainflow cycles have been presented. Two local definitions of RFCs were given by Rychlik [76-78] and Bishop and Sherratt [79]. From these definitions it is possible to formulate events for stochastic processes, which represent the forming of rainflow cycles, and are suitable for probabilistical computations. It will be shown later in this chapter that the statistical properties necessary for fatigue calculations can be extracted either from the time domain or from the power spectral densities (PSD). These two definitions break down the rainflow range mechanism into logical steps, which can be analyzed using Markov process theory.

Then, using a theoretically based relationship, the problem of obtaining the rainflow range density function from the PSD data is solved. The principal drawback is that the excitation acoustic load is assumed stationary, ergodic, and Gaussian, which is not the case in the stress response of panels subjected to high acoustic loads regardless of the state of the elevated thermal environment. By comparing the fatigue results from a *finite element analysis* (FEA) model generated PSD with FEA model generated time histories, it is possible to develop some conclusions about the models that have been analyzed in the present work. The best comparison is between FEA model generated time/PSD and experimentally obtained fatigue estimates. This will provide the ultimate validity test for the new techniques; unfortunately this will not be possible because experimental fatigue data are not available to the author presently.

The present chapter will consider fatigue life estimation in the time and frequency domains, but it will only define the Rychlik definition to obtain the rainflow range *probability distribution function* (PDF). The empirical closed form expression for the probability density function of rainflow ranges given by Dirlik [81] is also addressed. The Rychlik RFC method will be retained as the cycle counting method for fatigue life calculations. Finally, two extensions of the general fatigue life evaluation procedure have been introduced for better estimates of: (i) moderately large nonlinear random response (without temperature effects), and (ii) the *snap-through* or *oil canning* phenomenon (with temperature effects) between the two buckled positions.

3.1 Inputs for Fatigue Life Estimates

For fatigue life estimation the measured strains or stresses, which are also called loads in fatigue analysis, can be given in one of the two following forms:

(1) As a measurement of the time history of the stress or strain with some sampling frequency in Hertz. Such loadings will be denoted by $x(t)$, $0 \le t \le T$, where t is the time and T the duration of the measurement.

(2) In the frequency domain as a power spectrum. This means that the data are represented by a Fourier series

$$x(t) \approx m + \sum_{i=1}^{N} \left[a_i \cos(\omega_i t) + b_i \sin(\omega_i t)\right]$$

where $\omega_i = \frac{2\pi i}{T}$ are the angular frequencies, m is the mean of the signal, and a_i and b_i are Fourier coefficients.

3.2 Statistical Characterization

Some general properties of a measured load (type 1) can be summarized by using a few simple characteristics. Those are: the mean, m, defined as the average of all values; the standard deviation σ; the variance σ^2, which measures the variability around the mean in a linear and quadratic scale; the skewness, *skew*, which vanishes for symmetric distributions and becomes positive or negative if the distribution develops a longer tail to the right or the left of the mean; and the kurtosis, *kur*, which shows how much the load departs from an ideal Gaussian process. The mean and central moment quantities are estimated by,

$$m = \frac{1}{T}\int_0^T x(t)dt \tag{3.1}$$

$$\sigma^2 = \frac{1}{T}\int_0^T (x(t) - m)^2 dt \tag{3.2}$$

$$skew = \frac{1}{T}\int_0^T \frac{(x(t)-m)^3}{\sigma^3}dt \tag{3.3}$$

$$kur = \frac{1}{T}\int_0^T \frac{(x(t)-m)^4}{\sigma^4}dt - 3 \tag{3.4}$$

Another important property is the *crossing spectrum* or crossing intensity $\mu(u)$ defined as the intensity of up-crossings, the average number of up-crossings per time unit, of a level u by $x(t)$ as a function of u. The *mean frequency*, f_0, is usually defined as the number of times $x(t)$ crosses upwards the mean value normalized by the length of the interval T, i.e., $f_0=\mu(m)$, but in some cases f_0 will be defined as the average number of rainflow cycles per time unit. The irregularity factor, α, measures how dense the local extremes are relative to the mean frequency f_0. For a narrowband signal there will be only one local maximum between up-crossings of the mean level, giving an irregular factor equal to one. As the signal becomes more broadband, there is more than one local extreme yielding to an irregularity factor close to zero. The process of fatigue damage accumulation depends only on the values and the order of the local extremes in the load, i.e., the exact path is not important and the sequence of local extremes is called the *sequence of turning points* (TP). The statistical characterization is general in the sense that it can be applied to Gaussian and non-Gaussian processes.

3.3 Frequency Modeling

The most important characteristic of a load (type 2) in the frequency domain is its power spectrum

$$\hat{s}_i = \frac{\left(a_i^2 + b_i^2\right)}{2\Delta\omega} \tag{3.5}$$

where $\Delta\omega$ is the sampling interval, i.e. $\omega_i = i\Delta\omega$ and a_i, b_i are Fourier coefficients. The recorded data file $\hat{s}(\omega_i) = (\omega_i, \hat{s}_i)$ is called the power spectrum of $x(t)$. The sequence, $\phi_i = \arccos\left(a_i \big/ \sqrt{2\hat{s}_i \Delta\omega} \right)$ is called a sequence of phases and the Fourier series can be written as follows

$$x(t) \approx m + \sum_{i=1}^{N} \sqrt{2\hat{s}_i \Delta\omega} \cos(\omega_i t + \phi_i) \tag{3.6}$$

If the sampled signal contains exactly $2N+1$ points, then $x(t)$ is equal to its first Fourier series at the sampled points. In the special case when $N=2^n$, the so called *Fast Fourier Transform* (FFT) can be used in order to compute the Fourier coefficients, and the spectrum, from the measured signal (load) and, in reverse, the signal from the coefficients. The Fourier coefficients to the zero frequency of the Fourier series are just the mean of the signal, while the variance or zero-order spectral moment is given by

$$\sigma^2 \approx \int_0^\infty \hat{s}(\omega) d\omega = \Delta\omega \sum \hat{s}(\omega_i) \tag{3.7}$$

Similarly, higher-order spectral moments are defined by

$$m_i = \int_0^\infty \omega^i \hat{s}(\omega) d\omega \tag{3.8}$$

3.4 Rainflow Cycles, Crossings and Hysteresis Loops

As mentioned previously, in fatigue applications it is generally agreed that the shape of the load connecting two intermediate local extremes is of no importance, and only the values of the local minima and maxima of the load sequence influence the lifetime. Consequently, the load process can be characterized by its sequence of local extremes, also called *turning points*. Suppose that $\{X_t\}_{t\geq 0}$ represents a process with a finite number of local extremes occurring at the time period t_1, t_2, ... For simplicity, assume that the first local extreme is a minimum, and then the sequence of turning points can be denoted as

$$TP(\{X_t\}) = \{X_{t_1}, X_{t_2}, X_{t_3}, X_{t_4}, X_{t_5}, X_{t_6} \ldots\} = \{m_0, M_0, m_1, M_1, m_2, M_2, m_3, M_3, \cdots\} \quad (3.13)$$

where m_k denotes a minimum and M_k a maximum, see Figure 3.1.

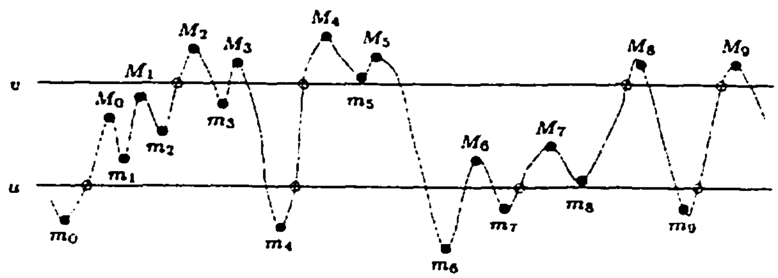

Figure 3.1 Load Curve where TP are Marked by Dots (•)

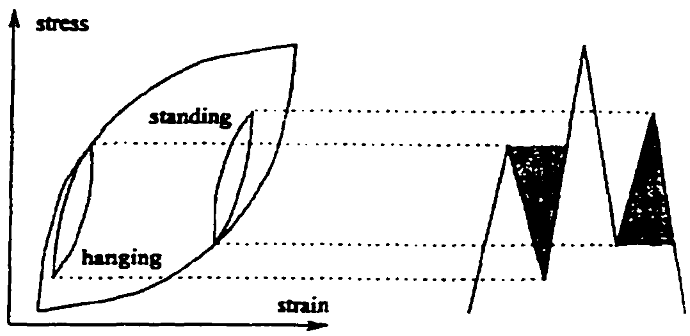

Figure 3.2 Hysteresis Loop in the Stress-Strain

As stated previously, the most widely used cycle counting method is the rainflow counting which was designed to catch both slow and rapid variations of the load by forming cycles by pairing high maxima with low minima even if they are separated by intermediate extremes. Each local maximum is used as the maximum of a hysteresis loop with an amplitude that is computed by the rainflow algorithm. What the algorithm really does is to count hysteresis cycles for the load in the stress-strain plane (Figure 3.2). As mentioned in the introduction, there are several ways of defining the RFC. However, they are all basically the same. The only difference is the treatment of the so-called residual, which is the hysteresis loops that were not closed. The RFC used in this work is the non-recursive algorithm equivalent to the original definition given by Rychlik [76].

The formal definition is:

Let X(t), $0 \le t \le T$, be a function with finitely many local maxima of height M_k occurring at times t_k. For the k^{th} maximum at time t_k define the following right and left minima

$$\begin{aligned} m_k^- &= \inf\{x(t) : t_k^- < t < t_k\} \\ m_k^- &= \inf\{x(t) : t_k < t < t_k^+\} \end{aligned} \tag{3.14}$$

where

$$\begin{aligned} t_k^- &= \begin{cases} \sup\{t \in [0,t_k) : X(t) > X(t_k)\}, \mathit{if}\, X(t) > X(t_k)\ \mathit{for\,some}\, t \in [0,t_k) \\ 0,\ \mathit{otherwise} \end{cases} \\ t_k^+ &= \begin{cases} \inf\{t \in (t_k,T] : X(t) > X(t_k)\}, \mathit{if}\, X(t) > X(t_k)\ \mathit{for\,some}\, t \in (t_k,T] \\ T,\ \mathit{otherwise} \end{cases} \end{aligned} \tag{3.15}$$

Then the k^{th} RFC is defined as (m_k^{RFC}, M_k), where

$$m_k^{RFC} = \begin{cases} \max(m_k^-, m_k^+),\ \mathit{if}\ t_k^+ < T \\ m_k^-,\ \mathit{if}\ t_k^+ = T \end{cases} \tag{3.16}$$

The definition is best understood graphically illustrated in Figure 3.3 and defined as: *From each local maximum M_k one shall try to reach above the same level, in the backward (left) and forward (right) directions, with a as small a downward excursion as* *possible. The minima, m_k^- and m_k^+ on each side are identified. That minimum which represents the smallest deviation from the maximum M_k is defined as the corresponding rainflow minimum m_k^{RFC}.*

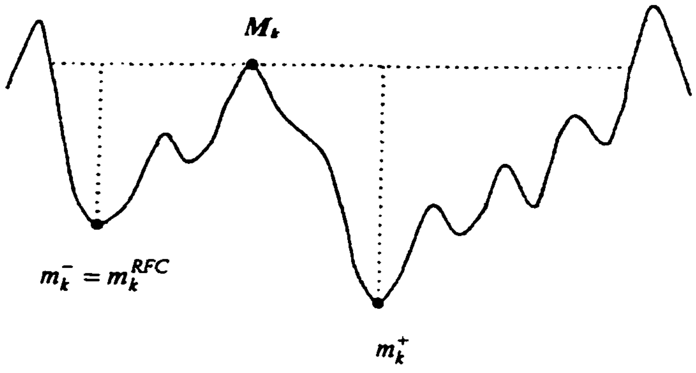

Figure 3.3 Definition of the Rainflow Cycle, as given by Rychlik [76]

Consider t_k being the time of the k^{th} local maximum with the corresponding rainflow amplitude $s_k^{RFC} = \left(M_k - m_k^{RFC}\right)/2$, the amplitude of the attached hysteresis loop. For very complicated loads, like a Brownian or chaotic motion, where there are infinitely many local extremes in a finite interval, the rainflow is redefined as follows. Rainflow minimum $m^{RFC}(t)$ for all time points t of a load $x(t)$ is defined in such a way that the rainflow amplitude $x(t)$- $m^{RFC}(t)$ is zero if the point $x(t)$ is not a strict local maximum of the load. It is also possible to divide the set of rainflow cycles into two groups, depending on whether the rainflow minimum occurs before or after the maximum. The two different kinds of cycles occur on an up-going or a down-going hysteresis arm, and are called hanging and standing RFC (see Figure 3.2), respectively. The standing cycles are defined as (m_k^{RFC}, M_k), when the minimum occurs before the maximum, and the hanging cycles are defined as (M_k, m_k^{RFC}), when the minimum occurs after the maximum. For a more precise definition the reader is referred to Rychlik [76]. The RFC counting can be interpreted as a pair of a minimum m_k^{RFC} and a maximum M_k, where the amplitude is the most important characteristic for fatigue evaluation. In fatigue estimates, a cycle is often represented as a range-mean pair. The definition of the amplitude, the range and the mean cycle is (Figure 3.4)

$$\begin{aligned} amplitude &= \left(M_k - m_k^{RFC}\right)/2 \\ range &= M_k - m_k^{RFC} \\ mean &= \left(M_k + m_k^{RFC}\right)/2 \end{aligned} \tag{3.17}$$

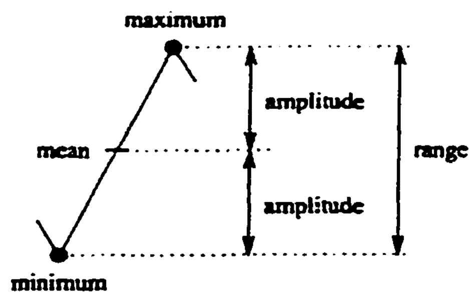

Figure 3.4 Definitions of Amplitude, Range and Mean

As will be shown in Chapter 4 the set of amplitudes is often represented in the form of a histogram or a cumulative histogram (Figure 4.7). The important problem is to find the true distribution of cycles or *Markov chain* as the duration T tends to infinity. This is a difficult problem that will be addressed later on in section 3.5.

Besides the RFC, another simpler definition is needed, namely the *min-max* cycles. From the turning points (TP) it is an easy process to extract the min-max cycles, also called *Peak-Through-Valley Cycle* (PTVC). The definition is as follows:

Let $X(t)$, $0 \leq t \leq T$, be a function with finitely many load maximum of height M_k occurring at times t_k. Then the k^{th} min-max cycle is defined as (m_k, M_k), where m_k is the minimum preceding M_k, and the k^{th} max-min cycle is defined as (M_k, m_{k+1}) and is the minimum succeeding M_k.

The observed cycles can be visualized as a cloud of points in the min-max plane (Figure 4.6).

3.5 Rainflow Matrix

Since the wave oscillation (load) intensity is closely related to the first passage problem, it can be practically handled if some Markov structure of the process is assumed. While Gaussian processes are an important class of models for linear problems, Markov processes are the appropriate models as far as rainflow models are concerned. In this section, the so-called *Markov Chain of TP* will be introduced.

An arbitrary load sequence of TP will be called a Markov chain of TP if it forms a Markov chain, i.e., if the distribution of a local extremum depends only on the value of the previous extremum. The elements in the histogram matrix of min-to-max cycles and max-to-min cycles are equal to the observed number of transitions from a minimum (or maximum) to a maximum (or minimum) of specified height. Consequently, the probabilistic structure of the Markov chain of TP is fully defined by the expected histogram matrix of min-to-max and max-to-min cycles, sometimes called *Markov Matrices*. In other words, the above can be restated as follows: From the discretized TP the cycles in the load can be extracted, e.g., RFC or min-max cycles. The cycle count can then be summarized in a two dimensional histogram and be represented by a matrix. Let us define for RFC the *rainflow matrix* F^{RFC}, for min-max cycles the *min-max matrix* F, and for max-min cycles the *max-min matrix* $\hat{F}$. Figure 3.5 illustrates the matrices F^{RFC}, F, and $\hat{F}$ for a discrete load. Finding the expected rainflow matrix is a difficult problem requiring significant computational time. Only explicit results are known for special classes of processes, e.g., if the load is stationary diffusion, a Markov chain, or a function of a vector valued Markov chain.

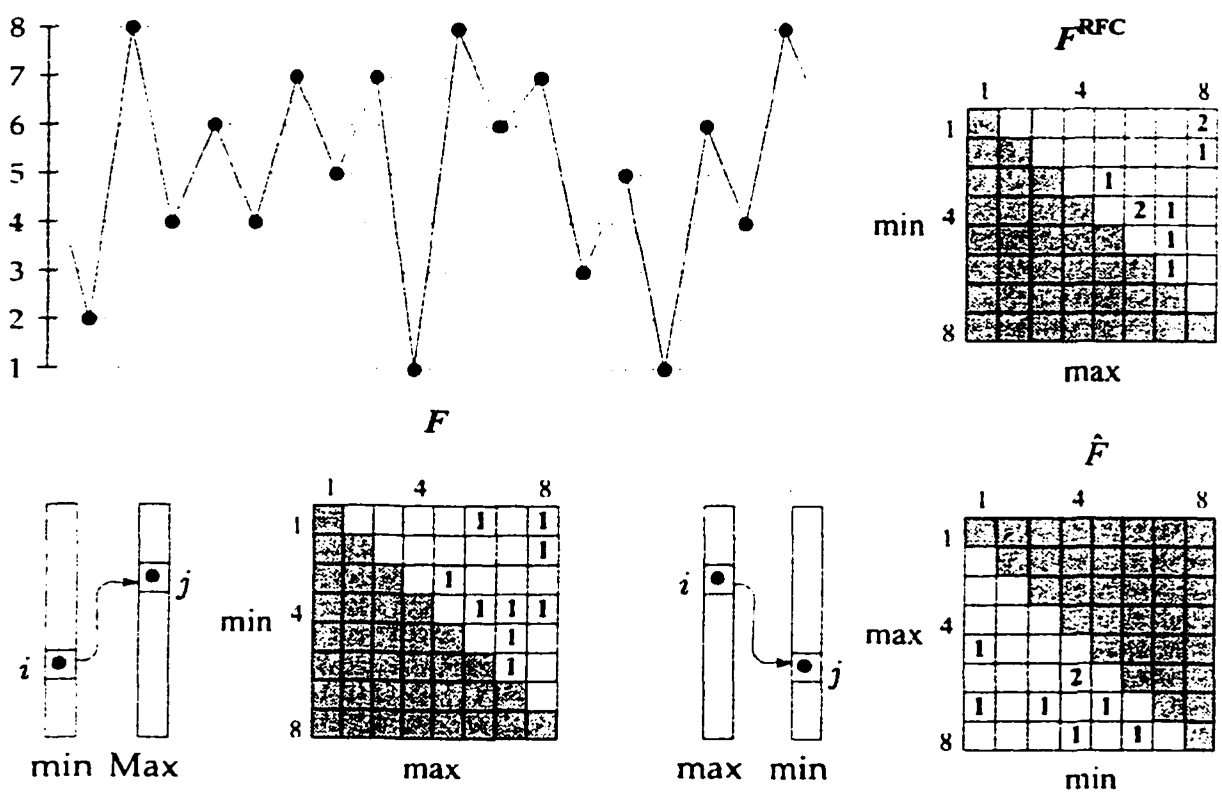

Figure 3.5 F^{RFC}, F and $\hat{F}$ Matrices for Discrete Loading Process

3.6 Damage Accumulation

For design purposes experiments are often made on a specimen of material subjected to a constant amplitude load, and one counts the number of cycles until specimen failure. The number of *load cycles* $N(s)$ as well as the amplitudes s are recorded. For small amplitudes no damage is generally observed even during extended experiments and the fatigue life is set to infinity, $N(s) \approx \infty$. In general one uses the Whöler (S-N) model,

$$N(s) = \begin{cases} K\, s_k^{-\beta} & s_k > s_\infty \\ \infty & s_k \le s_\infty \end{cases} \quad \text{with } s_k = \left(M_k - m_k^{RFC}\right)/2 \tag{3.18}$$

where s_∞ is called the *fatigue limit*, and K and β are material property dependent variables that can be approximated by their expected values $E[\beta]$ and $E[K]$. In the above equation s_k is identical to s_k^{RFC} defined in the previous section. The two constants K and β are determined by linear regression of experimental data on various material specimens under uniform loading.

For random loads of variable amplitude, the S-N curves and a cycle counting method are combined by means of the *Palmgren-Miner* linear damage accumulation theory to predict fatigue failure. The Palmgren-Miner hypothesis is that the fatigue damage incurred at a given load level is proportional to the sum of the number of cycles applied at that stress level divided by the total number of cycles required to cause failure at the same level. When the fatigue loading involves many levels of stress amplitude, the total damage is a sum of the different cycle ratios and failure occurs when the cycle ratio sum equals to unity, i.e.,

$$D = \sum_{k=1} \left(\frac{n_k}{N(s_k)} \right) = 1.0 \tag{3.19}$$

3.6.1 Time Domain

Combining Equations 3.18 and 3.19 in the time domain, with the assumption that if the k^{th} cycle has an amplitude s_k causing damage equal to $1/N(s_k)$ for random ergodic stationary processes, total damage is then

$$E[D(t)] = E\left[\sum_{t<t_k} \frac{1}{N(s_k)}\right] = E\left[\frac{1}{K}\sum_{t<t_k} s_k^{\beta}\right] = E[\frac{1}{K} D_{\beta}(t)] \tag{3.20}$$

where the sum contains all cycles that have been completed up to time t. If the total damage exceeds one at time t, the fatigue life T^f is reached. For high cycle fatigue, the time to failure is considered long, more than $10^5/f_0$, and then the damage, $D_\beta(t)$, can be approximated by its expected value $E[D_\beta(t)]$. A very simple life predictor is obtained when $E[K]$ is replaced by a constant equal to the median value of K. This leads to the simplified fatigue life predictor

$$T^f = \frac{1}{E[D(t)]} \tag{3.21}$$

3.6.2 Frequency Domain

In the time domain, the estimation of the probability distribution of the load amplitudes was achieved through means of a cycle counting, more precisely the rainflow cycle approach. When the load is expressed in the frequency domain, the probability amplitude distribution cannot not be extracted directly from the PSD except in some special cases. The spectral domain approach is a two-step procedure. The first part is to compute for a given load, stress having a specific covariance function or rather PSD, the so-called Markov matrix. That means joint density of the minimum and the following maximum. This is done for processes that are assumed Gaussian, which means that they are the sum of cosine functions with different frequencies, independent phases uniformly distributed and Rayleigh amplitudes. In the second part, using the approximation that the sequence of local extremes is a Markov chain, the rainflow matrix is computed. Note that the second step is totally independent of whether the process is Gaussian or not. Obviously, for nonlinear systems the phases are usually dependent and the amplitudes not Rayleigh, and hence the process is not Gaussian. Selecting a method of computing the Markov matrix may not be easy and depends on particular applications. This topic is the subject of extensive research within the oceanographic community that deals with fatigue life of offshore platforms [76-81, 87]. A theoretical solution based on the work of Rice [88] for Gaussian random ergodic stationary processes have been derived by Bishop and Sherratt [79-80].

3.7 Dirlik's Approximation

Dirlik [81] has produced an empirical closed form expression for the probability density function of rainflow ranges using extensive computer simulations to model the signals using the Monte Carlo technique. Dirlik's empirical relation is also based on stationary, ergodic and Gaussian processes with the Markov assumption. The empirical expression for rainflow ranges is expressed as

$$p(S) = \frac{\frac{D_1}{Q} e^{\frac{-Z}{Q}} + \frac{D_2 Z}{R^2} e^{\frac{-Z^2}{2R^2}} + D_3 Z e^{\frac{-Z^2}{2}}}{2\sqrt{m_0}} \tag{3.22}$$

where $p(S)$ is the probability density function of rainflow ranges of S, and

$$m_n = \int_0^\infty f^n G(f) df \tag{3.23}$$

$$\alpha = \frac{m_2}{\sqrt{m_0 m_4}} \tag{3.24}$$

$$x_m = \frac{m_1}{m_0}\sqrt{\frac{m_2}{m_4}} \tag{3.25}$$

$$D_1 = \frac{2\left(x_m - \alpha^2\right)}{1+\alpha^2} \tag{3.26}$$

$$D_2 = \frac{\left(1 - \alpha - D_1 + D_1^2\right)}{1-R} \tag{3.27}$$

$$D_3 = 1 - D_1 - D_2 \tag{3.28}$$

$$Q = \frac{1.25\left(\alpha - D_3 - D_2 R\right)}{D_1} \tag{3.29}$$

$$R = \frac{\alpha - x_m - D_1^2}{1 - \alpha - D_1 + D_1^2} \tag{3.30}$$

$$Z = \frac{S}{2\sqrt{m_0}} \tag{3.31}$$

and the stress range S is

$$S = 2\sqrt{m_0}Z \tag{3.32}$$

The total damage is given by

$$E[D] = E[P]\frac{T}{K}\int_0^{\infty} S^{\beta} p(S) dS = E[P]\frac{T}{K}\sum_{S<S_k} S^{\beta} p(S) \tag{3.33}$$

where $E[P]$ is the expected number of peaks defined as $E[P] = \sqrt{m_4/m_2}$, and S_k is the maximum design value of the ultimate stresses that for aluminum structures are in the neighborhood of 45,000 to 55,000 psi (310x10^6 to 379x10^6 Pa) in areas which are fatigue critical. The higher moments, m_2 and m_4, are calculated using Equation 3.23.

Note the importance of the rainflow amplitudes distribution and in particular the value of the material constant β-power in fatigue life prediction either from the time or frequency domains approaches.

3.8 Transformed Gaussian Processes (TGP)

The present section remains the subject of a great deal of research by the oceanographic community related to fatigue life of offshore platforms submitted to random sea loads. One possibility in approaching slightly non-Gaussian nonlinear processes in the frequency domain is to approximate them by transformed Gaussian processes $X(t) = G(\widetilde{X}(t))$, where $\widetilde{X}(t)$ is Gaussian and G a deterministic function. For fatigue analysis G should be related to the crossing intensity $\mu(u)$. Then, having a spectrum of transformation, the rainflow matrix can be approximated. There are several ways to proceed when selecting the transformation deterministic function G. The simplest alternative is to estimate the function G directly from data by some parametric means. A more physically motivated procedure is to use some of the parametric functions proposed in the literature, based on approximations of nonlinear wave theory. For instance, the transformation proposed by Ochi and Ahn [89] is a monotonic exponential function while Winterstein's model [90] is a monotonic cubic Hermite polynomial. Both transformations use moments of $X(t)$ to compute G. This approach is used in the present work to obtain an additional fatigue life estimate for the nonlinear problem yielding to moderately large displacements.

3.9 Rainflow Matrix for a Switching Markov Chain of Turning Points (SMCTP)

Processes in which the mean level or the standard deviation takes two distinct levels and changes abruptly are called *switching processes*. The most common case is when the load alternates between two different states. As long as the load is in one of the states, the RFC are made up of alternations between turning points belonging only to one part of the load. When the state changes there is the introduction of extra RFC with larger amplitude. These extra cycles are represented in the total rainflow matrix. For more details on the procedure, the reader is referred to Johannesson [91]. This approach is used in the present work for the *snap-through* phenomenon that occurs when a panel vibrates with small amplitudes alternating about the two thermally buckled positions.

CHAPTER 4

SOLUTION PROCEDURE

The previous two chapters have described the finite element modeling in structural degree of freedom of a panel subjected to high acoustic loads in an elevated thermal environment and the reliability theory needed for fatigue life estimations. In order to proceed with solutions of specific problems, various preliminary computational tasks need to be performed. These include solving the linear eigen-problems to obtain the frequencies and mode shapes for the modal transformation as well as the critical buckling temperature, all of which are required subsequently. Apart from these, accurate time histories of random pressure fluctuations with flat power spectral densities need to be generated at different sound pressure levels over a predetermined bandwidth. Numerical considerations like the integration scheme, time step selection, and removing the transient response to ensure accurate response statistics are also addressed. Furthermore, post-processing of the resultant displacement, strain/stress time histories and fatigue estimates require computation of power spectral densities, probability density functions and also various statistical moments such as mean, variance, skewness and kurtosis. Finally, the principal steps to follow and Matlab commands for accurate reliability calculations in the time and the frequency domain are highlighted with a numerical example. This chapter deals with these aspects and certain implementation considerations that are introduced throughout the different sections.

4.1 Equations of Motion in Modal Coordinates

The equations of motion in structural DOF, Equation 2.74, are general in the sense that they can be solved for any isotropic or composite panel. Moreover, the system equation of motion in structural DOF is transformed into a set of truncated modal coordinates that first requires the solution of the linear vibration problem

$$\omega_r^2 \begin{bmatrix} M_b & 0 \\ 0 & M_m \end{bmatrix} \begin{Bmatrix} \phi_b \\ \phi_m \end{Bmatrix}^{(r)} = \begin{bmatrix} K_b & K_B \\ K_B^T & K_m \end{bmatrix} \begin{Bmatrix} \phi_b \\ \phi_m \end{Bmatrix}^{(r)} \tag{4.1}$$

For unsymmetrically laminated composite panels, the laminate coupling stiffness $[B]$ is not zero, which leads to a non-null submatrix $[K_B]$. Consequently, the bending $\{\phi_b\}^{(r)}$ and in-plane $\{\phi_m\}^{(r)}$ modes are coupled in Equation 4.1. However, for isotropic or symmetric composites the laminate coupling stiffness [B] is null, and there is no coupling between the bending $\{\phi_b\}^{(r)}$ and in-plane $\{\phi_m\}^{(r)}$ modes. As a result, the in-plane displacement $\{W_m\}$ will be expressed as a function of the bending displacement $\{W_b\}$.

4.1.1 Symmetric Laminates

For symmetrically laminated composite and isotropic panels, the laminate coupling stiffness $[B]$ is null and the two submatrices in Equation 2.74 are

$$[K_B] = [K_{1NB}] = 0 \tag{4.2}$$

By neglecting the membrane inertia term, the membrane displacement vector can be expressed in terms of the bending displacement vector as

$$\{W_m\} = [K_m]^{-1}(\{P_{m\Delta T}\} - [K_{1mb}]\{W_b\}) \tag{4.3}$$

Then equations of motion can be written in terms of the bending displacement as

$$[M_b]\{\ddot{W}_b\}+([K_b]-[K_{N\Delta T}])\{W_b\}+[K_{1bm}][K_m]^{-1}\{P_{m\Delta T}\}$$
$$+[K_{1Nm}]\{W_b\}+([K_{2b}]-[K_{1bm}][K_m]^{-1}[K_{1mb}])\{W_b\}=\{P_{b\Delta T}\}+\{P_b(t)\} \tag{4.4}$$

In the above system, the nonlinear stiffness matrices can be expressed in terms of the modal coordinates. This is accomplished by expressing the panel response as a linear combination of some base functions (modal transformation) as

$$\{W_b\}=\sum_{r=1}^{n} q_r(t)\{\phi_b\}^{(r)}=[\phi]\{q\} \tag{4.5}$$

where $\{\phi_b\}^{(r)}$ corresponds to the normal modes of the linear vibration problem

$$\omega_r^2[M_b]\{\phi_b\}^{(r)}=[K_b]\ \{\phi_b\}^{(r)} \tag{4.6}$$

The nonlinear stiffness matrices $[K_{1bm}]$ and $[K_{2b}]$ are both represented as functions of $\{W_b\}$. They can be expressed as the sum of products of modal coordinates and nonlinear modal stiffnesses matrices as

$$[K_{1bm}]=[K_{1mb}]^T=\sum_{r=1}^{n} q_r(t)[K_{1bm}(\phi_b)]^{(r)} \tag{4.7}$$

$$[K_{2b}]=\sum_{r=1}^{n}\sum_{s=1}^{n} q_r(t)q_s(t)[K_{2b}(\phi_b)]^{(rs)} \tag{4.8}$$

where the super indexes of those non-linear modal stiffness matrices denote that they are assembled from the corresponding element non-linear stiffness matrices. Those non-linear stiffness matrices are evaluated with the corresponding element components, $\{w_b\}^{(r)}$, obtained from the known system mode $\{\phi_b\}^{(r)}$.

The element nonlinear stiffness matrix $[k_{1Nm}]$ is linearly dependent on the element displacement $\{w_m\}$ as shown in Equation 2.54.

$$[k_{1Nm}]=\frac{1}{2}[n_{1Nm}]=\frac{1}{2}\int_A [B_\theta]^T[N_m(w_m)][B_\theta]dA \tag{4.9}$$

Recalling the membrane displacement vector of Equation 4.3,

$$\begin{aligned}\{W_m\} &= [K_m]^{-1}(\{P_{m\Delta T}\} - [K_{1mb}]\{W_b\}) \\ &= [K_m]^{-1}\left(\{P_{m\Delta T}\} - \sum_{r=1}^{n}\sum_{s=1}^{n} q_r(t)q_s(t)[K_{1mb}]^{(s)}\{\phi_b\}^{(r)}\right) \\ &= \{W_m\}_{\Delta T} - \sum_{r=1}^{n}\sum_{s=1}^{n} q_r(t)q_s(t)\{W_m\}^{(rs)}\end{aligned} \tag{4.10}$$

It is observed that $[K_{1Nm}]$ is the sum of two matrices

$$[K_{1Nm}] = [K_{Nm}^{\Delta T}] - \sum_{r=1}^{n}\sum_{s=1}^{n} q_r(t)q_s(t)[K_{2Nm}(W_m)]^{(rs)} \tag{4.11}$$

The first $[K_{Nm}^{\Delta T}]$ is assembled from the element nonlinear stiffness matrices, and they are evaluated with the corresponding element components $\{w_m\}_{\Delta T}$ obtained from the known system $\{W_m\}_{\Delta T} = [K_m]^{-1}\{P_{m\Delta T}\}$. In addition, the second $[K_{2Nm}]^{(rs)}$ is evaluated similarly with the known system $\{W_m\}^{(rs)} = [K_m]^{-1}[K_{1mb}]^{(s)}\{\phi_b\}^{(r)}$.

Introducing a structural modal damping term $2\xi_r\omega_r\overline{M}_r[I]$, the modal damping, ξ_r, can be determined experimentally or pre-selected from a similar structure. The equations of motion, Equation 4.4, are reduced to a set of coupled modal equations as

$$[\overline{M}]\ \{\ddot{q}\} + 2\xi_r\omega_r\overline{M}_r[I]\ \{\dot{q}\} + ([\overline{K}_L] + [\overline{K}_{qq}])\ \{q\} = \{\overline{P}\} \tag{4.12}$$

where the diagonal modal mass is

$$[\overline{M}] = [\phi]^T[M_b]\ [\phi] = \overline{M}_r[I] \tag{4.13}$$

the linear and cubic terms are

$$[\overline{K}_L]\{q\} = [\phi]^T([K_b] - [K_{N\Delta T}] + [K_{Nm}^{\Delta T}])\ [\phi]\ \{q\} + [\phi]^T\sum_{r=1}^{n} q_r[K_{1bm}]^{(r)}\{W_m\}_{\Delta T} \tag{4.14}$$

$$\left[\overline{K}_{qq}\right]\{q\} = [\phi]^T \sum_{r=1}^{n}\sum_{s=1}^{n} q_r q_s \left([K_{2b}]^{(rs)} - [K_{2Nm}]^{(rs)} - [K_{1bm}]^{(r)}[K_m]^{-1}[K_{1mb}]^{(s)}\right)[\phi]\ \{q\} \quad (4.15)$$

and the modal thermal and random load vector is

$$\{\overline{P}\} = [\phi]^T \left(\{P_{b\Delta T}\} + \{P_b(t)\}\right) \quad (4.16)$$

The nonlinear random response for a given symmetric composite or isotropic panel at a certain temperature can thus be determined from Equation 4.12 or 4.21 by a numerical integration scheme.

4.1.2 Unsymmetric Laminates

For unsymmetrically laminated composite panels, the laminate coupling stiffness $[B]\neq 0$ leads to the two submatrices $[K_B]$ and $[K_{1NB}]$, neither of which are zero. The linear vibration from Equation 4.1 becomes

$$\omega_r^2 \begin{bmatrix} M_b & 0 \\ 0 & M_m \end{bmatrix} \begin{Bmatrix} \phi_b \\ \phi_m \end{Bmatrix}^{(r)} = \begin{bmatrix} K_b & K_B \\ K_B^T & K_m \end{bmatrix} \begin{Bmatrix} \phi_b \\ \phi_m \end{Bmatrix}^{(r)} \quad (4.17)$$

where the bending $\{\phi_b\}^{(r)}$ and in-plane $\{\phi_m\}^{(r)}$ modes are thus coupled. Consequently, the in-plane displacement $\{W_m\}$ does not need to be expressed as a function of the bending displacement $\{W_b\}$. Following the same procedure as for the symmetric laminates, the panel response is expressed as

$$\{W\} = \begin{Bmatrix} W_b \\ W_m \end{Bmatrix} = \sum_{r=1}^{n} q_r(t) \begin{Bmatrix} \phi_b \\ \phi_m \end{Bmatrix}^{(r)} = [\phi]\{q\} \quad (4.18)$$

The nonlinear stiffness matrices $[K_1]$ and $[K_2]$ can be expressed as the sum of products of modal coordinates and nonlinear modal stiffness matrices as

$$[K_1] = \sum_{r=1}^{n} q_r(t) \begin{bmatrix} [K_{1Nm}(\phi_m)]^{(r)} + [K_{1NB}(\phi_b)]^{(r)} & [K_{1bm}(\phi_b)]^{(r)} \\ [K_{1mb}(\phi_b)]^{(r)} & 0 \end{bmatrix}$$
$$= \sum_{r=1}^{n} q_r(t) [K_1]^{(r)} \tag{4.19}$$

and

$$[K_2] = \sum_{r=1}^{n} \sum_{s=1}^{n} q_r(t) q_s(t) [K_{2b}(\phi_b)]^{(rs)} \tag{4.20}$$

where the super indices of those nonlinear modal stiffness matrices denote that they are assembled from the corresponding element nonlinear stiffness matrices. The element nonlinear stiffness matrices are evaluated with the corresponding element components $\{w_b\}^{(r)}$ and $\{w_m\}^{(r)}$ obtained from the known system modes $\{\phi_b\}^{(r)}$ and $\{\phi_m\}^{(r)}$, respectively.

With the introduction of a structural modal damping $2\xi_r \omega_r \overline{M}_r [I]$, equations of motion (Equation 2.74b) reduce to a set of coupled modal equations as

$$[\overline{M}] \{\ddot{q}\} + 2\xi_r \omega_r \overline{M}_r [I] \{\dot{q}\} + ([\overline{K}_L] + [\overline{K}_q] + [\overline{K}_{qq}]) \{q\} = \{\overline{P}\} \tag{4.21}$$

where the diagonal modal mass and linear stiffness matrices are

$$[\overline{M}] = [\phi]^T [M] [\phi] = \overline{M}_r [I] \tag{4.22}$$

$$[\overline{K}_L] = [\phi]^T [K - K_{N\Delta T}] [\phi] \tag{4.23}$$

the quadratic and cubic terms are

$$[\overline{K}_q]\{q\} = [\phi]^T \sum_{r=1}^{n} q_r [K_1]^{(r)} [\phi] \{q\} \tag{4.24}$$

$$[\overline{K}_{qq}]\{q\} = [\phi]^T \sum_{r=1}^{n} \sum_{s=1}^{n} q_r q_s [K_{2b}]^{(rs)} [\phi] \{q\} \tag{4.25}$$

and the modal thermal and random load vector is

$$\{\overline{P}\} = [\phi]^T (\{P_{\Delta T}\} + \{P(t)\}) \tag{4.26}$$

The nonlinear random response for a given symmetric or unsymmetric composite panel at a certain temperature can then be determined from Equations 4.12 and 4.21 using numerical integration. The main three advantages of the modal transformation are the following:

(i) DOF of $\{q\}$ is small,

(ii) there is no need to assemble and update the nonlinear quadratic and cubic terms,

(iii) the time step of integration could be larger.

The DOF of $\{q\}$ depends on the number of modes that have to be considered in order to accurately capture the desired response. The accuracy of the solution is directly related to the discretizing or mesh size of the panel. Under those circumstances, a convergence test for modes and mesh sizes that will give a set of modal equations for accurate response must be performed prior to any further calculations. For instance, in the nonlinear random vibration problem of a rectangular isotropic plate, it was found that a mesh size of 14 by 10 in a quarter plate and the lowest four symmetric modes were sufficient in order to have converged solutions [92].

4.2 Loading Pressure Fluctuations

4.2.1 White Random Pressure Simulation

Consider a random pressure $p(x,y,t)$ acting on the surface of a high-speed flight vehicle. The pressure acting normal to the panel surface varies randomly in time and space along the surface coordinates x and y. The pressure $p(x,y,t)$ is characterized by a cross-spectral density function $G_p(\xi, \eta, \omega)$, where $\xi = x_1 - x_2$ and $\eta = y_1 - y_2$ are the spatial separations and ω is the frequency in rad/sec. The simplest form of the cross-spectral density is the truncated Gaussian white noise pressure, uniformly distributed with spatial coordinates x and y

$$G_p(\xi,\eta,f) = \begin{cases} G_0 & \text{if} \quad 0 \le f \le f_c \\ 0 & \text{if} \quad f < 0 \quad \text{or} \quad f > f_c \end{cases} \tag{4.27}$$

where G_0 is constant and f_c is the *upper cut-off frequency* in Hertz (Hz). The expression for G_0 can be written as [37]

$$G_0 = p_0^2 \, 10^{SPL/10} \tag{4.28}$$

where p_0 is the reference pressure, $p_0 = 2.90075\ 10^{-9}$ psi (20 μPa), and *Sound Pressure Level* (SPL) is expressed in *decibels* (dB). A typical simulated random load at 120 dB SPL is shown in Figure 4.1. The band-limited white noise is generated by a Fortran code that simulates a random pressure using complex numbers with independent random phase angles uniformly distributed between 0 and 2π. The PSD value of the random process is obtained by taking the ensemble average of the Fourier transform of the random load. The PSD value is then compared to the exact one given by Equation 4.28. The analyses

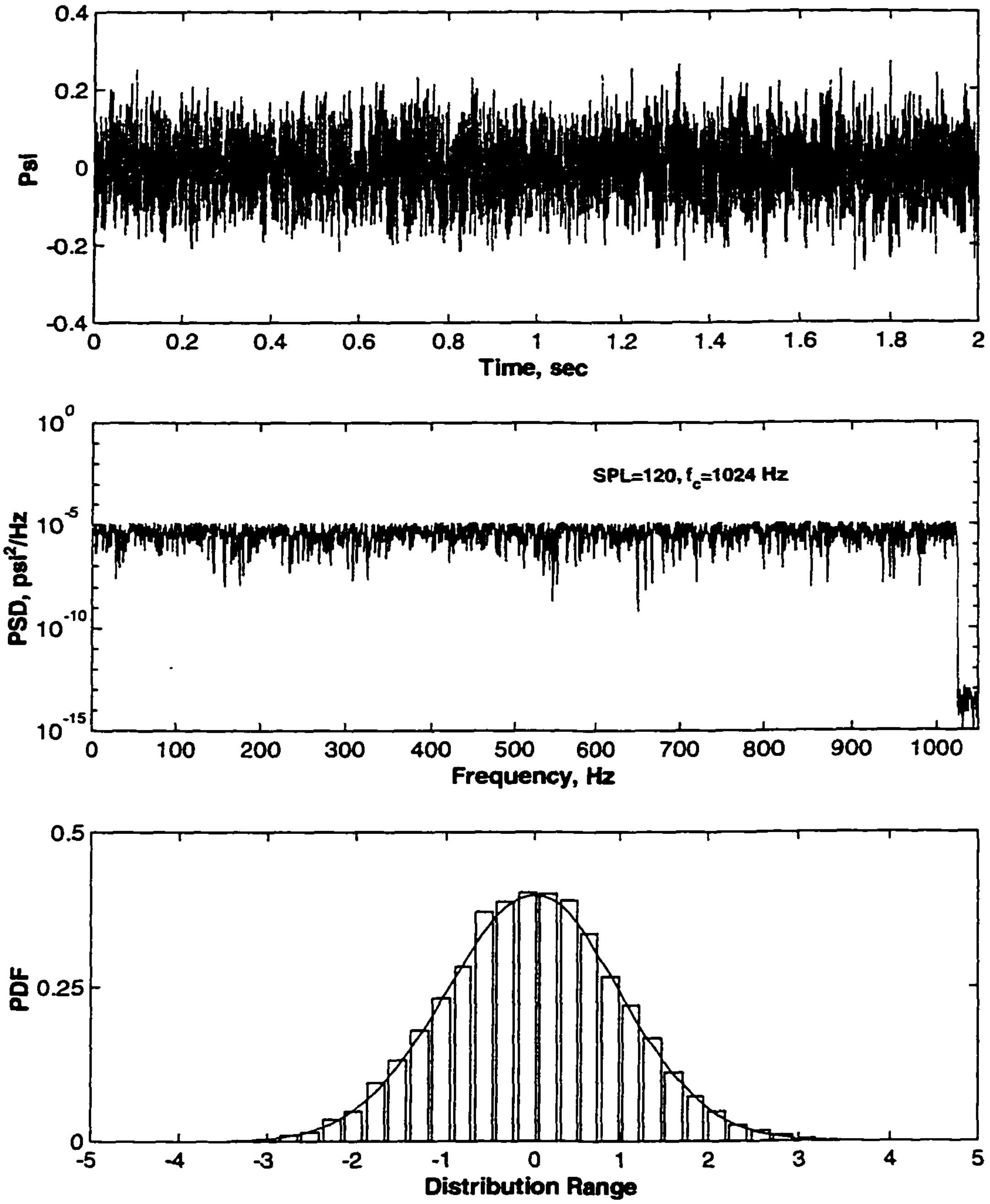

Figure 4.1 Random White Noise at SPL=120 dB and f_c=1024 Hz

presented are obtained for a cut-off frequency of 1024 Hz. The default selected frequency bandwidth in this work is $\Delta\omega$=0 rad/sec (1 cycle/sec) with the random load prescribed in decibels. For instance, a uniformly Gaussian random load of 120 dB over a frequency range of 0-1024 Hz corresponds to an *Overall Sound Pressure Level* (OASPL) of 150 dB.

The random input $p(x,y,t)$ was simulated using the Fortran code (Appendix B) given by Vaicaitis [93] with a total number of points of 16384, cut-off frequency 1024 Hz and time step 1/8192. Thus, the length of the simulated process is 1/8192 x 16384 = 2 seconds. The fundamental frequency of the panel selected for this study is about 107 Hz, and the fundamental period is 0.0093 second. Thus, the simulated process covers 214 natural periods of the panel [94]. It has been shown in previous studies that for a stationary response, reasonable statistical properties are obtained from a time history that contains more than 100 natural periods of the structure.

In Chapter 3, the FFT was selected to compute the power spectrum of the responses and it was seen that it is a numerically suitable technique when the total number of points is expressible as a power of two. The FFT is a complicated algorithm that becomes computationally lengthy when the input file size is not a power of two. For instance, note that the Fortran code for the white random pressure fluctuation simulation uses a similar FFT base. The total number of input points is 16384, which correspond to 2 to the 14th power.

4.2.2 Non-White (NW) Random Pressure Data

The random pressure fluctuations with *non-White* (or non-flat) characteristics have been obtained from recorded flight data provided by the Structural Dynamic Branch, AFRL at Wright-Patterson Air Force Base. The two microphone data files correspond to a B-1B aircraft with full afterburners in take-off configuration. The take-off data are broken into three sequences: (i) rolling, (ii) rotation, and (iii) gear-up. The two data files are not the same length in time. The first take-off sequence is about 35 seconds in duration while the second take-off sequence is much shorter and only lasts for about 15 seconds. More information about the experimental data can be found in Appendix C. In Figure 4.2, the time history, PDF and PSD of the NW pressure fluctuations are plotted. The PSD and PDF plots show that the two data sets still have Gaussian characteristics but a non-flat PSD. The principal indication of non-flat characteristics appears over 100-400 Hz interval, where a "hump" is observed. At first glance, two frequencies at about 180 and 350 Hz are especially pronounced.

4.2.3 Equivalent White Sound Pressure Level (EWSPL) Simulation

The SPL of the simulated white noise is obtained from the two *Root Mean Squares* (RMS) of the recorded flight pressure fluctuation data. The RMS can be obtained either from the time domain or from the frequency domain when integrating over the frequency range (Equation 4.28). Knowing the RMS value of the data recorded, Equation 4.28 can be solved for the *Sound Pressure Level* (SPL) that will constitute the input noise level for the *Equivalent White-Noise Sound Pressure Level* (EWSPL). The fact of having the same RMS value is equivalent to saying that the flight data (NW) and the EWSPL have equivalent power or the same area under the PSD curve. Figure 4.3 shows the PSD for the NW and the EWSPL for a sampling rate of 5000. It also appears that the modes within the 100-400 Hz range of the NW pressure will have the biggest impact in the response. The corresponding dB values for the EWSPL are also shown in Figure 4.3.

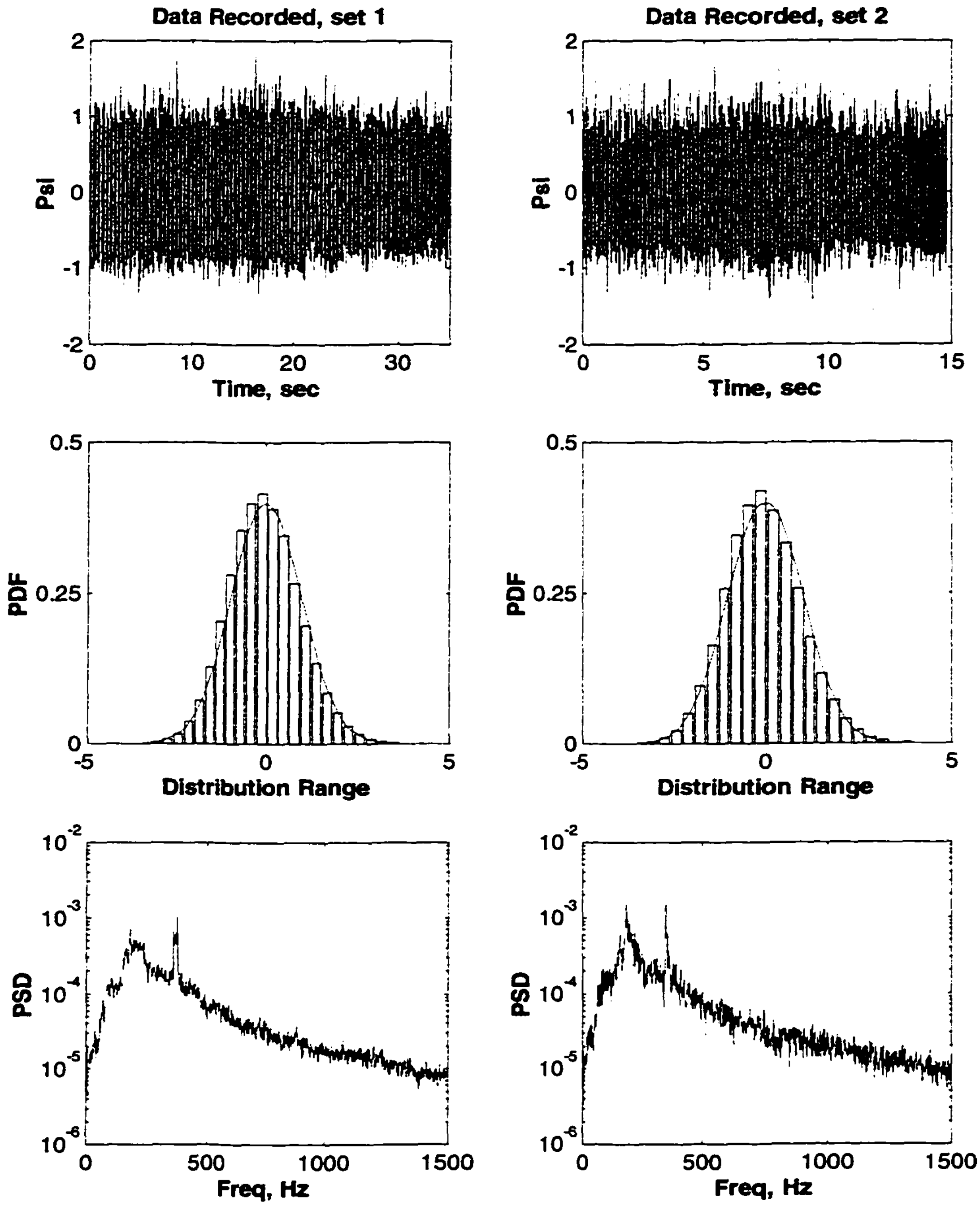

Figure 4.2 Time History, PDF and PSD of NW Pressure Fluctuations

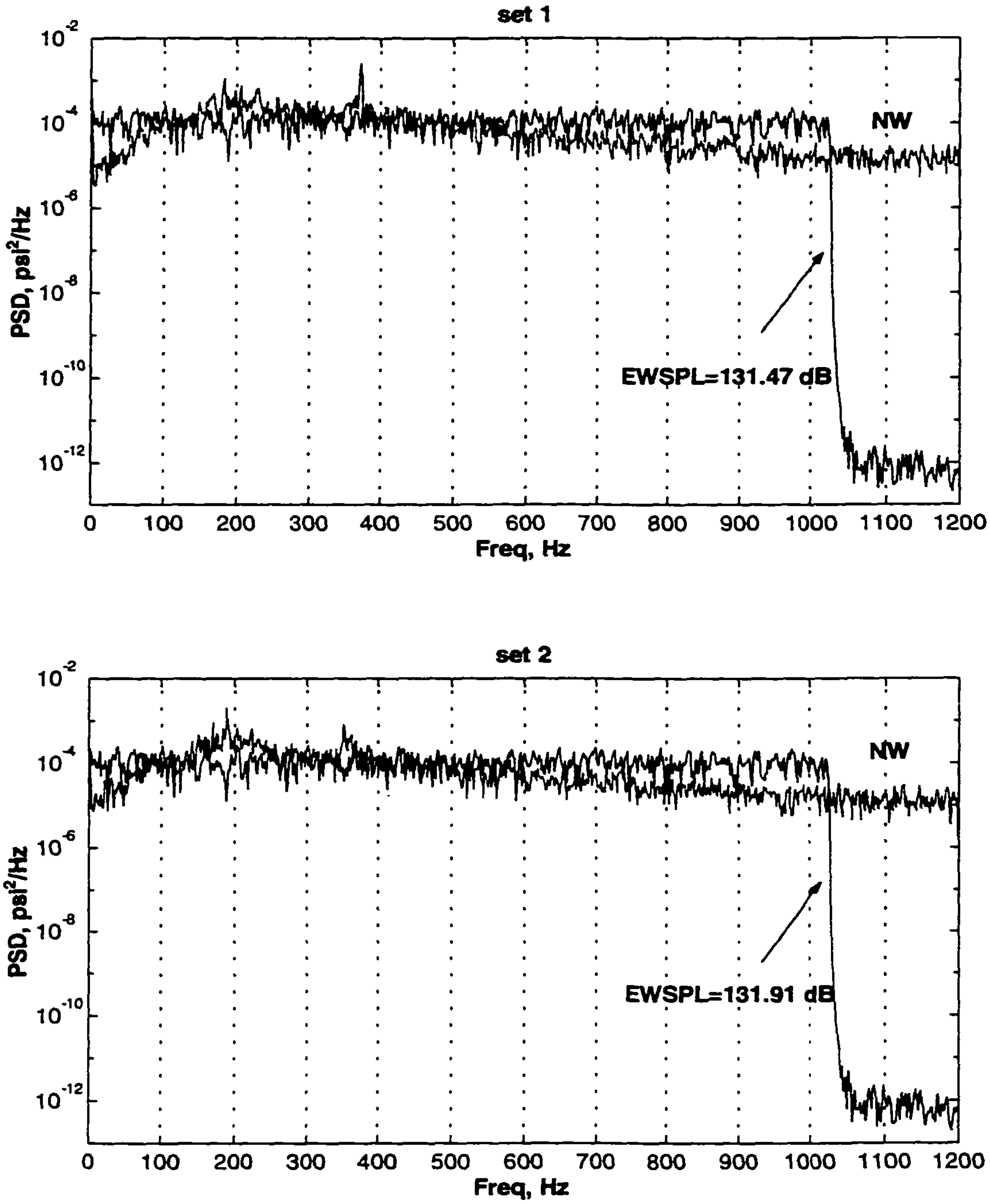

Figure 4.3 PSD of NW and EWSPL

4.2.4 Monte Carlo Simulation (MCS)

For the *Monte Carlo Simulation* (MCS) an ensemble of ten time histories is generated by specifying different seeds (ISEED, Appendix B) to the random number generator in the Fortran code described in section 4.2.1. The response statistics are generated from an ensemble of p=10 time histories at each load level. Estimates of the RMS displacement serve as a basic comparison with response of the two flight data sets (NWs), which essentially have the RMS as their basic unknown. Additionally, confidence intervals for the mean value of the RMS estimate are generated to quantify the degree of uncertainty in the results. For an input quantity x_i, whose value is estimated from p independent observations $x_{i,k}$ of x_i, are obtained under the same conditions of measurement. The input estimate is the *sample mean*

$$x_i = \overline{x}_i = \frac{1}{p}\sum_{k=1}^{p} x_{i,k} \tag{4.29}$$

and the standard uncertainty $u(x_i)$ to be associated with x_i is the estimated *standard deviation of the mean* [95]

$$u(x_i) = \sigma(\overline{x}_i) = \left[\frac{1}{n(n-1)}\sum_{k=1}^{p}\left(x_{i,k} - \overline{x}_i\right)^2\right]^{1/2} \tag{4.30}$$

4.3 Time Step Considerations

The time step of integration depends on the scheme selected (i.e., explicit or implicit), the element size and the order of nonlinearity to be studied. If an explicit integration scheme is selected, i.e., the system is *conditionally stable*, stability is achieved as soon as a solution is obtained. Conversely, the explicit integration schemes will diverge showing *instability* in the system. For an implicit scheme a solution is always obtained, i.e., the system is always *unconditionally stable.* It is widely recognized that an implicit scheme is faster than explicit schemes because a larger time step can be used for a converged solution. However, for an equal time step the explicit scheme is much faster than the implicit scheme because of its simplicity and ease in programming. In practical structural problems, engineers first try the implicit integration scheme because lower integrating time steps can be used. However, as soon as the time step becomes of the order of 10^{-4} for converged solutions, engineers switch to explicit schemes because they are more suitable for the computation.

Depending on the nonlinearity of the system a more or less refined mesh would be necessary to catch the response characteristics. The more nonlinear the system the more refined the mesh and the smaller the integrating time step. There are a variety of textbooks on numerical approaches that give empirical relations to estimate the maximum usable time steps for explicit and implicit schemes. For instance, Zienkiewics and Taylor [96] report empirical relations for the time step of integration as a function of the element size h. After this brief discussion, it becomes obvious that modal truncation reduces the step integration time by reducing the DOF. The mesh size remains the same for accuracy purposes. Computational time is also saved because the nonlinear matrices do not need to be assembled and updated at each time step.

One should also keep in mind the *Nyquist-Shannon* sampling theorem, which basically states that it is necessary to sample a time sequence at least two times faster than the highest frequency present in the waveform to uniquely resolve that frequency from the lower frequency

$$\Delta t_s \leq \frac{1}{2 f_c} \tag{4.31}$$

where f_c is the cut-off upper frequency of the uniformly random load generated.

Taking into consideration the above remarks, an appropriate time step was selected as follows. Knowing the highest frequency of the panel Δt_s is evaluated and used as the time integration step-size for a given loading. Then the step-size of integration is cut into one-half until the time histories of the response are found identical. For simplicity in the modal FEA code the time step, Δt, for the explicit integration scheme (Runge-Kutta) is selected as a power of two such that the specified loading at each Δt is maintained. As mentioned previously, a radix-2 number of time history samples is chosen to facilitate use of the FFT algorithm employed in the subsequent analysis. Note that for linear problems the Nyquist time-step, Δt_s, is generally sufficient for the explicit scheme. However, for nonlinear problems the identical verification of the responses for two decreasing consecutive time steps is required, which yields a much smaller integration time step.

4.4 Runge-Kutta Integration Scheme

The Runge-Kutta method [97] is an *explicit* step by step process in which an approximation q_{k+1} is obtained from q_k in such a way that the power series expansion of the approximation would coincide, up to terms of a certain h^N in the spacing $h=t_{k+1}-t_k$, with the actual Taylor series development of $q(t_k+h)$ in powers of h. No preliminary differentiation is needed, and this method has the advantage that no initial values are needed beyond the prescribed values. Instead of using values of the N derivatives at y at one point, only the values of the first derivatives at N suitably chosen points are required. In this work, given the initial values of the modal displacement $\{q\}$ and modal velocity $\{\dot{q}\}$, the nonlinear modal equation, given by Equation 4.12 or 4.21, is solved using the time domain numerical integration scheme for $\{q\}$. Once the modal displacement $\{q\}$ is known, the system nodal displacement vector is evaluated using Equation 4.5 or 4.18.

The fourth-order accuracy Runge-Kutta scheme, $O(h^4)$, is given by

$$q_{k+1} \cong q_k + \frac{1}{6}(b_1 + 2b_2 + 2b_3 + b_4) \tag{4.32}$$

where the coefficients b_1-b_4 are

$$\begin{aligned} b_1 &= hF(t_k,\, q_k) \\ b_2 &= hF\left(t_k + \frac{1}{2}h,\, q_k + \frac{1}{2}b_1\right) \\ b_3 &= hF\left(t_k + \frac{1}{2}h,\, q_k + \frac{1}{2}b_2\right) \\ b_4 &= hF(t_k + h,\, q_k + b_3) \end{aligned} \tag{4.33}$$

Because of the nature of the problem to be analyzed, the explicit integration scheme was selected over an implicit integration scheme for the following reasons:

(i) The computational ease of the Runge-Kutta method makes it quite simple to program and implement.

(ii) As explained in Chapter 3, fatigue life can be estimated from the power spectra where the accuracy of the response frequency content becomes critical for the evaluation of the higher moments. It was shown earlier that the *Nyquist-Shannon* sampling theorem requires that a time sequence be sampled at a rate greater than twice its highest frequency. For instance, for a cut-off frequency of 1024 Hz, the minimum time step is approximately $5\text{x}10^{-3}$ sec before any convergence criteria are even applied to the response.

4.5 Critical Buckling Temperature

The evaluation of the critical buckling temperature ΔT_r is derived for an arbitrary isotropic/composite plate from the nonlinear system equations of motion with the random loading $\{p_b(t)\}=0$, temperature distribution $\Delta T(x,y)$ and no inertia terms (Static Problem)

$$\left(\begin{bmatrix} K_b & K_{bm} \\ K_{mb} & K_m \end{bmatrix} - \begin{bmatrix} K_{N\Delta T} & 0 \\ 0 & 0 \end{bmatrix}\right)\begin{Bmatrix} W_b \\ W_m \end{Bmatrix}$$
$$+\left(\frac{1}{2}\begin{bmatrix} N_{1Nm}(W_m)+N_{1NB}(W_b) & N_{1bm}(W_b) \\ N_{1mb}(W_b) & 0 \end{bmatrix} + \frac{1}{3}\begin{bmatrix} N_{2b}(W_b) & 0 \\ 0 & 0 \end{bmatrix}\right)\begin{Bmatrix} W_b \\ W_m \end{Bmatrix} = \begin{Bmatrix} P_{b\Delta T} \\ P_{m\Delta T} \end{Bmatrix} \tag{4.34}$$

The evaluation of critical buckling temperature applies only to isotropic and/or symmetric laminates with the bending stiffness matrix $[B]$ equal to zero. On the other hand, for unsymmetical laminates ($[B] \neq 0$), the plate will experience finite large thermal deformation as shown in Figure 4.4.

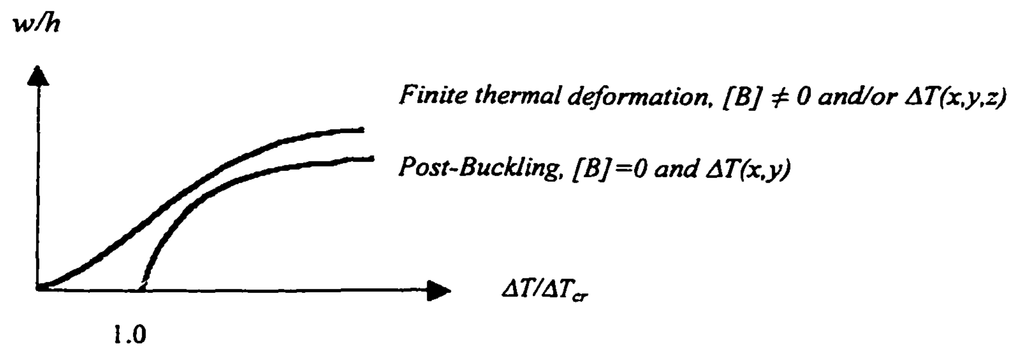

Figure 4.4 Buckling and Finite Thermal Deformation

Before buckling and just before reaching the critical buckling temperature, the plate remains flat with no bending, $\{W_b\}=0$. When the temperature is uniform through the thickness, the plate will only be subjected to a compressive thermal force $\{N_{\Delta T}\}$ since the thermal moments $\{M_{\Delta T}\}$ become zero after integration over the thickness. The bending stiffness matrix and bending displacement being zero implies that all the matrices depending on $[B]$ and $\{W_b\}=0$ become null

$$[K_{bm}]=[K_{mb}]=[N_{1NB}]=[N_{1bm}]=[N_{1mb}]=[N_{2b}]=0 \tag{4.35}$$

and the only nonlinear term that is not equal to zero is the first-order nonlinear incremental matrix $[N_{1Nm}]$ that depends on the membrane displacement $\{W_m\}$. Rewriting Equation 4.34 into two equilibrium equations:

Bending Equilibrium Equation

$$\left([K_b]-[K_{N\Delta T}]+\frac{1}{2}[N_{1Nm}(W_m)]\right)\{W_b\}=0 \tag{4.36}$$

Membrane Equilibrium Equation

$$[K_m]\{W_m\}=\{P_{m\Delta T}\} \tag{4.37}$$

From Equation 4.37 the membrane displacement needed for the evaluation of the first-order nonlinear incremental matrix $[N_{1Nm}]$ can be obtained from

$$\{W_m\}=[K_m]^{-1}\{P_{m\Delta T}\} \tag{4.38}$$

As mentioned previously the plate remains flat until the critical buckling temperature is reached. At that instant the plate buckles into one of two possible buckled positions. Consequently, resolving Equation 4.36 presents a stability problem that is resolved using the *First Order Truncated Taylor's Expansion*

$$\Psi(\{W_b\}+\{\Delta W_b\})=\Psi(\{W_b\})+\left[\frac{d\Psi(\{W_b\})}{d\{W_b\}}\right]\{\Delta W_b\}=0 \tag{4.39}$$

where the stability criterion is,

$$\{\Delta W_b\}>0, \text{ UNSTABLE}$$

$$\{\Delta W_b\}=0, \text{ CRITICAL} \tag{4.40}$$

$\{\Delta W_b\}<0$, STABLE

Returning to the buckling stability problem, it becomes

$$\Psi(\{W_b\}) = \left[K_b - K_{N\Delta T} + \frac{1}{2}N_{1Nm}\right]\{W_b\} \tag{4.41}$$

Substituting Equation 4.41 into Equation 4.39,

$$\begin{aligned}\Psi(\{W_b\}+\{\Delta W_b\}) &= \left[K_b - K_{N\Delta T} + \frac{1}{2}N_{1Nm}\right]\{W_b\} \\ &+ \left[\frac{d}{d\{W_b\}}\left(\left[K_b - K_{N\Delta T} + \frac{1}{2}N_{1Nm}\right]\{W_b\}\right)\right]\{\Delta W_b\} = 0\end{aligned} \tag{4.42}$$

Recall that just before reaching the critical buckling temperature, the plate remains flat with no bending, $\{W_b\}=0$. Consequently,

$$\left[K_b - K_{N\Delta T} + \frac{1}{2}N_{1Nm}\right]\{W_b\} = 0 \tag{4.43}$$

From the previous derivations, it is known that the matrices $[K_b]$ and $[K_{N\Delta T}]$ are independent on $\{W_b\}$, so

$$\begin{aligned}&\frac{d}{d\{W_b\}}([K_b - K_{N\Delta T}]\{W_b\}) \\ &= [K_b - K_{N\Delta T}]\end{aligned} \tag{4.44}$$

The differentiation of the first-order nonlinear matrix $[N_{1Nm}]$ that is evaluated with the membrane displacement $\{W_m\}$ involves some global characteristics of the $[N_1]$ matrix linearly dependent upon displacements $\{W\}=\{W_b, W_m\}^T$. The general concept is that the equilibrium equations, in terms of displacement, result in an unsymmetric secant matrix but with appropriated manipulations a symmetric secant matrix can be found for the nonlinear matrices $[N_1]$ and $[N_2]$. The proof of such a concept can only be derived at the element level, and following are some basic manipulations for the $[n_1]$ matrix. For more details the reader is referred to Wood and Schrefler [98]. The $[n_l]$ matrix with some of the conditions given in Equation 4.35 reduces to,

$$[n_1] = \begin{bmatrix} n_{1Nm} & n_{1bm} \\ n_{1mb} & 0 \end{bmatrix} \begin{Bmatrix} w_b \\ w_m \end{Bmatrix} \tag{4.45}$$

where in this case $\{w\}$ represents the element displacements before integration and assembly for prescribed kinematic boundary conditions.

Proceeding with the differentiation,

$$\frac{d}{d\{w\}}\left(\frac{1}{2}[n_1]\{w\}\right) = \frac{1}{2}[n_1] + \frac{1}{2}\left(\frac{d}{d\{w\}}[n_1]\right)\{w\} \tag{4.46}$$

where, using the relations given by Equation 2.51, the differentiation matrix is defined as

$$\frac{1}{2}\left(\frac{d}{d\{w\}}[n_1]\right)\{w\}$$

$$= \frac{1}{2}\begin{bmatrix} \left(\frac{d}{d\{w_b\}}[n_{1Nm}]\right)\{w_b\} + \left(\frac{d}{d\{w_b\}}[n_{1bm}]\right)\{w_m\} & \left(\frac{d}{d\{w_m\}}[n_{1Nm}]\right)\{w_b\} + \left(\frac{d}{d\{w_m\}}[n_{1bm}]\right)\{w_m\} \\ \left(\frac{d}{d\{w_b\}}[n_{1mb}]\right)\{w_b\} & \left(\frac{d}{d\{w_m\}}[n_{1mb}]\right)\{w_m\} \end{bmatrix} \tag{4.47}$$

and using the relations given by Equation 2.51

$$[\theta]^T[A][B_m]\{w_m\} = [\theta]^T\{N_m\} = [N_m][B_\theta]\{w_b\} \tag{2.51}$$

the following relation is derived

$$\left(\frac{d}{d\{w_b\}}[n_{1Nm}]\right)\{w_b\} + \left(\frac{d}{d\{w_b\}}[n_{1bm}]\right)\{w_m\}$$

$$
\begin{aligned}
&= \left(\frac{d}{d\{w_b\}} \int_A [B_\theta]^T [N_m][B_\theta] dA \right)\{w_b\} + \left(\frac{d}{d\{w_b\}} \int_A [B_\theta]^T [\theta]^T [A][B_m] dA \right)\{w_m\} \\
&= \int_A [B_\theta]^T \left(\frac{d}{d\{w_b\}} [N_m] \right)[B_\theta] dA \{w_b\} + \int_A [B_\theta]^T \left(\frac{d}{d\{w_b\}} [\theta]^T \right)[A][B_m] dA \{w_m\} \\
&= \int_A [B_\theta]^T [\theta]^T [A][B_m] dA \left(\frac{d}{d\{w_b\}} \{w_m\} \right) + \int_A [B_\theta]^T [N_m][B_\theta] dA \left(\frac{d}{d\{w_b\}} \{w_b\} \right) \\
&= \int_A [B_\theta]^T [N_m][B_\theta] dA \\
&= [n_{1Nm}]
\end{aligned}
\tag{4.48}
$$

Following the same procedure,

$$
\begin{aligned}
&\left(\frac{d}{d\{w_m\}} [n_{1Nm}] \right)\{w_b\} + \left(\frac{d}{d\{w_m\}} [n_{1bm}] \right)\{w_m\} \\
&= \left(\frac{d}{d\{w_m\}} \int_A [B_\theta]^T [N_m][B_\theta] dA \right)\{w_b\} + \left(\frac{d}{d\{w_m\}} \int_A [B_\theta]^T [\theta]^T [A][B_m] dA \right)\{w_m\} \\
&= \int_A [B_\theta]^T \left(\frac{d}{d\{w_m\}} [N_m] \right)[B_\theta] dA \{w_b\} + \int_A [B_\theta]^T \left(\frac{d}{d\{w_m\}} [\theta]^T \right)[A][B_m] dA \{w_m\} \\
&= \int_A [B_\theta]^T [\theta]^T [A][B_m] dA \left(\frac{d}{d\{w_m\}} \{w_m\} \right) + \int_A [B_\theta]^T [N_m][B_\theta] dA \left(\frac{d}{d\{w_m\}} \{w_b\} \right) \\
&= \int_A [B_\theta]^T [\theta]^T [A][B_m] dA \\
&= [n_{1bm}]
\end{aligned}
\tag{4.49}
$$

and

$$
\begin{aligned}
&\left(\frac{d}{d\{w_b\}} [n_{1mb}] \right)\{w_b\} \\
&= \left(\frac{d}{d\{w_b\}} \int_A [B_m]^T [A][\theta][B_\theta] dA \right)\{w_b\}
\end{aligned}
$$

$$
\begin{aligned}
&= \int_A [B_m]^T [A] \left(\frac{d}{d\{w_b\}} [\theta] \right) [B_\theta] dA \{w_b\} \\
&= \int_A [B_m]^T [A][\theta][B_\theta] dA \left(\frac{d}{d\{w_b\}} \{w_b\} \right) \\
&= \int_A [B_m]^T [A][\theta][B_\theta] dA \\
&= [n_{1mb}]
\end{aligned}
\tag{4.50}
$$

Similarly and recalling that the slope matrix $[\theta]$ is a function of $\{w_b\}$

$$
\begin{aligned}
&\left(\frac{d}{d\{w_m\}} [n_{1mb}] \right) \{w_m\} \\
&= \int_A [B_m]^T [A] \left(\frac{d}{d\{w_m\}} [\theta(w_b)] \right) [B_\theta] dA \{w_m\} \\
&= 0
\end{aligned}
\tag{4.51}
$$

Combining Equations 4.48 to 4.51 and replacing them in Equation 4.46, it is finally found that the differential of the first-order nonlinear matrix n_l is,

$$
\frac{d}{d\{w\}} \left(\frac{1}{2} [n_1] \{w\} \right) = [n_1] \tag{4.52}
$$

Even though the demonstration has to be carried out at the element level, the general concept can be extended to the assembled system, where the matrix $[N_{lNm}]$ of interest for the buckling temperature problem becomes,

$$
\frac{d}{d\{W\}} \left(\frac{1}{2} [N_{1Nm}] \{W\} \right) = [N_{1Nm}] \tag{4.53}
$$

After substitution of Equations 4.43, 4.44 and 4.53 into Equation 4.42, the first-order Taylor expansion of the bending stability equation reduces to

$$
\Psi(\{\Delta W_b\}) = \left[K_b - K_{N\Delta T} + N_{1Nm} \left(W_m = [K_m]^{-1} \{P_{m\Delta T}\} \right) \right] \{\Delta W_b\} = 0 \tag{4.54}
$$

where the $[K_b]$ is constant while $[K_{N\Delta T}]$ and $[N_{1Nm}]$ are linear functions of the temperature change $\Delta T(x,y)$. Applying the stability criteria $\{\Delta W_b\}=0$, the buckling temperature problem reduces to an eigenvalue problem in the form

$$[K_b]\{\phi\} = \lambda([K_{N\Delta T}] - [N_{1Nm}])\{\phi\} \tag{4.55}$$

and the critical temperature change is given by

$$\Delta T_{cr} = \lambda_1 \Delta T(x,y) \tag{4.56}$$

where λ_1 is the lowest eigen-value and $\{\phi\}_1$ the corresponding buckling mode shape.

The critical buckling temperature evaluation can be summarized as follows. For a given temperature distribution $\Delta T(x,y)$, the system membrane displacements $\{W_m\}$ are calculated with Equation 4.38, and from it the element deflections $\{w_m\}$ are extracted. The first-order element nonlinear incremental matrix $[n_{1Nm}]$ is evaluated with the vector $\{N_m\}=[A][B_m]\{w_m\}$, and then assembled to obtain $[N_{1Nm}]$. Finally, the eigen-problem equation is solved for the lowest eigenvalue, which is the ratio between the given temperature and the critical buckling temperature.

4.6 Post-Computation of Strains and Stresses

After the modal displacement $\{q\}$ for a given combination of acoustic load and the particular elevated temperature case is determined at each time step, $\{W_b\}$ and $\{W_m\}$ can be evaluated with Equation 4.5 and Equation 4.10 for symmetric panels

$$\{W_b\} = \sum_{r=1}^{n} q_r(t)\{\phi_b\}^{(r)} = [\phi]\{q\} \tag{4.5}$$

$$
\begin{aligned}
\{W_m\} &= [K_m]^{-1}(\{P_{m\Delta T}\} - [K_{1mb}]\{W_b\}) \\
&= [K_m]^{-1}\left(\{P_{m\Delta T}\} - \sum_{r=1}^{n}\sum_{s=1}^{n} q_r(t)q_s(t)[K_{1mb}]^{(r)}\{\phi_b\}^{(s)}\right) \\
&= [K_m]^{-1}\{P_{m\Delta T}\} - \sum_{r=1}^{n}\sum_{s=1}^{n} q_r(t)q_s(t)[K_m]^{-1}[K_{1mb}]^{(r)}\{\phi_b\}^{(s)}
\end{aligned}
\tag{4.10}
$$

and Equation 4.18 for unsymmetric panels

$$
\{W\} = \begin{Bmatrix} W_b \\ W_m \end{Bmatrix} = \sum_{r=1}^{n} q_r(t) \begin{Bmatrix} \phi_b \\ \phi_m \end{Bmatrix}^{(r)} = [\phi]\{q\} \tag{4.18}
$$

The element in-plane strain $\{\varepsilon^0\}$ and curvature $\{\kappa\}$ can be calculated using Equation 2.8 to Equation 2.13.

$$
\begin{aligned}
\{\varepsilon\} &= \{\varepsilon_m^0\} + \{\varepsilon_\theta^0\} + z\{\kappa\} \\
&= [B_m]\{w_m\} + \frac{1}{2}[\theta][B_\theta]\{w_b\} + [B_b]\{w_b\}
\end{aligned}
\tag{4.57}
$$

Note that for isotropic or symmetric composites the membrane displacement $\{W_m\}$, Equation 4.10, is the sum of two terms. The first term is constant, depending on the thermal membrane load $\{P_{m\Delta T}\}$, and the second is quadratically dependent on the modal displacement $\{q\}$. The total element strain is obtained from Equation 4.57 and stresses for the k^{th} layer are obtained using Equation 2.22

$$
\{\sigma\}_k = [\overline{Q}]_k\,(\{\varepsilon\} - \Delta T\{\alpha\}_k) \tag{4.58}
$$

and stress and strain in the material principal directions are then obtained using Equation 2.20. Using the above equations, the strain/stresses at any point in the plate can be computed. Because the derived finite element model is displacement based, the strains/stresses are discontinuous across element interfaces, including nodes. It was shown by Barlow [99], and Cook et al. [100], that strains and stresses are most accurate when computed at the (N-1) x (N-1) Gauss points of an element, where N x N is the

Gauss quadrature rule used to evaluate the bending stiffness matrices. For instance, the highest polynomial required in the strain/stress calculations for the BFS-C^1 conforming element is of a 9^{th} order. Knowing that a polynomial of degree $2N$-1 is integrated exactly by N points Gauss quadrature, five Gaussian points are sufficient to exactly compute the area integration. The linear bending stiffness matrices involved in the strain/stress calculation will then be derived using one order less for numerical integration, i.e., four Gaussian points will be retained. The result is then extrapolated to the nodal points or other desired points. If a full plate model is used the accuracy can also be improved by averaging the strain/stress from different local nodal values, which share the same global node number.

4.7 Data Manipulation

The panel is initially at rest. An initial transient response is therefore induced before the response becomes fully developed. The transient response must be eliminated to ensure that the accurate response statistics are recovered. For each input loading of time history, the first half-second of the response is taken out of the total run. In section 3.4 it was shown that in order to improve the FFT algorithm it was convenient to use a total number of points that will be a power of two. Consequently, for each displacement and strain/stress response the data were linearly interpolated in order to produce 2^n points where n is an integer. Under this format the data was used for statistical characterization as well as for fatigue estimation.

Recall from section 4.3.4 that for a Monte Carlo numerical simulation an ensemble of 10 time histories was merged together to form a single long time history of 10 x t_{total} seconds where t_{total} corresponds to the total time of each of the experimental data sets. On the other hand, note that since only two flight data ensembles (NW) are available, a Monte Carlo numerical simulation is not possible for the recorded data.

As mentioned above, the number of points and number of ensembles has an important role for the PSD calculation. The evaluation of the PSD using the Matlab command "pwelch" is defined as follows

$$[Pxx,F] = \text{pwelch}(x, NFFT, Fs, Window, Noverlap) \tag{4.59}$$

where x is a discrete-time signal, *NFFT* is an integer indicating the length of the FFT (in most cases equal to the number of points), *Fs* is the sampling frequency in Hz, *Window* is the length of the segments windowed with a *Hanning* window, *Noverlap* is the number of overlapping sections, *Pxx* is the PSD in power/Hz units and *F* is the frequency range in Hz. For instance, suppose that the response is constituted of 10 time histories with each one consisting of 8192 points. The "pwelch" command in Matlab is expressed as follows for a prescribed sampling frequency of 1 Hz.

$$[Pxx,F] = \text{pwelch}(x, 81920, 8192, \text{hanning}(8192), 0) \tag{4.60}$$

For frequent Matlab users it is important to note the difference between the "pwelch" command and the traditional "[*Pxx*,*F*]=psd(*x*)" command to estimate PSD's. Although the difference may be small, it is important because a density can be integrated to obtain an estimate of the average power over a given frequency interval, e.g., evaluation of the higher moments from PSD. After integration, units of power are obtained instead of power/freq units. Moreover, "pwelch" returns the single-sided spectrum by default. This means that the total power of the signal is contained in half the spectrum over the interval

0 to $Fs/2$. In other words, when the single sided PSD is integrated over the interval $[0,Fs/2]$, the *average power estimate* over the entire Nyquist frequency interval is evaluated. Of course, the same result may be obtained when integrating the double-sided PSD estimate, i.e., using the "psd(x)" command, over the interval $[-Fs/2,Fs/2]$. To do so, an additional scaling factor of 2 is introduced in the single-sided case. This results in an offset in dB of 10 x $log_{10}(2)$ =3 dB higher in the single-sided over the double-sided case.

4.8 Fatigue Estimates

Based on the information in Chapter 3, this section will explain through examples how to estimate fatigue life from the time and frequency domains. The majority of the selected examples were extracted from the Ph.D. dissertation of Johannesson [91]. The examples will also serve as a validation of the fatigue estimation subroutines used in the present work. The principal step in the solution procedure will be addressed explicitly by outlining the Matlab procedure necessary for their calculations. The data correspond to deep-water sea loadings used in oceanography for fatigue estimation of offshore platforms. In the time domain only one approach is considered, i.e., from the *rainflow cycle* (RFC) to fatigue life estimation with the only assumption of a piecewise stationary load. The frequency domain implies that the load has to be assumed ergodic, stationary and Gaussian. Some of the information in the next two sections may be repetitive from Chapter 3, but it is important for clarity purposes.

4.8.1 Time Domain

Basically, the way the RFC can be extracted from a load history, and how fatigue life can be estimated are shown. The first step in the analysis is the crossing intensity function $\mu(u)$, that is, the number of crossings per unit time that up-crosses the level u.

4.8.1.1 Crossing Intensity

The number of up-crossings as a function of level are calculated from the *sequence of turning points* (TP) extracted from the load. This is accomplish through the following Matlab subroutines

```
x=load.dat        % load
tp=dat2tp(x)      % Extract the TP from the load file                (4.61)
lc=tp2lc(tp)      % Calculates number of up-crossings from the TP
```

Figure 4.5 shows plots of the crossing intensity in (a) number of up-crossings for the sea load data, and (b) on a normal probability scale to see how much they deviate from a Gaussian process. *N* independent observations of identically distributed Gaussian variables form a straight line in log normal plot. It is readily observed that the crossing function data has Gaussian characteristics.

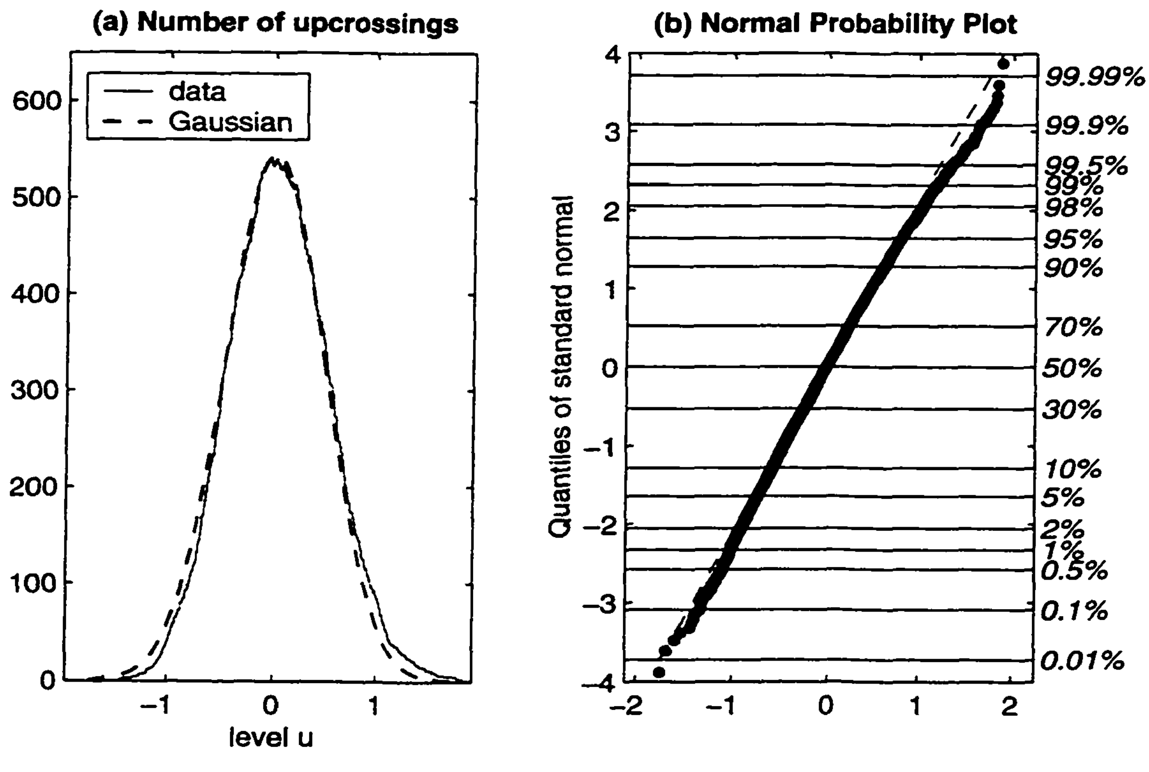

Figure 4.5 (a) Level Crossing Intensity and (b) Normal Probability Plot for Sea Load

4.8.1.2 Extraction of Rainflow Cycles

Recall from Chapter 3 that the RFC and min-max cycles are evaluated from the TP. Since each cycle is a pair of local maximum and local minimum in the load, the cycle count can be visualized as pair sets in the R^2-plane. The Matlab commands that extract the counting cycles from the TP are

```
RFC=tp2rfc(tp)      % Extract RFC from TP
MM=tp2mm(tp)        % Extract min-max from TP
```
(4.62)

Figure 4.6 shows the min-max and RFC in the load. The RFC contains more cycles with high amplitudes compared to min-max cycles. The set of pairs in the min-max cycle counting are more dispersed than in the RFC. This becomes more evident in the amplitude histograms shown in Figure 4.7.

4.8.1.3 Damage and Fatigue Life Estimate

Now that the load and the load probability distribution are known the damage and consequently the fatigue life can be calculated from Equation 3.20 and 3.21.

$$E[D(t)] = E\left[\sum_{t<t_k} \frac{1}{N(s_k)}\right] = E\left[K \sum_{t<t_k} s_k^{\beta}\right] = E[KD_{\beta}(t)] \tag{3.20}$$

$$T^f = \frac{1}{E[D_{\beta}(t)]} \tag{3.21}$$

where $s_k = s_k^{RFC} = \left(M_k - m_k^{RFC}\right)/2$. For the numerical application, K=1.818x10^9 and β=3.2. The Matlab commands are

```
T=x(end,1)-x(1,1)          % Period
D=cc2dam(RFC)/T            % Damage
Fatigue_life=K/D/3600      % Fatigue life in hours
```
(4.63)

The fatigue lives obtained in [91] and in the above calculations are identical. Both yield a fatigue life of 596.93x10^4 hours. Obviously this sea load data causes little damage to the structure since the failure time is about 700 years.

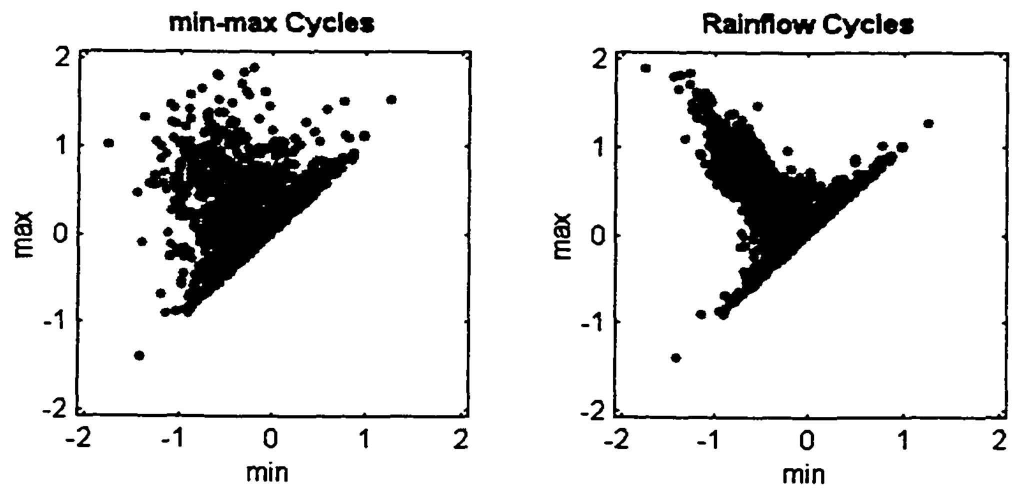

Figure 4.6 min-max and RFC Plots for Sea Data

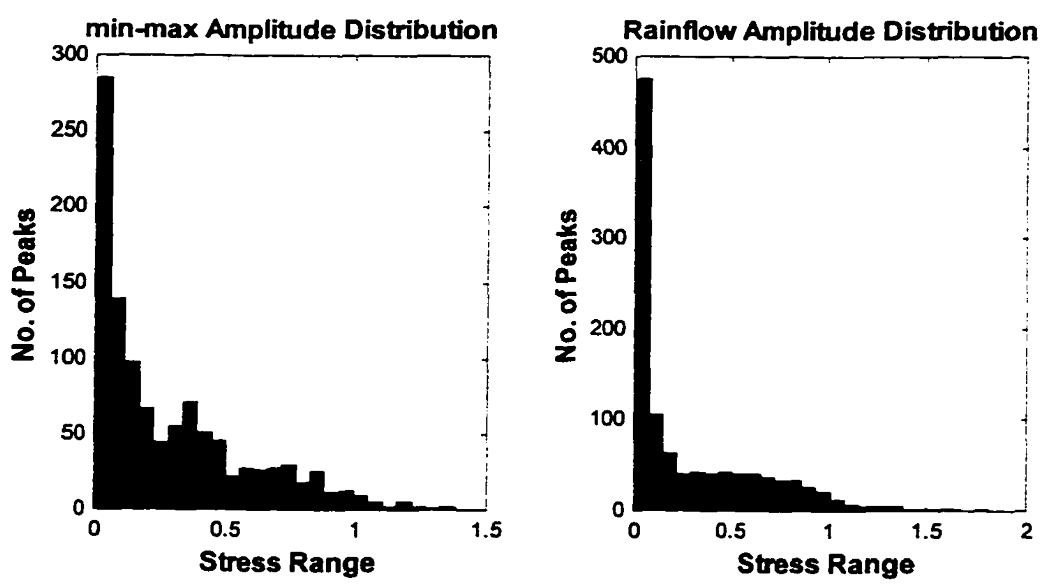

Figure 4.7 min-max Cycles and RFC Distribution of Sea Data

4.8.2 Switching Markov Processes

The theoretical background and validation behind the analysis of switching Markov processes are contained in Johannesson [91]. This approach permits the estimation of the fatigue life for a stationary-Gaussian process that has two different states of equilibrium. In the present work, the Switching Markov Process approach is used to estimate the fatigue life of panels whose dynamic response corresponds to a snap-through motion type. Basically, the former approach assumes that the mean level of a given load may take two distinct levels and change abruptly between the two stationary-Gaussian states. The change between the different states is assumed to be governed by a Markov chain.

In the following example the load corresponds to a sequence of the snap-through motions of the 15x12x0.06 in. isotropic panel that will be studied in detail in the next chapter. More precisely, the load (stress) corresponds to 1/32 of the SPL of the second set of non-white flight data (NW_2) at an ambient temperature of $\Delta T/\Delta T_{cr}$=2.0. The maximum stress response alternates between two different mean levels, corresponding to the two thermally buckled positions. The changes of states are defined as follows: (i) upper buckled position when the load value is positive, and (ii) downward buckled position when the stress value is negative. In Figure 4.8 the observed stress response is shown while the alternating lower curve monitored the occurrence of the load switches between the two states or buckled positions. As long as the load is in one of the states, the RFC are made up of alternations between TP belonging only to that part of the load. When the state changes, there is the introduction of an extra rainflow cycle with larger amplitude. These extra cycles can be seen in the total rainflow matrix shown in the 3-D plot of Figure 4.9.

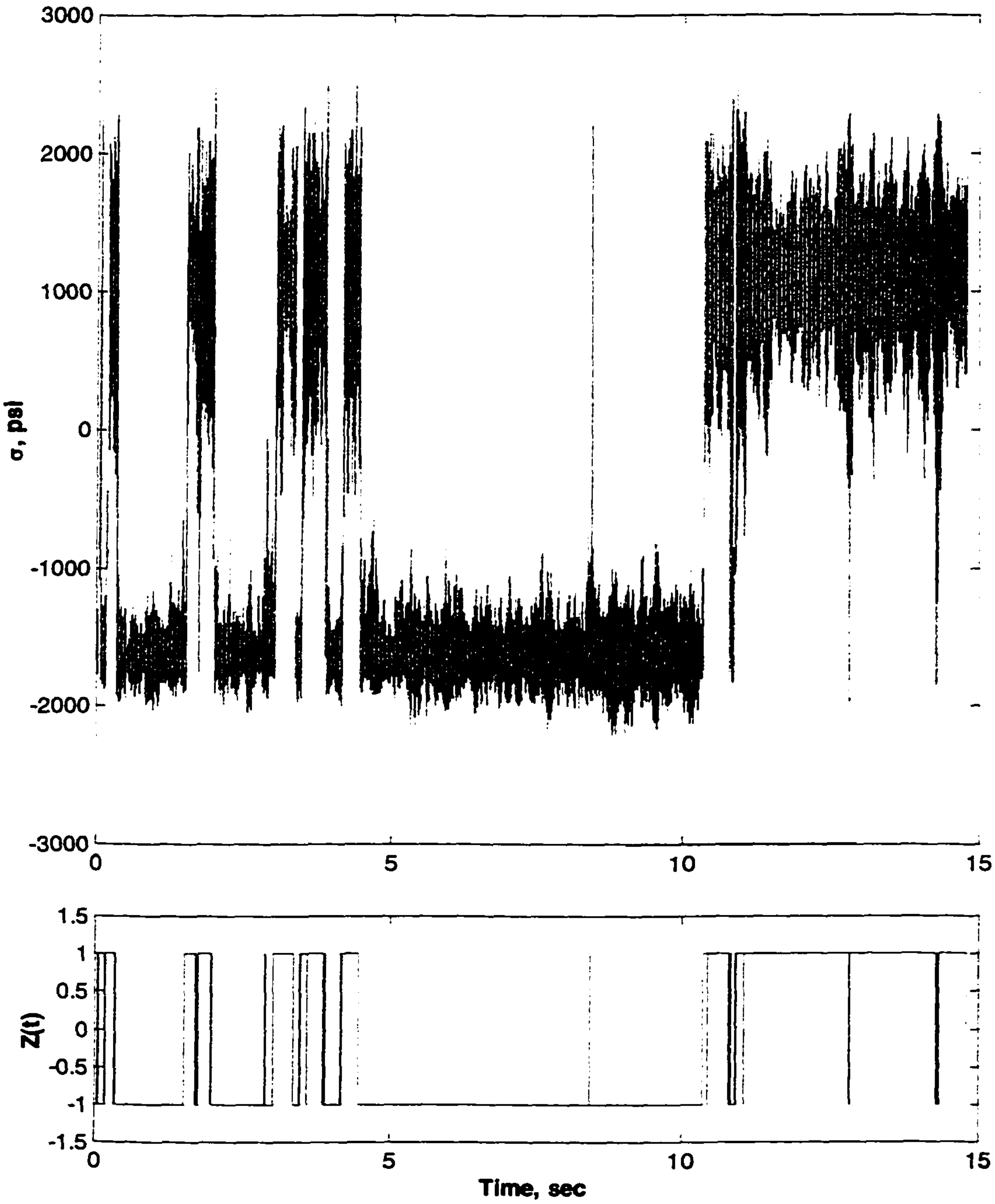

Figure 4.8 Switching Markov Process and States

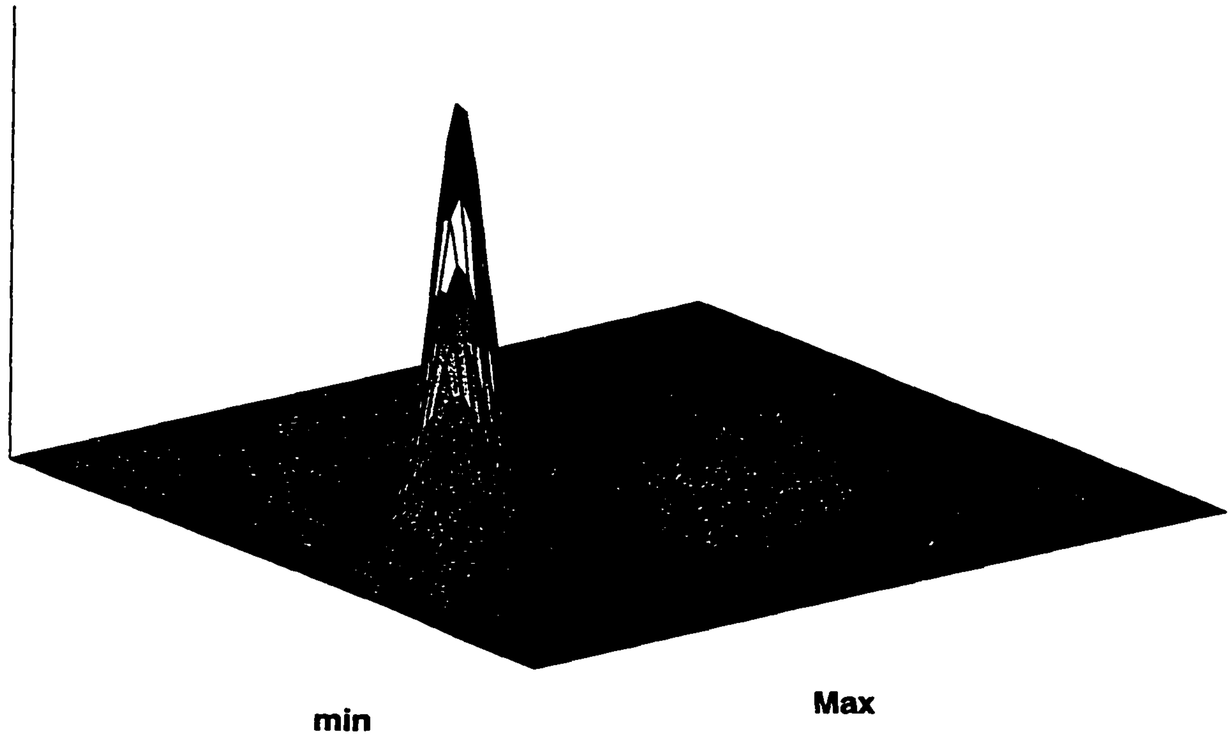

Figure 4.9 3-D Plot of Rainflow Matrix

The fatigue life estimates using the RFC time domain and the modified RFC for Rainflow Matrix for a Switching Markov Chain of Turning Points SMCTP are shown in Table 4.1. It is observed that SMCTP yields to lower fatigue life and consequently it is less conservative than the traditional RFC defined by Rychlik in [76].

Table 4.1

Comparison of Fatigue Estimates for Traditional RFC and SMCTP RFC

	RFC (Traditional)	**RFC (SMCTP)**
Fatigue (hours)	4.841×10^7	3.837×10^7

4.8.3 Frequency Domain

In this section the two possible approaches for fatigue estimation from the load spectrum are considered and compared. The first one is the direct application of the empirical relation derived by Dirlik (section 3.7.1) into the Palmgren-Miner damage equation. The second is the two-step procedure where the Markov matrix is evaluated by assuming that the TP obeys a Markov chain process, i.e., the evolution of the turning points depends only on the most recent local extreme and not on the whole history of turning points. Recall that the second step of the procedure is independent of the process, whether Gaussian or not. The methods needed for computing the Markov matrix can be complex and depend on the particular problem.

4.8.3.1 Dirlik's Approach and Transformed Gaussian Processes (TGP)

For nonlinear slightly non-Gaussian processes the method of using transformed Gaussian processes seems to yield good results in some special cases. The next Matlab elements develop the Winterstein function as a Gaussian transformation function where the transformation is chosen to be a monotonic cubic polynomial, calibrated such that the first four moments of the transformed model match the moments of the true process. The algebraic expression for the transformation is

$$G(x) = m + K \times \sigma\left[x_n + c_1\left(x_n^2 - 1\right) + c_2\left(x_n^3 - 3x_n\right)\right] \tag{4.64}$$

where m and σ are the mean and standard deviation, and

$$x_n = (x - m)/\sigma$$

$$K = \left(1 + 2c_1^2 + 6c_2^2\right)^{-1/2}$$

$$c_1 = \frac{skew}{6} \frac{\left(1 - 0.01|skew| + 0.3skew^2\right)}{\left(1 + 0.2kur\right)}$$

$$c_2 = 0.1\left(\left(1 + 1.25k\right)^{1/3} - 1\right)\left(1 - 1.43\frac{skew^2}{kur}\right)^{1-0.1(kur+3)^{0.8}}$$

For these numerical simulations of the fatigue estimates using the frequency domain no results were available for comparison in the existing literature. The frequency domain approach was then verified by using the sea load case of the previous section. The results obtained were in good agreement and are tabulated in Table 4.2.

Table 4.2

Comparison of Fatigue Estimates for Sea Load

	RFC (Time Domain)	**Gauss Transformation (Frequency Domain)**	**Dirlik (Frequency Domain)**
Fatigue (hours)	$596.931\text{x}10^4$	$599.218\text{x}10^4$	$601.0236\ \text{x}10^4$

It is immediately observed that the two frequency domain approaches are less conservative than the RFC method in the time domain.

In the next sample calculation a slightly nonlinear stress response is considered in order to show the sensitivity of the frequency domain approaches to a non-Gaussian load. The selected stress response has been extracted from old data and is not representative of any result that may appear later in this work. The important characteristic of such response is that its sequence of TP slightly deviates from a Gaussian distribution as is shown in Figure 4.10.

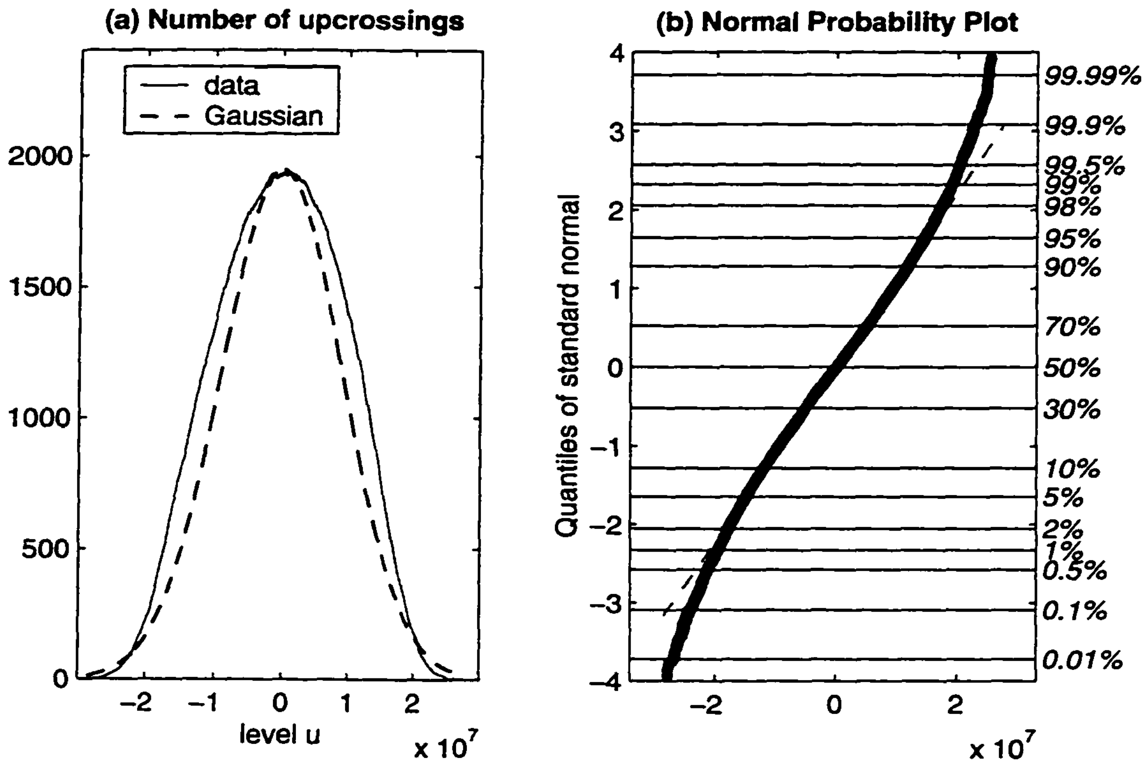

Figure 4.10 (a) Level Crossing Intensity and (b) Normal Probability Plot

Following the same procedures as for the previous examples, the fatigue life estimations for the different approaches are shown in Table 4.3

Table 4.3

Comparison of Fatigue Estimates for Non-Gaussian Load

	RFC (Time Domain)	Gauss Transformation (Frequency Domain)	Dirlik (Frequency Domain)
Fatigue (hours)	4.0511×10^5	23.124×10^7	9.163×10^7

It can be readily observed that the three fatigue life approaches give quite different results. The difference arises from the fact that the data PDF (or sequence of TP) is not exactly Gaussian and the peak distribution cannot be accurately estimated from the response PSD.

CHAPTER 5

RESULTS AND DISCUSSION

The nonlinear element equations developed in Equation 2.73 are general in the sense that they are applicable for beam [45], rectangular [46, 48, and 86], and triangular [47, 101, and 102] plate finite elements. The finite element employed in the present study is the BFS [84] C^1-conforming rectangular plate element, which has been developed in Chapter 2. Accurate nonlinear analytical multimode results and test data for isotropic or composite panels under acoustic and thermal loads are not available in the literature. Validation of the present nonlinear modal formulation will thus consist of the following two parts: (i) assess the accuracy of the left hand side of Equations 4.12 and 4.21, and (ii) validate the simulated random modal load $[\phi]^T\{P_b(t)\}$, and thermal modal load $[\phi]^T\{P_{b\Delta T}\}$ on the right side of the above mentioned equations. Mesh and modal convergences are then studied for accurate displacement and strain/stress responses. The numerical results presented in the following sections correspond to the panel center and stresses are calculated at the top surface, i.e., at $z = h/2$. In order to demonstrate the versatility of the present approach the results are divided into three sections. Results include: displacement and stress time histories, Probability Density Functions (PDF), Power Spectral Densities (PSD), cycles and amplitudes distributions, peak distributions, and finally threshold up-crossing rates.

Section 5.2 deals with the random response of an isotropic panel subjected to increasing pressure fluctuations. This allows observation of the shifting and broadening of the spectral peaks towards the higher frequencies (PSD), as well as the change in the response characteristics. In Section 5.3, the influence estimation of response characteristics on fatigue life is analyzed and discussed in detail for linear and nonlinear systems. For the numerical application, K=1.52x10^{25} and β=4.8 are employed for isotropic aluminum panels. Section 5.4 follows the same approach as the previous section, but this time the panel is also subjected to a uniform temperature distribution ΔT with $\Delta T/\Delta T_{cr}$=2.0. The panel responses show the three distinct motion zones: (i) small deflection random vibration about one of the two thermally buckled equilibrium positions, (ii) snap-through or oil-canning phenomenon between the two thermally buckled positions, and (iii) large amplitude nonlinear random vibration encompassing both thermally buckled positions. A small temperature ratio, $\Delta T/\Delta T_{cr}$=2.0, was selected in order to utilize the S-N curves at ambient temperature without introducing a large error in fatigue life estimates of isotropic panels. The temperature effect is not introduced in the composite panels because of their substantially larger critical buckling temperatures. Special attention will be focused on the fatigue life estimation of the snap-through or oil-canning phenomenon. Sections 5.5 and 5.6 discuss the influence of thermal effects in the response characteristics on fatigue life estimations. The traditional approaches are compared to the Switching Markov Processes [91] (SMCTP) when snap-through is encountered. Section 5.7 extends the fatigue life estimation analysis to composite structures. Fatigue design considerations of isotropic and composites panels based on S-N curves are discussed in detail. In addition, the influence of the material property, β, on fatigue life is addressed. Finally, Section 5.8 study in detail the responses and fatigue lives of an L-shaped panel subjected to acoustic load and $\Delta T/\Delta T_{cr}$=0.0 and 2.0.

5.1 Modal Finite Element Validation

5.1.1 Nonlinear Modal Stiffness Coefficients

Validation of the nonlinear modal formulation has already being verified via many previous published results. For instance, the accuracy of the nonlinear stiffness matrices in modal coordinates has been verified by Shi et al. [103] for nonlinear free vibration of fundamental and higher modes of plates and beams. However, the finite element modal equations for two-mode especially symmetric plate with [0/90/0] orthotropic laminates are compared in detail with a two-mode Duffing equations derived using the approximated classical continuum Galerkin's approach. The material properties are the following: E_1=22.5 Mpsi, E_2=1.17 Mpsi, G_{12}=0.66 Mpsi, ρ=0.1468x10^{-3} lb-sec^2/in.^{4} and ν_{12}=0.22. The derivation of the nonlinear stiffness matrices using the classical approach is given in Appendix D. This comparison permits a more physical insight into the values and the nature of each of the nonlinear stiffness matrices. For instance, for the lowest two modes (1,1) and (1,3), two nonlinear terms are null in the nonlinear Duffing equation. In the two modal equations, the coefficients to the modal displacement $\{q_{13}^3\}$ and $\{q_{13}^2 q_{11}\}$ are zero leaving each one of the two modal equations with only three nonlinear terms. The classical continuum and finite element nonlinear coefficients for a 14 by 10 by 0.04 in., simply supported [0/90/0] orthotropic plate, are shown in Table 5.1. Immovable in-plane boundary conditions $u(0,y)=u(a,y)=v(x,0)=v(x,b)=0$ are considered and the plate is modeled with 16 by 16 or 256 BFS elements in a quarter plate.

Generally, such a refined mesh is not necessary because the accuracy criterion is based on the finite displacement rather than the value of the nonlinear coefficients.

However, for comparison purposes a 16 by 16 mesh on a quarter plate was necessary to obtain good converged solutions.

Table 5.1

Nonlinear Coefficients for the 14x10x0.040 in. [0/90/0] Graphite-Epoxy Panel

	q_{11}^3	$q_{11}^2 q_{13}$	$q_{13}^2 q_{11}$	q_{13}^3
		Galerkin		
1st Eq.	$3.0111\text{x}10^5$	$-6.1445\ \text{x}10^4$	$2.2973\text{x}10^6$	0.0
2nd Eq.	$-2.0481\text{x}10^4$	$2.2973\text{x}10^6$	0.0	$1.9221\ \text{x}10^7$
		FE		
1st Eq.	$3.0123\text{x}10^5$	$-5.9851\text{x}10^4$	$2.3158\text{x}10^6$	$1.0448\text{x}10^{-5}$
2nd Eq.	$-1.9852\text{x}10^4$	$2.3105\text{x}10^6$	$3.0851\text{x}10^{-5}$	$1.9341\text{x}10^7$

FE: Finite Element on 16x16 Mesh in Quarter Plate

5.1.2 Random Load, $\{P_b(t)\}$

The validation of simulated random loads is by comparison of the linear displacements with linear analytical results shown in Table 5.2. Linear analytical displacement random response results for single and multiple modes are given in Appendix E. The random load considered is uniform over the panel and is simulated as described in Section 4.2.1. The FPK method [19,104] is an exact solution [105] to the nonlinear single DOF forced Duffing equation where the random input load and response are Gaussian with zero-mean. The FPK solution is compared with the present modal finite element time domain numerical simulation for one and four modes. Results are also shown in Table 5.2. Very good agreement is obtained for the linear systems where the error is less than 0.05%. The nonlinear system results are reasonably accurate except at the 100 dB SPL where the classic FPK solution is higher than the nonlinear finite element solution.

Table 5.2

Comparison of RMS W_c/h for a Simply Supported

15×12×0.040 in. Isotropic Plate

SPL	Linear Analytical		FE/L/NS		FPK [104,105]	FE/NL/NS	
(dB)	4 modes	7 modes	4 modes	Err.%	1 mode	1 mode	4 modes
90	0.2759	0.2759	0.2760	0.0362	0.249	0.257	0.266
100	0.8725	0.8725	0.8728	0.0362	0.592	0.565	0.578
110	2.7590	2.7590	2.7600	0.0362	1.187	1.283	1.432
120	8.7248	8.7250	8.7281	0.0362	2.200	2.389	2.572

FE: Finite Element; L: Linear; NL: Non-Linear; NS: Numerical Simulation

5.1.3 Thermal load, $\{P_{b\Delta T}\}$

Similarly, the validation of the thermal load is by comparison of the thermal deflections of a plate with all edges clamped under a uniformly distributed temperature. For finite element analyses, an 8 by 8 mesh models one quarter of the plate. The lowest four linear thermal critical buckling modes (1,1), (3,1), (1,3), and (3,3) are retained for the calculations. The displacements and stresses are compared with the Don Paul's 25 modal functions theoretical results [106] shown in Figure 5.1. From the figure it can be concluded that the agreement for the displacement is excellent, and the agreement for the stresses is acceptable. The slight difference in stresses may have two explanations: (i) the use of displacement-based finite elements and (ii) the number of modes (4) may not be sufficient.

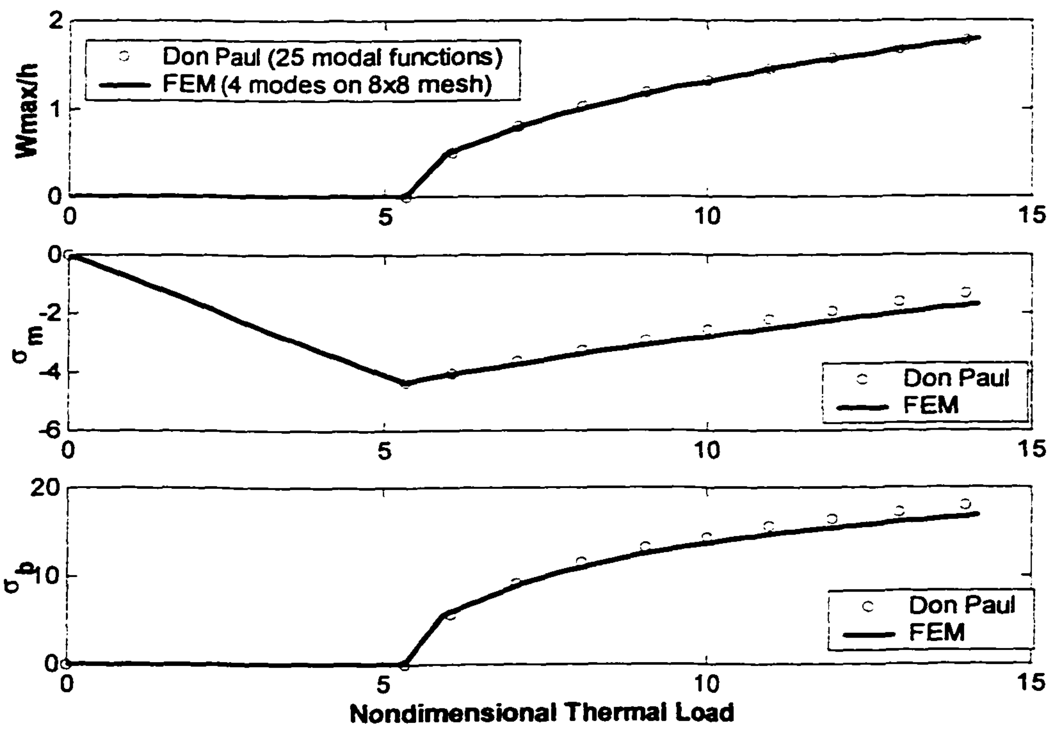

Figure 5.1 Comparison of Thermal Maximum Deflection and Stresses

5.1.4 Convergence Test

The number of modal coordinates to be included in the analyses for converged deflection and stress is studied first. The Root Mean Square (RMS) maximum non-dimensional deflection, and the RMS maximum stress versus number of modes at EWSPL of 131.91 dB using 1, 2, 4, and 6 modes are shown in Figure 5.2. It is concluded that four modes are sufficient for converged deflection and stress responses. Strain/Stresses are calculated at the top surface of the panel ($z=h/2$). For the 15 by 12 by 0.06 inches isotropic panel chosen in the numerical examples, the shearing stress is zero and the maximum principal strain/stress is in the y-direction. Even though converged displacement and strain/stress responses were found for four modes, it was decided to include in the calculations all the modes within the frequency range of the simulated random pressure fluctuations (0-1024 Hz).

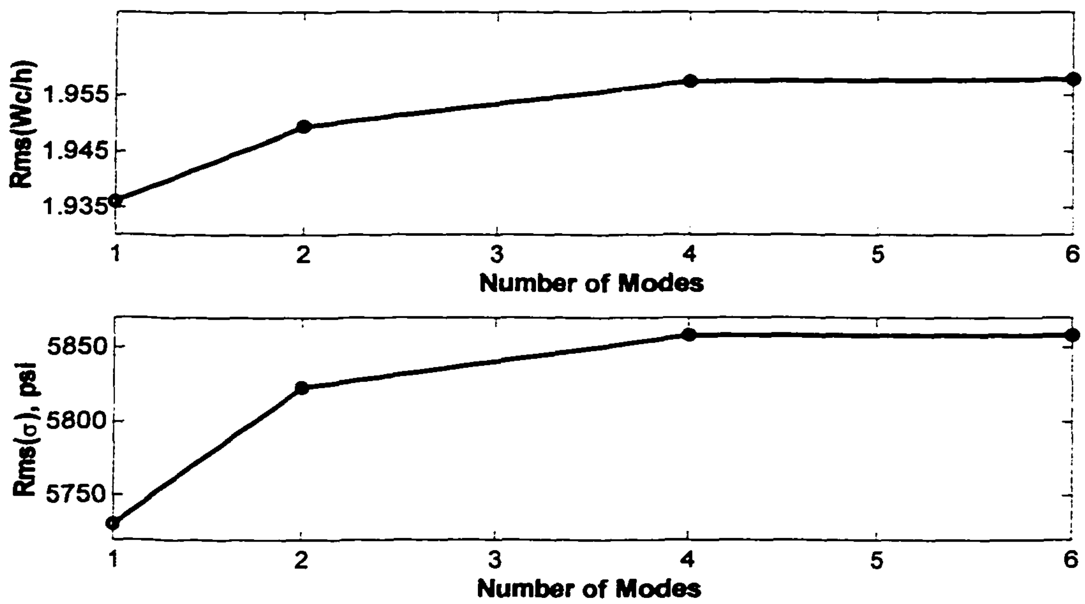

Figure 5.2 Convergence of RMS Maximum Deflection and Stress of a 15x12x0.060 in. Simply Supported Isotropic Plate at 131.91 dB SPL

Table 5.3 shows that the first five modes are inside the frequency range before the roll-off of the excitation PSD. The lowest five frequencies and their corresponding mode shapes are shown in Figure 5.3.

Table 5.3

Frequencies (Hz) of a Simply Supported 15×12×0.060 in. Isotropic Plate

Mode	(1,1)	(3,1)	(1,3)	(3,3)	(5,1)	(5,3)
Exact	80.516	331.818	473.277	724.645	834.618	1227.730
FE	80.516	331.818	473.292	724.655	834.668	1227.420

Two other studies for accurate and converged response predictions were also performed. They are the finite element mesh sizes and the integration time steps. For a five-mode solution, it was found that a quarter plate model of 14 by 10 mesh size is more than adequate. The time step of integration $\Delta t=1/8192=1.2207\times10^{-4}$ sec was first selected, then the time step was cut in half until time histories for two successively smaller integration time steps were found to be identical. Then, the maximum time step giving identical responses was found to be $\Delta t=1/8192$ sec. It is important to note that the response time histories time step convergence test must be performed at the highest SPL input. Having identical time histories at the high SPL input of 131.91 dB will assure the matching of the response time histories at all the lower SPL values.

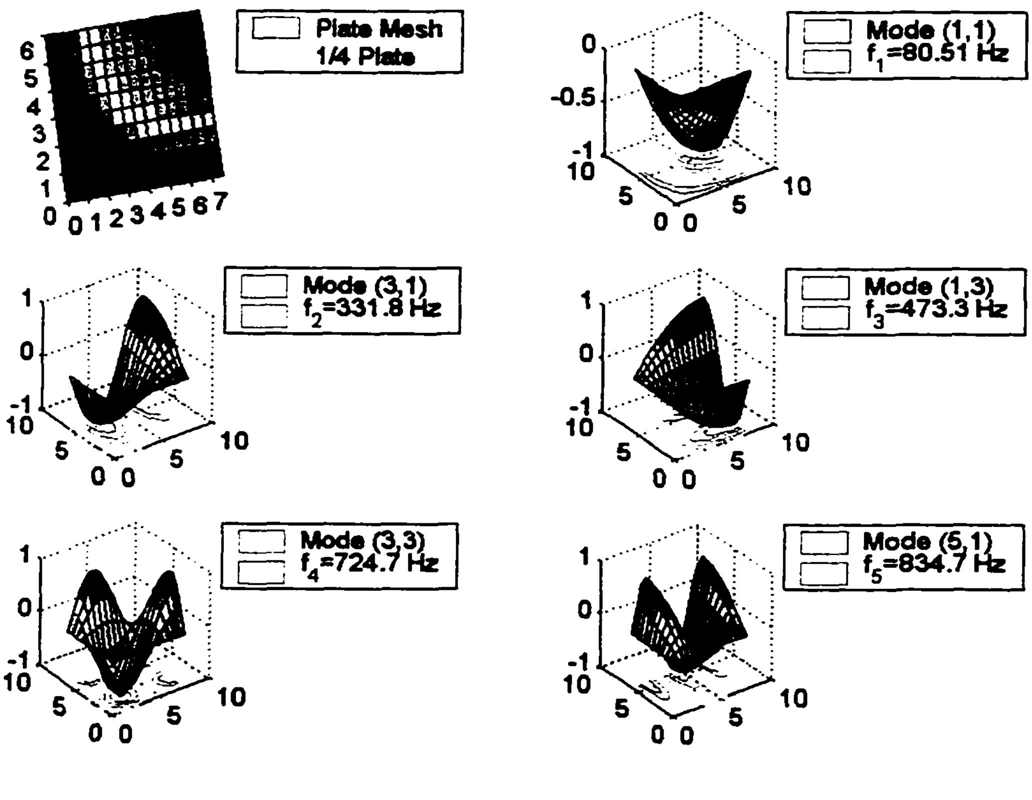

Figure 5.3 First Five Mode Shapes of a 15×12×0.060 in. Simply Supported Plate

5.2 Non-White (NW_2) Pressure Fluctuations at $\Delta T = 0$

A simply supported isotropic plate with immovable in-plane conditions $u(0,y)=u(a,y)=v(x,0)=v(x,b)=0$ is studied in detail. The plate is 15 by 12 by 0.06 in. and is modeled with 140 BFS elements in a quarter plate. The number of structural node DOF $\{W_b\}$ is 560 for the system equations given in Equation 4.4. The material properties are E=10.587 psi, ν=0.3, and $\rho=1.723\text{x}10^{-4}$ lbf-sec^2/in.^{4}. A proportional damping ratio of $\xi_r\omega_r=\xi_s\omega_s$ with ξ_l=0.02 is used. In order to have a better understanding of the different characteristics (Gaussian, Non-Gaussian) of nonlinear dynamic systems the highest original recorded pressure fluctuations (NW_2) is divided by the coefficients 256, 8, and 4. The sound pressure levels corresponding to each new input loading case are 83.75, 113.84 and 119.87 dB, respectively. Fatigue life estimates are evaluated for each one of the four case loadings. However, since only the original (highest SPL) data recorded sets are representative of a real-life loading, conclusions based on comparison with the EWSPL would only be addressed for the NW_1 (131.43 dB) and NW_2 (131.91 dB) in Section 5.3.

5.2.1 Time Histories and Probability Density Functions (PDF)

The time histories and PDF of maximum deflection and maximum principal stress are plotted in Figures 5.4 to 5.7. For the 83.75 dB sound pressure input, the panel response is linear and the time history for stress is similar to the displacement response (Gaussian). However, as the input levels increase and the panel exhibits nonlinear characteristics, the stress PDF progressively changes toward a more representative Rayleigh distribution shifted by the mean stress. Furthermore, the increase in mean stress with the increasing input sound pressure levels is shown in Figures 5.4 to 5.7 as well as in Table 5.4. The time history at the highest sound pressure level (131.91 dB) is clearly nonlinear ($W_c/h>1.0$), and the non-Gaussian stress behavior is demonstrated by the presence of a non-zero mean, shown in Figures 5.6, 5.7, and in the stress PSD in Figure 5.13. The large deviation from the Gaussian is more clearly observed on the strain PDF in Figures 5.6 and 5.7 and the larger kurtosis values in Table 5.4. The RMS, mean values and higher moments corresponding to input levels 83.75, 113.84, 119.87, and 131.9 dB are also shown in Table 5.4.

Table 5.4

Moments of the W_c/h and Maximum Stress for a 15x12x0.06 in.

Isotropic Plate at SPL=83.75, 113.84, 119.87 and 131.91 dB

SPL dB	RMS	Mean	Variance	Skewness	Kurtosis
		W_c/h			
83.75	0.0223	-0.000712	0.152	-0.00462	0.377
113.84	0.5737	-0.00103	0.770	0.141	-0.206
119.87	1.105	-0.00704	1.0701	0.00324	-0.570
131.91	1.958	-0.00819	1.424	-0.00295	-0.860
	psi	**Stress** **psi**	**$psi^2./psi^2.$**	**$psi^3./psi^3.$**	**$psi^4./psi^4.$**
83.75	47.00506	-0.605	6.855	0.091	0.997
113.84	1209.480	262.411	34.360	0.948	0.987
119.87	2575.842	989.884	48.765	1.290	1.899
131.91	5858.491	3195.180	70.0749	1.410	2.401

The increase in the mean stress and consequently the deviation from a Gaussian distribution is caused by the in-plane stretching due to the large panel deflections. Recall from chapter 2 that the in-plane strain $\{\varepsilon^o\}$ consists of two components, the membrane strain $\{\varepsilon_m^o\}$, and the non-linear von-Karman strain $\{\varepsilon_\theta^o\}$. The constitutive relation between strain and stress is given by the linear transformation in Equation 2.22. With the increasing degree of nonlinearity, the membrane displacements and the transverse displacements in the von-Karman terms tend to dominate the strain-displacement relations. These effects are clearly evident in Figures 5.7, 5.9, and 5.11 where the stress time histories and PDF for the higher SPLs (119.87 dB and131.9 dB) for the maximum stresses, and its two basic elements, pure bending and in-plane stress components, are plotted separately. Sometimes, for moderately large deflections ($W_c/h \leq 1.0$), various theories predict the nonlinear displacement response but use a linear stress-displacement relationship to obtain the stresses. When the linear stress term is mentioned above, it means that in the strain-displacement relation (Equation 2.8) only the bending strain $z\{\kappa\}$ is considered. By doing so, fatigue life estimation can be evaluated from the frequency domain without relaxing any assumption since the stress will have the same Gaussian characteristics as the displacement. This approach can be valid occasionally, but it does not give a realistic and consistent approach to calculate the fatigue life of structures subjected to large deflections. It should be noted that at the high SPL (131.91 dB) the maximum peak occurs at about 36,000 psi in Figure 5.7, which is just slightly below the yield strength (40,000 psi) for the 2014 aluminum alloy. This shows that for the chosen panel geometry the recorded pressure fluctuations (131.47 dB and 131.91 dB) are very high and should produce relatively low fatigue life estimates.

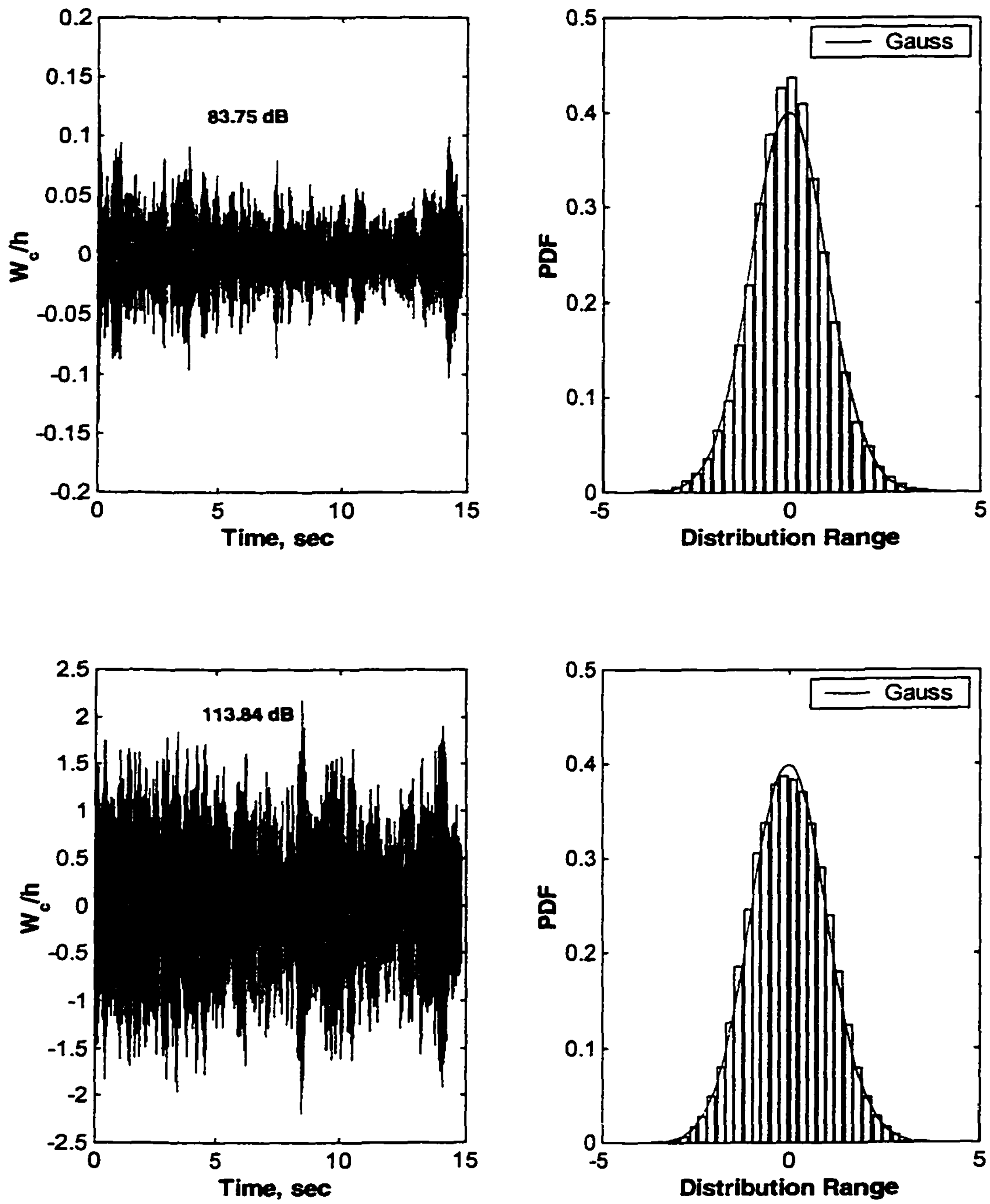

Figure 5.4 Displacement Time Histories and PDF of a 15x12x0.060 in. Simply Supported Isotropic Plate at SPL= 83.75 and 113.84 dB

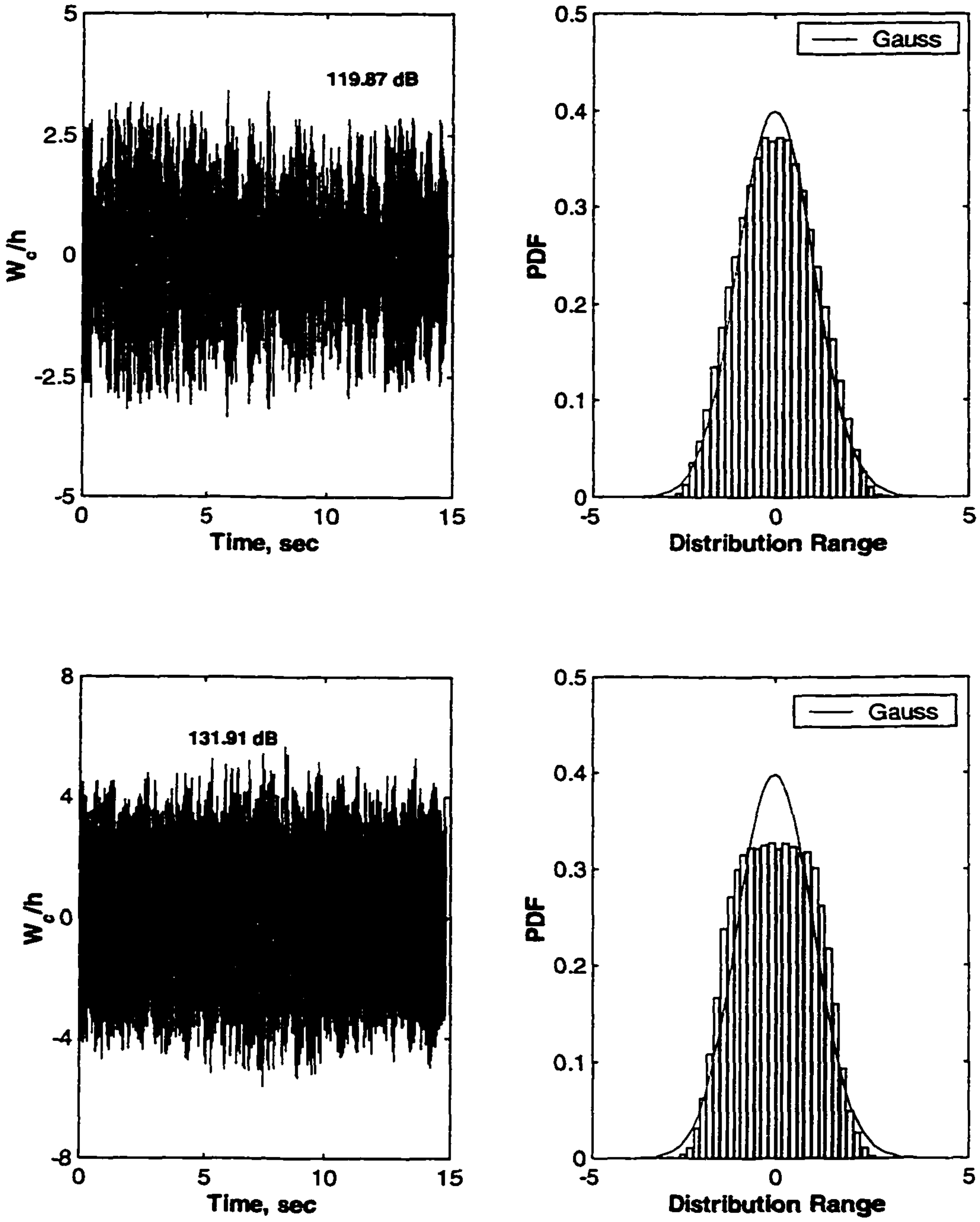

Figure 5.5 Displacement Time Histories and PDF of a 15x12x0.060 in. Simply Supported Isotropic Plate at SPL= 119.87 and 131.91 dB

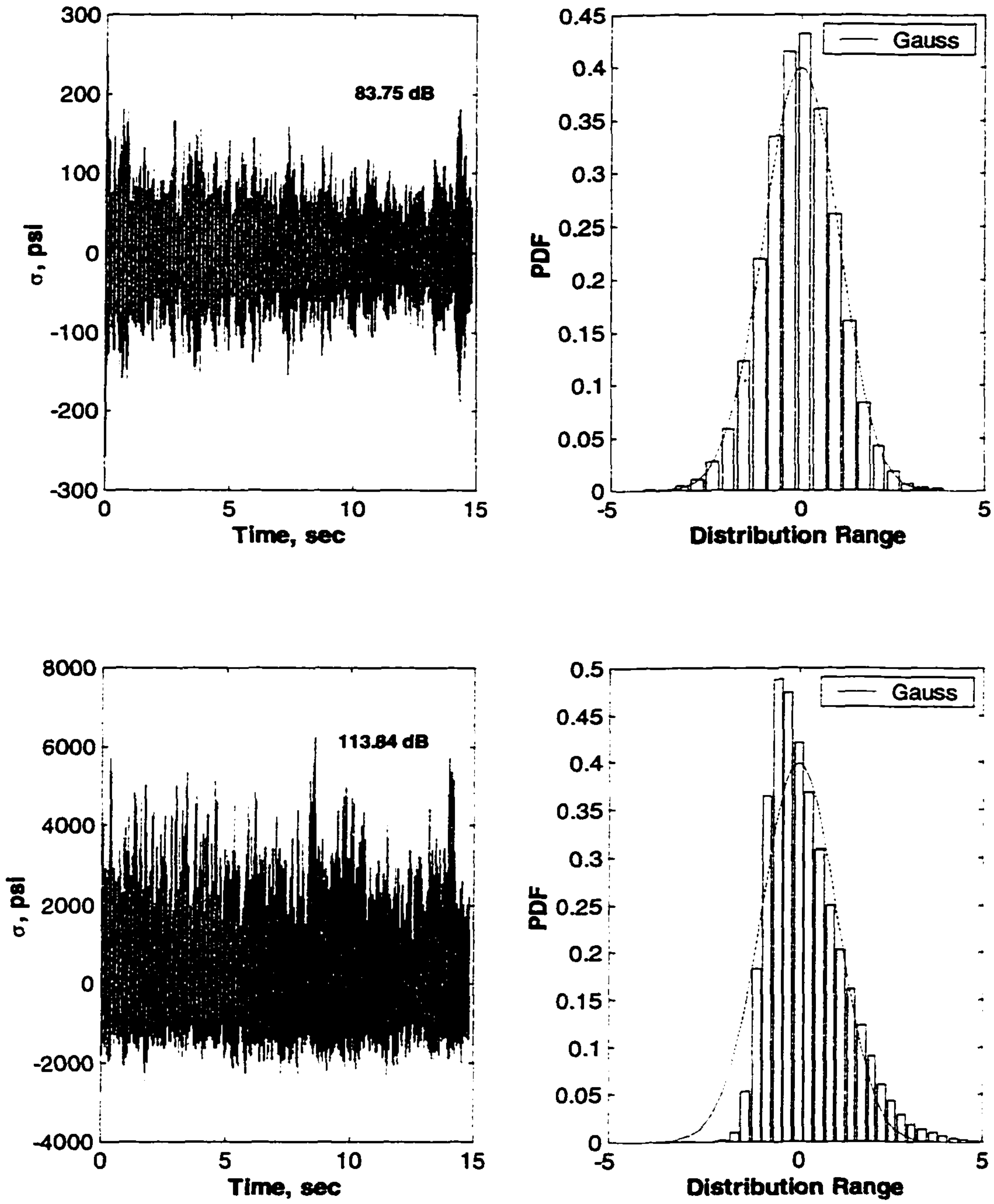

Figure 5.6 Maximum Stress Time Histories and PDF of a 15x12x0.060 in. Simply Supported Isotropic Plate at SPL= 83.75 and 113.84 dB

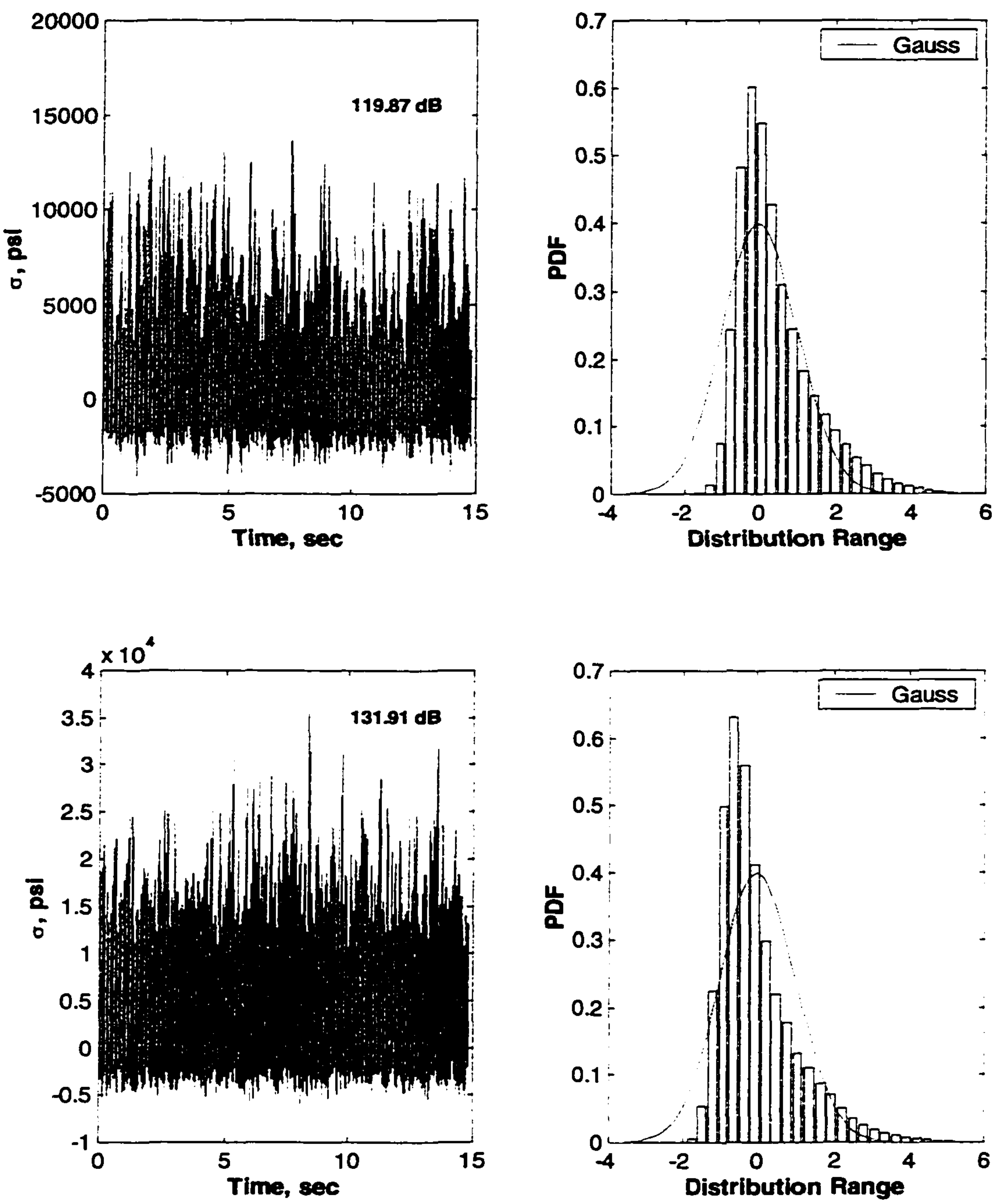

Figure 5.7 Maximum Stress Time Histories and PDF of a 15x12x0.060 in. Simply Supported Isotropic Plate at SPL= 119.87 and 131.91 dB

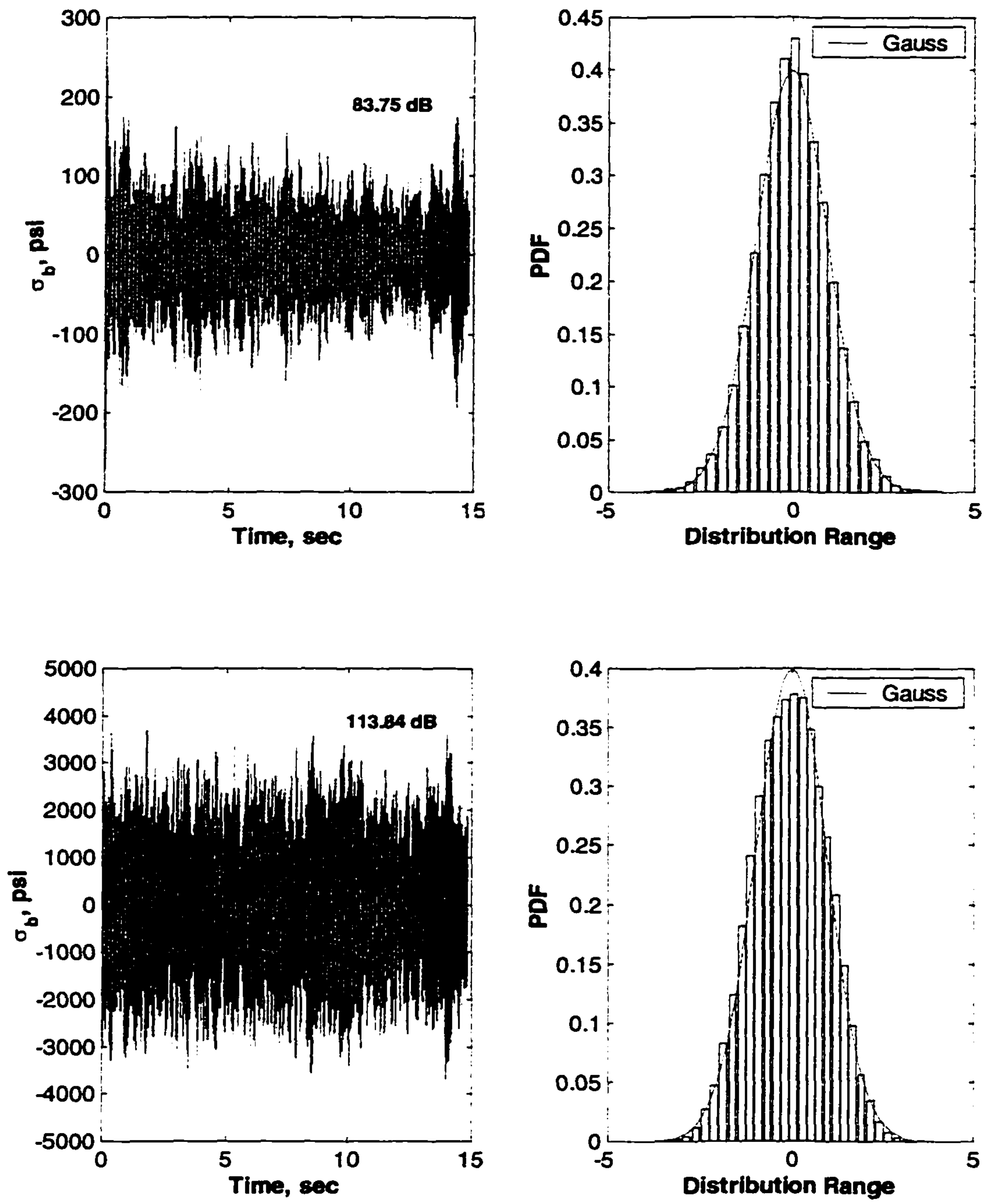

Figure 5.8 Bending Stress Component Time Histories and PDF of a 15x12x0.060 in. Simply Supported Isotropic Plate at SPL= 83.75 and 113.84 dB

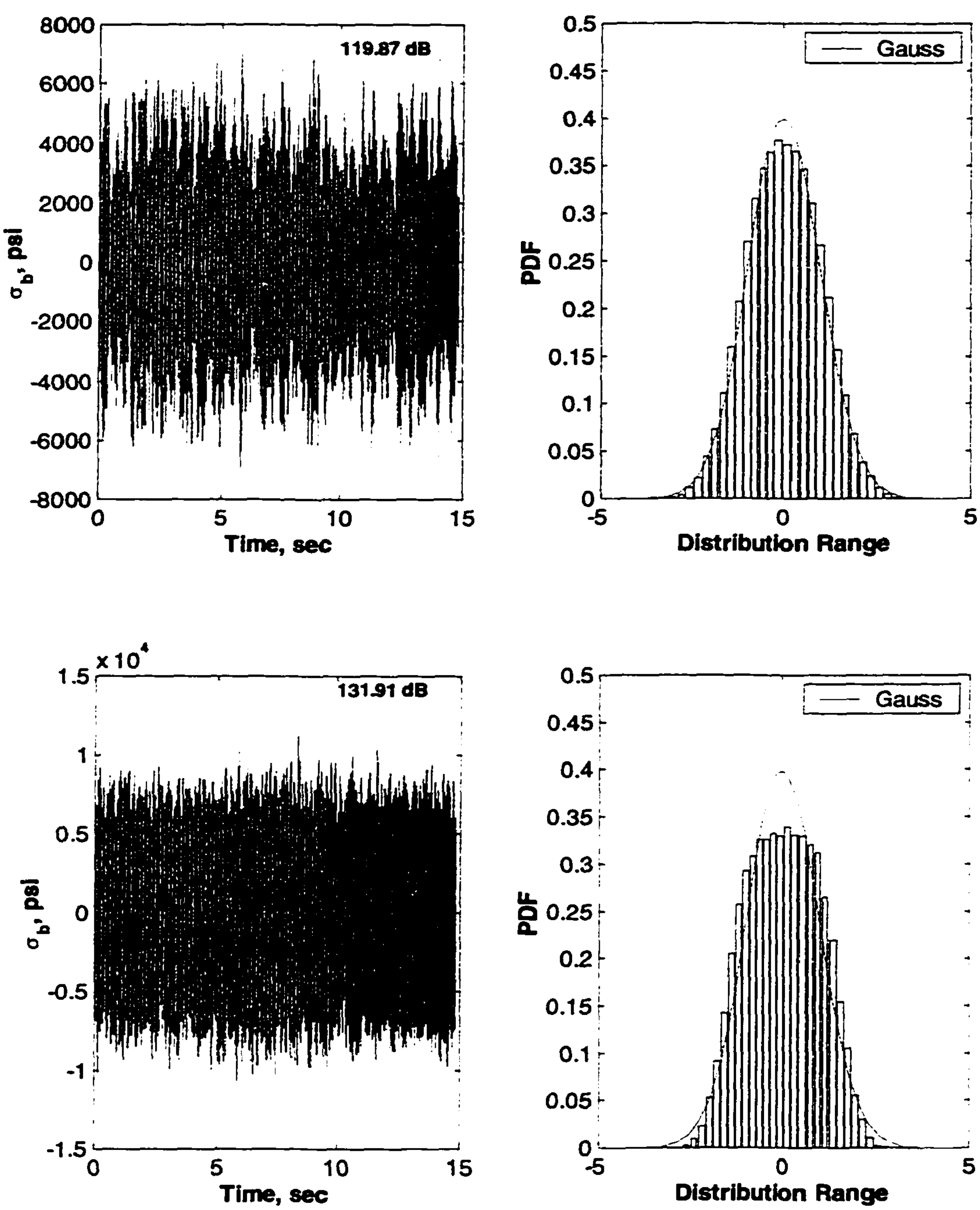

Figure 5.9 Bending Stress Component Time Histories and PDF of a 15x12x0.060 in. Simply Supported Isotropic Plate at SPL= 119.87 and 131.91 dB

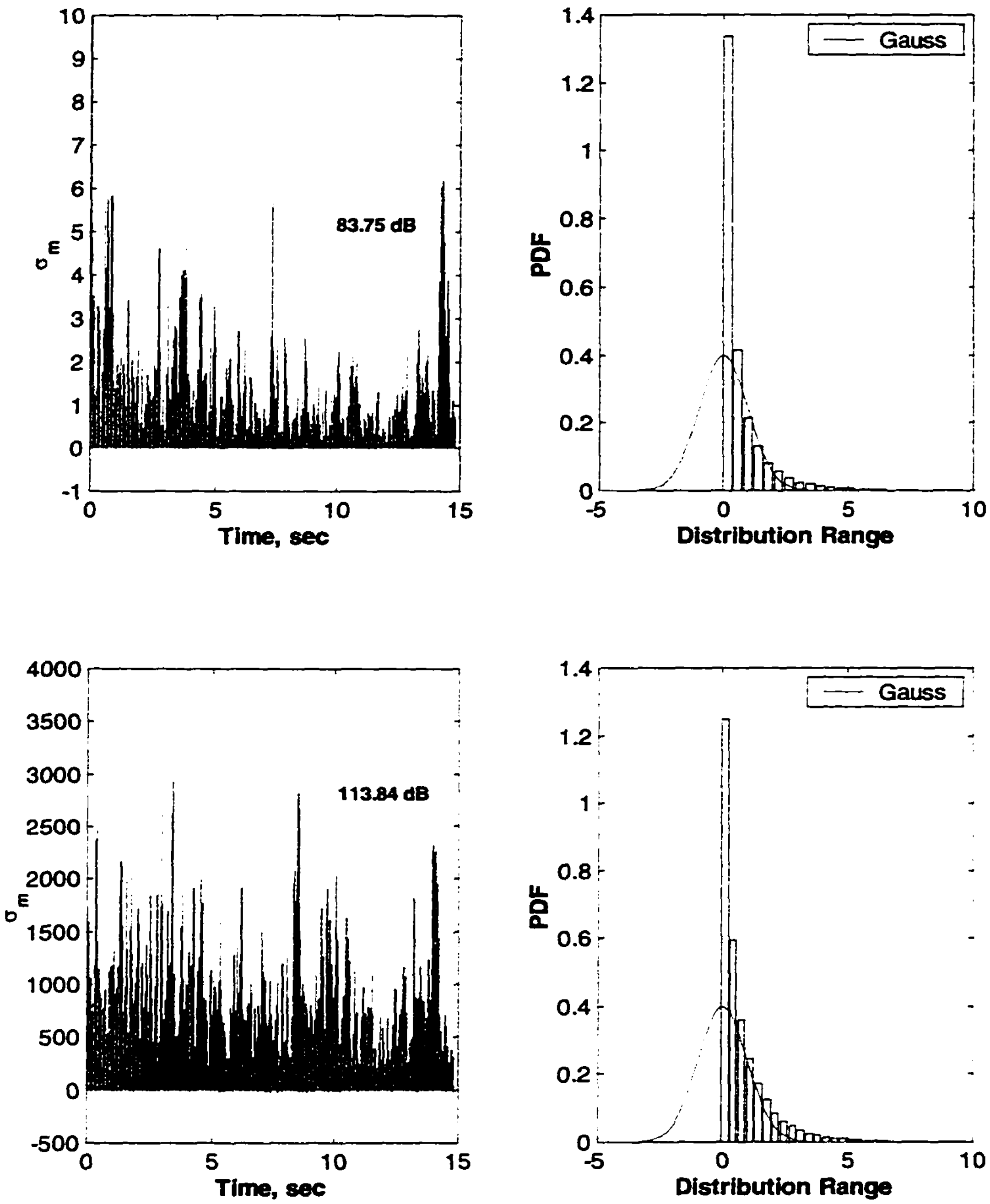

Figure 5.10 In-Plane Stress Component Time Histories and PDF of a 15x12x0.060 in. Simply Supported Isotropic Plate at SPL= 83.75 and 113.84 dB

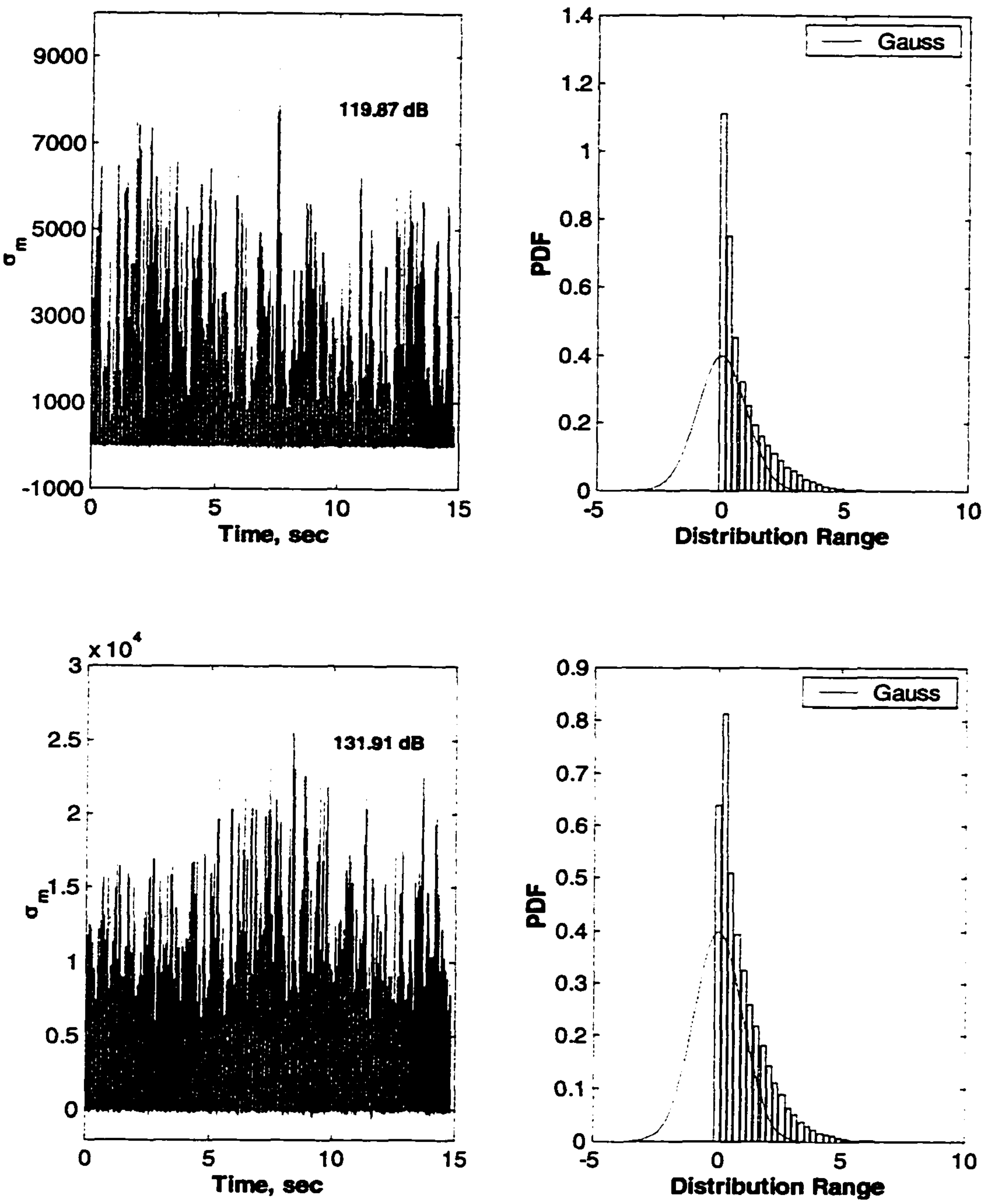

Figure 5.11 In-Plane Stress Component Time Histories and PDF of a 15x12x0.060 in. Simply Supported Isotropic Plate at SPL= 119.87 and 131.91 dB

5.2.2 Power Spectral Densities (PSD)

The PSD for deflection and maximum principal stress at different SPL are shown in Figures 5.12 and 5.13. At the lowest input level (83.75 dB) where the response is linear, distinct peaks can be observed at the lowest five natural frequencies given in Table 5.3. Furthermore, similar characteristics can be seen between the PSD of displacement and stress. The responses are basically small deflection (RMS(W_c/h)=0.0223) random vibration dominated by the fundamental mode (1,1). As the SPL increases, the distinct peaks that are characteristics of linear vibration tend to flatten and shift towards the higher frequencies. At the high input levels 119.87 dB and 131.91 dB in Figure 5.13, a mean value is observed (also see Table 5.4) and the distinct peaks are no longer evident and the PSD tends to exhibit the characteristics of a wide-band process.

The PSD for the bending and in-plane stress components are shown in Figures 5.14 and 5.15. For the bending component, a similar conclusion to that for the maximum stress can be drawn. For the in-plane PSD, it is important to note that at the lowest input level a multiplicity of peaks not corresponding to any of the five bending natural frequencies appear. Those small resonance peaks away from the linear frequencies result from the quadratic terms of the stress/strain relationship. Eventually, the peaks coalesce as the response PSD becomes highly nonlinear and exhibits a broadband behavior.

From all the PSD plots, it is observed that the frequency shifting and the peak broadening are more pronounced at the higher frequencies. For instance, there are five distinct peaks at the lowest SPL (83.75 dB), as the SPL increases the peaks tend to flatten and only one peak can be identified at the high 131.91 dB.

Some advantages of the present time domain modal formulation over the equivalent linearization (EL) technique as a basis for fatigue life calculations are worth mentioning. As it was mentioned in Chapter 3, it appears that fatigue life depends exclusively on the stress amplitude distribution. The EL uses a linearised system that inaccurately reflects the spatial distribution of the nonlinear system. Fatigue life calculations based on these quantities, i.e., moments of the stress from PSD (Equation 3.8), would consequently be affected significantly. Moreover, the use of the EL and fatigue life in the frequency domain requires some careful considerations. Recall that peaks in equivalent linear PSD might occur at the same frequencies as the fully nonlinear case but they would not reflect the broadening effect.

The other methods such as the Dirlik's and the Transformed Gaussian Processes (TGP), which are principally based on Rice work [88], have shown that signals exhibiting Gaussian probability density characteristics can be represented by an infinite number of sine waves combined with random phases, i.e., by continuous frequency spectra. The frequency spectrum defines the signal in a statistical sense so that the higher order probability density functions are derivable from the frequency spectrum. Based upon this, some relationships have been developed that allow estimation of the peak distribution when the response PSD is known. Figures 5.6 and 5.7 showed that the stress response is no longer Gaussian as the response becomes highly nonlinear. In that case, the statistical stress response characteristics are no longer properly defined by the PSD. The estimated probability peak distribution greatly overestimates the fatigue life, as will be shown later in this chapter in Table 5.5.

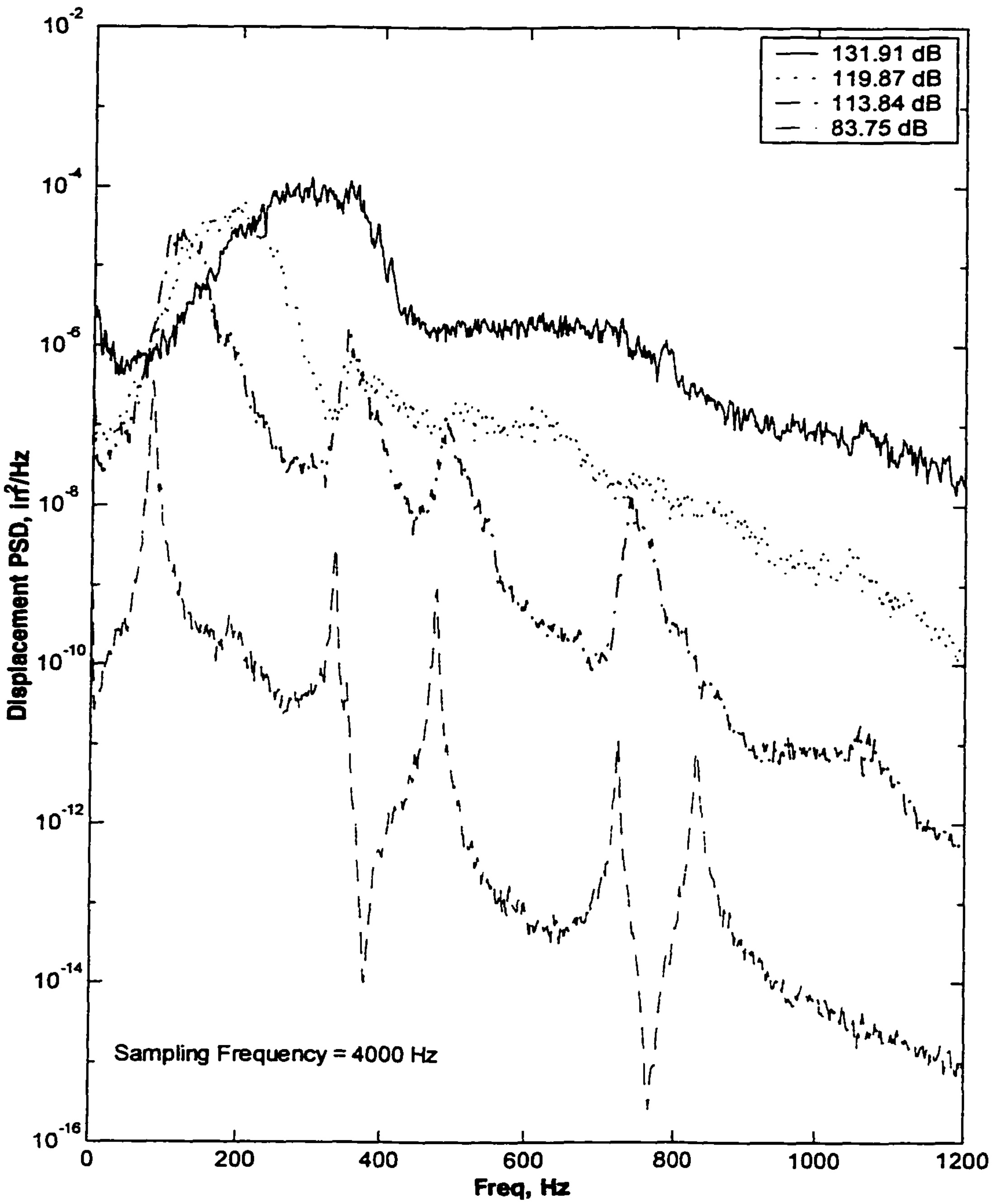

Figure 5.12 Displacement PSD of a 15x12x0.060 in. Simply Supported Isotropic Plate at SPL=83.75, 113.84, 119.87 and 131.91 dB

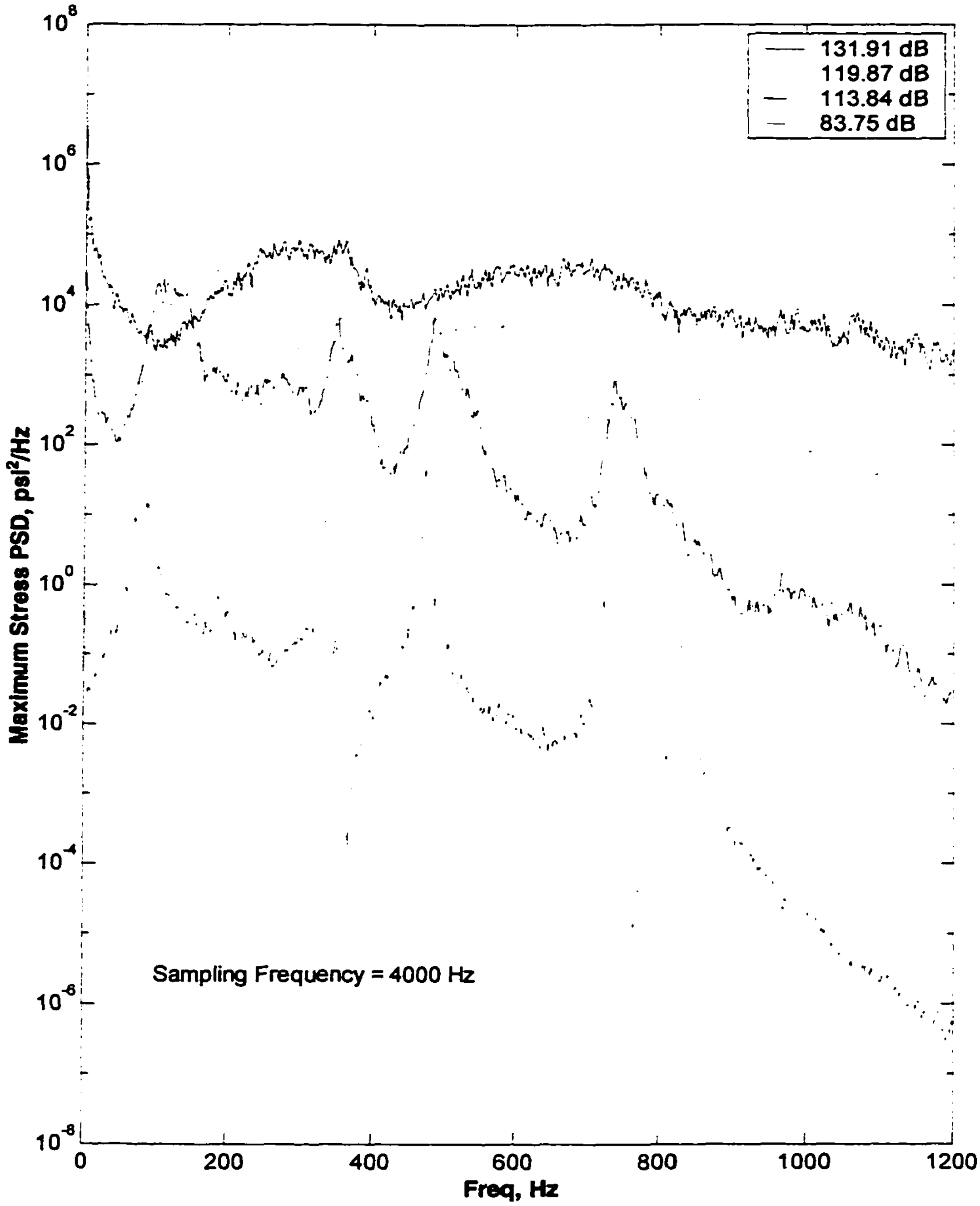

Figure 5.13 Maximum Stress PSD of a 15x12x0.060 in. Simply Supported Isotropic Plate at SPL=83.75, 113.84, 119.87 and 131.91 dB

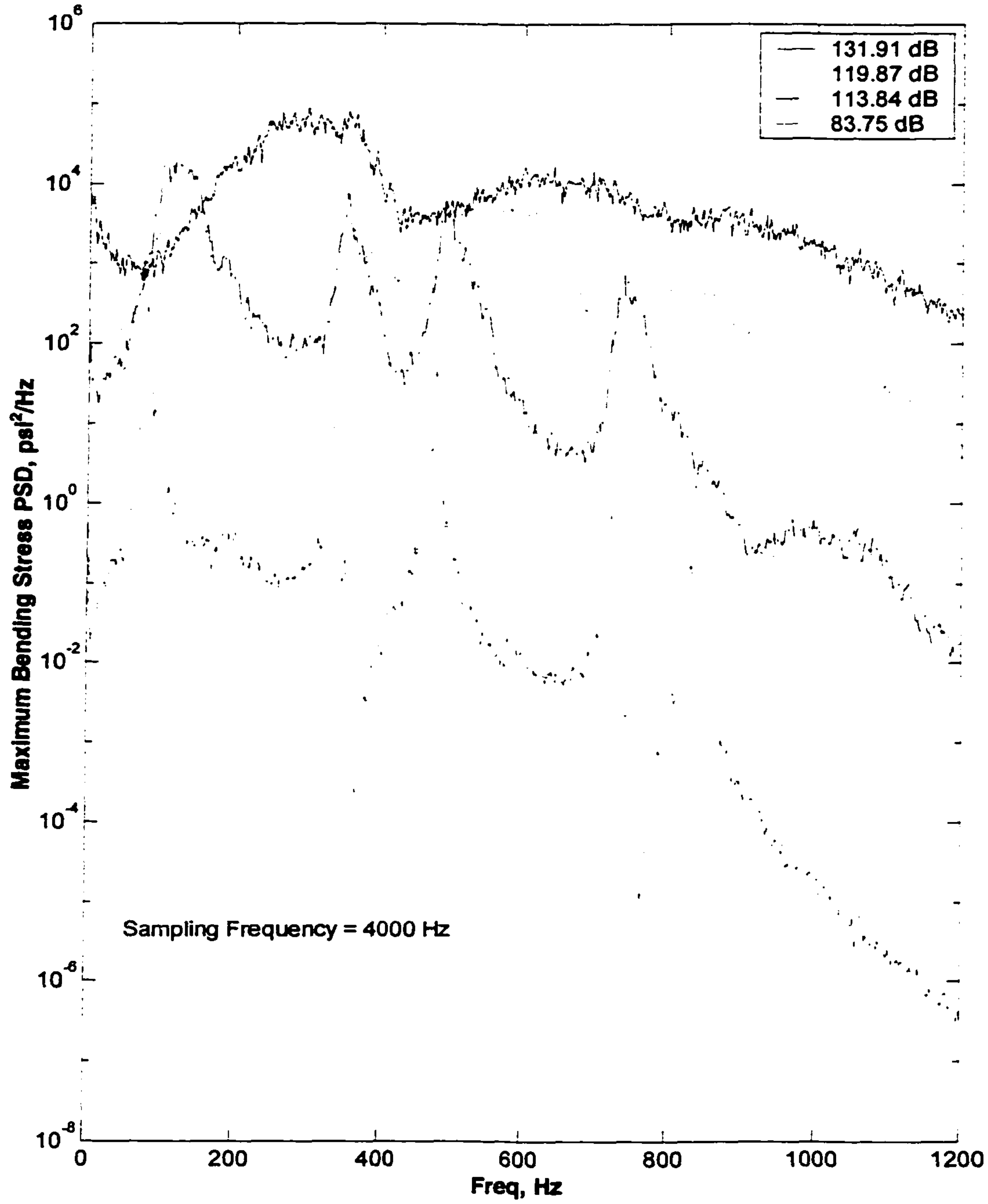

Figure 5.14 Bending Stress Component PSD of a 15x12x0.060 in. Simply Supported Isotropic Plate at SPL=83.75, 113.84, 119.87 and 131.91 dB

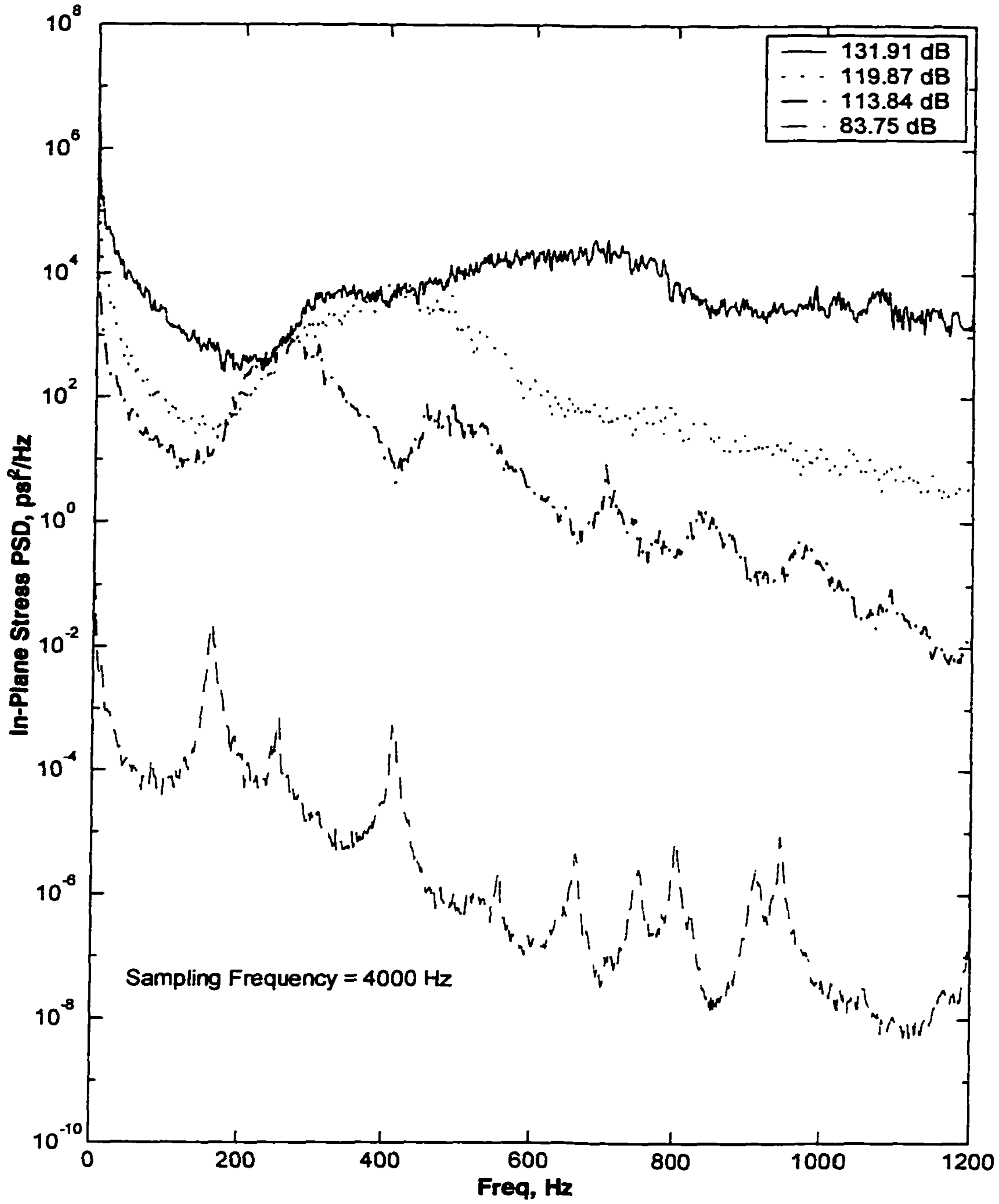

Figure 5.15 In-Plane Stress Component PSD of a 15x12x0.060 in. Simply Supported Isotropic Plate at SPL=83.75, 113.84, 119.87 and 131.91 dB

5.2.3 Amplitude Distribution Histograms (ADH)

The min-max (F) and RFC (F^{RFC}) cycles and positive amplitude distribution of the maximum principal stress for each of the loading cases are shown in Figures 5.15 to 5.18 where the normalized amplitude (maginitude/std) range is plotted versus the number of occurrences. In all loading cases it is clearly observed that the RFC contains more cycles with high amplitudes compared to min-max cycles. The sets of pairs in the min-max cycle counting plots are more dispersed than in the RFC plots at the lowest SPL. However, as the SPL increases the sets of pairs in the min-max cycle counting become more condensed and start to look like the RFC cycle counting. This becomes more evident in the amplitude histograms where the min-max and RFC cycles "spatial distribution shapes" approximate each other with the varying SPL. It is important to note though that the RFC cycles counting method still yields higher amplitudes than the min-max cycles counting approach.

For comparison, a Rayleigh distribution is given for each amplitude distribution plot. If the stress produced is *narrow-band* then by definition the stress time history has the appearance of a sine wave of slowly varying frequency and amplitude. For each upward crossing of zero, the time history displays a peak. For such process, the theoretical peak distribution is Rayleigh. When the stress time history is more complicated a number of "smaller" peak maxima (and minima) occur between the zeros. When the difference between a maximum and the succeeding minimum increases, the existence of these smaller peaks (with high frequency content) may become important. In this case, they will cause extra losses to be induced in the already pre-stressed material and thus, to a certain extent, may affect the fatigue life.

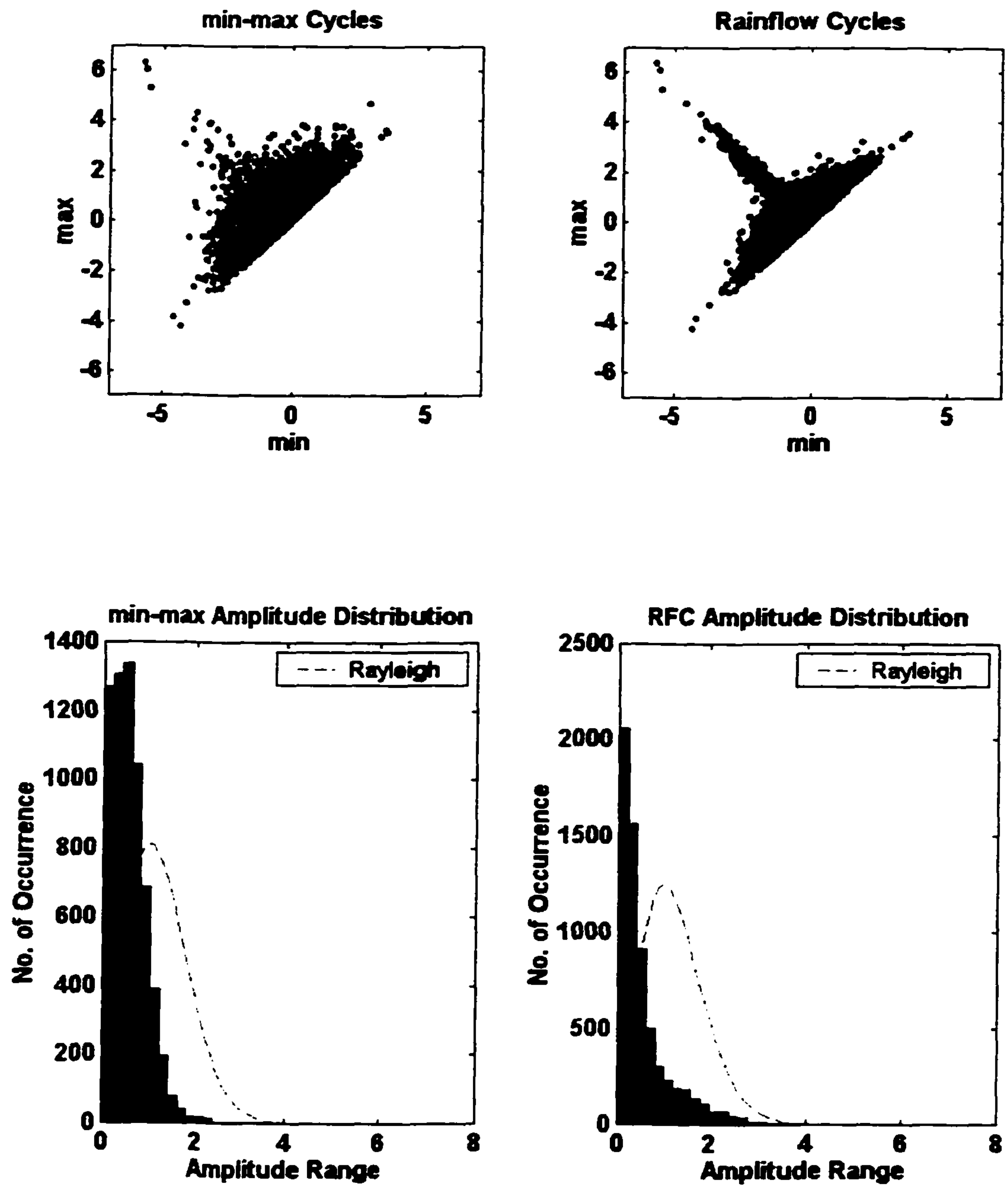

Figure 5.16 Cycles and Amplitude Distribution of Maximum Stress for a 15x12x0.060 in. Simply Supported Isotropic Plate at SPL=83.75 dB

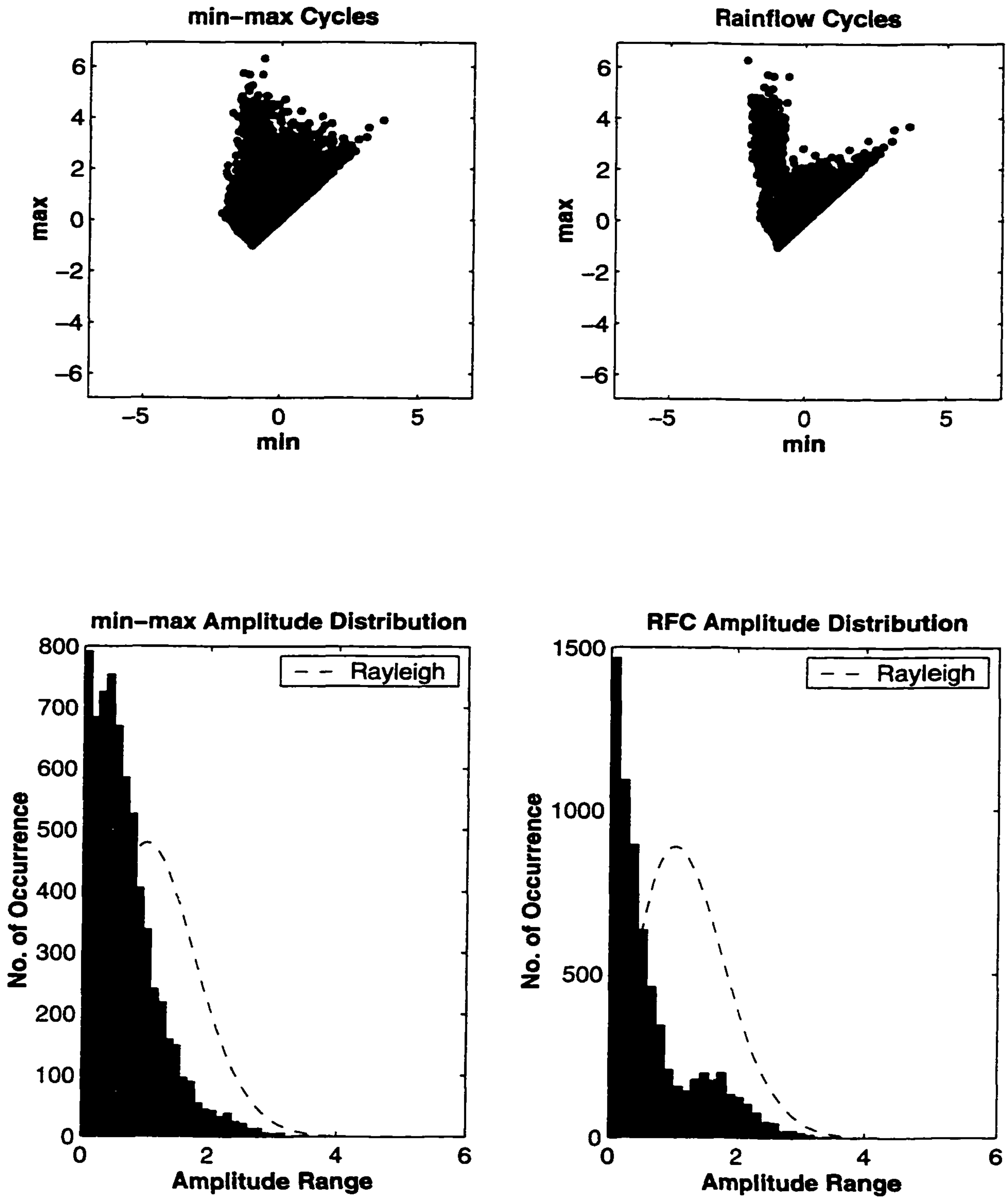

Figure 5.17 Cycles and Amplitude Distribution of Maximum Stress for a 15x12x0.060 in. Simply Supported Isotropic Plate at SPL=113.84 dB

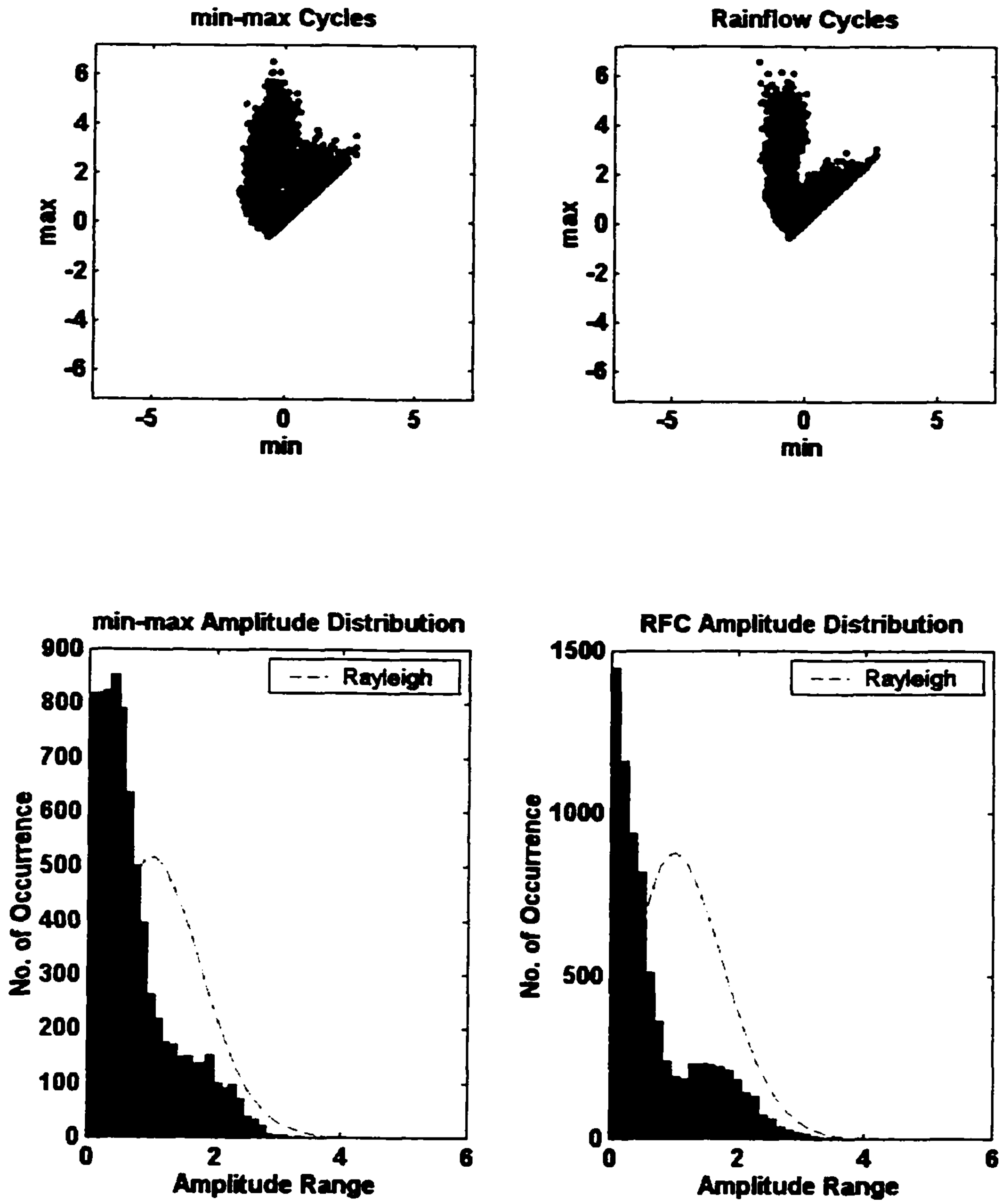

Figure 5.18 Cycles and Amplitude Distribution of Maximum Stress for a 15x12x0.060 in. Simply Supported Isotropic Plate at SPL=119.87 dB

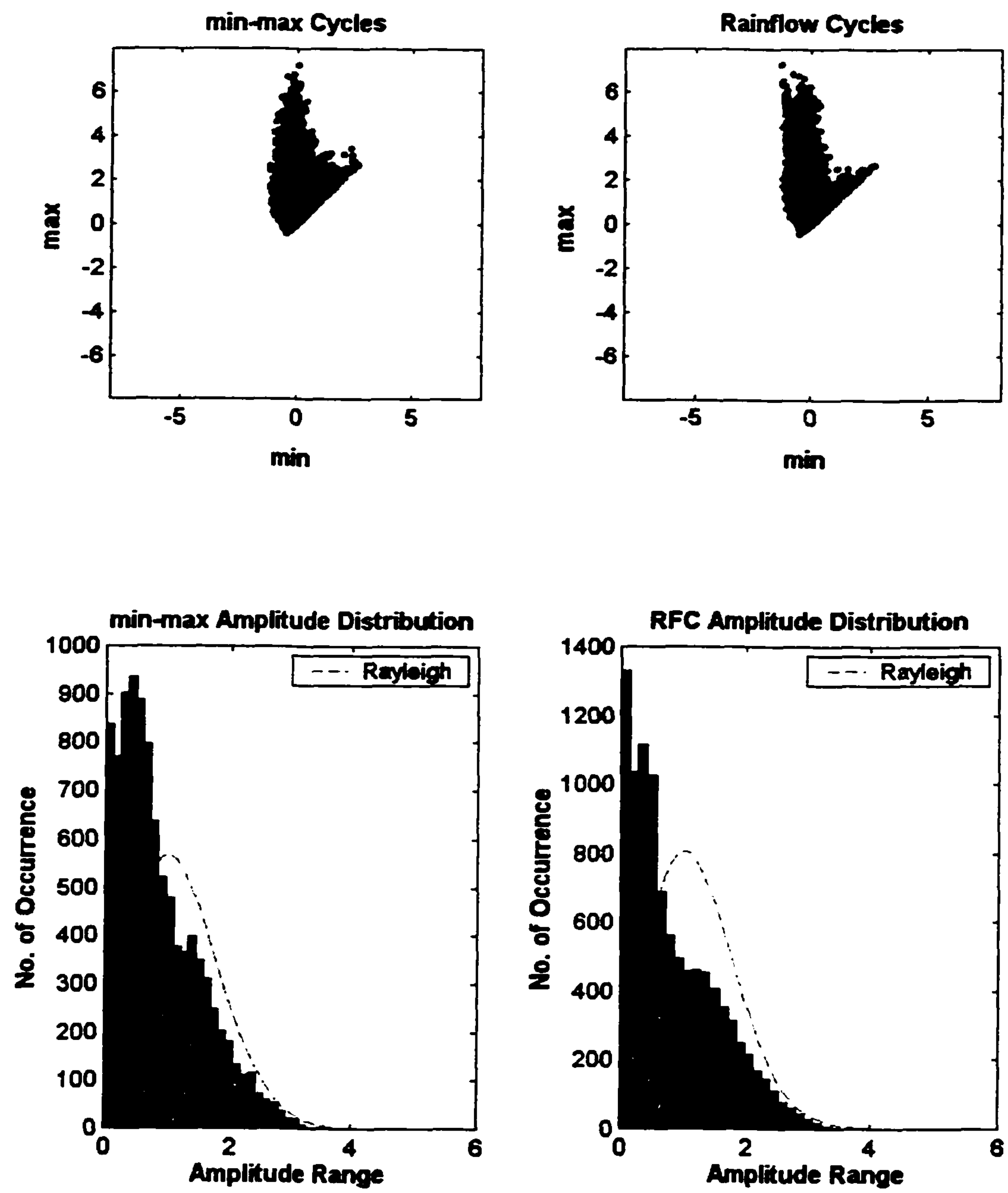

Figure 5.19 Cycles and Amplitude Distribution of Maximum Stress for a 15x12x0.060 in. Simply Supported Isotropic Plate at SPL=131.91 dB

5.2.4 Peak Distribution and Up-Crossing Threshold

The positive peak distributions for displacement and principal maximum stress at different SPL are shown in Figures 5.20 and 5.21. For comparison, a Rayleigh distribution is given with each displacement and stress peak distributions. At the low SPL (83.75 dB), when the response is linear, the displacement and stress response peak distributions are practically Rayleigh. The slight deviation from a pure Rayleigh distribution is due to the nature of the responses time histories that are not totally narrow-banded. As the responses become nonlinear with the increasing SPL, the peak distributions follow neither a Rayleigh nor a Gaussian distribution, and the tails of the peak distributions become fatter indicating the increase in nonlinearities. A *narrow-banded* signal has a "true" Rayleigh peak distribution while a *wide-banded* signal has a Gaussian type distribution based on theory. To obtain a "true" Rayleigh distribution only one peak maximum (or minimum) occur between two succeeding zero crossings of the signal, while in the case of a Gaussian type peak distribution "smaller" peak maxima (or minima) occur between the zeros. As a result, the positive peaks stress distribution that is a fundamental input for fatigue life analysis, will always lie between a Gaussian and Rayleigh distribution for random analysis.

The threshold up-crossing rates for the maximum principal stress are shown in Figure 5.22 for increasing SPL inputs. For a linear response of 83.75 dB, the threshold up-crossing rate closely approximates a theoretical Gaussian process and the number of cycles per second is 206. As the SPL input increases and the response becomes more Rayleigh-like, the up-crossing rates are 258, 360, and 522 peaks/sec for the 113.84, 119.87, and 131.91 dB inputs, respectively.

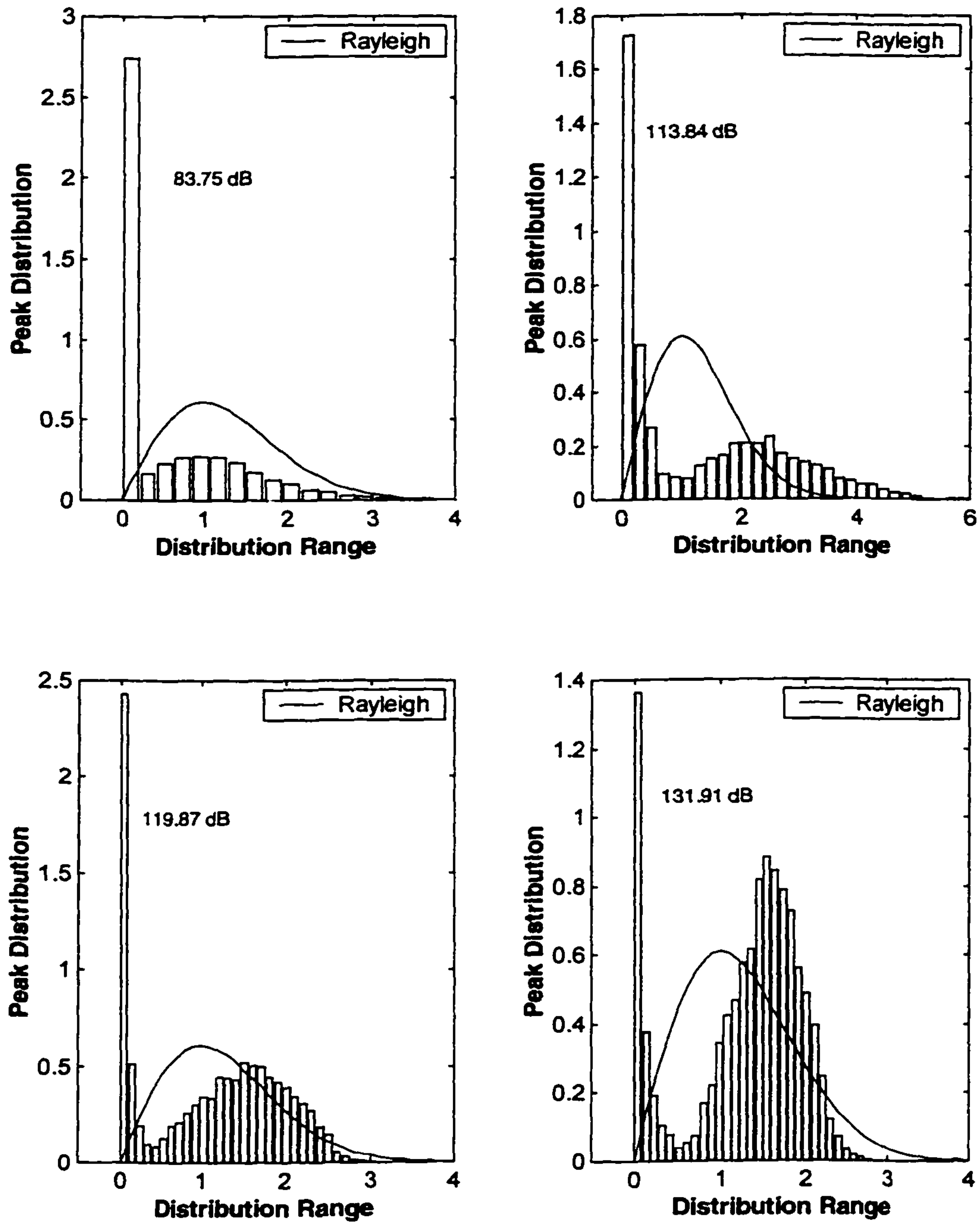

Figure 5.20 Displacement Peak Distribution for a 15x12x0.060 in. Simply Supported Isotropic Plate at SPL=83.75, 113.84, 119.87 and 131.91 dB

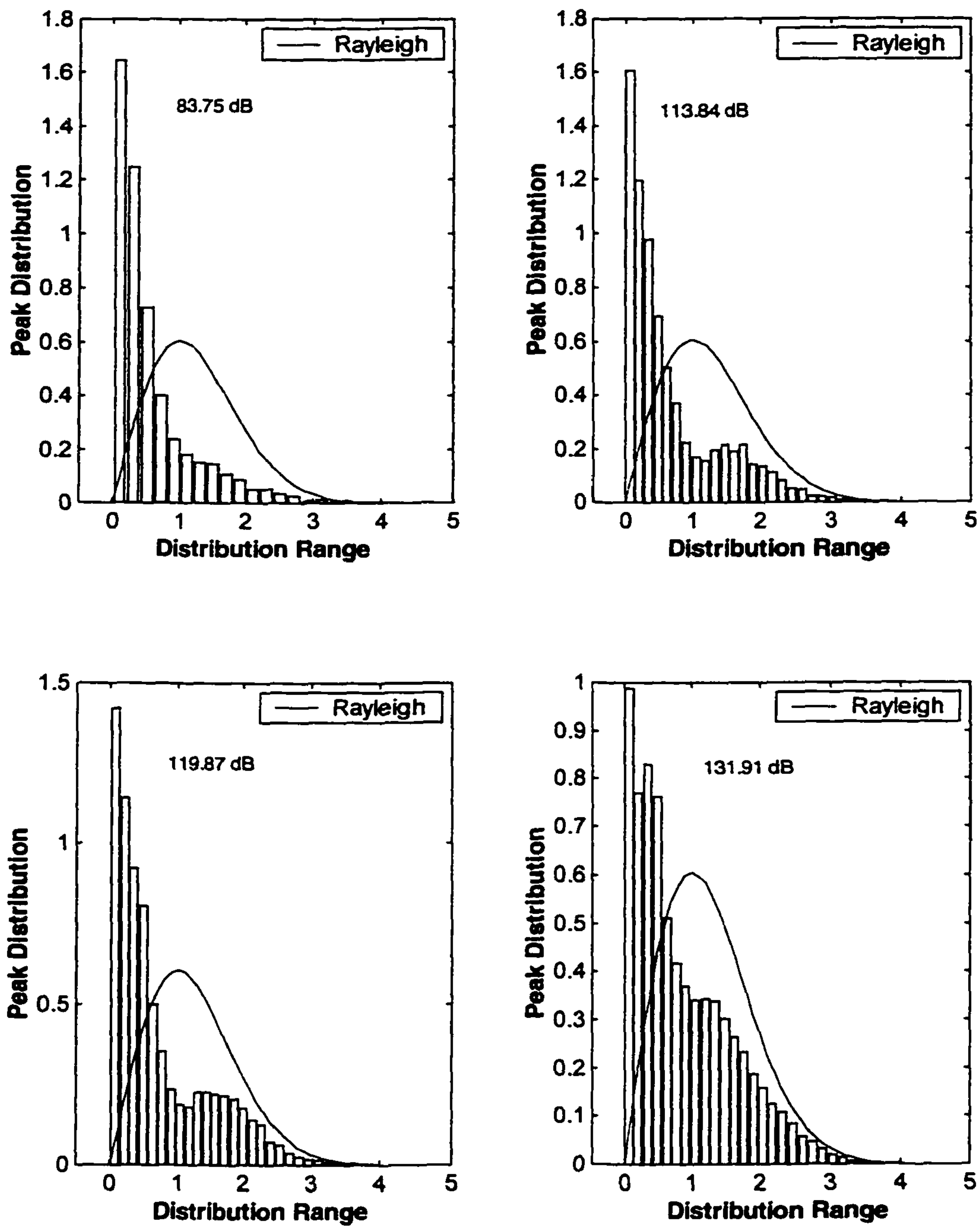

Figure 5.21 Maximum Stress Peak Distribution for a 15x12x0.060 in. Simply Supported Isotropic Plate at SPL=83.75, 113.84, 119.87 and 131.91 dB

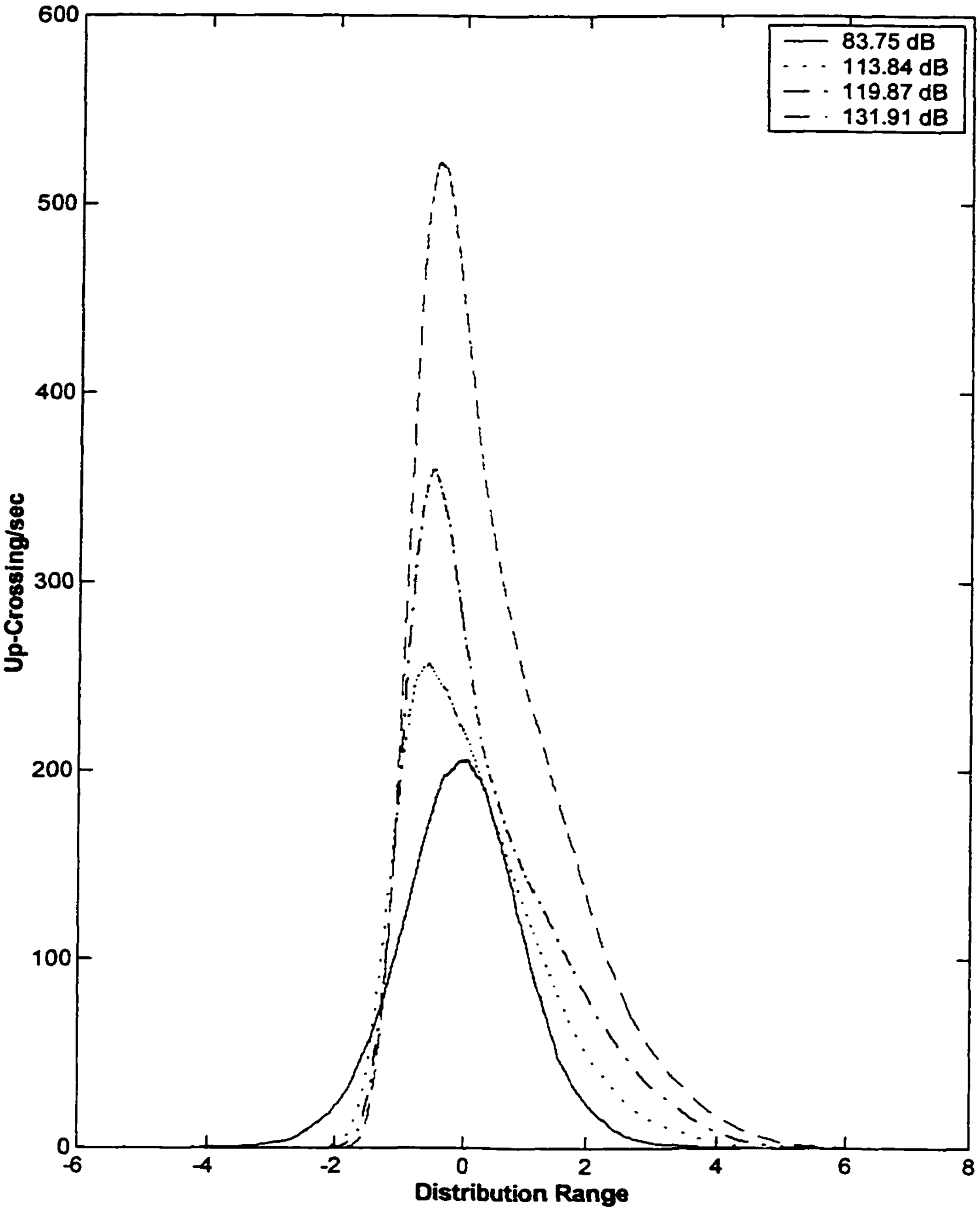

Figure 5.22 Threshold Up-Crossing Rates of Maximum Stress for a 15x12x0.060 in. Simply Supported Isotropic Plate at SPL=83.75, 113.84, 119.87 and 131.91 dB

5.2.5 Fatigue Life Estimates for NW_2

Fatigue life estimates for each of the four SPL cases just studied will be evaluated using the time and frequency domain methods. The fatigue approaches are the RFC in the time domain and Dirlik's and transformed Gaussian in the frequency domain. As mentioned earlier, since the recorded pressure fluctuations are only representative for the highest load inputs, fatigue life estimates from their corresponding simulated EWSPL will not be addressed. For each one of the fatigue estimation approaches the results are shown in Table 5.5.

Table 5.5

Fatigue Estimates in Hours for NW_2 at Different SPL

SPL (dB)	RFC (Time Domain)	TGP (Frequency Domain)	Dirlik (Frequency Domain)
83.75	2.59×10^{12}	1.67×10^{15}	1.65×10^{15}
113.84	5.58×10^{5}	9.77×10^{7}	1.39×10^{8}
119.84	1.43×10^{4}	4.33×10^{7}	3.71×10^{6}
131.91	276.90	1.64×10^{6}	4292

$K=1.52\times10^{25}$ and $\beta=4.8$

It can be readily observed that the two frequency domain approaches are less conservative than the RFC method. The discrepancy between the RFC time domain and the frequency approaches increases as the input level increases. That means as the response becomes more nonlinear the frequency domain approaches tend to overestimate the fatigue life. These results were expected, since as was mentioned previously in sections 5.2.3 and 5.2.4, the maximum stress PSD at high SPL does not properly characterize the statistical properties of the signal. As a result, the probability peak distribution is not estimated accurately, which produces the overestimate of fatigue life results. It is also concluded that the Winterstein TGP [90] approach is not applicable for processes that deviates slightly from a Gaussian distribution. Table 5.5 shows that for the three lower input levels the fatigue life can be assumed to be infinite, but that is not a realistic result. Consequently, in the following sections fatigue life estimates using the Winterstein TGP will be omitted. As mentioned earlier, only the original two recorded data sets correspond to an actual loading condition and the discussion of the other input loadings will not yield any realistic conclusion.

5.3 Non-White (NW) and Equivalent Sound Pressure Levels (EWSPL) at $\Delta T = 0$

In this section let us consider the two recorded B-1B flight data sets and their EWSPL, and let us estimate their fatigue life using the RFC and the Dirlik frequency approaches. The discussions and plots for NW_1 and NW_2 are similar. There were substantially no differences in the results, making the presentation of both sets of data redundant. Since some of the figures for NW_2 were presented in section 5.2, the present section will retain NW_1.

For the EWSPL a Monte Carlo numerical procedure was used with an ensemble of 10 time histories. In order to see how the PSD response was smoothed by calculating several realizations (Monte Carlo simulation), the PSD for the maximum principal stress of the recorded data NW_1 and its $EWSPL_1$ are shown in Figure 5.23. By taking an ensemble of 10 stress time histories and applying a Hanning window at the end of each ensemble the FFT is smoothed because it is calculated from the average of the 10 ensembles instead from only one realization. For the 10 stress time histories of both recorded data sets the uncertainty interval is 0.0040% for displacement and 11.61% for stress.

In addition, the amplitude distribution histograms (ADH) and fatigue life estimation based on pure bending stress from linear theory are included for comparison.

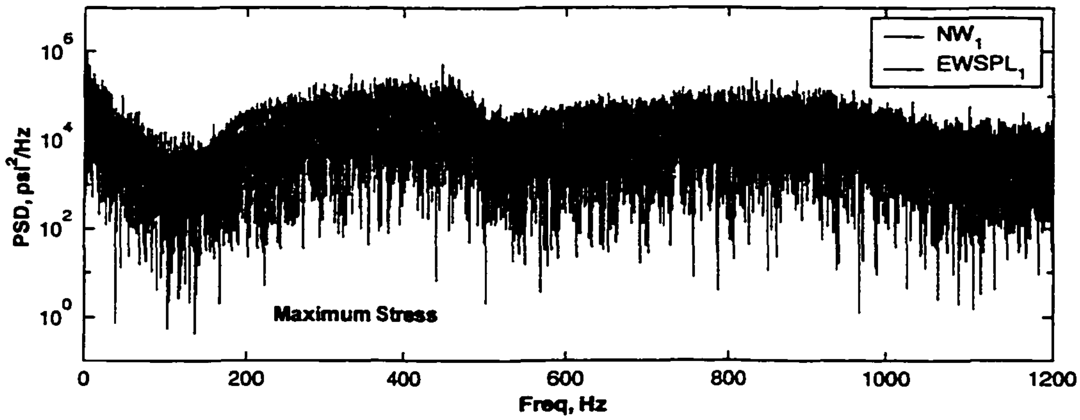

Figure 5.23 Monte Carlo Simulation/Data Smoothing

5.3.1 Amplitude Distribution Histograms (ADH)

The min-max and RFC cycles and ADH of the maximum stress and the pure bending stress are shown in Figures 5.24 to 5.27. As expected, in all cases it is clearly observed that the RFC contains more cycles with high amplitudes compared to min-max cycles, and that the set of pairs in the min-max cycle counting plots are more dispersed than in the RFC plots. In addition, the cycles for pure bending are much more dispersed than for the maximum stress. This phenomenon becomes clearer in the amplitude histograms where the maximum stress distribution deviates substantially from a "true" Rayleigh distribution (narrow-band). In addition, the amplitude distribution for maximum stress reveals an increase in amplitudes at the "tail" of the distribution that exert considerable influence on fatigue life estimates. A change in the magnitude of the amplitudes is not observed between the maximum and bending stress because the data previously were normalized. Otherwise, the magnitude of the bending stress should be higher (see section 5.3.2) because the calculated linear displacement is higher.

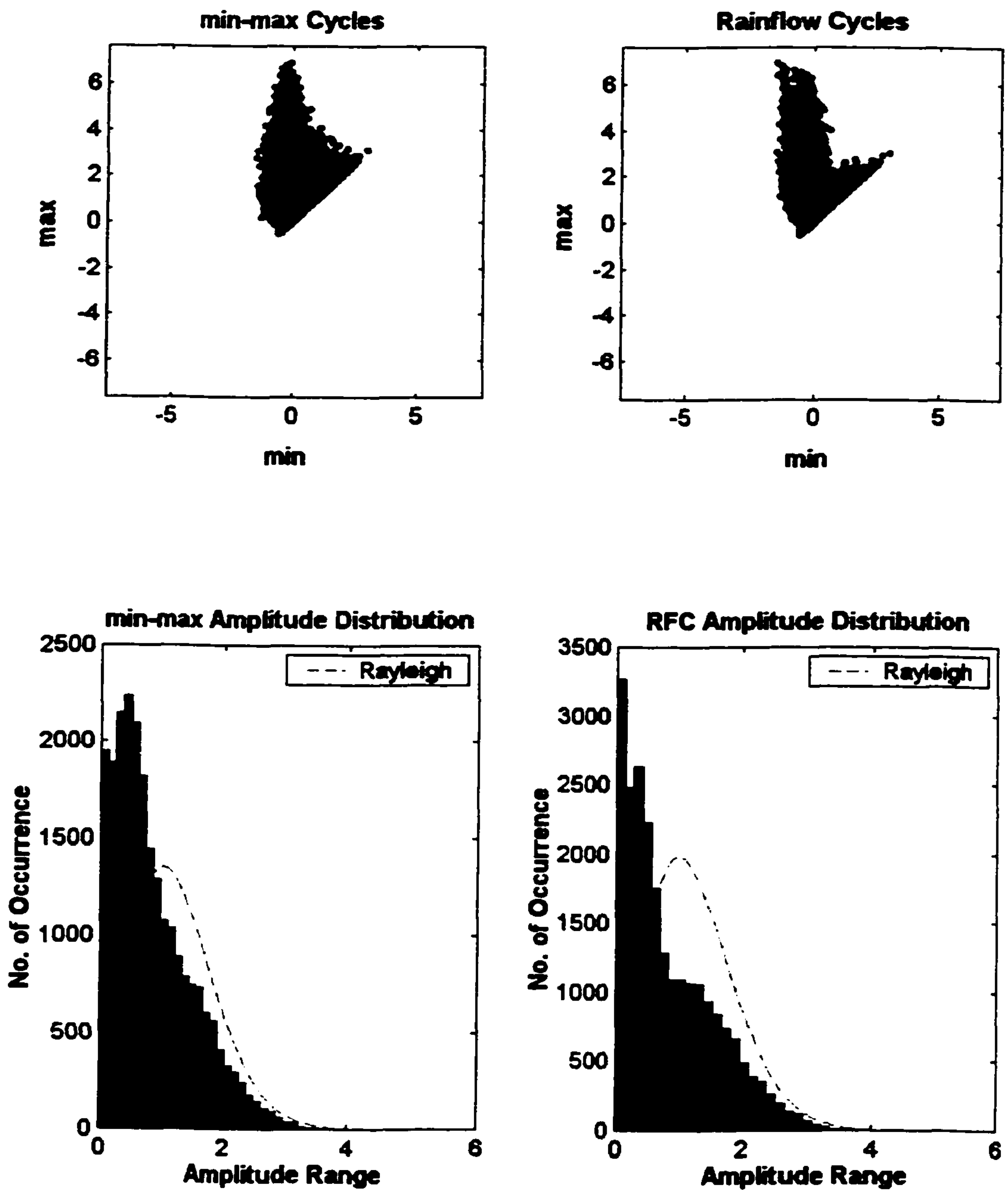

Figure 5.24 Cycles and Amplitude Distribution of Maximum Stress for a 15x12x0.060 in. Simply Supported Isotropic Plate at NW_1

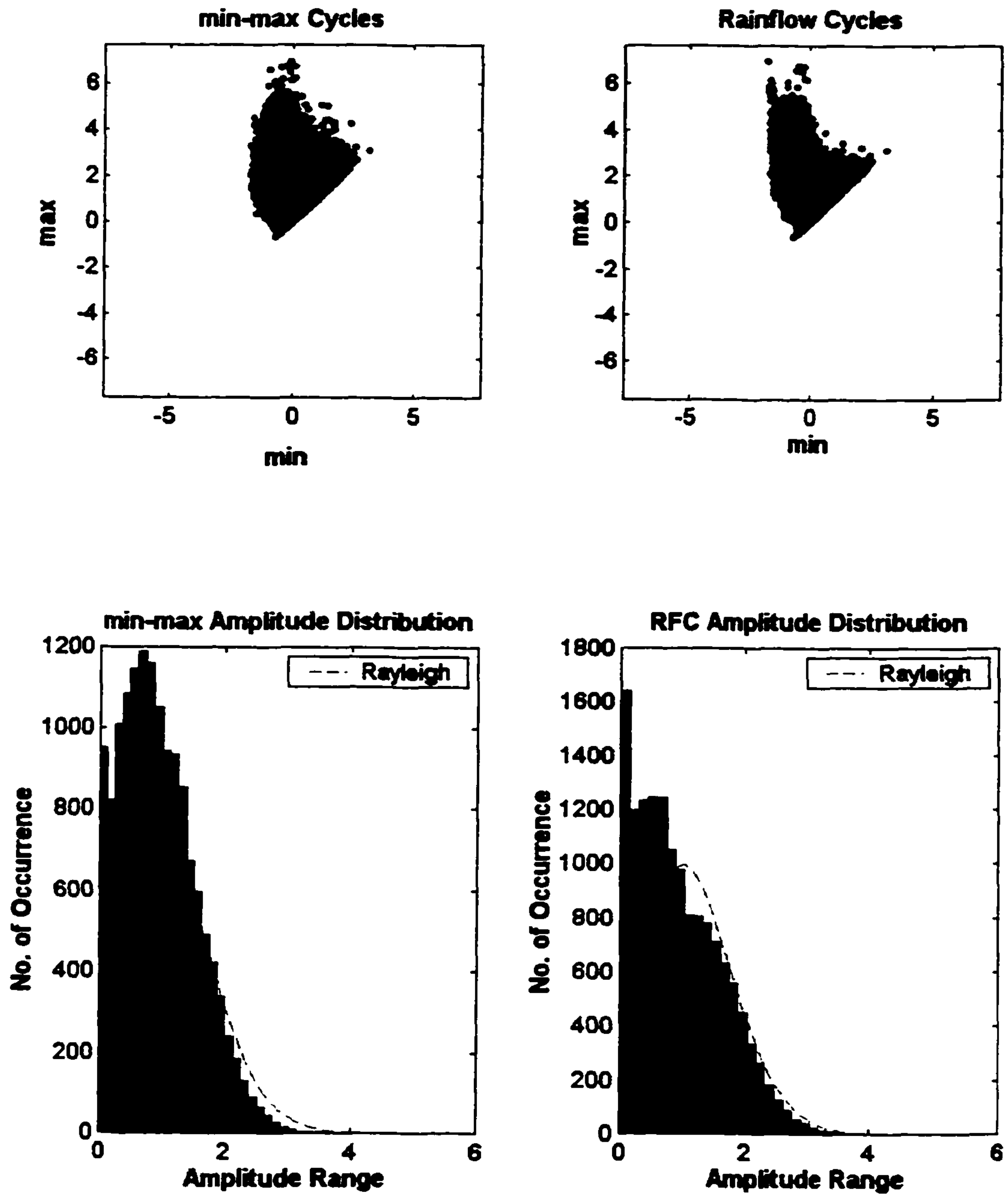

Figure 5.25 Cycles and Amplitude Distribution of Maximum Stress for a 15x12x0.060 in. Simply Supported Isotropic Plate at $EWSPL_1$

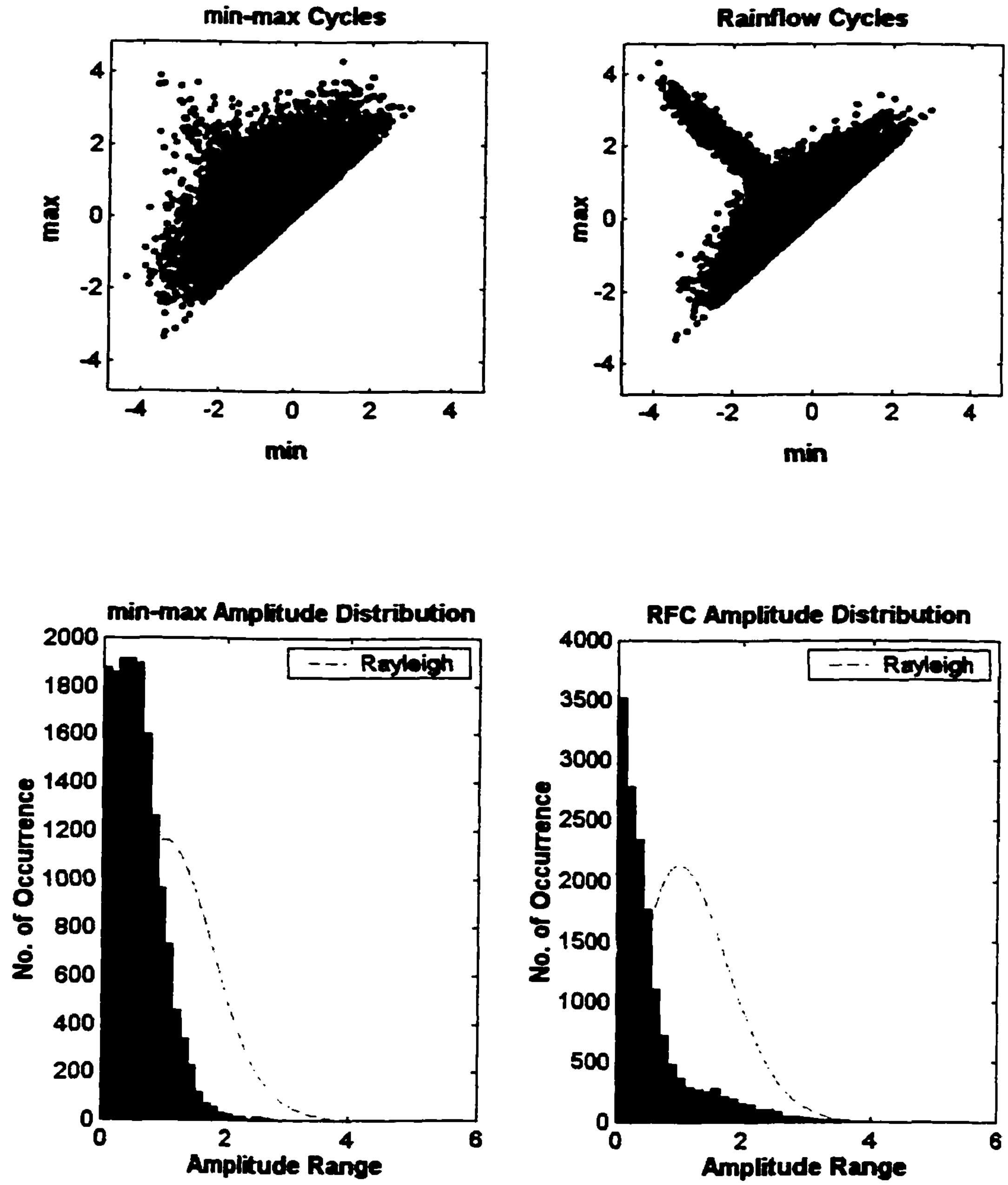

Figure 5.26 Cycles and Amplitude Distribution of Bending Stress for a 15x12x0.060 in. Simply Supported Isotropic Plate at NW_1

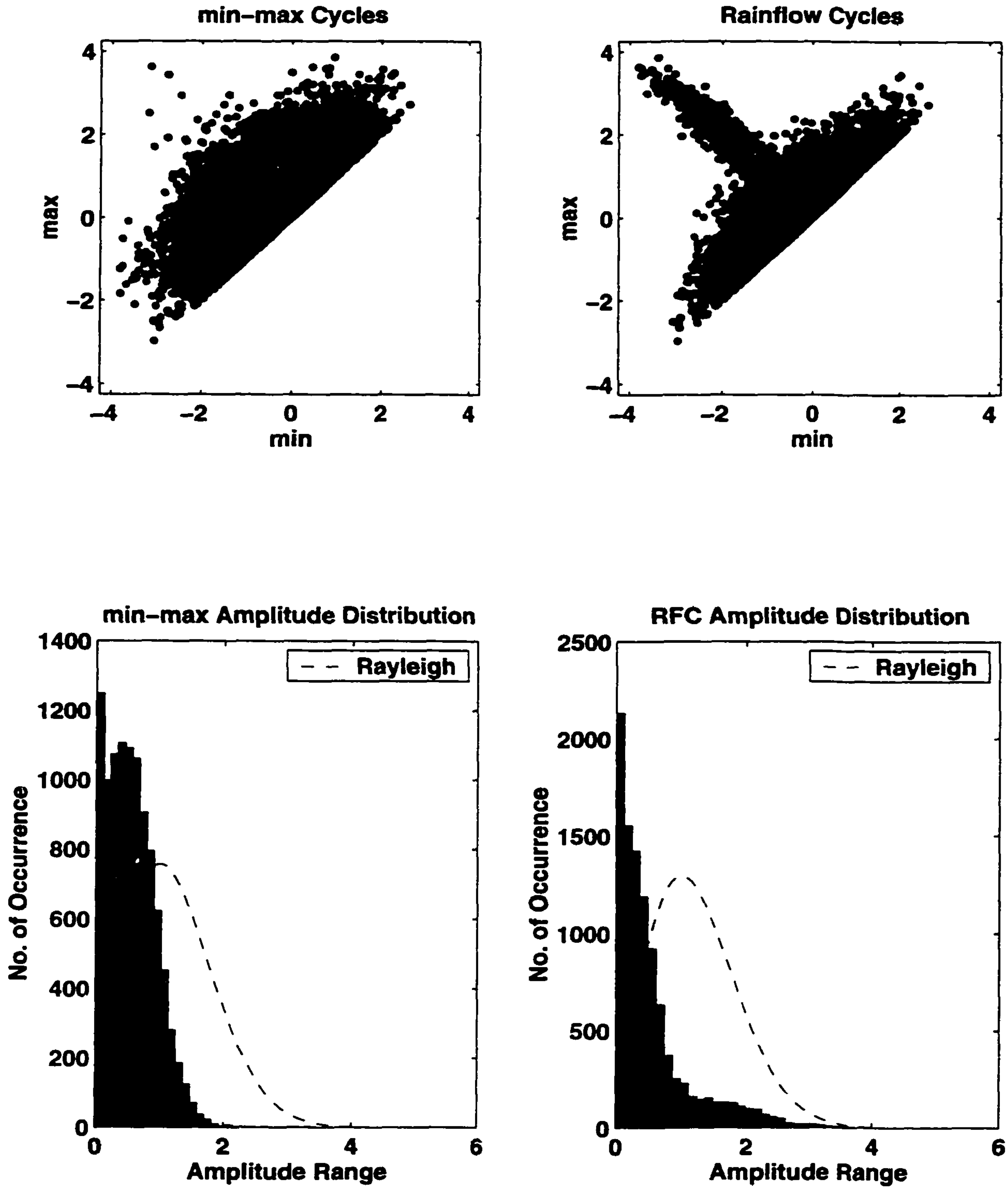

Figure 5.27 Cycles and Amplitude Distribution of Bending Stress for a 15x12x0.060 in. Simply Supported Isotropic Plate at $EWSPL_l$

5.3.2 Peak Distribution Histograms (PDH)

The peak distribution of the maximum stress and pure bending stress are shown in Figure 5.28. Recall that the last subplot in Figure 5.21 represents the peak distribution of the maximum stress for NW_2. As it can be observed from those figures, in all cases the PDH lie between a Gaussian and a Rayleigh distribution shifted by the mean stress value. For the linear stresses (pure bending, $z\{\kappa\}$), the response should be close to Gaussian (Figure 5.9) yielding a close peak Rayleigh distribution. On the other hand, the maximum stresses have a response that is close to Rayleigh (Figure 5.7) due to the membrane stress component that dominates the response at high SPL. For such processes, the PDH seems to deviate from a Rayleigh to a more Gaussian distribution. In addition, the PDH plots also show that a linear analysis gives higher stresses compared to the nonlinear analysis.

These results support the idea that it is not realistic to use a linear approach for the fatigue life estimation of large amplitude random vibrations. The sources of error in Equation 3.20 or 3.33 arise from both the stress amplitude range and the peak distribution. The first overestimates the stress amplitude range by using the linear displacement in the stress calculation. Secondly, the evaluated PDH show that the peaks are concentrated over a small portion of the distribution range. Both of these effects tend to underestimate the fatigue life of structural panels.

In the next section, the difference in fatigue life between the linear and nonlinear stresses will be quantified in the time domain (RFC) and the frequency domain (Dirlik).

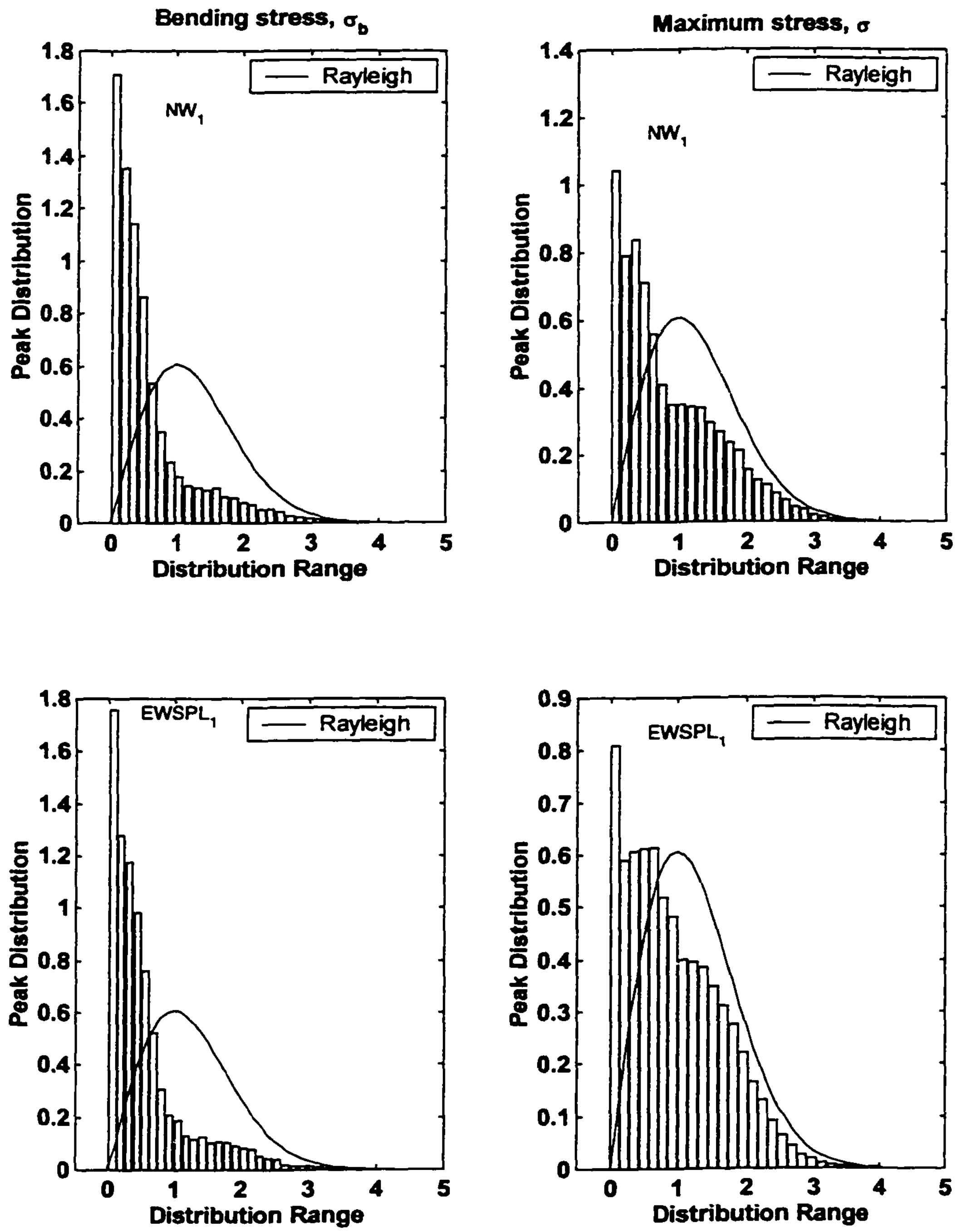

Figure 5.28 Maximum Stress Peak Distribution for a 15x12x0.060 in.

Simply Supported Isotropic Plate at NW_1 and $EWSPL_1$

5.3.3 Fatigue Life Estimates

Results for fatigue life estimates for the two-recorded data sets NW_1, NW_2 and their corresponding EWSPL are given in Table 5.6. Throughout the discussion, it should be noted that the time domain RFC gives the more realistic and accurate solution because it is not limited by the ergodic stationary and Gaussian process assumptions [74].

Table 5.6

Fatigue Life Estimates in Hours for NW and EWSPL

	RFC		Dirlik	
	Linear	**Nonlinear**	**Linear**	**Nonlinear**
NW_1	16.11	322.27	6766	62635
$EWSPL_1$	12.11	406.22	6174	92198
NW_2	10.52	276.90	4992	43112
$EWSPL_2$	9.49	310.58	3814	63785

K=1.52x10^{25} and β=4.8

When the stress response analysis is performed using a linear structural or plate analysis, the fatigue life can be estimated from either the time or frequency domain. In the linear analysis, the PDF of the sequence of TP of the load is always near Gaussian with zero mean and Rayleigh peak distributions. Theses with the stationary assumption satisfy all the conditions of the frequency domain approach. However, Table 5.6 shows that at high SPL (131.47 and 131.91 dB) the fatigue life for the RFC and Dirlik approach differ considerably. Similarly, when the stress response analysis is performed using a nonlinear analysis at high SPL the fatigue life for the RFC and Dirlik approach differ significantly. However, this time the sequence of TP of the stress is non-Gaussian and the peak distribution does not follow a likely Rayleigh distribution. The Dirlik's frequency domain approach idealizes the load as a stationary and Gaussian process, which means that it is completely characterized by its cross-spectral density function and the first moments of the PSD. Nevertheless, for nonlinear responses the load is not Gaussian and the frequency phases are non-Rayleigh dependent on amplitudes; these lead to significant errors that underestimate the accumulated damage as shown in Table 5.6. It can be concluded that the frequency approaches are only applicable to linear or very slightly nonlinear stationary Gaussian processes. The only fatigue method really applicable to nonlinear stationary non-Gaussian processes is the RFC time domain.

These results should catch the attention of the sonic fatigue design community, since it appears that the commonly used linear approach produces to high structural stress penalties compared with the stress when the nonlinear analysis was used. It also appears that the flight non-white stress responses are giving more conservative fatigue estimates (11-20%) than their corresponding $EWSPL_{1,2}$. No further discussions are made on the former point since in order to be conclusive, more refined studies involving extensive experimental work are required.

5.4 Non-White Pressure Fluctuations at ΔT =2.0

This section follows a similar outline as in section 5.2 except that it will not be divided into multiple sub-sections and the data considered for the plots is NW_2. The mode shapes used to resolve the combined thermal and acoustic problem are the linear thermal critical buckling modes given by Equation 4.55. The material properties are the same as given previously with an additional coefficient of thermal expansion α=$12.5\times10^{-6}/^{0}\text{F}$, and a proportional damping ratio of $\xi_r\omega_r=\xi_s\omega_s$ with ξ_1=0.02. In order to observe the three distinct panel motion response characteristics, (i) small deflection random vibration about one of the two thermally buckled equilibrium positions, (ii) snap-through or oil-canning phenomenon between the two thermally buckled positions, and (iii) large amplitude nonlinear random vibration covering both thermally buckled positions at a fixed thermal load, the highest recorded data set (NW_2) is divided by the coefficients 256 and 32. The corresponding new input SPLs are 83.75 and 101.80 dB, respectively. Figures 5.29 and 5.30 show the three distinctive displacement and maximum stress responses, and resultant PDF at $\Delta T/\Delta T_{cr}$=2.0. At 83.75 dB and $\Delta T/\Delta T_{cr}$=2.0, the time histories in Figures 5.29 and 5.30 show clearly the linear random responses about one of the thermally buckled positions. In this case, a static mean response for deflection $(W_c/h)_{\Delta T}= \pm 0.8463$ and stress $(\sigma_y)_{\Delta T}=1655.871$ psi is introduced. The PDF is Gaussian shifted by the mean value response and normalized with the standard deviation (magnitude/std). The response PSD plots in Figures 5.31 and 5.32 show the general increase of the panel vibration frequencies, e.g., from 80.516 Hz (Figures 5.12 or 5.13 at ΔT=0 or Table 5.3) to 113.97 Hz (Figures 5.31 and 5.32 at $\Delta T/\Delta T_{cr}$=2.0) for the fundamental mode (1,1). As the SPL increased to 101.80 dB, the time histories show that snap-through motions and the deflection PDF has two noticeable peaks (non-Gaussian). This occurs because the panel is vibrating about the two equilibrium positions, and confirms clearly the drawback in using the EL approach with the Gaussian response assumption. The EL technique [45-47] can only predict one of the two equilibrium positions. At the high SPL of 131.91 dB, the large deflection RMS W_c/h is 1.9770 that covers both buckled positions. The broadening and shifting of the peaks in the PSD plots in Figures 5.31 and 5.32 further observe nonlinearities.

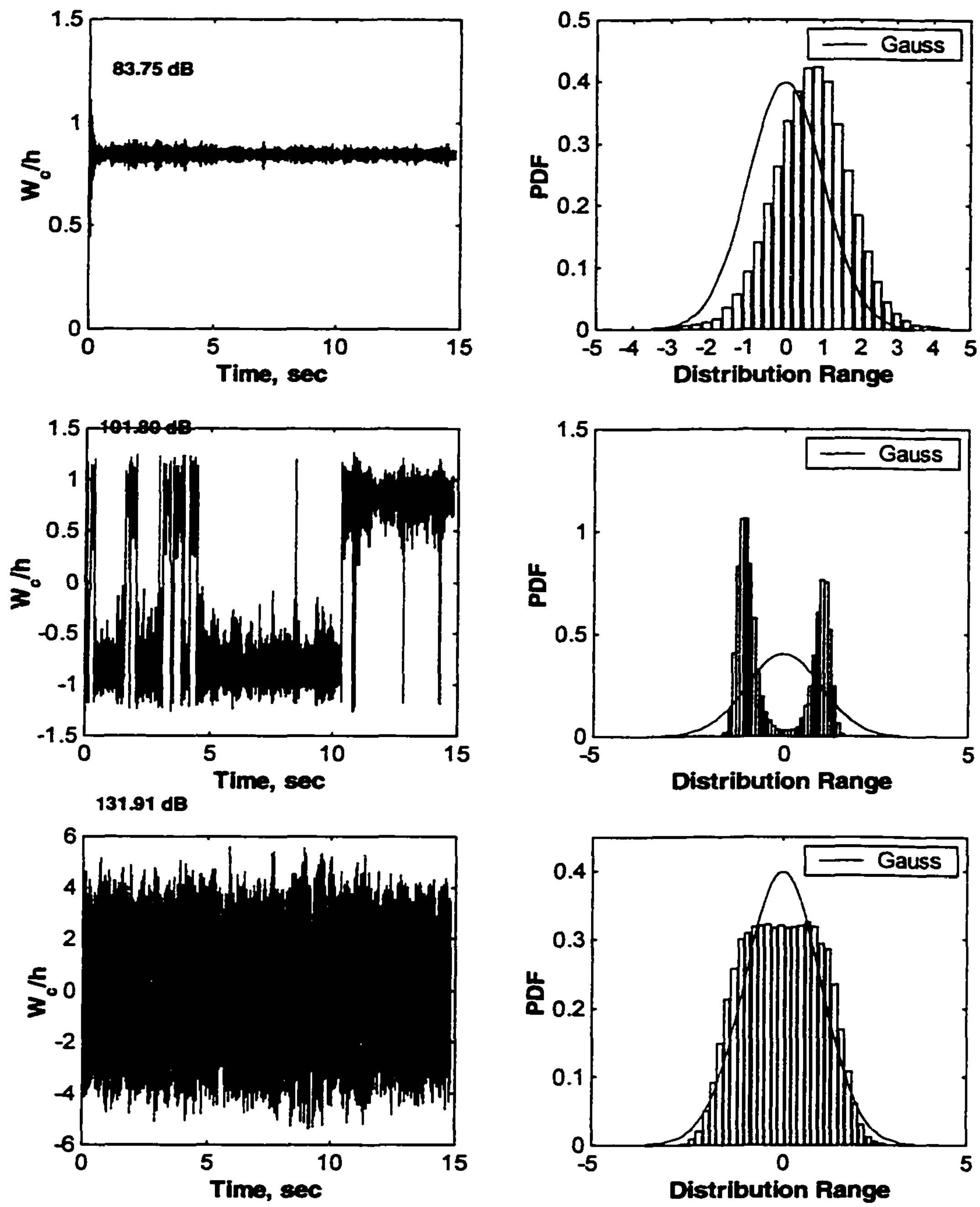

Figure 5.29 Displacement Time Histories and PDF for a 15x12x0.060 in. Simply Supported Isotropic Plate at SPL= 83.75, 101.80, 131.91 dB and $\Delta T/\Delta T_{cr}$=2.0

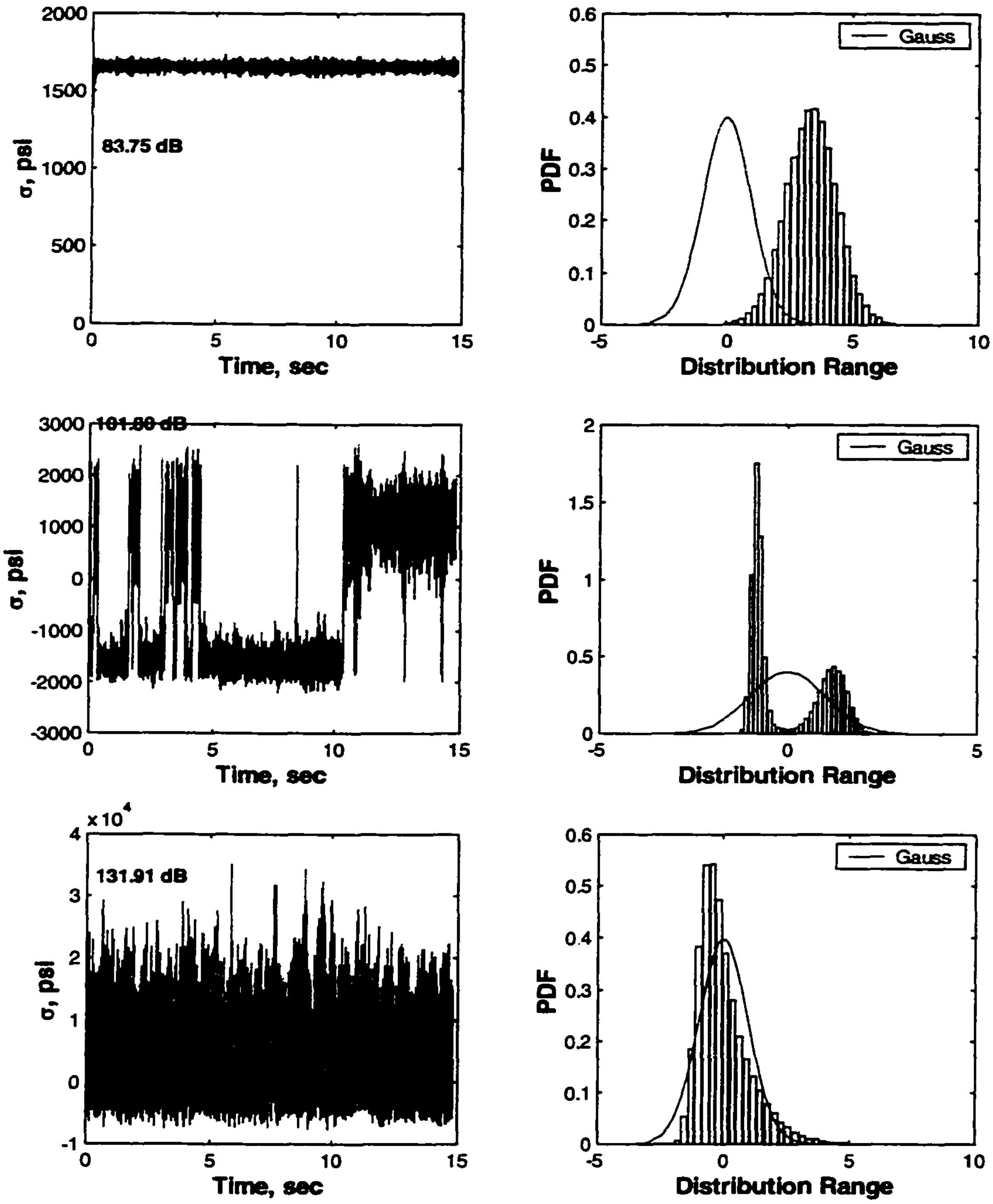

Figure 5.30 Maximum Stress Time Histories and PDF for a 15x12x0.060 in. Simply Supported Isotropic Plate at SPL= 83.75, 101.80, 131.91 dB and $\Delta T/\Delta T_{cr}$=2.0

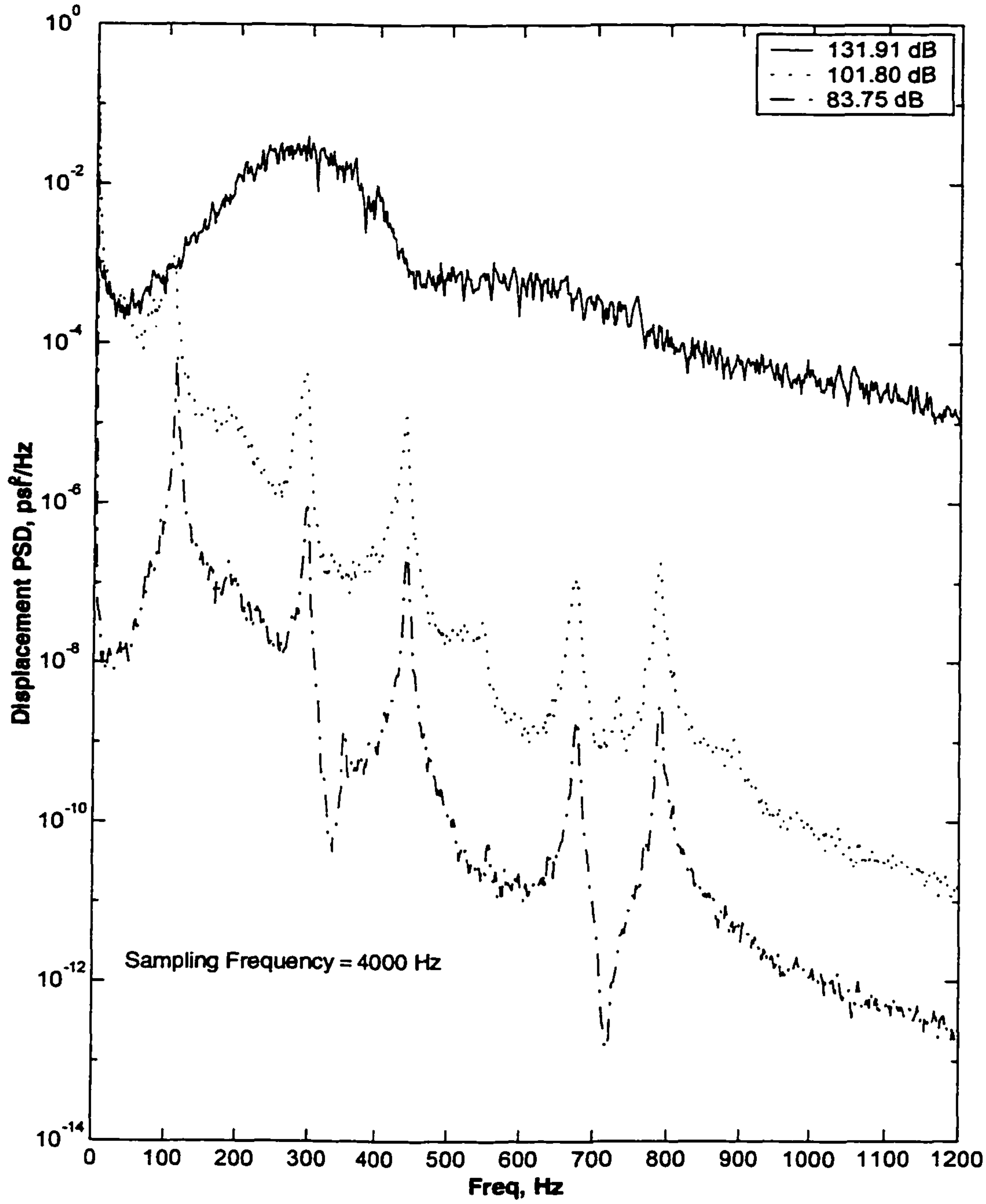

Figure 5.31 Displacement PSD for a 15x12x0.060 in. Simply Supported Isotropic Plate at SPL= 83.75, 101.80, 131.91 dB and $\Delta T/\Delta T_{cr}$=2.0

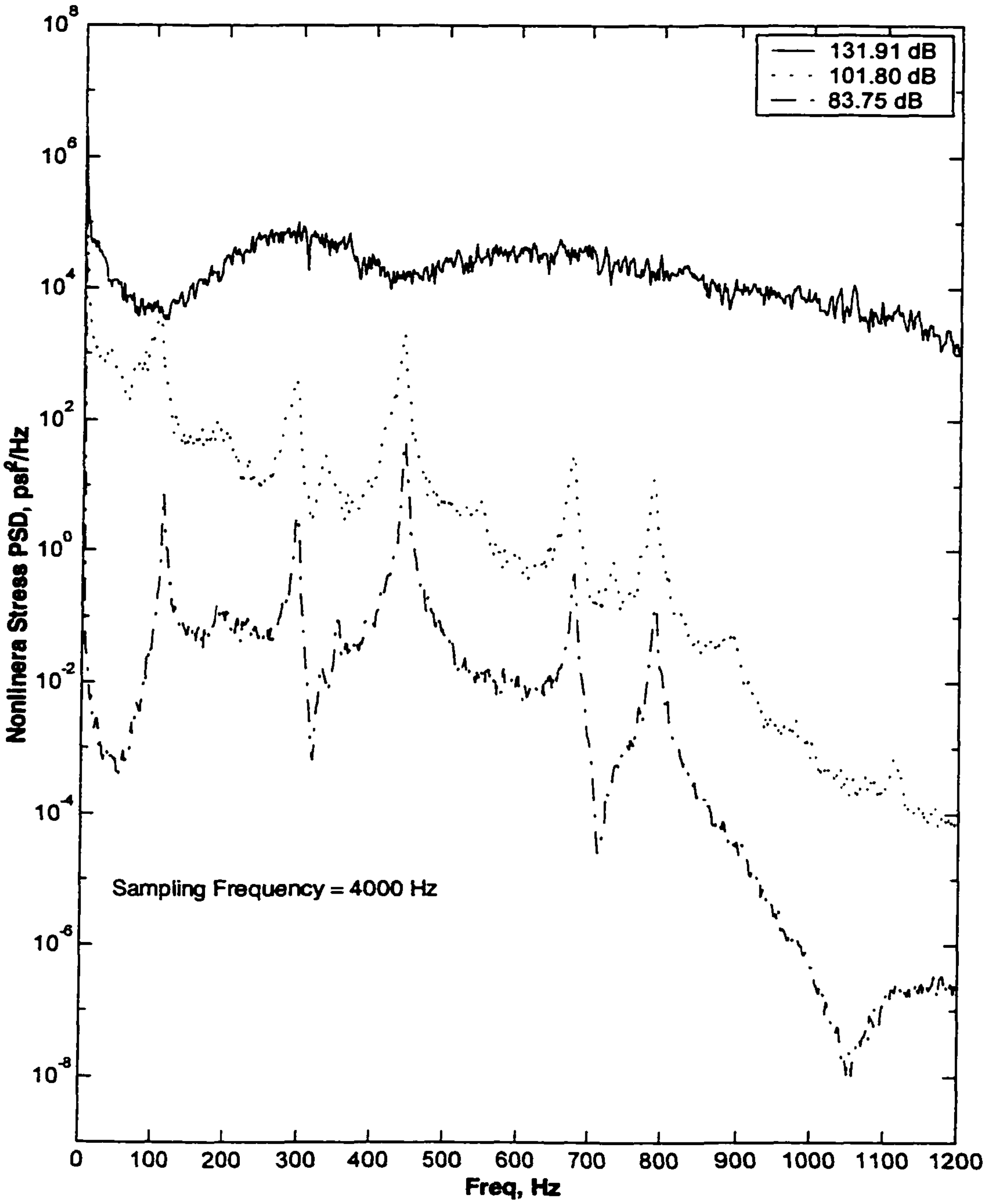

Figure 5.32 Maximum Stress PSD for a 15x12x0.060 in. Simply Supported Isotropic Plate at SPL= 83.75, 101.80, 131.91 dB and $\Delta T/\Delta T_{cr}$=2.0

The RMS, mean values, and higher moments corresponding to input levels of 83.75, 101.80 and 131.9 dB are also shown in Table 5.7. Recall the skewness and kurtosis computed for room temperature ($\Delta T/\Delta T_{cr}$=0.0) from the stress time histories in Table 5.4. At room temperature the kurtosis and skewness increase as the input SPL is increased. At $\Delta T/\Delta T_{cr}$=2.0, the stability problem introduced by the combined loading (thermal and acoustic) does not exhibit a clear pattern for the third and fourth moment behavior. These effects correspond to a loss of symmetry and flattening of the stress PDF that is mainly due to the increase of the in-plane stress.

Table 5.7

Moments of the W_c/h and Maximum Stress of the 15x12x0.06 in.

Isotropic Plate at SPL=83.75, 101.80, 131.91 dB and $\Delta T/\Delta T_{cr}$=2.0

SPL dB & $\Delta T/\Delta T_{cr}$=2.0	RMS	Mean	Variance	Skewness	Kurtosis
		W_c/h			
83.75	0.8174	0.8463	0.1390	0.0959	0.377
101.80	0.7773	-0.1198	0.8922	0.2782	-1.729
131.91	1.9770	-0.0083	1.4309	-0.00390	-0.894
	psi	Stress psi	$psi^2./psi^2.$	$psi^3./psi^3.$	$psi^4./psi^4.$
83.75	1656.048	1655.871	4.922	7.103	291.159
101.80	1432.842	-541.269	36.423	0.518	-1.475
131.91	5729.120	2561.306	71.587	1.246	1.960

At the low 83.75 dB SPL, the thermal load produces thermal post-buckling of the panel and small random vibrations are induced about one of the buckled states. At 131.91 dB, the panel exhibits large amplitude vibrations between the two equilibrium positions. For these two states, the displacement and stress responses are similar (Gaussian), and consequently their ADH, peak distributions, and up-crossing rate plots can be described similarly. However, the snap-through phenomena only appear under certain combined thermal and acoustic loads. This kind of phenomenon has frequently been found in experimental tests [50, 107]. Murphy [51] studied this stability problem and found that snap-through motion could not be excited in all instances. At times the only responses the panel can exhibit are small or large amplitude vibrations about one or the other of the two buckled positions, respectively. Amplitude Distribution Histograms (ADH), peak distributions and up-crossing threshold crossing rates per unit time for snap-through motion are illustrated. Figures 5.33 and 5.34 show the ADH, peak distributions, and threshold crossing rates of the maximum principal stress. It can be observed from these results that the stress response is no longer Gaussian and the peak distribution and up-crossings do not follow a Rayleigh distribution. In addition, the snap-through phenomenon introduces some difficulties for the evaluation of the probability peak distribution by shifting from one equilibrium position to another. This topic will be studied in more detail in the next section. It should be noted that many adverse thermal conditions that could result in degradation of fatigue life have not been considered in the modal finite element model. Temperature dependent material properties such as strength and stiffness that could affect the panel responses considerably and consequently the fatigue life (S-N curves) are not represented in this work.

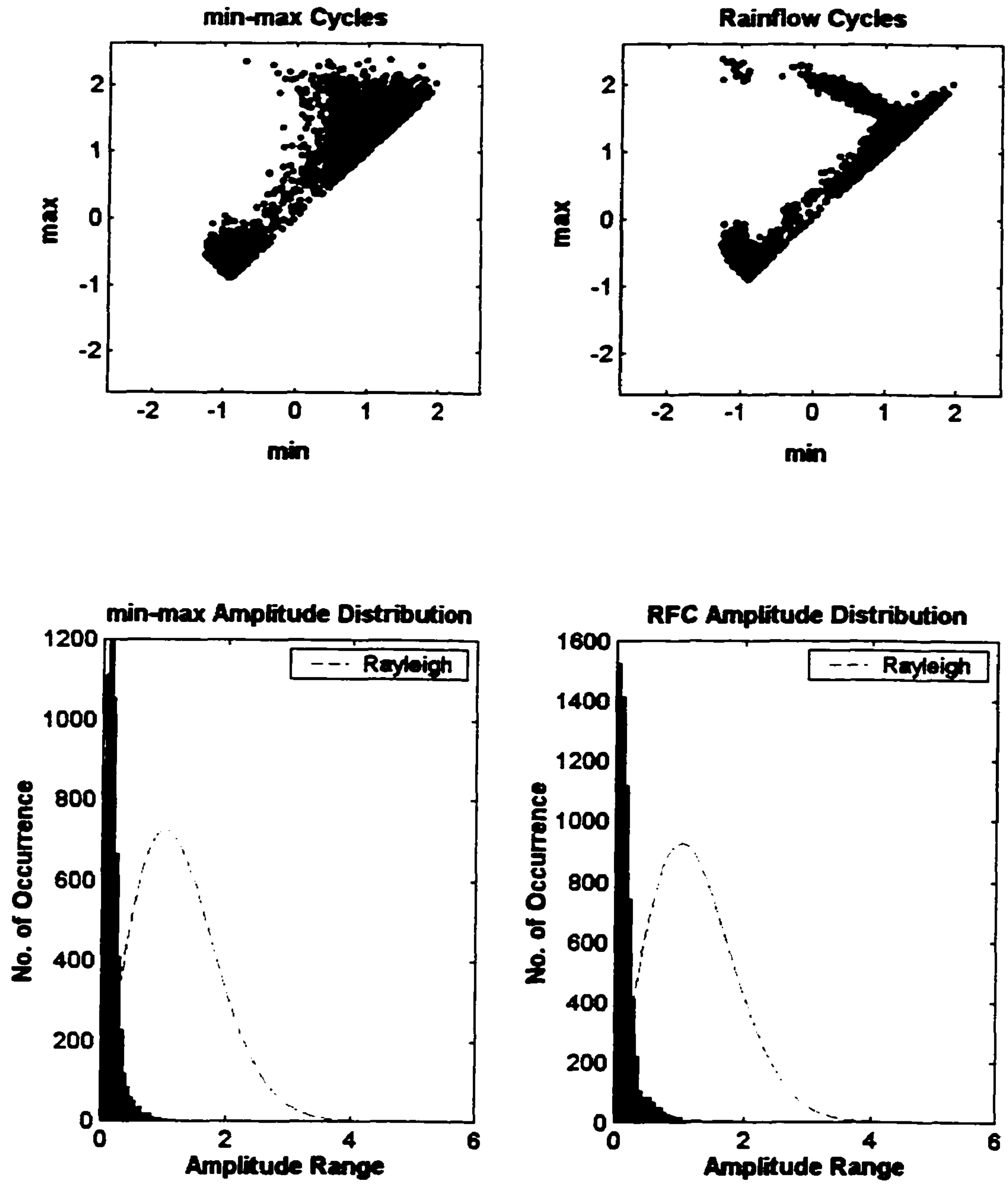

Figure 5.33 Cycles and Amplitude Distribution of Maximum Stress for a 15x12x0.060 in. Simply Supported Isotropic Plate at SPL=101.80 dB and $\Delta T/\Delta T_{cr}$=2.0

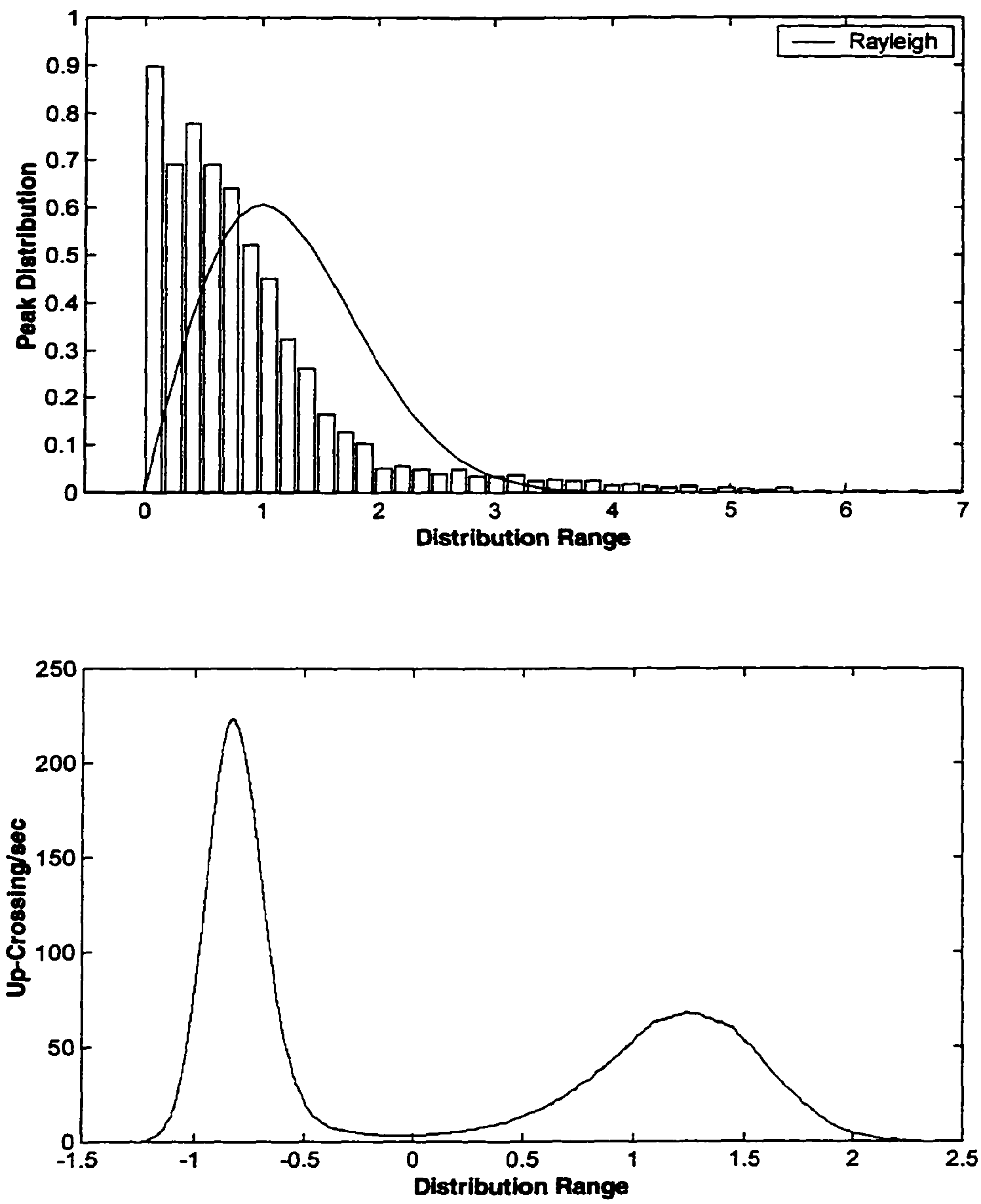

Figure 5.34 Peak Distribution and Up-Crossing for Maximum Stress for a 15x12x0.060 in. Simply Supported Isotropic Plate at SPL=101.80 dB and $\Delta T/\Delta T_{cr}$=2.0

5.5 Snap-Through Fatigue Life Estimate

The theoretical details of the transformation (SMCTP) of the traditional RFC [76] to estimate fatigue life of dynamic responses whose mean level may take two distinct levels are contained in Johannesson [91]. The snap-through fatigue life estimates using the two RFC approaches are shown in Table 5.8. In the SMCTP the abrupt alternation between the two buckled positions are introduced in the RFC (Figure 4.9). The account of those extra peaks yields lower fatigue life estimates. The difference in fatigue life between the EWSPL and NW is due to the number of times the process switches between the two buckled positions. Figure 5.35 shows the maximum principal stress time histories and states of NW_2 and its corresponding $EWSPL_2$. From the states plot, it is observed that the NW_2 response contains a larger number of alternations that yield to a lower fatigue life. It is concluded that the snap-through fatigue life estimate rapidly deteriorates with increasing number of alternations. Consequently, for structural safety purposes, the design of panels at high acoustic load in a thermal environment should avoid to have any snap-through motion. For structural reliability, it is better to have a higher RMS stress value (higher SPL at constant $\Delta T/\Delta T_{cr}$) but a more stable motion. The in-plane stress component has the effect of stabilizing the panel responses at high temperatures.

Table 5.8

Comparison of Fatigue Life Estimates in Hours for Traditional RFC

and SMCTP RFC for Snap-Through of NW and EWSPL

SPL=101.80 dB and $\Delta T/\Delta T_{cr}$=2.0	**RFC (Traditional)**	**RFC (SMCTP)**
$EWSPL_1$	11.985×10^7	9.989×10^7
NW_1	9.531×10^7	7.521×10^7
$EWSPL_2$	6.349×10^7	5.298×10^7
NW_2	4.841×10^7	3.837×10^7

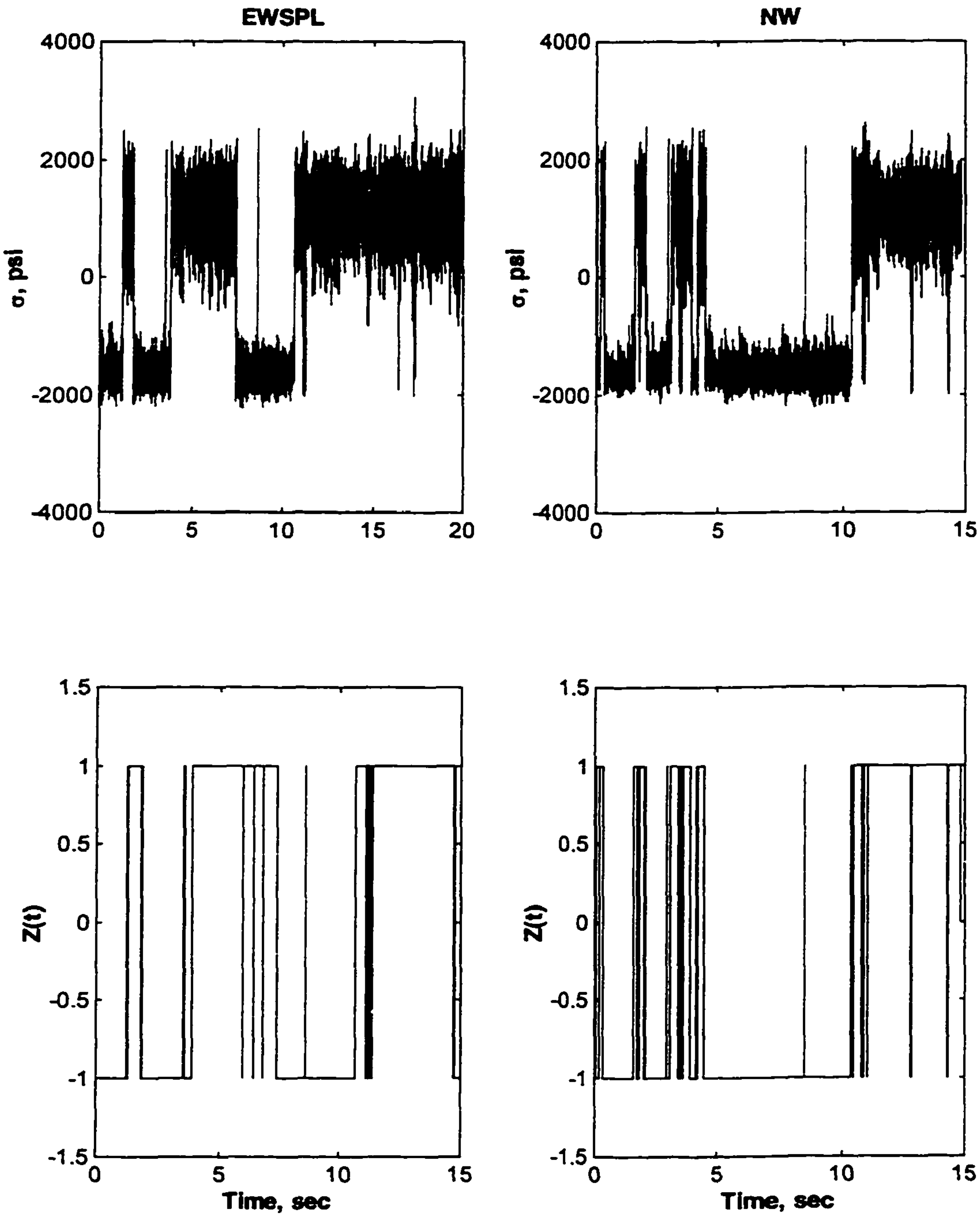

Figure 5.35 Maximum Stress Time Histories and States for a 15x12x0.060 in. Simply Supported Isotropic Plate at SPL=101.80 dB (NW_2) and $\Delta T/\Delta T_{cr}$=2.0

5.6 Non-White (NW) and Equivalent Sound Pressure Levels (EWSPL) at ΔT =2.0

Fatigue life estimates results for the recorded pressure fluctuations NW_1, NW_2, and their corresponding EWSPL at a uniform temperature distribution of $\Delta T/\Delta T_{cr}=2.0$ are given in Table 5.9. These values are compared with the reliability estimates with no temperature effects in the third column of Table 5.6. Results show that the panels under the combined acoustic and thermal load have shorter fatigue life.

Table 5.9

Fatigue Life Estimates in Hours for

NW and EWSPL at $\Delta T/\Delta T_{cr}=2.0$

	RFC
NW_1	252.24
$EWSPL_1$	307.58
NW_2	219.43
$EWSPL_2$	229.77

$K=1.52\text{x}10^{25}$ and $\beta=4.8$

Time histories, up-crossing threshold and peak distribution of maximum stress for NW_2 at $\Delta T/\Delta T_{cr}=0$, 2.0 are shown in Figure 5.36. From these figures it is observed that there is a very slight differences in response characteristics at the high SPL due to the temperature distribution differential. The displacement RMS responses are only increased by 1 % while the RMS stress responses are decreased about 2 % (see Tables 5.4 and 5.7 at SPL=131.91 dB). The small reduction in stresses is easily understood by looking at Equation 4.58. The buckling temperature being low ($\Delta T_{cr}=2.0751^{\circ}$F), the thermal stress component has little contribution on the total stress at high SPL for the studied panel geometry. However, fatigue life estimates at $\Delta T/\Delta T_{cr}=2.0$ are reduced about 20-26 % based on fatigue lives at ambient temperature, i.e., at $\Delta T/\Delta T_{cr}=0$. The drastic difference in fatigue life arises from the RFC method described in Section 3.4. Physically, the thermal post-buckling deflection adds some stiffness to the structure that becomes a little bit *snappy* under random loading. This is not reflected in the RMS or mean values, but it has direct impact on the stress amplitudes. Recall that the fatigue life (Equation 3.20) depends on the stresses amplitudes $s_k^{RFC} = \left(M_k - m_k^{RFC}\right)/2$ and their peak distribution. A slight difference in the cycle counting method could yield very different results because the stress amplitude is raised to the power of the material property β that is equal to 4.8. Mentioning the material properties, the present finite element modal formulation assumes temperature independent properties. If temperature dependent material properties were included in the formulation the difference in fatigue life would probably be more pronounced (different S-N curve). In addition, the stress responses proceeding from NW give 4 and 29 % lower fatigue life estimates than their corresponding EWSPL, respectively. Once again, this last observation is not conclusive because it is only based on the actual non-white pressure fluctuations and given panel geometry. The differences in fatigue estimation may also arise from the duration of the fluctuating pressure time histories that can have considerable influence on the statistical characteristics of the responses, i.e., Gaussian, non-Gaussian, stationary, and non-stationary. Undoubtedly, more work is required to make sure that NW stress responses yield more conservative fatigue life estimates than the stress responses of an equal power EWSPL. Similarly, a more detailed study of sources of nonlinearities of the stress response is required. Finally, the former study could include initial geometric imperfections, temperature dependent material properties, aerodynamic loads, and load sequencing, just to mention a few.

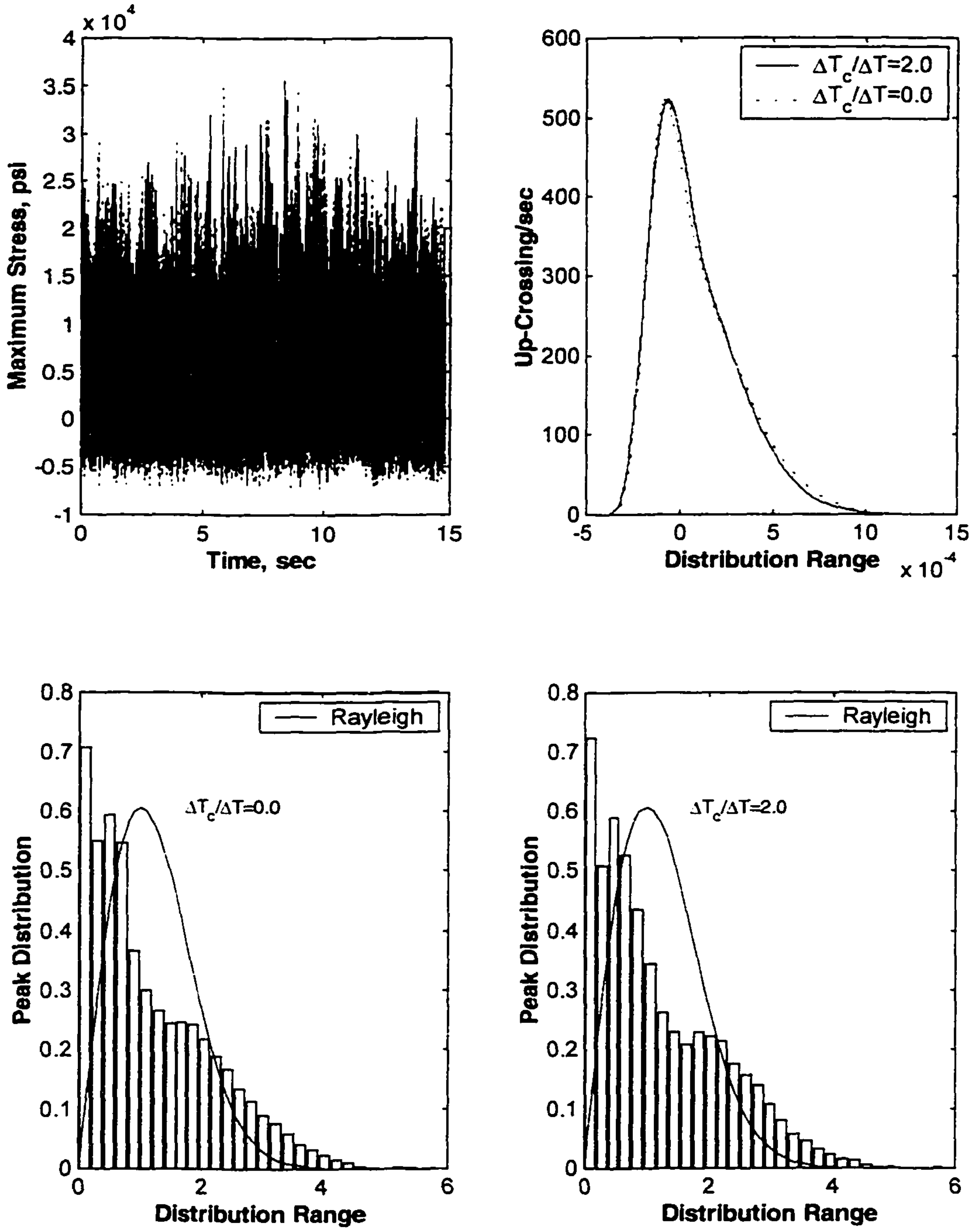

Figure 5.36 Time Histories, Up-Crossing Threshold and Peak Distribution of Maximum Stress for NW_2 at $\Delta T/\Delta T_{cr}$=0.0 and 2.0

5.7 Fatigue Life Design Considerations of Isotropic and Composite Panels

In this last section different parameters influencing the panel fatigue life are studied in detail. First, based on S-N curves of an isotropic and a composite panels the strain/stress region more suitable for fatigue life are studied in detail. Finally, the influence of material property β and structural damping ξ are considered.

5.7.1 S-N Curves for Aluminum and Graphite-Epoxy Panels

For fatigue life design purposes the S-N curves for different material and loading conditions can be used as a first guideline. Depending on the estimated RMS stress/strain value and the desired number of cycles (fatigue life) the most adequate material can be selected. Figure 5.37 shows the S-N curves for Aluminum and Graphite-Epoxy panels. Material properties of Aluminum and Graphite-Epoxy are given in Sections 5.2 and 5.1.1, respectively. From Figure 5.37 it appears that for high RMS strain values the Aluminum has a longer fatigue life than Graphite-Epoxy. However, for low-medium strain values the Graphite-Epoxy demonstrated longer reliability than Aluminum. As a numerical example, an Aluminum plate and a special orthotropic $[0/90/0]_s$ Graphite-Epoxy plate of dimension 15 by 12 by 0.060 inches with identical structural damping (ξ_l=2%) subjected to (NW_2) are studied. The numerical example shows that for the given load condition a Graphite-Epoxy panel yields a longer fatigue life than Aluminum. In reality, the advantage of the composite panel is even greater since the matrix (Epoxy) has a higher structural damping ratio than Aluminum. Section 5.7.3 shows that by increasing the damping ratio, the stress response characteristics are changed and fatigue life is increased considerably. Icons on the Figure 5.37 mark the fatigue life for each of the two panels.

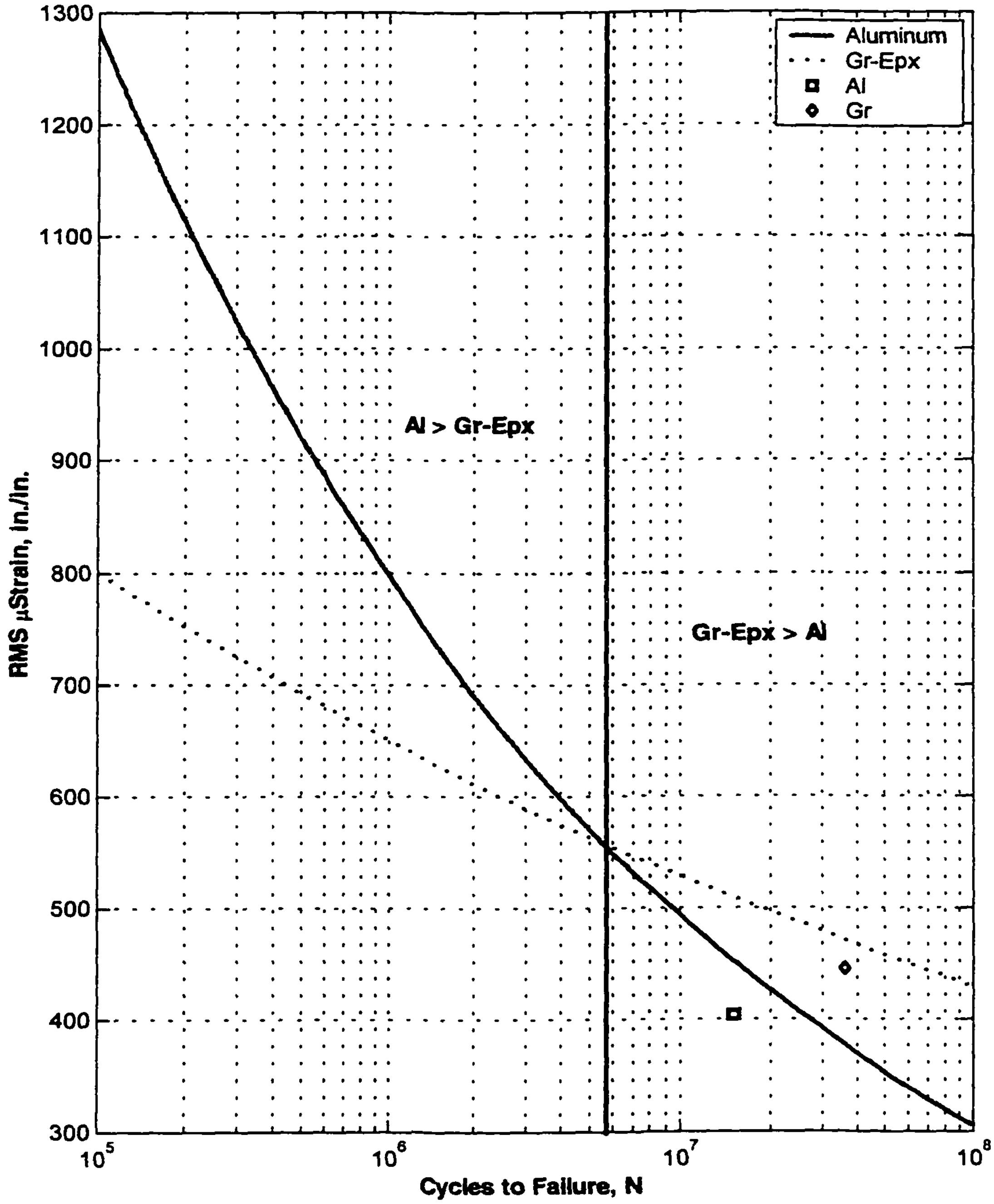

Figure 5.37 S-N Curves for Aluminum (Al) and Graphite-Epoxy (Gr-Epx)

5.7.2 Influence of Material Property β on Fatigue Life

Next, the influence of the material property, β, obtained by linear regression of a given S-N curve is analyzed. By analyzing the behavior of β, the influence of the second independent material property, K, is studied simultaneously. The two material properties are related by Equation 3.18 as $K = N s_k^{\beta}$. The damage intensity as a function of the first material property β is shown in Figure 5.38 for the Aluminum. The plot shows the increase in damage with increasing β. A similar conclusion could have been inferred from Equations 3.20 or 3.33 where the total damage is a function of the stress amplitudes raised to the power β.

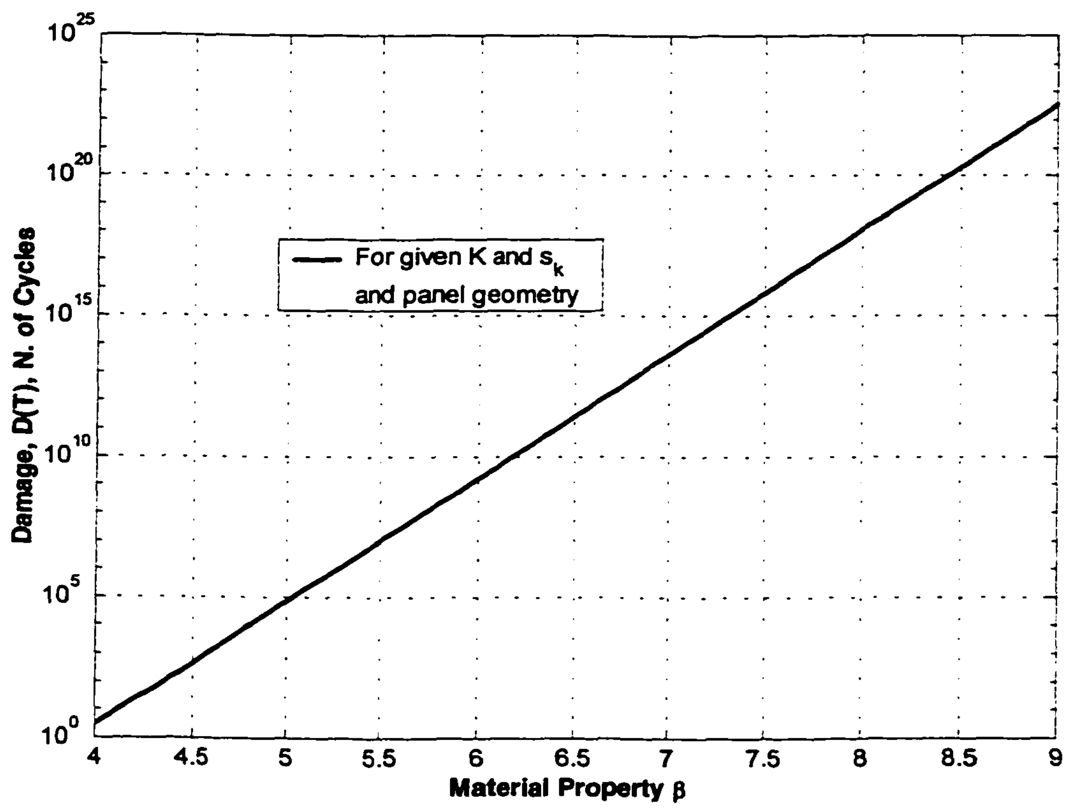

Figure 5.38 Damage Intensity as Function of Material Property β

5.8 Nonrectangular Composite Panel with Mixed Boundary Conditions

Finally, in order to show the versatility of the finite element modal formulation a $[0/90/0]_s$ Graphite-Epoxy panel with complex platform and boundary conditions is studied in detail for $\Delta T/\Delta T_{cr}$=0.0 and 2.0. The panel geometry and boundary conditions are shown in Figure 5.39. The 14 by 10 by 0.060 in. L-shaped plate is modeled with a 14 by 10 mesh or 84 BFS elements in a full plate. The Graphite-Epoxy properties are given in Section 5.1.1 with coefficients of thermal expansion α_1=-0.04x10^{-6}/°F, α_2=16.7x10^{-6}/°F and proportional damping ratio of $\xi_r\omega_r=\xi_s\omega_s$ with ξ_l=0.02. All modes within the cut-off frequency range (1024 Hz) are included for maximum displacement and strain response calculations.

5.8.1 Maximum Deflection and Stress Responses

The elements where maximum deflection and maximum strain occurred are searched and located at each integration time step. During the entire integration process, the node or location of the maximum deflection remains unchanged. However, the node for the maximum strain oscillates among the four nodes of the BFS element [84] of maximum strain. The element of maximum strain is obtained by searching the maximum strain component, x, y, or xy at each element node. The element of maximum strain being located, the maximum principal strain is first calculated at Barlow's points then extrapolated at the desired node point as described in Section 4.6. In Figure 5.39 the element of maximum displacement is indicated by the letter "A," while the letter "B" indicates the element for maximum strain.

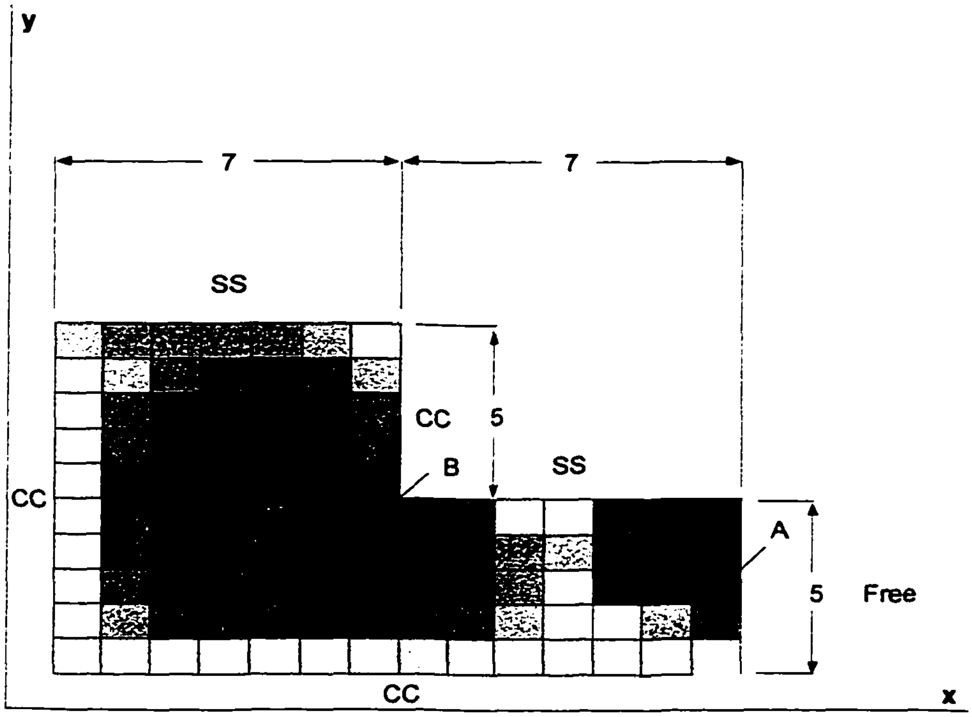

Figure 5.39 Nonrectangular Panel with Mixed Boundary Conditions

5.8.2 Nonrectangular Composite Panel Under Non-White (NW) Pressure Fluctuations at ΔT=0.0

Time histories and PDF for maximum deflection, W_m/h, and maximum strain, ε, are shown in Figures 5.40. Figure 5.41 illustrates ADH and peak probability distribution of maximum strain. From the deflection/strain time histories, Figure 5.40, it is observed that the panel exhibits linear vibrations. The responses PDF are close to Gaussian distribution as shown in Figure 5.40. Rainflow ADH and probability peak distribution in Figure 5.41 revealed that the response peaks slightly deviates from a Rayleigh distribution. The deviation from Rayleigh for the linear vibration was explained in detail in Section 5.2.4.

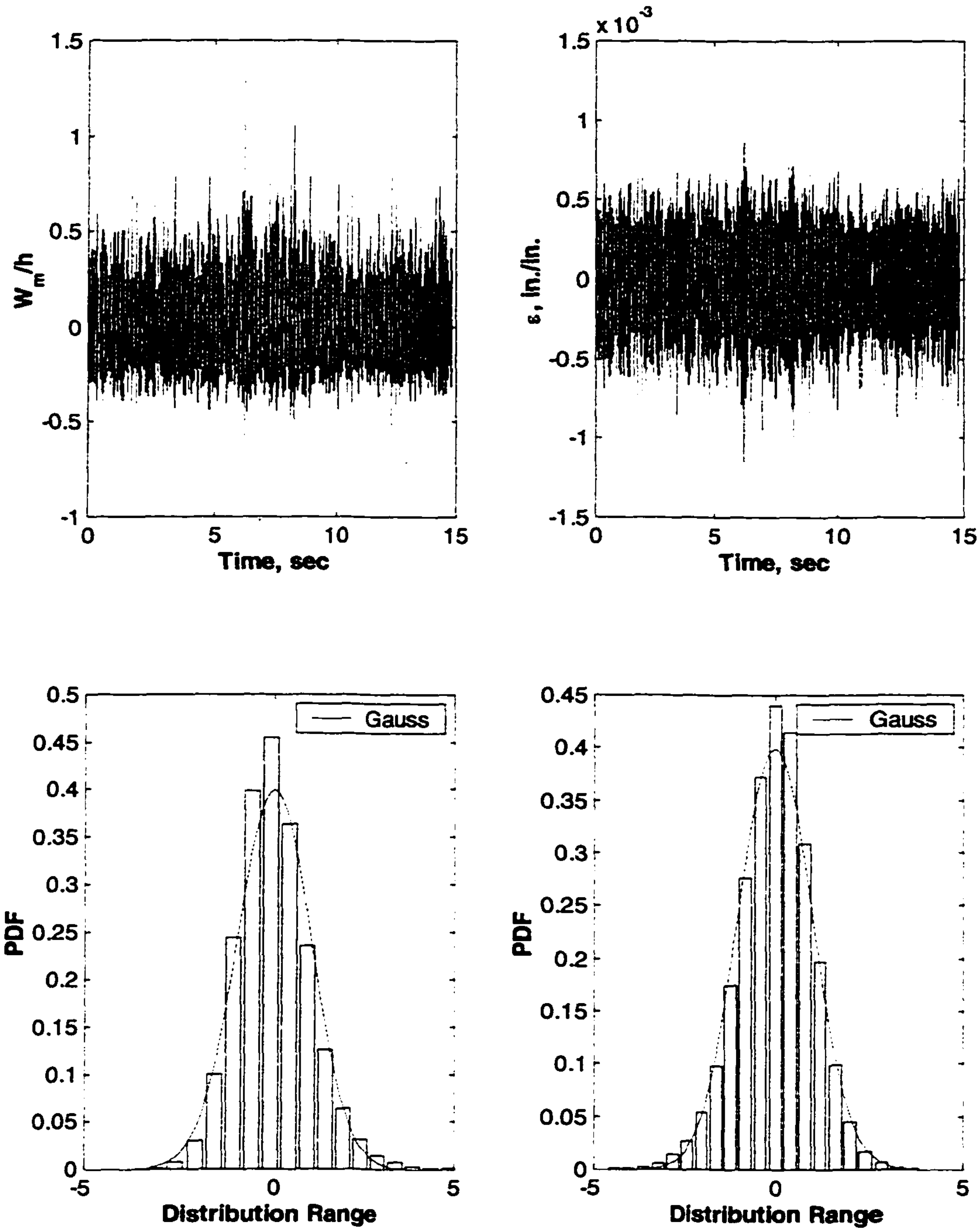

Figure 5.40 Displacement and Maximum Strain Time Histories and PDF for a 14x10x0.060 in. $[0/90/0]_s$ L-Shaped Panel at SPL=131.91 dB and $\Delta T/\Delta T_{cr}$=0.0

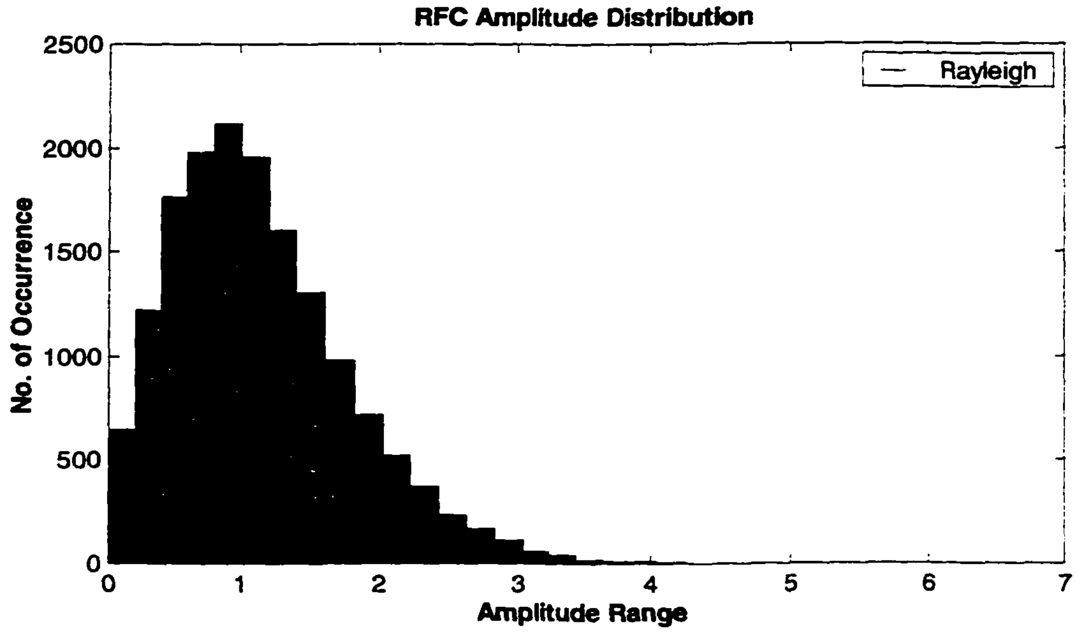

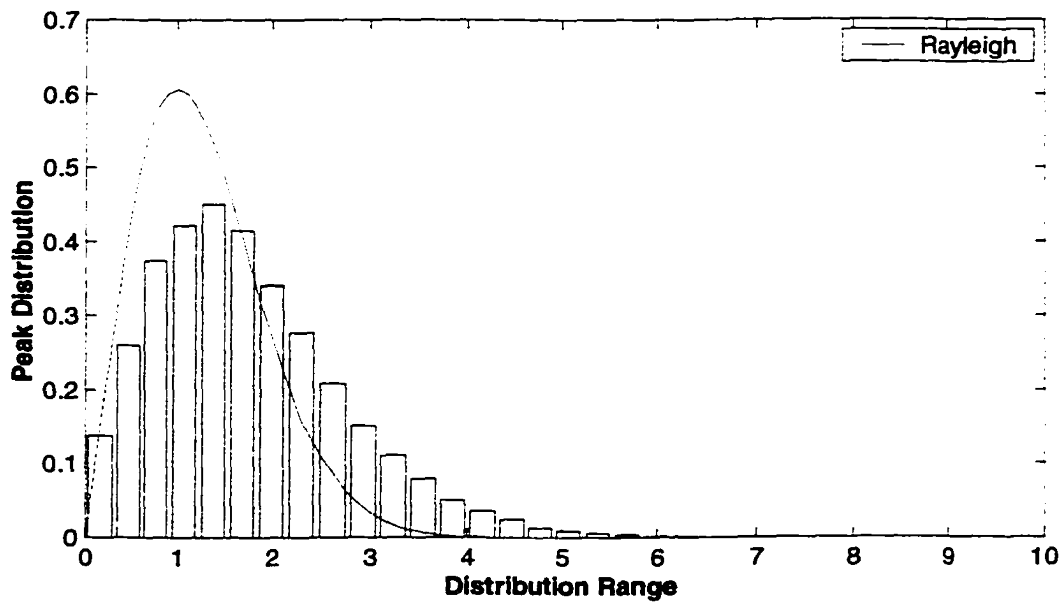

Figure 5.41 ADH and Peak Distribution of Maximum Strain for a 14x10x0.060 in.

$[0/90/0]_s$ L-Shaped Panel at SPL=131.91 dB and $\Delta T/\Delta T_{cr}$=0.0

5.8.3 Nonrectangular Composite Panel Under Non-White (NW) Pressure Fluctuations at $\Delta T/\Delta T_{cr}$=2.0

Figure 5.42 shows that the panel exhibits small vibrations about one of the two buckled positions, and the responses PDF are close to Gaussian distribution shifted by the mean value (normalized with the standard deviation). Figure 5.43 reveals that rainflow ADH and probability peak distribution slightly deviate from Rayleigh.

5.8.4 Fatigue Life Estimates for NW_2 and $EWSPL_2$ at $\Delta T/\Delta T_{cr}$=0.0 and 2.0

Fatigue life estimates for the recorded pressure fluctuations NW_2 and its corresponding EWSPL at uniform temperature distributions of $\Delta T/\Delta T_{cr}$=0.0 and 2.0 are given in Table 5.10. Results show that the panel under recorded pressure fluctuations, NW_2, yields to slightly shorter fatigue life than its EWSPL at $\Delta T/\Delta T_{cr}$=0.0 and 2.0. An interesting result is that at the same acoustic loading fatigue life at ΔT=0 is a lower than at $\Delta T/\Delta T_{cr}$=2.0. This result is not physically correct but can be explained as follows. For this composite panel the buckling temperature is high (ΔT_{cr}= 21.517 ^{0}F) and thermal effects are not negligible. Consequently, S-N curves have to take into consideration of thermal effects for composite materials.

Table 5.10

Fatigue Life Estimates in Hours of L-Shaped Panel for

NW_2 and $EWSPL_2$ at $\Delta T/\Delta T_{cr}$=0.0 and 2.0

	RFC	
	$\Delta T/\Delta T_{cr}$=0.0	$\Delta T/\Delta T_{cr}$=2.0
NW_2	1.101×10^9	1.117×10^9
$EWSPL_2$	1.120×10^9	1.162×10^9

K=1.37x10^{-28} and β=9.97

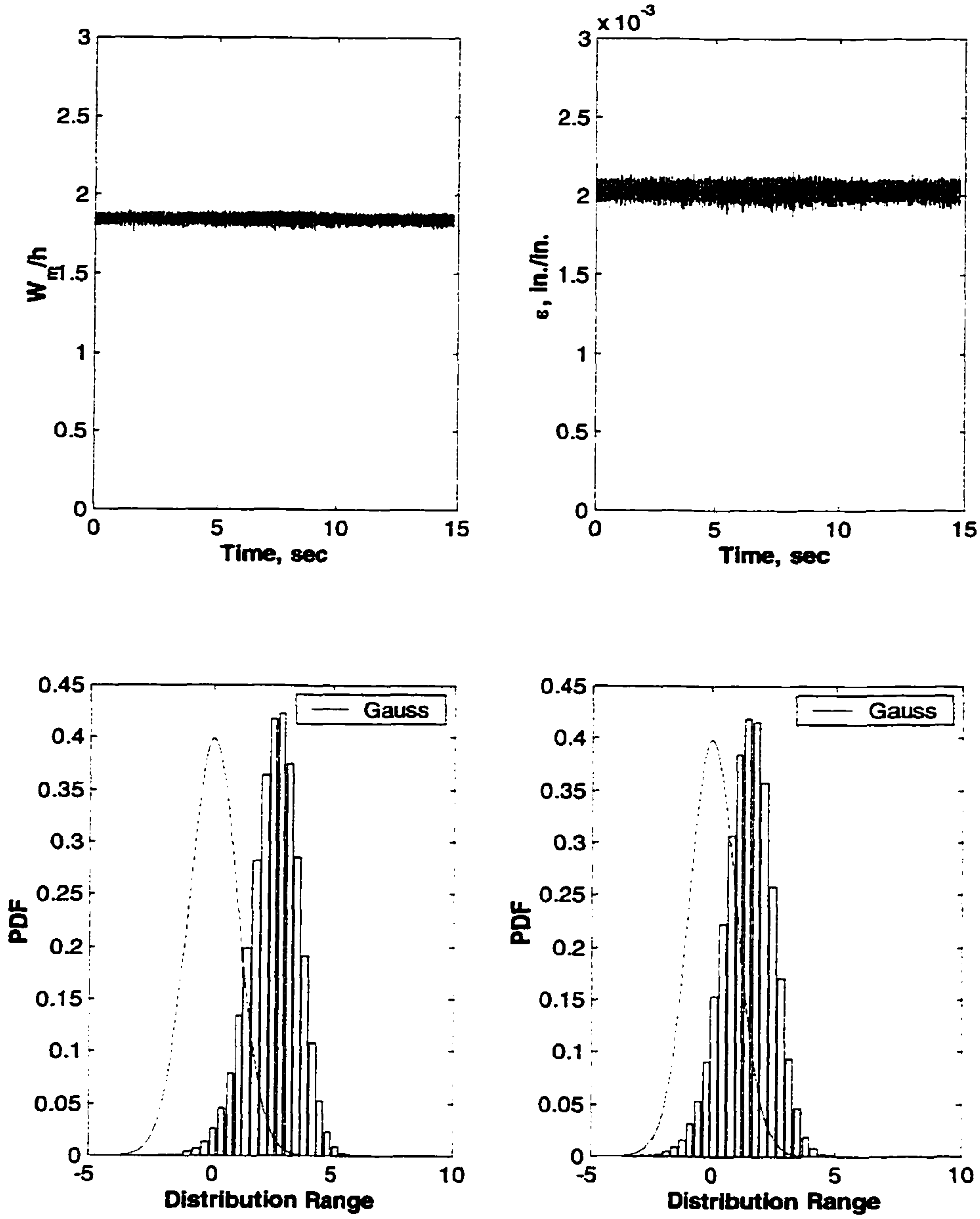

Figure 5.42 Displacement and Maximum Strain Time Histories and PDF for a 14x10x0.060 in. $[0/90/0]_s$ L-Shaped Panel at SPL=131.91 dB and $\Delta T/\Delta T_{cr}$=2.0

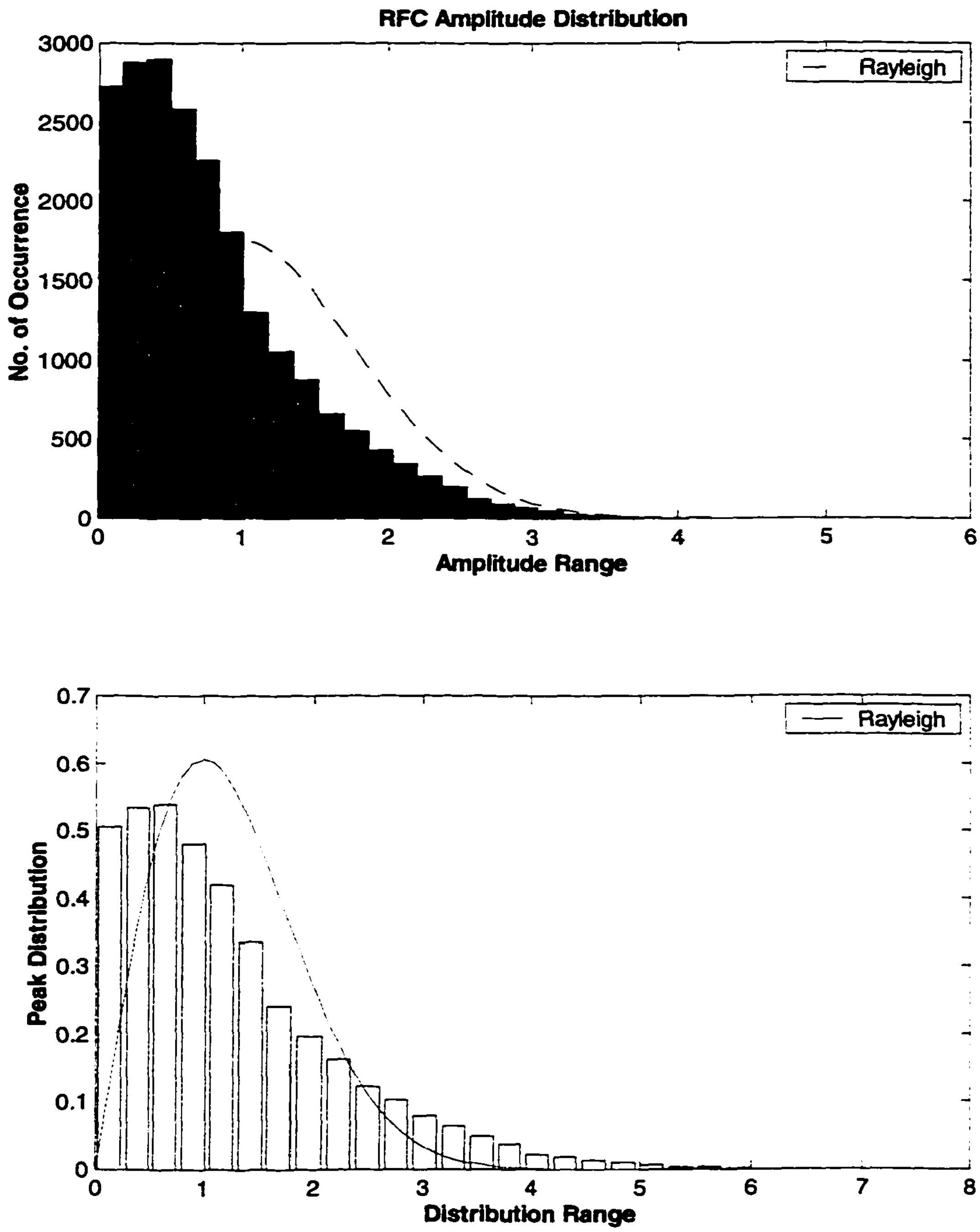

Figure 5.43 ADH and Peak Distribution of Maximum Strain for a 14x10x0.060 in. $[0/90/0]_s$ L-Shaped Panel at SPL=131.91 dB and $\Delta T/\Delta T_{cr}$=2.0

CHAPTER 6

CONCLUSION

It is revealed that the actual flight acoustic pressure fluctuations are of high intensity, nearly Gaussian and non-white. A versatile and efficient finite element time domain modal formulation with the Monte Carlo approach is employed to determine the panel nonlinear response with non-Gaussian probability density functions. The non-Gaussian response characteristics arise from nonlinearities of structural systems and not from the load that is of Gaussian character. Higher order correlations and spectra are utilized to represent these processes in time and frequency domains, respectively. The Palmgren-Miner damage theory and the rainflow counting cycles (RFC) method are used for fatigue estimation of complex random responses. Results showed that the traditional sonic fatigue methods with stationary Gaussian white-noise acoustic pressure are conservative. Limited flight data of non-white PSD give shorter fatigue life estimates by 10-20%.

The finite element time domain modal formulation is presented for the prediction of nonlinear random response of isotropic and orthotropic panels subjected to acoustic pressure fluctuations within or without an elevated thermal environment. The modal formulation has been proven to be computationally efficient because the number of modal equations is small compare with the structural degree of freedom approach; the nonlinear modal stiffness matrices are constant matrices and the time step of integration could be reasonably large. Another advantage of the present finite element model is that it can be easily modified to take into considerations more physical input characteristics.

In this respect, it is becoming increasingly apparent that the development of supersonic/hypersonic vehicles cannot become commercially viable until the fatigue aspects of severe aerodynamic loadings, in addition to combined acoustic and thermal loads, are better understood. The magnitude and character of the stress response depends on the structural geometry and its orientation with respect to the flow. A complete description of the panel motion requires consideration of the influence of thermal effects (convective and aerodynamic), and the variation of the wind velocities from point to point on the structure. In the early stages of takeoff, the aft surface Thermal Protection Systems (TPS) will be in the near field of the noise radiated from the engine exhaust. As the speed increases, the effect of engine exhaust noise (except near the exhaust nozzles) will decrease, and at Mach 1 and higher speeds the acoustic loads are expected to be negligible. However, at supersonic and hypersonic speeds, the fluctuating surface pressures due to convecting turbulent boundary layer excitation will become significant. In addition, local impinging shocks on the structural surface can induce severe dynamics loads. As future work, an extension of the present finite element model including aerodynamics loads (supersonic and hypersonic) and its coupling with thermal loads will help the design and in understanding the behavior of future high-speed flight vehicles.

The majority of the methods used presently for fatigue life estimation consider the loads and responses as stationary and Gaussian. However, the maximum stress response is shown to be non-Gaussian and peaks do not follow a Rayleigh type distribution. It is known that for linear systems subjected to a Gaussian input the type of distribution is always Gaussian, i.e., it does not change in the nonstationary state. This, however, is not true for nonstationary states of nonlinear systems [108]. Aircraft and spacecraft are designed to perform a variety of missions for different flight regimes. Therefore, response calculations and fatigue life estimates of the surface panels should reflect the different mission profiles since drastic changes in acoustic, thermal, and aerodynamic conditions can be produced. This will lead to the consideration of nonstationary random processes in sonic fatigue design. In this respect, the most significant shortcoming of the widely used Palmgren-Miner hypothesis is that it does not account for sequential effects; that is, it assumes that damage caused by a stress cycle is independent of where it occurs in the load time history. The nonstationary fatigue design area is wide open since there is no single established cycle counting method in the literature for responses with nonstationary characteristics. For instance, the widely recognized rainflow cycle counting method considers the stress response as a Markov process that is limited by the stationary assumption. Finally, the RFC has been used for many years, but it cannot be accommodate all types of stationary and non-Gaussian response processes. In this work, the rainflow analysis of switching Markov loads [91] was extended for the first time to estimate the fatigue life of stationary snap-through or oil-canning phenomena in the Aerospace field.

REFERENCES

1. Niu, M. N. Y., *Airframe Structural Design,* Conmilit Press Ltd., 1988, pp. 567-569.

2. Miner, M. A., "Cumulative Damage in Fatigue," Journal of Applied Mechanics, Vol. 12, 1945, pp. 159-164.

3. Lighthill, M.J., "On Sound Generated Aerodynamically I: General Theory," Proceedings of Royal Society, 1952, pp. 564-587.

4. Lighthill, M.J., "On Sound Generated Aerodynamically II: Turbulence as a Source of Sound," Proceedings of Royal Society, 1953, pp. 1-32.

5. ESDU Engineering Data, "Acoustic Fatigue," Vols. 1-6, ESDU International, Ltd. London, sheets, 87002, 870029, 89011, 78004, 80040, 81018, 72016, 74016, 74025 and 85027.

6. Lansing, D.L., Drischler, T.J. and Mixon, J.S., "Dynamic Loading of Aircraft Surfaces Due to Jet Exhaust Impigement," AGARD CP 113, 1972.

7. Scholton, R., " Influence of the Ground on the Near Field Noise Levels of a Jet Supported V/STOL," AGARD CP 113, 1973.

8. Bull, M.K., "Wall-Pressure Fluctuations Associated with Subsonic Turbulent Boundary Layer Flow," Journal of Fluids Mechanics, 28, 1967, pp. 719.

9. Mixson, J.S. and Roussos, L.A., "Acoustic Fatigue: Overview of Activities at NASA Langley," NASA TM 89143, 1987.

10. Coe, C.F. and Chyu, W.J., "Pressure Fluctuation Inputs and Response of Panels Underlying Attached and Separated Supersonic Turbulent Boundary Layers," NASA TM-X 62189, 1972.

11. Coe, C.F. and Chyu, W.J., "Pressure Fluctuation Inputs and Response of Panels Underlying Attached and Separated Supersonic Turbulent Boundary Layers," Section 5, AGARD CP-113, 1973.

12. Bisplinghoff, R.L., "Some Structural and Aeroelastic Considerations of High Speed Flight," 19th Wright brothers lecture, Journal of the Aeronautical Science, Vol. 23, No. 4, 1956, pp. 289-329.

13. Van Driest, E.R., "The Problem of Aerodynamic Heating," Aeronautical Engineering Review, Vol. 15, No. 10, 1956, pp. 26-41.

14. Truitt, R.W., *Fundamentals of Aerodynamic Heating*, Ronald Press, New York, 1960.

15. Hoff, N.J., "The Thermal Barrier Structures," Transactions of American Society of Mechanical Engineers, Vol. 27, No. 5, 1955, pp. 759-763.

16. Heldenfels, R.R., "Frontier of Flight Structural Design," Aeronautics and Astronautics, Proceedings of Durand Centennial Conference, Stanford University, August 1959.

17. Crandall, S. H. and Zhu, W. Q., "Random Vibration: A Survey of Recent Developments," Journal Applied Mechanics, Transactions of the ASME 50th Anniversary, Vol. 50, 1983, pp. 953-962.

18. To, C. W. S., "The Response of Nonlinear Structures to Random Excitation," Shock and Vibration Digest, Vol. 16, April 1984, pp. 13-33.

19. Roberts, J.B., "Techniques for Nonlinear Random Vibration Problems," Shock and Vibration Digest, Vol. 16, September 1984, pp. 3-14.

20. Spanos, P. D. and Lutes, L. D., "A Primer of Random Vibration Techniques in Structural Engineering," Shock and Vibration Digest, Vol. 18, April 1986, pp. 3-9.

21. Caughey, T. K., "Derivation and Application of the FPK Equation to Discrete Nonlinear Dynamic Systems to White Random Excitation," Journal Acoustic Society of America, Vol. 35, November 1963, pp. 1683-1692.

22. Roberts, J. B., "Response of Nonlinear Mechanical Systems to Random Excitation, Part I: Markov Methods," Shock and Vibration Digest, Vol. 13, April 1981, pp. 17-28.

23. Caughey, T. K. and Ma, F., " The Exact Steady-State Solution of a Class of Nonlinear Stochastic Systems," International Journal Nonlinear Mechanics, Vol. 17, No. 3, 1982, pp. 137-142.

24. Lyon, R. H., "Response of a Nonlinear String to Random Excitation," Journal Acoustic Society of America, Vol. 32, No. 8, 1960, pp. 953-960.

25. Crandall, S. H., "Perturbation Techniques for Random Vibration of Nonlinear Systems," Journal Acoustic Society of America, Vol. 35, No. 11, 1963, pp. 1700-1705.

26. Iwan, W. D. and Yang, M. I., "Application of Statistical Linearization Techniques to Nonlinear Multi-Degree of Freedom Systems," Journal of Applied Mechanics, Vol. 39, June 1972, pp. 545-550.

27. Booton, R. C., "The Analysis of Nonlinear Control Systems with Random Inputs," Circuit Theory, IRE Transactions, Vol. 1, 1954, pp. 32-34.

28. Caughey, T. K., "Equivalent Linearization Techniques," Journal Acoustic Society of America, Vol. 35, No. 11, 1963, pp. 1706-1711.

29. Atalik, T. S. and Utku, S., "Stochastic Linearization of Multi-Degree-of-Freedom Nonlinear Systems," Earthquake Engineering and Structural Dynamics, Vol. 4, July-August 1976, pp. 411-420.

30. Roberts, J. B. and Spanos, P. D., *Random Vibration of Statistical Linearization*, John Wiley & Sons, NY, 1990.

31. Sakata, M. and Kimura, K., "Calculation of the Non-Stationary Mean Square Response of a Nonlinear System Subjected to Non-White Excitation," Journal of Sound and Vibration, Vol. 73, 1980, pp. 333-343.

32. Shinozuka, M., "Monte Carlo Solution of Structural Dynamics," International Journal of Computers and Structures, Vol. 2., 1972, pp. 855-874.

33. Shinozuka, M. and Wen, Y. K., "Monte Carlo Solution of Nonlinear Vibrations," AIAA Journal, Vol. 10, No. 1, 1972, pp. 37-40.

34. Shinozuka, M. and Jan, D. M., "Digital Simulation of Random Processes and Its Applications," Journal of Sound and Vibration, Vol. 25, 1972, pp. 111-128.

35. Rudder, F. F. and Plumblee, H. E., "Sonic Fatigue Design Guide for Military Aircraft," AFFDL-TR-74-112, Wright-Patterson AFB, OH, 1975, pp. 489.

36. Holehouse, I., "Sonic Fatigue Design Guide Techniques for Advanced Composite Structures," Ph. D. Dissertation, University of Southampton, UK, 1984.

37. Vaicaitis, R., "Recent Advances of Time Domain Approach for Nonlinear Response and Sonic Fatigue," Proceedings 4th International Conference on Structural Dynamics, ISVR, University of Southampton, UK, July 1991, pp. 84-103.

38. Vaicaitis, R., "Time Domain Approach for Nonlinear Response and Sonic Fatigue of NASP Thermal Protection Systems," Proceedings of 32nd Structures, Structural Dynamics, and Materials Conference, Baltimore, MD, April 1991, pp. 2685-2708.

39. Arnold, R. R. and Vaicaitis, R., "Nonlinear Response and Fatigue of Surface Panels by the Time Domain Monte Carlo Approach," WRDC-TR-90-3081, Wright-Patterson AFB, OH, 1990.

40. Vaicaitis, R. and Kavallieratos, P. A., "Nonlinear Response of Composite Panels to Random Excitation," Proceedings 34th Structures Structural Dynamics, and Materials Conference, La Jolla, CA, April 1993, pp. 1041-1049.

41. Lee, J., "Large-Amplitude Plate Vibration in an Elevated Thermal Environment," Applied Mechanics Reviews, Vol. 46, Part 2, 1993, pp. S242-254.

42. Lee, J., "Random Vibration of Thermally Buckled Plates: I. Zero Temperature Gradient Across the Plate Thickness," AIAA Progress Series in Aeronautics and Astronautics, E.A. Thorton. Editor, 1995.

43. Lee, J., "Improving the Equivalent Linearization Technique for Stochastic Duffing Oscillators," Journal of Sound and Vibration, Vol. 186(5), 1995, pp. 846-855.

44. Crandall, S. H., "Non-Gaussian Closure for Random Vibration of Non-Linear Oscillators," International Journal Non-Linear Mechanics, Vol. 15, 1980, pp. 303-313.

45. Locke, J. E, and Mei, C., "A Finite Element Formulation for the Large Deflection Random Response of Thermally Buckled Beams," AIAA Journal, Vol. 28, 1990, pp. 2125-2131.

46. Locke, J. E., "A Finite Element Formulation for the Large Deflection Random Response of Thermally Buckled Structures," Ph.D. Dissertation, Old Dominion University, Norfolk, VA, 1988.

47. Mei, C. and Chen, R. R., "Finite Element Nonlinear Random Response of Composite Panels of Arbitrary Shape to Acoustic and Thermal Loads Applied Simultaneously," WL-TR-97-3085, Wright-Patterson AFB, OH, 1997.

48. Shi, Y. and Mei, C., "Coexisting Thermal Postbuckling of Composite Plates with Initial Imperfections Using Finite Element Modal Methods," Proceedings 37th Structures, Structural Dynamics, and Materials Conference, Salt Lake City, UT, April 1996, pp. 1355-1362.

49. Ng, C. F. and Clevenson. S. A., "High-Intensity Acoustic Tests of a Thermally Stresses Plate," Journal of Aircraft, Vol. 28, No. 4, 1991, pp. 275-281.

50. Istenes, R. R., Rizzi, S. A. and Wolfe, H. F., "Experimental Nonlinear Random Vibration Results of Thermally Buckled Composite Panels," Proceedings of 36th Structures, Structural Dynamics, and Materials Conference, New Orleans, LA, April 1995, pp. 1559-1568.

51. Murphy, K. D., "Theoretical and Experimental Studies in Nonlinear Dynamics and Stability of Elastic Structures," Ph.D. Dissertation, Duke University, Durham, NC, 1994.

52. Murphy, K. D., Virgin, L. N. and Rizzi, S.A., "Experimental Snap-Through Boundaries for Acoustic Excited Thermally Buckled Plates," Experimental Mechanics, Vol. 36, No. 4, 1996, pp. 312-317.

53. Mei, C. and Wolfe, H. F., "On Large Deflection Analysis in Acoustic Fatigue Design," Random Vibration: Status and Recent Development, The S.H. Crandall Festschrift, Elsevier Science, 1986, pp. 279-302.

54. Benaroya, H. and Rebak, M., "Finite Element Methods in Probabilistic Structural Analysis: A Selective Review," Applied Mechanics Reviews, Vol. 41, No. 5, 1988, pp. 201-213.

55. Clarkson, B. L., "Review of Sonic Fatigue Technology," NASA CR-4587, 1994.

56. Wolfe, H. F., Shroger, C.A., Brown, D.L. and Simmons, L.W., "An Experimental Investigation of Nonlinear Behavior of Beams and Plates Excited to High Levels of Dynamic Response," WL-TR-96-3057, Wright-Patterson AFB, OH, 1995.

57. ASCE Committee on Fatigue and Fracture Reliability, series of articles on Fatigue and Fracture Reliability, Journal of the Structural Division, ASCE, 108 (ST1), 1982, pp. 3-88.

58. Madsen, H. O., Krenk, S. and Lind, N. C., *Methods of Structural Safety*, Prentice Hall, Englewood Cliffs, New Jersey, 1986.

59. Palmgren, A., "Die Lebensdaner von Kugellageru," Zeitshrift des Vereins Deutsher Ingenieure, Vol. 68, 1924, pp. 339-341.

60. Marco, S. M. and Starkey, W. L., "A Concept of Fatigue Damage," ASME Transactions, Vol. 76, 1954, pp. 627.

61. Shanley, F. R., "A Theory of Fatigue Based on Unbonding during Reversed Slip," The Rand Corporation, 1952, pp. 350.

62. Corten, H.T. and Dolan, T.J., "Cumulative Fatigue Damage," in Proceedings of the International Conference on Fatigue of Metals, ASME and IME, Institution of Mechanical Engineers, London, U.K., 1956, pp. 235-246.

63. Henry, D. L., "Theory of Fatigue Damage Accumulation in Steel," ASME Transactions, Vol. 77, 1955, pp. 913.

64. Bolotin, V.V., *Prediction of Service Life Machines and Structures*, ASME Press, New York, 1989.

65. Kachanov, L. M., *Introduction to Continuum Damage Mechanics*, Martinus-Nijhoff Publishers, Dordrecht, Netherlands, 1986.

66. Vakulenko, A. A. and Kachanov, L. M., "Continuum Theory of Cracked Media," Mekhanika Tverdogo Tela, Vol. 4, 1971, pp. 159-166.

67. Murakami, S., and Ohno, N., "A Continuum Theory of Creep and Creep Damage," in Creep in Structures, Springer-Verlag, Berlin, 1981, pp. 422-444.

68. Sidoroff, F., "Description of Anisotropic Damage Application to Elasticity," in Physical Non-Linearities in Structural Analysis, Proceedings of the IUTAM Symposium, Senlis, France, 1980, pp. 237-234.

69. Sobczyk, K. and Spencer, B. F. Jr., *Random Fatigue: From Data to Theory*, Academic Press, 1992, pp. 63.

70. Hammond, J. K. and Moss, J., "Time-Frequency Spectra for Nonstationary Signals," Proceedings of Workshop on Nonstationary Stochastic Processes and Their Applications, Ed. by A.G. Miamee, Hampton, VA, August 1991, pp. 1-21.

71. Merritt, R. G., "Laboratory Simulation of Nonstationary Environments," Proceedings of Workshop on Nonstationary Stochastic Processes and Their Applications, Ed. by A.G. Miamee, Hampton, VA, August 1991, pp. 22-37.

72. Piersol, A. G., "Optimum Analysis Procedures for Nonstationary Vibroacoustic Data Measured During Space Vehicle Launches," Proceedings of Workshop on Nonstationary Stochastic Processes and Their Applications, Ed. by A.G. Miamee, Hampton, VA, August 1991, pp. 62-80.

73. Dargahi-Noubary, G. R., "A Uniformly Modulated Nonstationary Model for Seismic Records," Proceedings of Workshop on Nonstationary Stochastic Processes and Their Applications, Ed. by A.G. Miamee, Hampton, VA, August 1991, pp. 81-101.

74. Dowling, N. E., "Fatigue Failure Predictions for Complicated Stress-Strain Histories," Journal of Materials, Vol. 7, 1972, pp. 71-87.

75. Matsuishi, M. and Endo, T., "Fatigue of Metals Subject to Varying Stress," paper presented to Japan Society of Mechanical Engineers, Japan, 1968.

76. Rychlik, I., "A New Definition of the Rain-Flow Cycle Counting Method," International Journal of Fatigue, Vol. 9, 1987, pp. 119-121.

77. Rychlik, I., "Rain-Flow Cycle Distribution for Ergodic Load Processes," SIAM Journal of Applied Mathematics, Vol. 48, 1988, pp. 662-679.

78. Rychlik, I., "Simple Approximation of the rain-Flow Cycle Distribution for Discretized Random Loads," Probabilistic Engineering Mechanics, Vol. 4, 1989, pp. 40-48.

79. Bishop, N. W. N. and Sherratt, F., "Fatigue Life Prediction from Power Spectral Density Data. Part 1, Traditional Approaches and Part 2, Recent Developments," Environmental Engineering, Vol. 2, Nos. 1 and 2, 1989.

80. Bishop, N. W. N. and Sherratt, F., "A Theoretical Solution for the Estimation of Rain-flow Ranges from Power Spectral Density Data. Fatigue fracture Engineering Material Structures, Vol. 13, No. 4, 1990, pp: 311-326.

81. Dirlik, T., *Application of Computers in Fatigue Analysis*, Ph.D. Dissertation University of Warwick, 1985.

82. Robinson, J. H., Chiang, C. K. and Rizzi, S. A., "Nonlinear Random Response Prediction Using MSC/NASTRAN, NASA Technical Memorandum 109029, 1993.

83. Rizzi, S. A., and Muravyov, A. A., "Improved Equivalent Linearization Implementations Using Nonlinear Stiffness Evaluation." NASA Technical Memorandum, 2001-210838, 2001.

84. Bogner, F. K., Fox, R. L. and Schmit, L. A., "The Generation of Inter-Element Compatible Stiffness and Mass Matrices by the Use of Interpolation Formulas," AFFDL-TR-66-80, Wright-Patterson AFB, OH, 1996, pp. 396-443.

85. Green, P. D. and Killey, A., "Time Domain Dynamic Finite Element Modeling in Acoustic Fatigue Design," Proceedings 6th International Conference on Structural Dynamics, ISVR, 1997, pp. 1007-1026.

86. Robinson, J. H., "Finite Element Formulation and Numerical Simulation of the Large Deflection Random Vibration of Laminated Composite Plates," MS Thesis, Old Dominion University, 1990.

87. Rychlik, I., "Simulation of Load Sequences from Rainflow Matrices: Markov Method, Statistical Research Report, Department of Mathematical Statistics, Lund, 1995, pp. 1-23.

88. Rice, S. O., "Mathematical Analysis of Random Noise," Selected Papers on Noise and Stochastic Processes, Dover, New York, 1954.

89. Ochi, M. K. and Ahn, K., "Probability Distribution Applicable to Non-Gaussian Random Processes," Probabilistic Engineering Mechanics, Vol. 9, 1994, pp. 255-264.

90. Winterstein, S. R., "Nonlinear Vibration Models for Extremes and Fatigue," Journal of Engineering Mechanics, ASCE, Vol. 114, No. 10, 1988, pp. 1772-1790.

91. Johannesson, P. "Rainflow Analysis of Switching Markov Loads," PhD. Dissertation, Lund Institut of Technology, Sweden, 1999.

92. Mei, C., Dhainaut, J. M., Duan, B., Spotswwood, S. M. and Wolfe, H. F., "Nonlinear Random Response of Composite Panels in an Elevated Thermal Environment," AFRL-VA-WP-TR-2000-3049, WPAFB, OH, 2000.

93. Arnold, R. R. and Vaicaitis, R., "Nonlinear Response and Fatigue of Surface Panels by the Time Domain Monte Carlo Approach," WRDC-TR-90-3081, Wright-Patterson AFB, OH, 1990.

94. Stearns, S. and David, R., *Signal Processing Algorithms in Matlab*, Prentice Hall, Allan V. Oppenheim, Series Editor. New Jersey, 1996.

95. Taylor, B. N. and Kuyatt, C. E., "Guidelines for Evaluating and Expressing the Uncertainty of NIST Measurement Results," NIST, TN 1297, 1994, p. 8.

96. Zienkiewics and Taylor, *The Finite Element Method*, Mc-Graw Hill, 4th Edition, Vol. 2, 1991, pp. 356.

97. Hildebrand, F. B., *Advanced Calculus for Applications*, Prentice-Hall, 2nd Edition, Englewood-Cliffs, New Jersey, 1976, pp. 102-105.

98. Wood, R. D. and Schrefler, B., "Geometrically Non-Linear Analysis – A Correlation of Finite Element Notations," International Journal for Numerical Methods in Engineering, Vol. 12, 1978, pp. 635-642.

99. Barlow, J., "Optimal Stress Locations in Finite Element Models," International Journal for Numerical Methods in Engineering, Vol. 10, 1976, pp. 243-251.

100. Cook, R. D., Malkus, D. S. and Plesha, M. E., "Concepts and Applications of Finite Element Analysis," 3rd Edition, John Wiley, New York, 1989, p. 189.

101. Xue, D. Y., "A Finite Element Frequency Domain Solution of Nonlinear Panel Flutter with Temperature Effects and Fatigue Life Analysis," Ph.D. Dissertation, Old Dominion University, Norfolk, VA, 1991.

102. Xue, D. Y. and Mei, C., "Finite Element Nonlinear Panel Flutter with Arbitrary Temperatures in Supersonic Flow," AIAA Journal, Vol. 31, 1993, pp. 154-162.

103. Shi, Y., Lee, R. and Mei, C., "A Finite Element Multimode Method to Nonlinear Free Vibrations of Composite Plates," AIAA Journal, 1997, Vol. 35, pp. 159-166.

104. Bolotin, V.V., *Random Vibration of Elastic Systems*, Martinus Nijhoff Publishers, 1984, pp. 290-292.

105. Chiang, C.K., "A Finite Element Large Deflection Multi-Mode Random Response Analysis of Complex Panels with Initial Stresses Subjected to Acoustic Loading," Ph.D. Dissertation, Old Dominion University, Norfolk, VA, 1988.

106. Paul, Donald, .B, "Large Deflections of Clamped Rectangular Plates with Arbitrary Temperature Distributions," Vol. 1, AFWAL-TR-81-3003, 1982.

107. Ng, C. F., "The influence of Snap-Through Motion on the Random Response of Curved Panels to Intense Acoustic Excitation," Proceedings of the Third International Conference on Recent Advances in Structural Dynamics, AFWAL, OH, July 1998, pp. 617-627.

108. Schuëller, G. I. And Bucher, C. G., "Non-Gaussian Response of Systems Under Dynamic Excitation," Stochastic Structural Dynamics, Progress in Theory and Applications, Elsevier Applied Science, 1988, pp. 235.

109. Lutes, D.L. and Sarkani, S., *Stochastic Analysis of Structural and Mechanical Vibrations*, Prentice-Hall, New Jersey 07458, 1997.

APPENDICES

A. Transformation Matrices $[T_b]$ and $[T_m]$

The displacement vector of the BFS finite element is

$$\{\delta\} = [w, \quad w_{,x}, \quad w_{,y}, \quad w_{,xy}, \quad u, \quad v]^T \tag{A.1}$$

The displacement vector includes the transverse displacement vector $\{w, w_{,x}, w_{,y}, w_{,xy}\}$ and the membrane vector $\{u, v\}$. The element transverse displacement function w and the in-plane displacement functions u, v are approximated as a bi-cubic and a bi-linear polynomial functions in x and y, which can be written as

$$\begin{aligned} w &= a_1 + a_2 x + a_3 y + a_4 x^2 + a_5 xy + a_6 y^2 + a_7 x^3 + a_8 x^2 y + a_9 xy^2 + a_{10} y^3 \\ &+ a_{11} x^3 y + a_{12} x^2 y^2 + a_{13} xy^3 + a_{14} x^3 y^2 + a_{15} x^2 y^3 + a_{16} x^3 y^3 \\ &= [H_w(x,y)]_{1x16} \{a\}_{16x1} \end{aligned} \tag{A.2}$$

$$\begin{aligned} u &= b_1 + b_2 x + b_3 y + b_4 xy \\ &= [H_u(x,y)]_{1x8} \{b\}_{8x1} \end{aligned} \tag{A.3}$$

$$\begin{aligned} v &= b_5 + b_6 x + b_7 y + b_8 xy \\ &= [H_v(x,y)]_{1x8} \{b\}_{8x1} \end{aligned} \tag{A.4}$$

The coordinates of a 4-node rectangular plate element is shown below

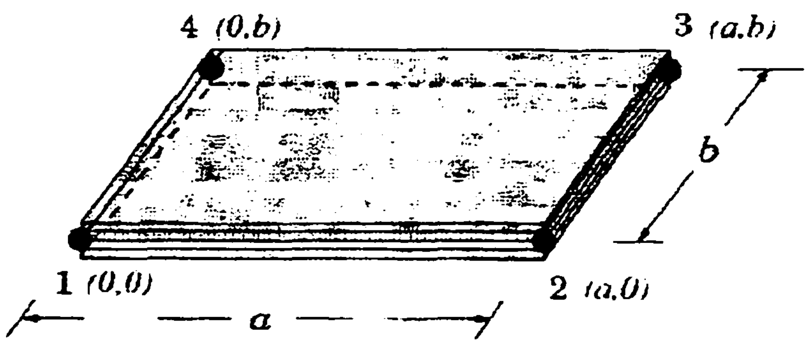

The displacement vector of membrane and transverse displacement can be expressed for the BFS C^1-conforming element as

$$\begin{Bmatrix} u \\ v \end{Bmatrix} = \begin{bmatrix} 1 & x & y & xy & 0 & 0 & 0 & 0 \\ 0 & 0 & 0 & 0 & 1 & x & y & xy \end{bmatrix} \begin{Bmatrix} b_1 \\ \vdots \\ b_8 \end{Bmatrix} \tag{A.5}$$

$$\begin{Bmatrix} w \\ w_{,x} \\ w_{,y} \\ w_{,xy} \end{Bmatrix} = \begin{bmatrix} 1 & x & y & x^2 & xy & y^2 & x^3 & x^2y & xy^2 & y^3 & x^3y & x^2y^2 & xy^3 & x^3y^2 & x^2y^3 & x^3y^3 \\ 0 & 1 & 0 & 2x & y & 0 & 3x^2 & 2xy & y^2 & 0 & 3x^2y & 2xy^2 & y^3 & 3x^2y & 2xy^3 & 3x^2y^3 \\ 0 & 0 & 1 & 0 & x & 2y & 0 & x^2 & 2xy & 3y^2 & x^3 & 2x^2y & 3xy^2 & 2x^3y & 3x^2y^2 & 3x^3y^2 \\ 0 & 0 & 0 & 0 & 1 & 0 & 0 & 2x & 2y & 0 & 3x^2 & 4xy & 3y^2 & 6x^2y & 6xy^2 & 9x^2y^2 \end{bmatrix} \begin{Bmatrix} a_1 \\ \vdots \\ a_{15} \\ a_{16} \end{Bmatrix} \tag{A.6}$$

Substituting the nodal coordinates into Equation A.5, the nodal displacement $\{w_m\}$ can be expressed in the matrix form as $\{w_m\}_{8x1} = [T_m]^{-1}_{8x8}\{b\}_{8x1}$,

$$\begin{Bmatrix} u_1 \\ u_2 \\ u_3 \\ u_4 \\ v_1 \\ v_2 \\ v_3 \\ v_4 \end{Bmatrix} = \begin{bmatrix} 1 & 0 & 0 & 0 & 0 & 0 & 0 & 0 \\ 1 & a & 0 & 0 & 0 & 0 & 0 & 0 \\ 1 & a & b & ab & 0 & 0 & 0 & 0 \\ 1 & 0 & b & 0 & 0 & 0 & 0 & 0 \\ 0 & 0 & 0 & 0 & 1 & 0 & 0 & 0 \\ 0 & 0 & 0 & 0 & 1 & a & 0 & 0 \\ 0 & 0 & 0 & 0 & 1 & a & b & ab \\ 0 & 0 & 0 & 0 & 1 & 0 & b & 0 \end{bmatrix} \begin{Bmatrix} b_1 \\ b_2 \\ b_3 \\ b_4 \\ b_5 \\ b_6 \\ b_7 \\ b_8 \end{Bmatrix} \tag{A.7}$$

The in-plane transformation matrix $[T_m]$ is therefore obtained by inverting the above matrix $[T_m]^{-1}$.

Similarly, substituting the nodal coordinates into Equation A.6, the nodal displacement $\{w_b\}$ can be expressed in the matrix form as $\{w_b\} = [T_b]^{-1}\{a\}$,

$$
\begin{Bmatrix} w_1 \\ w_2 \\ w_3 \\ w_4 \\ w_{,x1} \\ w_{,x2} \\ w_{,x3} \\ w_{,x4} \\ w_{,y1} \\ w_{,y2} \\ w_{,y3} \\ w_{,y4} \\ w_{,xy1} \\ w_{,xy2} \\ w_{,xy3} \\ w_{,xy4} \end{Bmatrix}
=
\begin{bmatrix}
1 & 0 & 0 & 0 & 0 & 0 & 0 & 0 & 0 & 0 & 0 & 0 & 0 & 0 & 0 & 0 \\
1 & a & 0 & a^2 & 0 & 0 & a^3 & 0 & 0 & 0 & 0 & 0 & 0 & 0 & 0 & 0 \\
1 & a & b & a^2 & ab & b^2 & a^3 & a^2b & ab^2 & b^3 & a^3b & a^2b^2 & ab^3 & a^3b^2 & a^2b^3 & a^3b^3 \\
1 & 0 & b & 0 & 0 & b^2 & 0 & 0 & 0 & b^3 & 0 & 0 & 0 & 0 & 0 & 0 \\
0 & 1 & 0 & 0 & 0 & 0 & 0 & 0 & 0 & 0 & 0 & 0 & 0 & 0 & 0 & 0 \\
0 & 1 & 0 & 2a & 0 & 0 & 3a^2 & 0 & 0 & 0 & 0 & 0 & 0 & 0 & 0 & 0 \\
0 & 1 & 0 & 2a & b & 0 & 3a^2 & 2ab & b^2 & 0 & 3a^2b & 2ab^2 & b^3 & 3a^2b^2 & 2ab^3 & 3a^2b^3 \\
0 & 1 & 0 & 0 & b & 0 & 0 & 0 & b^2 & 0 & 0 & 0 & b^3 & 0 & 0 & 0 \\
0 & 0 & 1 & 0 & 0 & 0 & 0 & 0 & 0 & 0 & 0 & 0 & 0 & 0 & 0 & 0 \\
0 & 0 & 1 & 0 & a & 0 & 0 & a^2 & 0 & 0 & a^3 & 0 & 0 & 0 & 0 & 0 \\
0 & 0 & 1 & 0 & a & 2b & 0 & a^2 & 2ab & 3b^2 & a^3 & 2a^2b & 3ab^2 & 2a^3b & 3a^2b^2 & 3a^3b^2 \\
0 & 0 & 1 & 0 & 0 & 2b & 0 & 0 & 0 & 3b^2 & 0 & 0 & 0 & 0 & 0 & 0 \\
0 & 0 & 0 & 0 & 1 & 0 & 0 & 0 & 0 & 0 & 0 & 0 & 0 & 0 & 0 & 0 \\
0 & 0 & 0 & 0 & 1 & 0 & 0 & 2a & 0 & 0 & 3a^2 & 0 & 0 & 0 & 0 & 0 \\
0 & 0 & 0 & 0 & 1 & 0 & 0 & 2a & 2b & 0 & 3a^2 & 4ab & 3b^2 & 6a^2b & 6ab^2 & 9a^2b^2 \\
0 & 0 & 0 & 0 & 1 & 0 & 0 & 0 & 2b & 0 & 0 & 0 & 3b^2 & 0 & 0 & 0
\end{bmatrix}
\begin{Bmatrix} a_1 \\ a_2 \\ a_3 \\ a_4 \\ a_5 \\ a_6 \\ a_7 \\ a_8 \\ a_9 \\ a_{10} \\ a_{11} \\ a_{12} \\ a_{13} \\ a_{14} \\ a_{15} \\ a_{16} \end{Bmatrix}
\tag{A.8}
$$

where the bending transformation matrix $[T_b]$ is therefore obtained by inverting the above matrix $[T_b]^{-1}$.

B. Fortran Code for Gaussian-Stationary Random Load Generation

```
C***********************************************************************
C
C                                    SIMLOAD
C
C***********************************************************************
C   N                    --NO. OF INTERVALS IN THE SPECTRUM
C                          N  SHOULD BE AN INTEGER POWER OF TWO
C   NPT                  --NO.OF POINTS FOR THE TIME SERIES
C                          NPT SHOULD BE INTEGER POWER OF TWO. NPT>N
C   ISEED                --RANDOM NUMBER SEED
C   TTOTAL  = N/FMAX        TTOTAL IS THE TOTAL INTEGRATION TIME
C   DT = N/(NPT*FMAX)   DT IS THE INTEGRATION TIME STEP SIZE
C--------------------------------------------------------------
C***********************************************************************
C INSTRUCTIONS FOR SETTING THE DATA
C -----------------------------------------------------------------------
C 1- TAKE HIGHEST FREQUENCY, FMAX
C 2- MINIMUM TIME STEP IS STEP_MIN=1/(2.5xFMAX)
C 3- N=FMAX x 2
C 4- PICK UP TOTAL RUNNING TIME (1 SEC, 2 SEC ...) T_total=N/FMAX
C 5- SELECT NPT TO SATISFY 2-
C                                          N
C                                 STEP=-----------
C                                      NPT x FMAX
C
C***********************************************************************
    PROGRAM SIMLOAD
    IMPLICIT REAL*8 (A-H,O-Z)
C     COMMON /XFER/ISTEP,DSTEP,DT,Y(16384)
C     COMMON /XFER/DT,Y(16384)
C     REAL*8 DT,Y(2)
       DIMENSION X(16384),Y(16384),SP(2048),W(2048),RAND(16384)
    COMPLEX X,ZIMAG
       OPEN (1,file='d:\research\load_st\pressure.dat')
       OPEN (2,file='d:\research\load_st\npt.dat')
       OPEN (3,file='d:\research\load_st\fmax.dat')
       OPEN (4,file='d:\research\load_st\n.dat')
       DATA FMAX/1024./
       DATA N,NPT /2048,16384/
C***********************************************************************
C                            INITIALIZE VARIABLES
C***********************************************************************
C     SPL=120
```

```
C     SPP = 8.41438*10**(-18.+SPL/10.)
      PI = 3.1415926
      PI2 = PI*2.0
      NP1 = N+1
      ZIMAG = CMPLX(0.0,1.0)
      SPPW = SPP/PI2
      WU = FMAX*PI2
      DW = WU/FLOAT(N)
      DO 119 I=1,NP1
       SP(I) = SPPW
       W(I) = (I-1)*DW
119   CONTINUE
      AREA = SPP*FMAX
      SQ2DW = DSQRT(2.0*DW)
      TTOTAL=PI2/DW
      DT=TTOTAL/FLOAT(NPT)
C***********************************************************************
C  SET X(1)=0. IN ORDER TO OBTAIN NEW MEAN ZERO TIME SERIES
C**C*********************************************************************
X(1)=CMPLX(0.0,0.0)
  DO 50 I=N+1,NPT
        X(I)=CMPLX(0.0,0.0)
50    CONTINUE
C***********************************************************************
C     GENERATE RANDOM PHASE ANGLES UNIFORMLY DISTRIBUTED
BETWEEN  ZERO AND 2.*PI
C***********************************************************************
      ISEED=12357
         DO 51 I=1,N
51    RAND(I)=RAN(ISEED)
      DO 60 I=2,N+1
       PHI=RAND(I-1)*PI2
       P1=SQ2DW*DSQRT(SP(I))
       X(I)=P1*CDEXP(-ZIMAG*PHI)
60    CONTINUE
C***********************************************************************
C                       PERFORM FORWARD TRANSFORM
C***********************************************************************
      CALL FFT(X,NPT,1)
C***********************************************************************
C                                 GET REAL PART
C***********************************************************************
      DO 70 I=1,NPT
         Y(I)=REAL(X(I))
70    CONTINUE
         WRITE(1,FMT=100) Y
```

```
100  FORMAT (f18.8)
       WRITE (2,*) NPT
       WRITE (3,*) FMAX
       WRITE (4,*) N,DT,SPP
       STOP
       END

C*********************************************************************
C
C                                   FFT
C
C*********************************************************************
    SUBROUTINE FFT(X,N,K)
       IMPLICIT INTEGER(A-Z)
       REAL*4 GAIN,PI2,ANG,RE,IM
       COMPLEX X(N),XTEMP,T,U(16),V,W
       LOGICAL NEW
       DATA PI2,GAIN,NO,KO/6.283185307,1.0,0,0/

       NEW=NO.NE.N
       IF(.NOT.NEW)GOTO 2
       L2N=0
       NO=1
1    L2N=L2N+1
    NO=NO+NO
       IF(NO.LT.N)GOTO 1
       GAIN=1.0/N
       ANG=PI2*GAIN
       RE=COS(ANG)
       IM=SIN(ANG)
2    IF(.NOT.NEW.AND.K*KO.GE.1)GOTO 4
    U(1)=CMPLX(RE,-SIGN(IM,FLOAT(K)))

       DO 3 I=2,L2N
3    U(I)=U(I-1)*U(I-1)

    KO=K
4    SBY2=N

    DO 7 STAGE=1,L2N
        V=U(STAGE)
        W=(1.0,0.0)
        S=SBY2
        SBY2=S/2
        DO 6 L=1,SBY2
         DO 5 I=1,N,S
```

```
            P=I+L-1
            Q=P+SBY2
            T=X(P)+X(Q)
            X(Q)=(X(P)-X(Q))*W
5         X(P)=T
6       W=W*V
7     CONTINUE

      DO 9 I=1,N
          INDEX=I-1
          JNDEX=0
          DO 8 J=1,L2N
            JNDEX=JNDEX+JNDEX
            ITEMP=INDEX/2
            IF(ITEMP+ITEMP.NE.INDEX)JNDEX=JNDEX+1
            INDEX=ITEMP
8         CONTINUE
        J=JNDEX+1
          IF(J.LT.I)GOTO 9
          XTEMP=X(J)
          X(J)=X(I)
          X(I)=XTEMP
9     CONTINUE

      IF(K.GT.0)RETURN

        DO 10 I=1,N
10      X(I)=X(I)*GAIN

      RETURN
        END
```

C. Recorded Flight Data

Data set 1:

```
B-1B AEB Baseline Flight # 1
 Ground - max AB - takeoff roll
TIME HISTORY - AMPLITUDE
 0.32692307E+04  0.15294118E-03  0.00000000E+00  0.10944930E+02
   1    1    5     MIKE 5     71564   0.35681E+00
```

```
B-1B AEB Baseline Flight # 1
 Ground - max AB - rotate
TIME HISTORY - AMPLITUDE
 0.32692307E+04  0.15294118E-03  0.00000000E+00  0.89407883E+01
   1    1    5     MIKE 5     58460   0.37086E+00
```

```
B-1B AEB Baseline Flight # 1
 Ground - max AB - gear up
TIME HISTORY - AMPLITUDE
 0.32692307E+04  0.15294118E-03  0.00000000E+00  0.14953213E+02
   1    1    5     MIKE 5     97772   0.32552E+00
```

Data set 2:

```
B-1B AEB Baseline Flight # 2
 Ground - max AB - roll
TIME HISTORY - AMPLITUDE
 0.32692307E+04  0.15294118E-03  0.00000000E+00  0.49325061E+01
   1    1    5     MIKE 5     32252   0.36949E+00
```

```
B-1B AEB Damped Flight # 2
 max AB - rotate
TIME HISTORY - AMPLITUDE
 0.32692307E+04  0.15294118E-03  0.00000000E+00  0.49318943E+01
   1    1    5     MIKE 5     32248   0.38909E+00
```

```
B-1B AEB Damped Flight # 2
 max AB - gear up
TIME HISTORY - AMPLITUDE
 0.32692307E+04  0.15294118E-03  0.00000000E+00  0.49325061E+01
   1    1    5     MIKE 5     32252   0.33682E+00
```

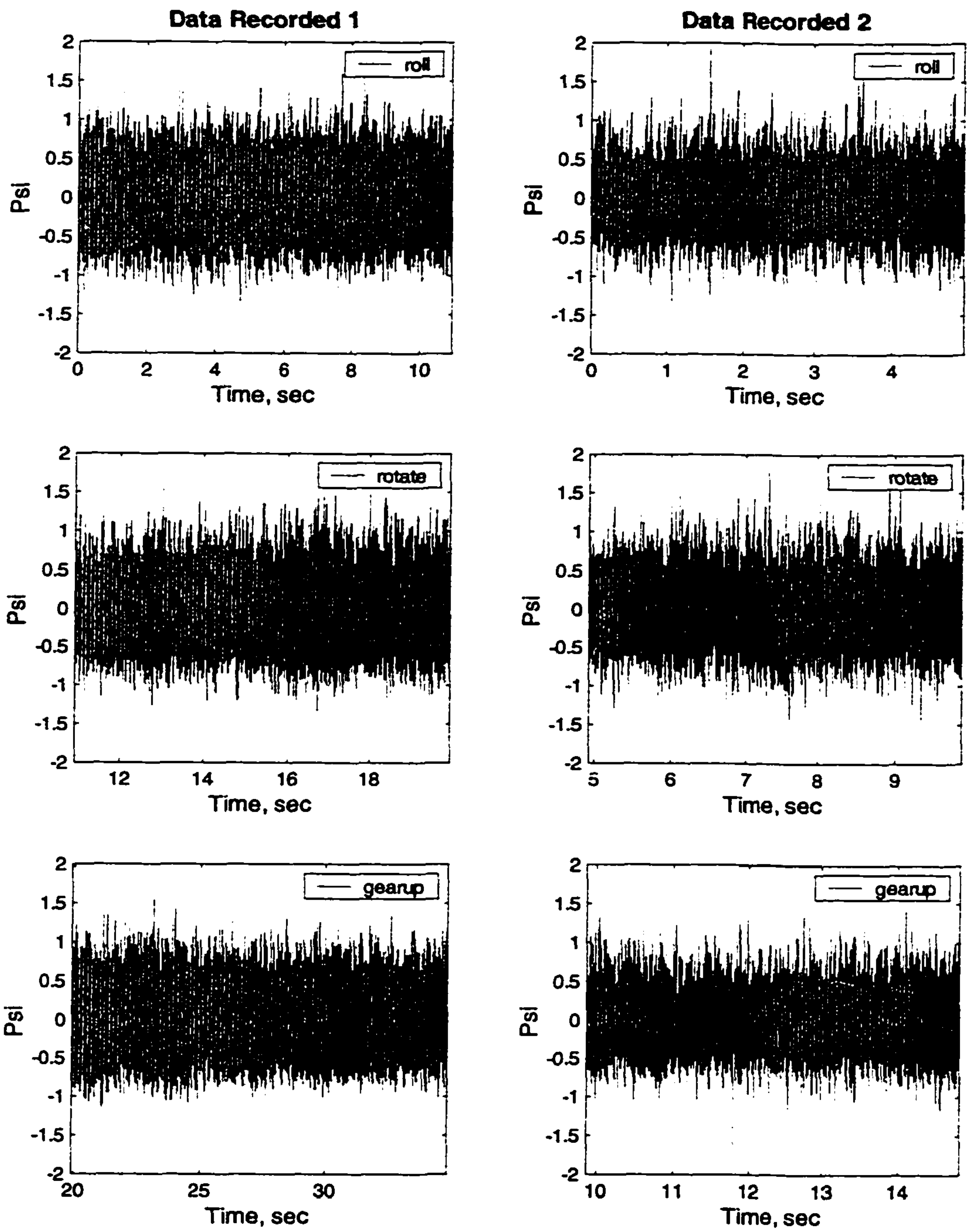
Data Recorded 1
Data Recorded 2
roll
rotate
gearup
Psi
Time, sec

D. Continuum Classical Solution

1. Equation of Motion

The classical plate thin-plate theory based on the Kirchhoff hypothesis and the von Karman-type geometric nonlinearity lead to the total strains

$$\varepsilon_x = \varepsilon_x^o + z\kappa_x \tag{D1a}$$

$$\varepsilon_y = \varepsilon_y^o + z\kappa_y \tag{D1b}$$

$$\gamma_{xy} = \gamma_x^o + z\kappa_{xy} \tag{D1c}$$

where the membrane strains are defined as

$$\varepsilon_x^o = u,_x + \frac{1}{2} w,_x^2 \tag{D2a}$$

$$\varepsilon_y^o = v,_y + \frac{1}{2} w_y^2 \tag{D2b}$$

$$\gamma_{xy}^o = u,_y + v,_x + w,_x \, w,_y \tag{D2c}$$

and assuming that the slopes $w,_x^2, w,_y^2, w,_x \, w,_y$ are very small compared to unity, the middle surface curvatures can be written as

$$\kappa_x = -w,_{xx} \qquad \kappa_y = -w,_{yy} \qquad \kappa_{xy} = -2w,_{xy} \tag{D3}$$

The dynamic composite plate nonlinear equations are obtained by applying the d'Alembert's principle to an element of the k^{th} layer of the laminate. Integrating the d'Alembert's equations over the thickness of the plate h, gives the following equations

$$N_{x,x} + N_{xy,y} = \rho u_{,tt} \qquad N_{xy,x} + N_{y,y} = \rho v_{,tt} \tag{D4}$$

$$M_{x,xx} + 2M_{xy,xy} + M_{y,yy} = N_x w_{,xx} + 2N_{xy} w,_{xy} + N_y w,_{yy} + p(x,y,t) = \rho h w,_{tt} \tag{D5}$$

where the average mass density of the composite laminate is defined by

$$\rho = \int_{-h/2}^{h/2} \rho_o^k dz \tag{D6}$$

The constitutive relations for a laminated composite plate are

$$\begin{Bmatrix} N \\ M \end{Bmatrix} = \begin{bmatrix} A & B \\ B & D \end{bmatrix} \begin{Bmatrix} \varepsilon^o \\ \kappa \end{Bmatrix} \tag{D7}$$

where the laminate stiffness A, B, and D are defined by the following integrals

$$(A_{ij}, B_{ij}, D_{ij}) = \int_{-h/2}^{h/2} (1, z, z^2)(\overline{Q}_{ij})_k dz, \quad i, j = 1, 2, 6 \tag{D8}$$

and the matrix $\overline{Q}$ is the transformed reduced stiffness matrix.

For a specially orthotropic plate, the component $A_{16} = A_{26} = D_{16} = D_{26} = B_{ij} = 0$.

Equation (D7) can be rewritten as the half-inverted constitutive equation,

$$\begin{Bmatrix} \varepsilon^o \\ M \end{Bmatrix} = \begin{bmatrix} A^* & 0 \\ 0 & D^* \end{bmatrix} \begin{Bmatrix} N \\ \kappa \end{Bmatrix} \tag{D9}$$

where

$$A^* = A^{-1} \qquad D^* = D \tag{D10}$$

The Airy stress function F is defined such that

$$N_x = F,_{yy} \qquad N_y = F,_{xx} \qquad N_{xy} = -F,_{xy} \tag{D11}$$

Assuming that the effect of the in-plane inertia forces can be neglected, the inertia terms in u and v in equation (D4) can be dropped. Replacing equations (D3), (D7), (D9), and (D11) in equation (D5) leads to the equation of motion in the transverse direction.

$$\rho h \ddot{w} = L_1 w - \phi(F, w) - p = 0 \tag{D12}$$

where L_1 is a linear operator defined as

$$L_1 = D_{11}^{*}\frac{\partial^4}{\partial x^4} + (D_{12}^{*} + 2D_{66}^{*})\frac{\partial^4}{\partial x^2 \partial y^2} + D_{22}^{*}\frac{\partial^4}{\partial y^4} \tag{D13}$$

and $\phi(F,w)$ represents the nonlinear terms expressed as

$$\phi(F,w) = F,_{yy}\, w,_{xx} - 2F,_{xy}\, w,_{xy} + F,_{xx}\, w,_{yy}$$

To ensure uniqueness in the solution the compatibility equation is derived by combining the second derivatives of the membrane strain equations (D2)

$$\varepsilon^{o}_{,yyx} + \varepsilon^{o}_{y,xx} - \gamma^{o}_{xy,xy} + \frac{1}{2}\phi(w,w) = 0 \tag{D14}$$

Combining equations (D9), (D11), and (D14) the compatibility equation can be rewritten

$$L_2 F + \frac{1}{2}\phi(w,w) = 0 \tag{D15}$$

where L_2 is a new linear operator defined as

$$L_2 = A_{22}^{*}\frac{\partial^4}{\partial x^4} + (A_{12}^{*} + A_{66}^{*})\frac{\partial^4}{\partial x^2 \partial y^2} + A_{11}^{*}\frac{\partial^4}{\partial y^4} \tag{D16}$$

Equations (D12) and (D15) are the dynamic governing equations of motion of a specially orthotropic composite plate undergoing moderately large deflections. The solution of these equations in the general case is unknown. In the present work, the approximate Galerkin's approach has been retained.

2.2 Method of analysis for lowest two modes (1,1) and (1,3)

Consider a rectangular [0/90/0] orthotropic composite plate of dimensions a by b by h. The boundary conditions are simply supported boundary and are defined as,

$$\begin{aligned} x = \pm a: &\quad w = 0 \quad D_{11} w,_{xx} + D_{12} w,_{yy} = 0 \\ x = \pm b: &\quad w = 0 \quad D_{12} w,_{xx} + D_{22} w,_{yy} = 0 \end{aligned} \tag{D17}$$

The deflection function, $w(x,y,t)$, that satisfies the equations of motions (D12), (D15) as well as the boundary conditions (D17) for two arbitrary modes is

$$w(x,y,t) = h\left[q_{m_1n_1}(t)\sin(\frac{m_1\pi x}{a})\sin(\frac{n_1\pi y}{b}) + q_{m_3n_3}(t)\sin(\frac{m_3\pi x}{a})\sin(\frac{n_3\pi y}{b})\right] \quad \text{(D18)}$$

Under a uniform loading only the odd modes are not zero. Consequently, the lowest two modes are either (1,1), (1,3) or (1,1), (3,1). For the present case, the dimensions a and b of the rectangular orthotropic plate gives the second lowest mode for $m_3 = 1$, $n_3 = 3$. The transverse displacement becomes

$$w(x,y,t) = h\left[q_{11}(t)\sin(\frac{\pi x}{a})\sin(\frac{\pi y}{b}) + q_{13}(t)\sin(\frac{\pi x}{a})\sin(\frac{3\pi y}{b})\right] \quad \text{(D19)}$$

Replacing (D19) in the compatibility equation (D15) and solving the partial differential equation term by term leads to particular solution of the stress function $F = F_p + F_h$, which is has the form

$$F_p = F_{p1}\,Cos\left[\frac{2\pi x}{a}\right] + F_{p2}\,Cos\left[\frac{2\pi y}{b}\right] + F_{p3}\,Cos\left[\frac{4\pi y}{b}\right] + F_{p4}\,Cos\left[\frac{6\pi y}{a}\right] + F_{p5}\,Cos\left[\frac{2\pi x}{a} - \frac{4\pi y}{b}\right] +$$
$$F_{p6}\,Cos\left[\frac{2\pi x}{a} - \frac{2\pi y}{b}\right] + F_{p7}\,Cos\left[\frac{2\pi x}{a} + \frac{2\pi y}{b}\right] + F_{p8}\,Cos\left[\frac{2\pi x}{a} + \frac{4\pi y}{b}\right]$$

where the coefficients are

$$F_{p1} = \frac{a^2h^2(q_{11}^2 + 9q_{13}^2)}{32\,b^2A_{22}}$$

$$F_{p2} = \frac{b^2h^2q_{11}(q_{11} - 2q_{13})}{32a^2A_{11}}$$

$$F_{p3} = \frac{b^2 h^2 q_{11} q_{13}}{64 a^2 A_{11}}$$

$$F_{p4} = \frac{b^2 h^2 q_{13}^2}{288 a^2 A_{11}}$$

$$F_{p5} = \frac{a^2 b^2 h^2 q_{11} q_{13}}{32(16a^4 A_{11} + 4a^2 b^2 (2A_{12} + A_{66}) + b^4 A_{22})} \tag{D20}$$

$$F_{p6} = -\frac{a^2 b^2 h^2 q_{11} q_{13}}{8(a^4 A_{11} + a^2 b^2 (2A_{12} + A_{66}) + b^4 A_{22})}$$

$$F_{p7} = \frac{a^2 b^2 h^2 q_{11} q_{13}}{8(a^4 A_{11} + a^2 b^2 (2A_{12} + A_{66}) + b^4 A_{22})}$$

$$F_{p8} = \frac{a^2 b^2 h^2 q_{11} q_{13}}{32(16a^4 A_{11} + 4a^2 b^2 (2A_{12} + A_{66}) + b^4 A_{22})}$$

The homogenous solution F_h is assumed such it satisfies the inplane boundary conditions. For immovable edges, the inplane boundary conditions are

$$\begin{aligned} &x = 0, a : F_{xy} = 0 \qquad \iint(\varepsilon_x^o - \frac{1}{2} w,_x^2)dxdy = 0 \\ &x = 0, b : F_{xy} = 0 \qquad \iint(\varepsilon_y^o - \frac{1}{2} w,_y^2)dxdy = 0 \end{aligned} \tag{D21}$$

and the assumed homogenous solution is

$$F_h = \overline{N}_y \frac{x^2}{2} + \overline{N}_x \frac{y^2}{2}$$

Substituting (D2) and (D11) into (D21) and integrating over the surface gives,

$$\overline{N}_x = \frac{\pi^2 h^2 (a^2 A_{11}^* (q_{11}^2 + 9q_{13}^2) - b^2 A_{22}^* (q_{11}^2 + q_{13}^2)}{8a^2 (A_{12}^{*2} - A_{11}^* A_{22}^*)} \tag{D22}$$

$$\overline{N}_y = \frac{\pi^2 h^2 (b^2 A_{12}^{*}(q_{11}^2 + q_{13}^2) - a^2 A_{11}^{*}(q_{11}^2 + 9q_{13}^2)}{8a^2(A_{12}^{*2} - A_{11}^{*}A_{22}^{*})}$$

Substituting the stress function F into the equation of motion (D12) and applying Galerkin's method yields to the two modes modal equations.

$$\begin{aligned}
\ddot{q}_{11} + \omega_{o1}^2 q_{11} + \beta_{a1} q_{11}^3 + \beta_{b1} q_{11} q_{13}^2 + \beta_{c1} q_{11}^2 q_{13} + \beta_{d1} q_{13}^3 &= p_o(t)/m_1 \\
\ddot{q}_{13} + \omega_{o2}^2 q_{13} + \beta_{a2} q_{11}^3 + \beta_{b2} q_{11} q_{13}^2 + \beta_{c2} q_{11}^2 q_{13} + \beta_{d2} q_{13}^3 &= p_o(t)/m_2
\end{aligned} \qquad \text{(D23)}$$

where the linear frequencies terms are

$$\begin{aligned}
\omega_{01}^2 &= \frac{\pi^4 (b^4 D_{11}^{*} + 2a^2 b^2 (D_{12}^{*} + 2D_{66}^{*}) + a^4 D_{22}^{*}}{a^4 b^4 h\rho} \\
\omega_{02}^2 &= \frac{\pi^4 (b^4 D_{11}^{*} + 18a^2 b^2 (D_{12}^{*} + 2D_{66}^{*}) + 81a^4 D_{22}^{*}}{a^4 b^4 h\rho}
\end{aligned} \qquad \text{(D24)}$$

the modal masses are

$$\begin{aligned}
m_1 &= \frac{16}{\pi^2 h^2 \rho} \\
m_2 &= \frac{16}{3\pi^2 h^2 \rho}
\end{aligned} \qquad \text{(25)}$$

and the non linear terms are

$$\beta_{a1} = \frac{\pi^4 h(a^4 A_{11}^{*} + b^4 A_{22}^{*})}{16a^4 b^4 \rho A_{11}^{*} A_{22}^{*}} - \frac{\pi^4 h(a^4 A_{11}^{*} - 2a^2 b^2 A_{12}^{*} + b^4 A_{22}^{*})}{8a^4 b^4 \rho (A_{12}^{*2} - A_{11}^{*} A_{22}^{*})}$$

$$\begin{aligned}
\beta_{b1} = {} & \frac{\pi^4 h(9a^4 A_{11}^{*} + 4b^4 A_{22}^{*})}{16a^4 b^4 \rho A_{11}^{*} A_{22}^{*}} - \frac{\pi^4 h(9a^4 A_{11}^{*} - 10a^2 b^2 A_{12}^{*} + b^4 A_{22}^{*})}{8a^4 b^4 \rho (A_{12}^{*2} - A_{11}^{*} A_{22}^{*})} \\
& + \frac{\pi^4 h}{\rho(a^4 A_{11}^{*} + a^2 b^2 (2A_{12}^{*} + A_{66}^{*}) + b^4 A_{22}^{*})} + \frac{\pi^4 h}{16\rho(16a^4 A_{11}^{*} + 4a^2 b^2 (2A_{12}^{*} + A_{66}^{*}) + b^4 A_{22}^{*})}
\end{aligned}$$

$$\beta_{c1} = -\frac{3\pi^4 h}{16\rho a^4 A_{11}^{*}} \tag{D26}$$

$$\beta_{d1} = 0$$

$$\beta_{a2} = -\frac{\pi^4 h}{16\rho a^4 A_{11}^{*}}$$

$$\beta_{b2} = \frac{\pi^4 h(9a^4 A_{11}^{*} + 4b^4 A_{22}^{*})}{16a^4 b^4 \rho A_{11}^{*} A_{22}^{*}} - \frac{\pi^4 h(9a^4 A_{11}^{*} - 10a^2 b^2 A_{12}^{*} + b^4 A_{22}^{*})}{8a^4 b^4 \rho(A_{12}^{*2} - A_{11}^{*} A_{22}^{*})} + \frac{\pi^4 h}{\rho(a^4 A_{11}^{*} + a^2 b^2 (2A_{12}^{*} + A_{66}^{*}) + b^4 A_{22}^{*})}$$

$$\beta_{c2} = 0$$

$$\beta_{d2} = \frac{\pi^4 h(81a^4 A_{11}^{*} + b^4 A_{22}^{*})}{16a^4 b^4 \rho A_{11}^{*} A_{22}^{*}} - \frac{\pi^4 h(81a^4 A_{11}^{*} - 18a^2 b^2 A_{12}^{*} + b^4 A_{22}^{*})}{8a^4 b^4 \rho(A_{12}^{*2} - A_{11}^{*} A_{22}^{*})}$$

E. Linear Random Vibration

From PDE for an isotropic rectangular plate,

$$\rho h \frac{\partial^2 w}{\partial t^2} + D\nabla^4 w = p_0(t) \tag{E1}$$

For a simply supported boundary condition, the plate deflection and mode shape are

$$w(x, y, t) = \sum_m \sum_n q_{mn}(t)\phi_{mn}(x, y)$$

$$\phi_{mn}(x, y) = \sin\left(\frac{m\pi x}{a}\right) \times \sin\left(\frac{m\pi y}{b}\right) \tag{E2}$$

After substitution of Equation (E2) into Equation (E1) and applying the modal orthogonality condition, the modal equations are

$$\ddot{q}_{mn} + \omega_{mn}^2 q_{mn} = \frac{p_0(t)}{m_{mn}}, \qquad m, n=1,3,5\ldots \tag{E3}$$

Adding a structural damping,

$$\ddot{q}_{mn} + 2\xi_{mn}\omega_{mn}\dot{q}_{mn} + \omega_{mn}^2 q_{mn} = \frac{p_0(t)}{m_{mn}} \tag{E4}$$

$$\omega_{mn} = \pi^2 \sqrt{\frac{D}{\rho h}}\left[\left(\frac{m}{a}\right)^2 + \left(\frac{n}{b}\right)^2\right] \text{ rad/sec} \tag{E5}$$

$$m_{mn} = \frac{mn\pi^2 \rho h}{16} \tag{E6}$$

where ω_{mn} and m_{mn} are the natural frequency and modal mass, respectively.

The response to Equation (E4) is given by Equations (3-57) and (7-37) in reference [109],

$$E[q_{mn}^2] = \frac{\pi \times S_0(f)}{8m_{mn}^2 \xi_{mn} \omega_{mn}^3} \tag{E7}$$

set mn=r and kl=s,

$$E[q_{mn}q_{kl}] = E[q_r q_s] = \frac{(\xi_r\omega_r + \xi_s\omega_s)S_0(f)}{m_r m_s\left[(\omega_r^2 - \omega_s^2)^2 + 4\omega_r\omega_s(\xi_r\omega_r + \xi_s\omega_s)(\xi_r\omega_s + \xi_s\omega_r)\right]} \tag{E8}$$

The root mean square of maximum deflection from Equation (E2) is

$$\begin{aligned} RMS(w_{\max}) &= \left\{E\left[\left(\sum_{r=1}^{n} q_r\right)^2\right]\right\}^{1/2} \\ &= \left\{E[q_1^2] + E[q_2^2] + \ldots + 2E[q_1q_2] + \cdots\right\}^{1/2} \end{aligned} \tag{E9}$$

CURRICULUM VITA
for
Jean-Michel Dhainaut

DEGREES:

Doctor of Philosophy (Aerospace Engineering), Old Dominion University, Norfolk, Virginia, December 2001.

Master of Science (Aerospace Engineering), Parks College of Saint Louis University, Saint Louis, Missouri, May 1998.

Bachelor of Science (Aerospace Engineering), Parks College of Saint Louis University, Saint Louis, Missouri, May 1997.

PROFESSIONAL CHRONOLOGY:

Department of Aerospace Engineering, Old Dominion University, Norfolk, Virginia

Research Assistant, August 1998-December 2001.

Department of Aerospace Engineering, Parks College of Saint Louis University, Saint Louis, Missouri

Assistant Professor, January 1996-May 1998.

CONSULTING/PART TIME EMPLOYMENT:

NASA Contract. Research Grant NAG-1-2294

Air Force Contract 33615-98-D-3210

ONERA, France. Summer 1997

British Aerospace (AIRBUS), Chester, U.K. Summer 1996

Aerospatiale (AIRBUS), Toulouse, France. Summer 1995

SCIENTIFIC AND PROFESSIONAL SOCIETES MEMBERSHIP:

AIAA Member

SCHOLARLY ACTIVITIES COMPLETED:

1- J. M. Dhainaut, "Modeling and Wind Tunnel Flutter Testing of Large Aircraft Wings," Master Thesis, Parks College, May 1998.

2- J. M. Dhainaut and M. Ferman, "Experiences with the Design, Fabrication and Testing of a Scaled Flutter Model of a Large Transport Wing in The Parks College Wind Tunnel," ASEE Conference, Oshkosh, July 1999.

3- J. M. Dhainaut, B. Duan, C. Mei, S. M. Spottswood and H. F. Wolfe, "NonLinear Response of Composite Panels to Random Excitations at Elevated Temperatures," Proceedings 7th International Conference on Structural Dynamics, Institute of Sound and Vibration Research, University of Southampton, UK, July 2000, pp: 769-784.

4- J. M. Dhainaut, B. Duan, C. Mei, S. M. Spottswood and H. F. Wolfe, "NonLinear Random Response of High-Speed Flight Vehicle Surface Panels," Proceedings 3rd International Conference on Nonlinear Problems in Aviation and Aerospace, Embry-Riddle Aeronautical University, Daytona Beach, FL, May 2000.

5- C. Mei, J. M. Dhainaut, B. Duan, S. M. Spotswwood and H. F. Wolfe, "Nonlinear Random Response of Composite Panels in an Elevated Thermal Environment," AFRL-VA-WP-TR-2000-3049, WPAFB, OH, October 2000.

6- C. Mei and J. M. Dhainaut, "Comparison of Fatigue Life Estimation Using Equivalent Linearization and Time Domain Simulation Methods," Final Report for NASA Grant NAG-1-2294, Old Dominion University Research Foundation, Norfolk, VA, May 2001.

7- J. M. Dhainaut, C. Mei, S. M. Spottswood and H. F. Wolfe, "Nonlinear Panel Response to Nonwhite Acoustic Excitation," Submitted for Presentation at the USAF Aircraft Structural Integrity Program Conference, Williamsburg, VA, December 2001.

8- J. M. Dhainaut, C. Mei, S. M. Spottswood and H. F. Wolfe, "Sonic fatigue Design and Nonlinear Panel Response to Flight Nonwhite Pressure Fluctuations," Submitted for Presentation at the 43rd AIAA Structures, Structural Dynamics and Materials Conference, Denver, CO, April 2002.